

AFIT/DS/ENP/92-5

AD-A258 814



①

EXCITATION AND DE-EXCITATION MECHANISMS

OF Er-DOPED GaAs AND AlGaAs

DISSERTATION

David W. Elsaesser, Captain, USAF

AFIT/DS/ENP/92-5

DTIC
SELECTE
JAN 06 1993
S B D

244

93-00167

Approved for public release; Distribution unlimited

93 1 04 022

EXCITATION AND DE-EXCITATION MECHANISMS OF Er-DOPED GaAs AND AlGaAs

DISSERTATION

Presented to the Faculty of the School of Engineering

of the Air Force Institute of Technology

Air University

In Partial Fulfillment of the

Requirements for the Degree of

Doctor of Philosophy

David W. Elsaesser, B. S., M. S.

Captain, USAF

December 1992

Approved for public release; Distribution unlimited

EXCITATION AND DE-EXCITATION MECHANISMS

OF Er-DOPED GaAs AND AlGaAs

David W. Elsaesser, B.S., M.S.

Captain, USAF

Approved:

DTIC QUALITY INSPECTED 8

Accession For	
NTIS GRA&I	<input checked="checked" type="checkbox"/>
DTIC TAB	<input type="checkbox"/>
Unannounced	<input type="checkbox"/>
Justification	
By	
Distribution/	
Availability Codes	
Dist	Avail and/or Special
A-1	

Yang Kee Seo

3 Dec 1992

Robert Z Hengshold

3 Dec 1992

Edward S. Kolesar

3 Dec 1992

Keith R. Evans

3 Dec 1992

Accepted:

Robert Hahn L

Dean, School of Engineering

Preface

This work involved mostly the electrical characterization of semiconductors. Preparation of the samples required great effort and I called upon the assistance of many individuals, mostly members of the Solid State Electronic Directorate of Wright Labs. Specifically, I am indebted to John Hoelscher for the days he spent doing O, Mg, and Si ion implantation. Mike Cheney, Belinda Johnson, and Bob Fitch provided invaluable advice and council on the fabrication of diodes. Larry Calahan showed an incredible amount of patience with the hundreds of dicing and bonding requests. His assistance was much very much appreciated. I am especially grateful to Dan Johnstone for preserving the DLTS system I used while at Wright Labs. Both Dan and Millard Mier were very kind to make this system available and to provide me with the helium necessary to perform measurements. Finally, for assistance in work performed at AFIT, I would like to thank Greg Smith, the finest technician in the Air Force.

For technical guidance I was, of course, assisted primarily by my advisor, Dr. Yung Kee Yeo, without whose encouragement I would not have undertaken the doctoral program. I also appreciate the time Dr. Robert Hengehold has taken out of his busy schedule as physics department head to steer my research. I am also grateful to Keith Evans who was very generous with MBE-grown Er-doped samples. Further, his willingness to discuss the physics of the Er-doped material was always welcomed. I consider him to be a model scientist. Additionally, I would like to thank these individuals, who also served as committee members, including Lieutenant Colonel Edward Kolesar, for their efforts in reading this document.

Finally, I am especially indebted to my beautiful girlfriend Kristina Retrum. She provided invaluable assistance in restructuring the awful sentences I produced in the original draft. She is certainly a genius, and hopefully, I will be blessed with her company for many years to come.

David W. Elsaesser

Table of Contents

	Page
Preface	iii
List of Figures	viii
List of Tables	xx
Abstract	xxii
I. Introduction	1
1.1. Problem Statement	2
1.2. Sequence of Presentation	6
II. Electron Levels in Semiconductors	8
2.1. Donors and Acceptors	9
2.2. Occupancy of Donor and Acceptor Levels	11
2.3. Electrical and Optical Transitions at Deep Centers	13
III. Characterization Techniques	18
3.1. Hall Effect Measurements	18
3.1.1. Temperature-Dependent Hall Effect Measurements	20
3.2. Capacitance Spectroscopy	24
3.2.1. Majority and Minority Carrier Traps and Shape of the Capacitance Transient	28
3.2.2. Deep Level Transient Spectroscopy	32

3.2.3. Isothermal Transient Capacitance Measurements	34
3.2.4. Experimental and Analytical Implementation	36
3.2.5. Nonexponentiality	41
3.2.5.1. Large Trap Concentrations	41
3.2.5.2. Field-Enhanced Emission	44
3.3. Optical Measurements	48
IV. Sample Preparation and Growth	53
4.1. Ion Implantation	53
4.2. MBE Growth	57
4.3. Ion Implantation vs. MBE Growth	59
4.4. Formation of p^+n and n^+p Junctions	61
V. Properties of Rare Earth Elements in III-V Semiconductors	65
5.1. Introduction	65
5.2. Rare Earth Elements	66
5.3. Electrical Properties of RE-Doped III-V Compounds	70
5.3.1. Donor or Acceptor Behavior	70
5.3.2. Deep States in III-V:RE	71
5.3.3. Donor Gettering or Purification by REs	72

5.4. Excitation Mechanisms	74
IV. Results and Discussion	78
6.1. Introduction	78
6.2. Erbium Doping and Electrical Behavior	79
6.2.1. Ion-Implanted Material	79
6.2.1.1. Effect of Er on $\text{Al}_x\text{Ga}_{1-x}\text{As}$ Substrates	89
6.2.2. Er-Doped, MBE-Grown GaAs and AlGaAs	92
6.2.3. Summary and Discussion	99
6.3. Effect of Er on Deep States in GaAs and AlGaAs Obtained by DLTS Measurements	106
6.3.1. DLTS Measurements on Ion-Implanted GaAs	108
6.3.2. DLTS Measurements on Er-Implanted $\text{Al}_x\text{Ga}_{1-x}\text{As}$	126
6.3.3. DLTS Measurements on MBE-Grown, Er-Doped GaAs	134
6.3.4. Summary and Discussion	136
6.3.4.1. Er-Related Centers in GaAs	138
6.3.4.2. Non Er-Related Hole Trap in GaAs	148
6.3.4.3. Effect of Er Implantation on EL2 and M3 Electron Traps	154
6.3.4.4. Er-Implantation Effect on Deep Centers in AlGaAs	157

	<i>Page</i>
6.4. Annealing Studies and Excitation Mechanisms of Er in GaAs and AlGaAs .	158
6.4.1. Effect of Annealing Conditions on Er-Implanted GaAs	159
6.4.1.1. Er-Doped, MBE-Grown AlGaAs	175
6.4.2. Discussion	177
6.4.2.1. Er-4f Luminescence Excitation and Quenching Mechanisms	182
6.5. Electroluminescence of Er-Doped GaAs	194
VII. Conclusion and Recommendations	198
7.1. Contributions	199
7.2. Overall Behavior of Er-Doped GaAs	205
7.3. Recommendations	206
Bibliography	213
Vita	221

List of Figures

	Page
1. Attenuation vs. wavelength for silica based optical fibers grown by vapor-phase axial deposition (VAD), inside vapor deposition (IVD), and outside vapor deposition (OVD) (after Pearsall)	4
2. Band gap vs. alloy parameter for systems of interest in silica-based optical fiber communications (These fibers have a minimum dispersion at 1.3 μm and a minimum of attenuation at 1.55 μm , after Pearsall)	5
3. Ionization energies of various impurities and defects in GaAs (after Sze)	10
4. Sah's diagram showing the possible energy conserving mechanisms by which charges are exchanged between the conduction and valence bands and electron levels lying deep inside the band gap (Processes a, b, c, and d designate electron capture, electron emission, hole capture, and hole emission, respectively.)	14
5. An arbitrarily shaped sample for van der Pauw measurements showing (a) resistivity configuration and (b) Hall effect configuration	19
6. Schematic diagram of an automated Hall effect system used for high resistivity and temperature-dependent Hall effect measurements	21
7. Temperature-dependent Hall effect data for a relatively deep Si donor in $\text{Al}_{0.5}\text{Ga}_{0.5}\text{As}:\text{Si}$ and a relatively shallow Be acceptor in $\text{GaAs}:\text{Be}$ (Both samples were grown by molecular beam epitaxy.)	23
8. Emission of electrons trapped at centers located in the depletion region of a p^+n junction	26

9.	Saturation injection biasing sequence: (a) steady-state reverse bias, hole traps empty, (b) large forward bias, capture of holes, (c) original reverse bias reestablished, emission of holes, capacitance decreasing	29
10.	Majority-carrier biasing sequence: (a) steady-state reverse bias, electron traps empty, (b) reduced reverse bias with no hole injection, capture of electrons (c) original reverse bias reestablished, emission of electrons, capacitance increasing	30
11.	Capacitance transient shape for saturation injection biasing of p^+n or n^+p junctions, after Sah (The cases are: (1) $e_n^t/e_p^t > c_p^t/c_n^t$, (2) $e_n^t/e_p^t = c_p^t/c_n^t$ and (3) $e_n^t/e_p^t < c_p^t/c_n^t$.)	32
12.	Rate-window concept developed by Lang	33
13.	DLTS plots using different rate windows which show the response of the native EL2 defect in GaAs	35
14.	Rate-window plots for n-type $Al_{0.4}Ga_{0.6}As:Si$ sample showing the DX emission which consists of at least three centers (It is not possible to resolve these centers with the standard rate-window analysis.)	37
15.	Experimental apparatus for performing the isothermal transient capacitance measurements	39
16.	Sequence of transients arising from the EL2 defect in GaAs (Data is shown from 260 K to 400 K, in intervals of 4 K. Each transient is acquired on three separate linear scales, and analyzed for an exponential or multiexponential decay for subsequent Arrhenius analysis.)	40

17.	Schottky diode with a donor center acting as an electron trap showing the depletion width w , the λ -region, and the charge densities	43
18.	Simulated rate-window plots for an n-type GaAs Schottky diode with a shallow-dopant concentration of $N_S = 10^{16} \text{ cm}^{-3}$, a reverse bias of 2 V, and with various electron trap densities, N_T , for an electron trap with $E_T = 0.3 \text{ eV}$ and $\sigma_n = 10^{-14} \text{ cm}^2$. . .	45
19.	Arrhenius analysis of simulated capacitance transients using equation (59) for an n-type GaAs Schottky diode with a shallow dopant concentration of $N_S = 10^{16} \text{ cm}^{-3}$ and an electron trap density $N_T = 0.9 N_S$, with $E_T = 0.3 \text{ eV}$ and $\sigma_T = 10^{-14} \text{ cm}^2$. . .	46
20.	Poole-Frenkel field-enhanced emission, after Schroder	47
21.	Photoluminescence (PL) apparatus for measuring optically active transitions	50
22.	Response of the grating and detector combination in the experimental configuration in Figure 21 relative to a 1000 °C blackbody	51
23.	Typical ion implantation apparatus (after Böer)	54
24.	Damage resulting from a light or heavy implanted ion (after Ghandi)	54
25.	Theoretical LSS distributions for the Er atoms in GaAs after implantation of the given fluences at an energy of 1 MeV	56
26.	Molecular beam epitaxial growth system (after Stradling)	58

27.	Calibration of Er source for the growth of Er-doped GaAs and AlGaAs structures by MBE, showing (a) Er-concentration profile for growths at various Er-cell temperatures and (b) Arrhenius analysis of the temperature-activated dopant density $[Er] = 1.18 \times 10^{31} \exp(-1.95 \text{ eV}/kT)$	60
28.	LSS distributions for Mg and Si ions implanted in GaAs with a fluence of 10^{14} cm^{-2} at an energy of 40 keV (These implants are used to form p^+ or n^+ layers, respectively, for the formation of p^+n and n^+p diodes.)	62
29.	Dimensions and structure of the p^+n or n^+p mesa diodes fabricated using photolithography for DLTS and electroluminescence measurements	63
30.	Square of the radial wave functions for the 4f, 5s, 5p, and 6s orbitals of the Gd^+ ion obtained using Hartree-Fock calculations (after Dieke)	70
31.	SIMS measurement of the as-implanted Er distributions in a GaAs substrate for Er fluences of $\Phi_{Er} = 5 \times 10^{12}$ and $5 \times 10^{13} \text{ cm}^{-2}$ at an energy of 1 MeV (The theoretical LSS distributions are shown as solid lines.)	80
32.	SIMS profiles of Er in GaAs after a 1 MeV implant with a fluence of $\Phi_{Er} = 5 \times 10^{13} \text{ cm}^{-2}$ for the as-implanted substrate after an RTA of 750 °C for 15 seconds, and after an RTA of 850 °C for 15 seconds	81
33.	Capacitance-voltage (CV) carrier profiles for an n-type substrate implanted with Er at fluences of $\Phi_{Er} = 5 \times 10^{12}$, 1×10^{13} , and $5 \times 10^{13} \text{ cm}^{-2}$, each with an energy of 1 MeV and each annealed at 825 °C for 12 seconds	84

34. CV carrier profiles for Er implanted at a fluence of $\Phi_{\text{Er}} = 5 \times 10^{12} \text{ cm}^{-2}$ and with an implant energy of 1 MeV into an n-type GaAs substrate with $n \approx 3 \times 10^{17} \text{ cm}^{-3}$. . 85

35. CV carrier profiles for an Er implant at a fluence of $\Phi_{\text{Er}} = 5 \times 10^{12} \text{ cm}^{-2}$ implanted into a p-type GaAs substrate with $p \approx 4 \times 10^{16} \text{ cm}^{-3}$ 86

36. Temperature-dependent hole concentration and resistivity of a p-type substrate with no treatment, and the same substrate implanted with Er at a fluence of $\Phi_{\text{Er}} = 5 \times 10^{13} \text{ cm}^{-2}$ and at an energy of 1 MeV, and annealed at 750 °C for 15 seconds (Solid symbols represent the Er-doped sample.) 87

37. Temperature-dependent electron concentration and resistivity of an n-type substrate with no treatment, and the same substrate implanted with Er at a fluence of $\Phi_{\text{Er}} = 5 \times 10^{13} \text{ cm}^{-2}$ and an energy of 1 MeV, and annealed at 750 °C for 15 seconds (Solid symbols represent the Er-doped sample.) 88

38. CV profiles of p⁺n diodes showing the effect of Er on the n-type carriers in AlGaAs, with Al mole fraction $x = 0.1, 0.2, 0.3$, and 0.4 , and with Er implanted at a fluence of $\Phi_{\text{Er}} = 10^{13} \text{ cm}^{-2}$ at an energy of 1 MeV (The dashed lines represent the carrier concentration in the control sample and the solid lines give the carrier concentration in the Er-implanted sample) 91

39. PL measurements of sample x044 GaAs:Er, x058 Al_{0.33}Ga_{0.67}As:Er, and x027 Al_{0.5}Ga_{0.5}As:Er with a nominal Er-doping of $[\text{Er}] = 6 \times 10^{18} \text{ cm}^{-3}$, $6 \times 10^{18} \text{ cm}^{-3}$, and $1.5 \times 10^{19} \text{ cm}^{-3}$, respectively 93

40.	Effect of the GaAs substrate temperature on the Er-incorporation efficiency as well as Er diffusion and "surface riding" during the MBE growth of GaAs:Er with $[\text{Er}] \approx 3 \times 10^{18} \text{ cm}^{-3}$	94
41.	Temperature-dependent Hall effect measurements on the MBE-grown, Er-doped GaAs samples x045 2° <100> 111B and x0452d (Room-temperature measurements are given in Table 7.)	96
42.	Band-edge luminescence of GaAs:Er samples (Sample x051 shows the presence of Mn-related donor-acceptor and conduction-band-acceptor recombination. Sample x102, which shows no Mn emissions, was grown after the Er source was replenished.) . .	98
43.	Temperature-dependent Hall effect measurements of the MBE-grown GaAs sample x105 grown after the Er cell was replenished (The measurements for samples x0452d and x045 2° <100> 111B are repeated to demonstrate that the p-type conductivity in x105 is related to a much deeper center.)	100
44.	Variation of the Γ , L, and X conduction bands, and the dominant Si donor level, that is, the DX center, with Al mole fraction x	105
45.	Rate-window plots showing the effect of the Er implants with fluences of $\Phi_{\text{Er}} = 5 \times 10^{12}$, 10^{13} , and $5 \times 10^{13} \text{ cm}^{-2}$, and an ion energy of 1 MeV on n-type GaAs substrates (All data was obtained using minority carrier injection biasing, and the various peaks are identified for discussion in the text. The rate window is 29706 s^{-1} .) .	109

46.	Electric field dependence of the low temperature peaks observed in the n-type GaAs samples implanted with Er at a fluence of $\Phi_{\text{Er}} = 5 \times 10^{12} \text{ cm}^{-2}$ and at an energy of 1 MeV (The rate window is 29706 s^{-1} .)	111
47.	Depletion width vs. applied bias for the various DLTS measurements shown in Figure 46	112
48.	Capacitance transients recorded between 80 and 128 K for the n-type GaAs substrate 02-PR-1748, with Er-implanted at a fluence of $\Phi_{\text{Er}} = 10^{13} \text{ cm}^{-2}$ and at an energy of 1 MeV (The transients have an increasing time constant with temperature, indicating incomplete capture at a deep center.)	114
49.	DLTS spectra for Er implants in n-type GaAs at the indicated fluence and an energy of 1 MeV, as well as Pr implants in n-type GaAs at 390 keV (Common peaks represent centers which are most likely due to ion-implantation damage. The rate window is 29706 s^{-1} .)	116
50.	DLTS measurement of p-type Schottky diodes GaAs:Cu with Cu implanted at a fluence of $\Phi_{\text{Cu}} = 5 \times 10^{13} \text{ cm}^{-2}$ and at an energy of 370 keV, using majority carrier biasing, and DLTS measurements performed on the n-type GaAs Er-implanted samples with the high and low Er fluences using injection biasing on p ⁺ n diodes (The rate window is 29706 s^{-1} .)	118
51.	Arrhenius plots for centers Cu2, (i), (j) and (k) in GaAs from the current work (HB3 and HB4 were measured by Lang and attributed to Fe and Cu impurities, respectively.) .	121

52. Rate-window plots for the p-type GaAs substrate with Er implanted at a fluence of $\Phi_{\text{Er}} = 5 \times 10^{12} \text{cm}^{-2}$ and at an energy of 1 MeV, and a p-type control sample with no Er implant (The measurement for the n-type sample with the same Er fluence is shown for comparison. The rate window is 29706 s^{-1} .) 122

53. Arrhenius analysis for hole traps (a) — (e) occurring in Er-implanted GaAs (The data for center (c) is plotted with open circles.) 124

54. Arrhenius analysis for hole traps (g) — (k) occurring in Er-implanted GaAs (The data for center (g) is plotted with open circles.) 125

55. DLTS measurements using majority carrier biasing on p^+n GaAs diodes for different Er fluences, as well as for the control sample which was not implanted with Er (The rate window is 0.742 s^{-1} .) 127

56. Comparison of the Arrhenius behavior for electron traps (l), (m), and (n) found in this work, as well as M3 and EL2 obtained, respectively, from Buchwald and Matrin . 129

57. Rate-window plots using injection biasing for n-type $\text{Al}_x\text{Ga}_{1-x}\text{As:Er}$ for $x=0, 0.1, 0.2, 0.3$, and 0.4 with Er implanted at a fluence of $\Phi_{\text{Er}} = 10^{13} \text{ cm}^{-2}$ and at an energy of 1 MeV as well as control samples, which are shown with dashed curves (The rate window = 29706 s^{-1} .) 130

58. Rate-window plots using majority carrier biasing for n-type $\text{Al}_x\text{Ga}_{1-x}\text{As:Er}$ for $x = 0.2, 0.3$, and 0.4 with Er implanted at a fluence of $\Phi_{\text{Er}} = 10^{13} \text{ cm}^{-2}$ and an energy of 1 MeV, as well as control samples, which are shown with dashed curves (The deep level observed is the DX center. The rate window used is 29706 s^{-1} .) 132

59.	Rate-window plots using injection biasing for n-type $\text{Al}_x\text{Ga}_{1-x}\text{As}:\text{Er}$ for $x = 0, 0.1, 0.2, 0.3,$ and 0.4 with Er implanted at a fluence of $\Phi_{\text{Er}} = 10^{13} \text{ cm}^{-2}$ and at an energy of 1 MeV, as well as control samples, which are shown with dashed curves (The rate window is 0.742 s^{-1} .)	133
60.	Rate-window plots for MBE-grown GaAs samples x048 and x051 (The measurements are shown for injection biasing and majority carrier biasing. The DLTS measurements for the injection sequence on the n-type GaAs substrate 02-PR-1748 implanted with Er at a fluence of $\Phi_{\text{Er}} = 5 \times 10^{12} \text{ cm}^{-2}$ and at an energy of 1 MeV is shown for comparison.)	137
61.	Rate-window plots for the MBE-grown GaAs sample x009b with $[\text{Er}] = 4.6 \times 10^{19} \text{ cm}^{-3}$ and annealed either at 750°C for 15 seconds or at 825°C for 12 seconds; and for the ion-implanted GaAs sample with Er implanted at a fluence of $\Phi_{\text{Er}} = 10^{13} \text{ cm}^{-2}$ and at an energy 1 MeV, all under injection biasing conditions (The rate window is 29706 s^{-1} .)	139
62.	$\text{ErAs}_4\text{Ga}_{12}$ cluster used in the local-density-functional DV-X α cluster calculations by Saito and Kimura	146
63.	PL of the Er^{3+} -4f transition near $1.54 \mu\text{m}$, as well as broad bands in the semi-insulating GaAs sample implanted with Er at a fluence of $\Phi_{\text{Er}} = 10^{13} \text{ cm}^{-2}$ and at an energy of 1 MeV as a function of annealing temperature	161
64.	CV profiles obtained using Schottky diodes on the p-type GaAs substrate 3B-PR-840 implanted with Er at a fluence of $\Phi_{\text{Er}} = 10^{13} \text{ cm}^{-2}$ and at an energy of 1 MeV that was rapid thermally annealed at $650, 750, 850,$ and 900°C for 15 seconds	162

65. DLTS measurements of the p-type GaAs substrate 3B-PR-840 implanted with Er at fluence of $\Phi_{\text{Er}} = 10^{13}$ and at an energy of 1 MeV that was rapid thermally annealed at 650, 750, 850, and 900 °C for 15 seconds (Each sample was measured with a majority carrier biasing sequence of 0 V forward and 1 V reverse (0,-1). DLTS measurements on the Er-implanted p⁺n GaAs diodes using injection biasing are shown for comparison. The rate window is 29706 s⁻¹.) 164

66. Arrhenius analysis of the (g) center in the p-type GaAs sample implanted with Er at a fluence of $\Phi_{\text{Er}} = 10^{13} \text{ cm}^{-2}$ and at an energy of 1 MeV that was annealed at either 650 or 750 °C for 15 seconds (The shift in the trap signature is due to the large concentration of the level in the sample annealed at 750 °C.) 166

67. PL of the p-type GaAs substrate 3B-PR-840 implanted with Er at a fluence of $\Phi_{\text{Er}} = 10^{13} \text{ cm}^{-2}$ and at an energy of 1 MeV that was rapid thermally annealed at 650, 750, 850, and 900 °C for 15 seconds (This plot shows the broad bands as well as Er-4f emissions near 1.54 μm.) 168

68. PL of the p-type GaAs substrate 3B-PR-840 implanted with Er at a fluence of $\Phi_{\text{Er}} = 10^{13} \text{ cm}^{-2}$ and at an energy of 1 MeV that was rapid thermally annealed at 650, 750, 850, and 900 °C for 15 seconds (The structure of the Er-4f emissions near 1.54 μm is shown to demonstrate the presence of at least two centers.) 169

69. Near-band-edge PL of the p-type GaAs substrate 3B-PR-840 implanted with Er at a fluence of $\Phi_{\text{Er}} = 10^{13} \text{ cm}^{-2}$ and at an energy of 1 MeV that was rapid thermally annealed at 650, 750, 850, and 900 °C for 15 seconds 171

70.	PL of the p-type GaAs substrate 3B-PR-840 implanted with Er at a fluence of $\Phi_{\text{Er}} = 5 \times 10^{12} \text{ cm}^{-2}$ and at an energy of 1 MeV that was rapid thermally annealed at 725, 750, 775, and 800 °C for 15 seconds (This plot shows broad bands as well as Er-4f emissions near 1.54 μm).	172
71.	DLTS measurements of the p-type GaAs substrate 3B-PR-840 implanted with Er at a fluence $\Phi_{\text{Er}} = 5 \times 10^{12} \text{ cm}^{-2}$ and at an energy of 1 MeV that was rapid thermally annealed at 725, 750, 775, and 800 °C for 15 seconds (Each sample was measured with a majority carrier biasing sequence of 0 V forward and 1 V reverse (0,-1). The rate window is 29706 s^{-1} .)	173
72.	Er-4f PL intensity and Hall effect electron concentration as a function of the Er-doping density in MBE-grown Er-doped $\text{Al}_{0.5}\text{Ga}_{0.5}\text{As}$	176
73.	Exciton-mediated Er^{3+} -4f PL excitation and thermal quenching model for the type T1 center in GaAs:Er	184
74.	Excitation model T2a for exciton-mediated excitation of the Er^{3+} -4f shell and thermal quenching for the type T2 center in GaAs:Er	186
75.	Excitation model T2b for excitation and quenching of the Er^{3+} -4f PL of the T2 center in GaAs:Er	188
76.	Excitation model T2c for direct excitation of the Er^{3+} -4f shell and Auger de-excitation for the T2 center in GaAs:Er	190
77.	Er^{3+} PL excitation and quenching model for the T3 center in GaAs:Er	192

78. Injection electroluminescence measurements of p^+n and n^+p Er-doped GaAs diodes . 196
79. PL measurements of GaAs:Nd, with Nd implanted at a fluence of $\Phi_{Nd} = 3 \times 10^{13} \text{ cm}^{-2}$ and at an energy of 1 MeV that was rapid thermally annealed under the conditions listed in the figure 207
80. PL measurements of GaAs:Pr, with Pr implanted at a fluence of $\Phi_{Pr} = 10^{13} \text{ cm}^{-2}$ and an energy of 390 keV that was rapid thermally annealed under the conditions listed in the figure 208
81. PL measurements of $\text{Al}_{0.29}\text{Ga}_{0.71}\text{As}:(\text{Er}+\text{O})$ with: (i) Er implanted at a fluence of $\Phi_{Er} = 5 \times 10^{13} \text{ cm}^{-2}$ and at an energy of 1 MeV, and (ii) O implanted with various fluences at an energy 110 keV, and rapid thermally annealed at 750 °C for 15 seconds . 211
82. PL measurements of $\text{Al}_{0.29}\text{Ga}_{0.71}\text{As}:(\text{Er}+\text{O})$ with: (i) Er implanted at a fluence of $\Phi_{Er} = 5 \times 10^{13} \text{ cm}^{-2}$ at an energy of 1 MeV, and (ii) O implanted at a fluence of $\Phi_{O} = 10^{14} \text{ cm}^{-2}$ at an energy of 110 keV, and rapid thermally annealed under the conditions listed in the figure 212

List of Tables

	Page
1. Electron and hole capture and emission rates for thermal, optical, and Auger mechanisms.	15
2. Amplitudes of the two exponential components used to fit the nonexponential decay resulting from a simulation of the effect of large trap concentrations	47
3. Projected ranges and straggles for the RE ions and implant energies used in this investigation (after Pomrenke)	55
4. Important properties of the rare earth atoms in the order of increasing atomic number (Included are the valence configuration of the free atom, its electronegativity, and ionic radius in the 3+ oxidation state, as reported by Cotton and Wilkinson . Other important metallic elements are given for comparison.)	67
5. Effect of Er doping on semi-insulating (SI), n-type, and p-type GaAs substrates as determined by room temperature Hall effect measurements (All samples were annealed at 750 °C for 15 seconds using the RTA method.)	82
6. Effect of Er-doping on $\text{Al}_x\text{Ga}_{1-x}\text{As}$ substrates as determined by room-temperature Hall effect measurements	90
7. GaAs:Er layers grown by MBE on different substrate orientations which consistently show p-type conductivity (This p-type conductivity is due to Mn contamination in the Er source.)	95
8. Metallic contaminants in the MBE Er source in parts-per-million (ppm) as measured by the supplier, Rare Earth Products, using X-ray fluorescence spectrometry	97

9.	Sample structures grown for the Er concentration study	101
10.	Room-temperature Hall effect measurements on MBE-grown $\text{Al}_{0.5}\text{Ga}_{0.5}\text{As}:(\text{Er}+\text{Si})$ with $[\text{Si}] = 2 \times 10^{18} \text{ cm}^{-3}$, and various Er concentrations	101
11.	Activation energies and thermal capture cross sections for the various centers measured in this work	110
12.	Activation energies and capture cross sections for mid-gap hole traps in GaAs as measured in this investigation and as reported by Lang, et al. and Mitonneau, et al. .	119
13.	Electron traps found in the n-type MOCVD-grown GaAs substrate 02-PR-1748 as well as in the Er-implanted GaAs substrates	128
14.	Structures for the lightly Er-doped MBE-grown GaAs, consisting of n^+p and p^+n junction diodes with Er in the n-type or p-type material, respectively (The nominal Si and Be dopant concentrations are shown along with the measured free carrier concentrations determined from the CV profiles)	135
15.	Structure for the Er-doped MBE-grown GaAs sample x009b; heavily Er doped . . .	138
16.	Summary of the various deep levels found in GaAs:Er and their likely microscopic natures	201

Abstract

Electrical and optical characterization have been performed on GaAs and $\text{Al}_x\text{Ga}_{1-x}\text{As}$ samples doped with Er either by ion implantation or during Molecular Beam Epitaxial (MBE) growth. The electrical techniques of Deep Level Transient Spectroscopy (DLTS) and Temperature-Dependent Hall Effect (TDH) indicated that Er primarily formed two electrically active centers in both materials. The first center gave rise to a hole trap at $E_v + 35 \text{ meV}$, which was thought to be due to Er substituting for a Ga atom (Er_{Ga}) and giving rise to an isoelectronic impurity potential. The second center also gave rise to a hole trap at approximately $E_v + 360 \text{ meV}$, and was attributed to an Er atom occupying an interstitial position (Er_i). Annealing studies performed on Er-implanted GaAs indicated that the Er_{Ga} center preferentially formed at higher annealing temperatures ($> 850^\circ\text{C}$), with the Er_i reaching a maximum concentration at an annealing temperature of around 750°C . Additionally, optical characterization performed by Photoluminescence (PL) measurements showed that the Er_i center gave much stronger Er-related emissions due to the transition $^4\text{I}_{13/2} \rightarrow ^4\text{I}_{15/2}$ in the unfilled Er^{3+} -4f shell than was observed for 4f-emissions associated with the Er_{Ga} center. Mechanisms for the excitation and de-excitation of the Er-4f shell in GaAs, consistent with all experimental observations, were proposed. DLTS measurements also detected the presence of a large concentration of Ga-antisite (Ga_{As}) defects as well as As-interstitial (As_i) defects. Based upon reports of Er^{3+} -4f emissions from four distinct Er-centers, two other likely Er-centers were proposed, $\text{Er}_{\text{Ga}}\text{-Ga}_{\text{As}}$ and $\text{Er}_{\text{Ga}}\text{-As}_i$.

DLTS measurements performed on Er-implanted $\text{Al}_x\text{Ga}_{1-x}\text{As}$ ($x = 0.1, 0.2, 0.3, 0.4$) showed a drastic decrease in the concentration of deep centers with increasing Al mole fraction. This effect was attributed to a reduction in the concentration of Er-related and damage-related deep centers. In addition, the concentration of the DX center in $\text{Al}_x\text{Ga}_{1-x}\text{As}$ was not affected by the implantation of Er, indicating that Er and Si were not forming complexes in AlGaAs. Further, a similar rate of Er diffusion in GaAs and AlGaAs led to the conclusion that the free electron reduction observed in Er-implanted GaAs:Si was not due to donor gettering but to compensation from Er-related and damage-related deep centers. Finally, electrical and optical characterization of Er-doped MBE-grown $\text{Al}_{0.5}\text{Ga}_{0.5}\text{As}$ indicated that the solubility limit of Er in this material was possibly as high as $2 \times 10^{19} \text{ cm}^{-3}$, as compared to $7 \times 10^{17} \text{ cm}^{-3}$ in GaAs.

I. Introduction

The introduction of impurities with open cores into crystalline hosts has been a field of spectroscopic study for many years (37:Chapters 8,9). Impurity introduction allows the energy of primary crystal excitations to be channeled into atomic-like excitations of the cores. Such impurities are the transition metals (TM), which have their 3d, 4d, or 5d shells partially filled, the lanthanides or rare earth (RE) elements, and the actinides, with unfilled-4f and 5f shells, respectively. Although these systems are interesting on their own merit, they also are potentially technologically important, since excitation of these atomic core transitions may provide the required gain for laser transitions (37:Chapter 9). In fact, the Cr^{3+} ion in the Al_2O_3 crystal led to the first successful demonstration of lasing (60), i.e., the Ruby laser. Another well known solid state laser is the neodymium YAG (YAG : Nd) laser, which operates on internal transitions in the unfilled 4f shell of the RE ion neodymium (Nd^{3+}) in yttrium aluminum garnet (YAG = $\text{Y}_3\text{Al}_5\text{O}_{12}$).

An important difference between the RE ions and the TM ions in solids is the relative extent to which their unfilled valence orbitals interact with neighboring atoms. For example, the iron group TMs have the electronic configuration $[\text{Ne}]3s^23p^63d^n4s^2$, and $n \leq 10$. The valence 3d electrons are located largely outside of the core, and hence, participate in covalent or ionic bonding with host atoms. The emissions involved with their excited electronic states are, therefore, strongly affected by the crystal environment, and likewise the lattice site which they occupy. Furthermore, since they are more strongly coupled to the lattice, the excited ions can nonradiatively decay and transfer energy back to the crystal. However, for the RE atoms, with an electronic configuration $[\text{Pd}]4f^n5s^25p^66s^2$ and $n \leq 14$, the 4f electrons are primarily located in the core and are largely shielded from the crystal field by the $5s^2$ and $5p^6$ electrons. Hence, the energies of the various spin-orbit states of the $4f^n$ configuration, and thus, the emission wavelengths corresponding to transitions amongst these states, are largely independent of the crystal site and even crystal host. Furthermore, since the 4f shells are not well coupled to the

lattice, the excited 4f shells are not as likely to nonradiatively transfer energy back to the crystal. Finally, the weak coupling to the lattice also implies that the 4f transitions maintain their narrow atomic-like line widths and emission wavelengths, independent of host temperature.

1.1 Problem Statement

Unfortunately, the YAG or Ruby ionic crystal hosts are insulating, and so the RE-4f transitions are typically excited optically, such as, through the intervention of a flash lamp (103). If however, these ions are incorporated into a semiconductor whose electrical properties are readily altered by the introduction of donors and acceptors, then it may be possible to directly excite these atoms, with the application of a potential across the sample. Emissions resulting from the radiative decay of this excited state would be known as electroluminescence (EL); for example, the RE ions located in the interfacial region of a pn junction. The application of a forward bias across the junction will allow large concentrations of electrons and holes to overlap and recombine in the presence of the RE atom, possibly resulting in a transfer of the band gap energy into the 4f shell.

However, two complications arise. First, the RE ion itself may affect the electrical properties of the device. Specifically, the RE ion may occupy any substitutional or interstitial position in the crystal structure, or it may form complexes with other impurities or defects already present. Any of these centers may act as donors or acceptors, or they may give rise to a level deep in the band gap. If the RE ion acts as an acceptor, it may also act to compensate shallow donors in n-type material, so that the originally intended device structure may be nullified. On the other hand, if the RE ion gives rise to a deep level near the center of the band gap, it may act as a nonradiative recombination center, thereby reducing the RE³⁺ luminescent efficiency. The second problem is that in order to make such a device efficient, it is necessary to have an understanding of the mechanism by which the energy of the semiconductor band gap is actually coupled into the RE ion's 4f shell.

Various mechanisms for exciting the RE ion's 4f shell are possible. For instance, a hot electron may inelastically scatter, transferring part of its kinetic energy into the RE ion's core. Alternatively, an electron-hole pair may radiatively recombine with the emitted photon being reabsorbed by the RE ion's 4f shell, thereby exciting it. Also, the potential generated by the RE

impurity itself may be critical to the excitation mechanism; for example, the RE ion may have an electron attractive potential. Upon laser excitation or carrier injection, the RE center may capture an electron, thus becoming negatively charged. Subsequently, a hole may be attracted to this center, forming a bound exciton, which may nonradiatively transfer its energy to the 4f shell. On the other hand, depending upon the depth of this electron trap in the band gap, it may be energetically impossible to transfer the necessary excitation to the 4f shell.

One of these mechanisms may provide a more efficient means of excitation compared to the others. Furthermore, the most efficient excitation may occur for a specific RE center in the semiconductor. Thus, the more knowledge that is available concerning the nature of the RE centers, the more likely it is that their concentrations may be altered in order to improve the quantum efficiency for the RE^{3+} excitation. Therefore, it is apparent that an investigation of certain basic material and electronic properties of RE-doped semiconductors must be undertaken before attempting to fabricate optoelectronic devices, such as light-emitting diodes or semiconductor lasers.

The RE elements have only been recently investigated in the technologically important III-V semiconductors. The first RE-4f emissions in a III-V compound were obtained for ytterbium (Yb) in InP by Zakharenkov et al. (106) in 1981. These emissions, which result from a transition $^2F_{5/2} \rightarrow ^2F_{7/2}$ in the spin-orbit split levels of the Yb^{3+} ($4f^{13}$) ion, are typically much more intense than other III-V:RE combinations and, consequently, InP:Yb has been thoroughly investigated. However, for device applications, the most interesting RE is erbium (Er). This is due to the fact that the transition between the first excited state and the ground state of the Er^{3+} -4f shell ($4f^{11}$), $^4I_{13/2} \rightarrow ^4I_{15/2}$, occurs at a wavelength of $1.54 \mu\text{m}$ (corresponding to an energy of about 0.805 eV) which is close to the wavelength of minimum attenuation in silica-based optical fibers ($1.55 \mu\text{m}$). As shown in Figure 1, the attenuation coefficient for the band-edge emissions in GaAs at $0.83 \mu\text{m}$ is roughly an order of magnitude larger than for the Er-4f shell emissions at $1.54 \mu\text{m}$ (67:174). The product of the attenuation coefficient and the distance traversed by the optical signal is exponentiated in order to obtain the intensity at the relative receiver. Thus, even though the Er-emissions at the source may be much weaker than the GaAs band edge emissions, they will probably be more intense than the band-edge emissions, upon reaching the detector.

Previously, the most promising technique for obtaining the $1.5 \mu\text{m}$ emission wavelengths necessary for optical fiber communications was through the use of band gap engineering (67:177).

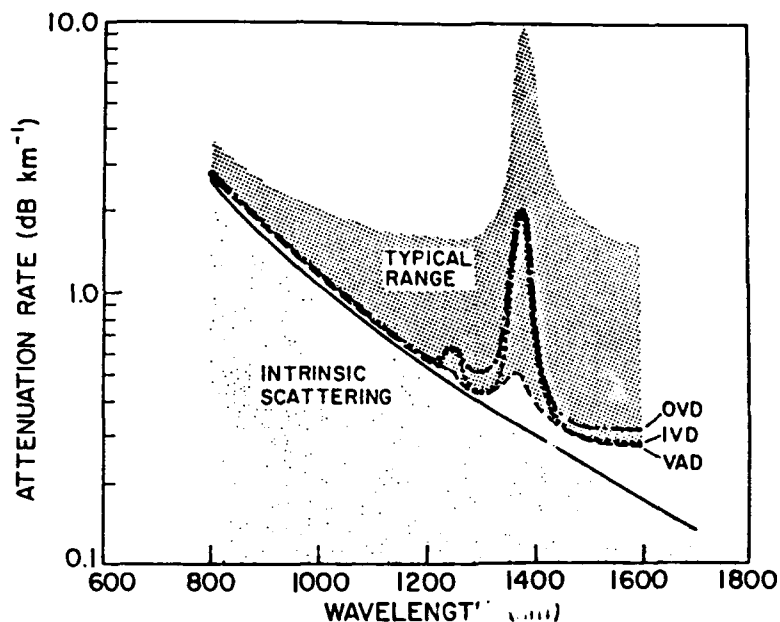


Figure 1. Attenuation vs. wavelength for silica based optical fibers grown by vapor-phase axial deposition (VAD), inside vapor deposition (IVD), and outside vapor deposition (OVD) (after Pearsall (67))

As shown in Figure 2, the alloy composition of the $\text{Ga}_x\text{In}_{1-x}\text{As}_y\text{P}_{1-y}$ system, as well as the $\text{Al}_x\text{Ga}_{1-x}\text{Sb}$ system, may be varied to adjust their band gaps to the desired wavelengths for optical fiber communications. Unfortunately, there are a couple of problems with these sources. The first problem is that the band edge emissions shift as a function of increasing temperature due to the decreasing band gap energy, typically $5 - 7 \text{ }^\circ\text{C}$ near room temperature. Secondly, the band edge emissions may be relatively broad, as much as $100 \text{ }^\circ\text{A}$, and so the effects of optical dispersion of the signal propagating along the fiber-optic cable may limit the ultimate data transmission rate, even if the signal intensity is not a problem. However, due to the shielding provided by the $5s^2$ and $5p^6$ electrons, the Er-4f emission wavelengths are expected to be nearly independent of temperature and to have atomic-like line widths, typically less than $1 \text{ }^\circ\text{A}$. Thus, the Er-4f emissions are ideal for optical fiber communications.

Fabrication of Er-doped devices has already been undertaken. For instance, Tsang and Logan (92) attempted to combine the beneficial aspects of the Er emissions with the excitation

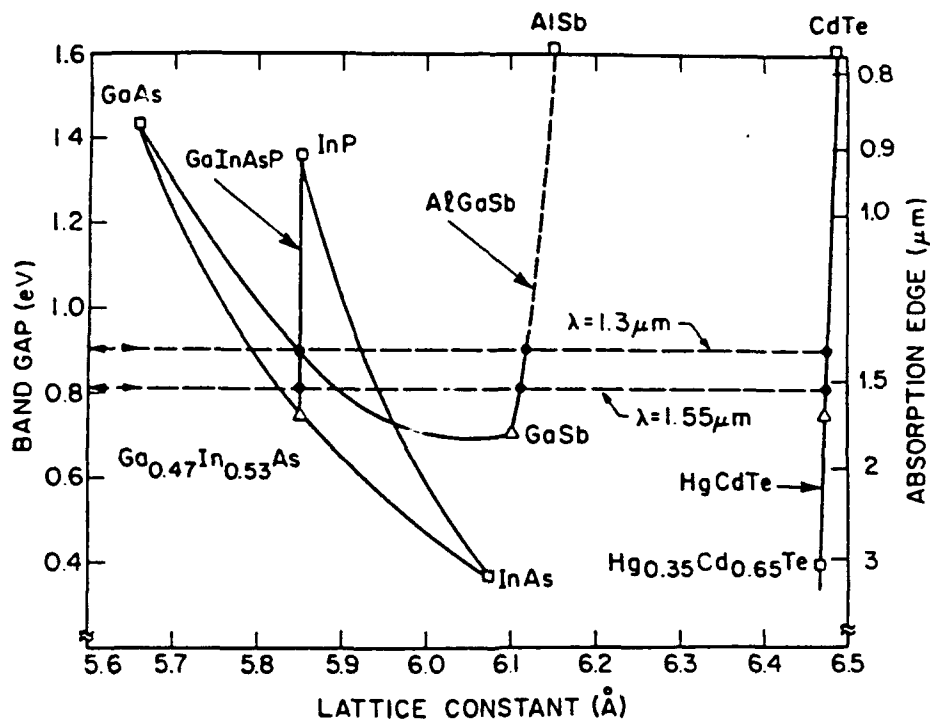


Figure 2. Band gap vs. alloy parameter for systems of interest in silica-based optical fiber communications (These fibers have a minimum dispersion at $1.3 \mu\text{m}$ and a minimum of attenuation at $1.55 \mu\text{m}$, after Pearsall (67))

energy available from the InGaAsP crystal. Specifically, they doped the active region of an InGaAsP heteroepitaxial ridge overgrown (HRO) laser with Er atoms (91). The InGaAsP alloy was adjusted so that the band gap energy was resonant with the $\text{Er}^{3+} {}^4\text{I}_{13/2} \rightarrow {}^4\text{I}_{15/2}$ transition energy. This structure resulted in single mode laser operation, as well as a much smaller shift in the mode wavelength with temperature ($\sim 1 \text{ \AA}/^\circ\text{C}$) as compared to laser structures without Er-doping ($\sim 5 \text{ \AA}/^\circ\text{C}$). This feature was attributed to an enhancement in the gain profile of the laser by the excited Er^{3+} atoms. Unfortunately, Ziel (95) later showed that the observed single mode behavior was instead due to a spectrally dependent loss mechanism, caused principally by inhomogeneities in the active layer, presumably due to the interference in growth by Er doping. These defects resulted in a large scattering loss except at one wavelength. This certainly underscores the need for a careful material characterization effort prior to attempting to fabricate devices.

While an investigation of the RE Er in InGaAsP or AlGaSb might be more interesting since their band gap energies can be adjusted above and below that energy which is necessary to excite the $1.54\ \mu\text{m}$ Er^{3+} transition, this study will instead focus on Er in the GaAs and AlGaAs systems. The primary reason is that these systems are more technologically mature and, hence, the material is more readily available than for InGaAsP or AlGaSb systems. These materials also have band gaps larger than 0.805 eV, and so there is sufficient energy available to excite the Er^{3+} -4f shell from the ground state $^4\text{I}_{15/2}$ to the first excited spin-orbit level $^4\text{I}_{13/2}$.

This investigation will focus primarily on the electrical properties of Er-doped GaAs and AlGaAs. While many optical studies have been performed on these systems, there has been little or no investigation on the effect of Er-incorporation on their electrical properties. Furthermore, in order to have a complete understanding of the excitation of the Er^{3+} -4f core, it is essential to detect any Er-related electronic states introduced into the crystal. Although Er-related centers with levels in the band gap may seriously effect the electrical behavior of the crystal, they may also provide the means of efficiently transferring crystal energy into the 4f shell. This has been found to be the case for InP:Yb.

1.2 Sequence of Presentation

Prior to discussing the electrically active Er-related centers formed in GaAs and AlGaAs, it is necessary to be familiar with the general nature of electrically active centers in the band gap due to the introduction of impurities. Therefore, in Chapter 2, **Electron Levels in the Band Gap**, a discussion of the relevant parameters characterizing impurity states or defect centers will be given. The electrical and optical techniques used to extract these parameters will be the subject of Chapter 3, **Characterization Techniques**. Since this dissertation is focusing on the electrical properties of Er-doped GaAs and AlGaAs, attention will be focused on the electrical techniques used in this study, the Hall effect and Deep Level Transient Spectroscopy (DLTS). The two techniques used to introduce the Er impurities into the GaAs and AlGaAs crystals, Ion Implantation and Molecular Beam Epitaxy (MBE), will be the subject of Chapter 4, **Er-doping and Sample Preparation**. The strengths and weaknesses of each technique will be addressed. In the final background chapter, **Properties of RE Atoms in Semiconductors**, a review the properties of the RE atoms, as well as the electrical behavior previously observed for other III-V:RE systems, will be given. Furthermore, common excitation mechanisms proposed for

the RE atoms in these systems will be discussed. With this background, electrical and optical measurements performed on various Er-implanted and MBE-grown Er-doped GaAs and AlGaAs layers will be presented in Chapter 6, **Results and Discussion**. Comparisons will be made of the electrical and optical behavior of Er atoms, which will facilitate identifying the various likely excitation mechanisms for the Er^{3+} -4f emissions. Finally, these results and the contributions made to the body of scientific knowledge will be summarized in Chapter 7, **Conclusions and Recommendations**. The findings of the dissertation will suggest areas for future study of REs in III-V semiconductors. Continued work in these areas will no doubt reveal the most likely means for obtaining enhanced emissions in RE-doped III-V semiconductors.

II. Electron Levels in Semiconductors

The extent to which crystals, especially semiconductors, are useful, is largely determined by the degree to which their optical and electrical characteristics are altered when externally stimulated. For example, when a forward bias is applied to a pn-junction diode, current readily flows through the diode, but with the application of a reverse bias, very little current flows through the device. This unique behavior has invoked the fabrication of rectifiers to select only one voltage polarity from a set of input signals. Likewise, if the forward-biased pn junction were fabricated on a direct-band-gap semiconductor, it may be used instead as a light emitting diode (LED) for electroluminescent displays, or possibly, as a semiconductor laser.

The alteration of a semiconductor's properties is generally accomplished by the selective introduction of imperfections into the otherwise perfect crystal structure. These imperfections abruptly alter the perfect periodic structure of the crystal and introduce a short-range potential, which changes the electrical and optical behavior of the crystal. An imperfection in a crystal may be caused by: (a) the replacement of a lattice atom by a foreign atom (impurity), (b) the appearance of defects in the crystal structure, such as interstitials or vacancies, or (c) complexes between (a) and (b). Imperfections of type (a) are those most commonly used in semiconductor device engineering and typically include the introductions of atoms which increase or reduce the carrier concentration of the crystal: that is, donors, acceptors, or compensation centers. Imperfections of types (b) and (c) are not usually desirable since their concentrations are difficult to control.

In the current chapter, the important properties of imperfection centers in semiconductors will be reviewed. In general, such centers either act as donors or acceptors, and the exact definition of these terms are provided in the first section. An electron level in the band gap which is associated with a given imperfection center may be occupied by an electron, or conversely by a hole, as the probability of their occupancy will be discussed in the second section. This steady-state property is generally observed by measuring the free electron or hole carrier concentration, which can readily be accomplished by the Hall effect experiment. Further, the temperature dependence of the carrier concentration may often be used to determine the concentration of donor or acceptor centers, as well as their position with respect to the band edges. In the final section, the rate at which carriers are exchanged between the valence or conduction bands and

the imperfection centers will be reviewed. The rate coefficients introduced will determine the relative likelihood that a given center will trap either an electron or a hole. An expression for the temperature dependence of the thermal emission rate of a trapped charge to the bands will be also developed. The temperature dependence of this emission rate, which depends upon the depth of the center, is typically determined experimentally by the Deep Level Transient Spectroscopy (DLTS) experiment.

2.1 Donors and Acceptors

An impurity or defect introduced into an otherwise perfect semiconductor crystal may introduce a bound (i.e., localized) state with an energy level lying within the band gap. For instance, a silicon atom substituting for a gallium atom in the compound semiconductor GaAs, denoted by Si_{Ga} , will bind its fourth valence electron by only 6 meV, and hence produce an electron level which is located only 6 meV below the conduction band edge. On the other hand, if a Si atom occupies an As site, Si_{As} , it will tend to accept an electron from the valence band to complete its covalent bonding requirements. The resulting hole in the valence band will be bound by 35 meV, which implies that the electron state introduced into the band gap is 35 meV above the valence band edge. Such states are typically referred to as shallow donors and acceptors, respectively. They are ionized at all but the lowest temperatures, typically $\gtrsim 20$ K, by simple agitation of the crystal, i.e., phonons.

However, the introduction of impurities that are not in adjacent columns of the periodic table may produce energy states which are much deeper in the band gap. For instance, Cr_{Ga} can bind an electron by 0.7 eV. The excitation of this electron to the conduction band would then be described by the equation, $\text{Cr}^{2+} + 0.7 \text{ eV} \rightarrow \text{Cr}^{3+} + e_{\text{cb}}$, which is denoted by (2+/3+), where e_{cb} represents an electron in the conduction band. Cr^{3+} is the neutral state of Cr_{Ga} , and hence the Cr^{2+} state is referred to as a Cr acceptor level. Also, an electron in the conduction band may lose 0.7 eV and form the Cr^{2+} state in which case, this state acts as an electron trap. Finally, the electron at this trap may lose (1.52 - 0.7) eV and fall into an unoccupied valence band energy level. That is, the Cr impurity may act as a recombination center for conduction band electrons and valence band holes. Figure 3, taken from Sze (86:21), shows the energy levels which are associated with various impurities introduced into GaAs. Although there is no clear separation in ionization energy, E_I , between deep and shallow levels, a generally accepted definition is given

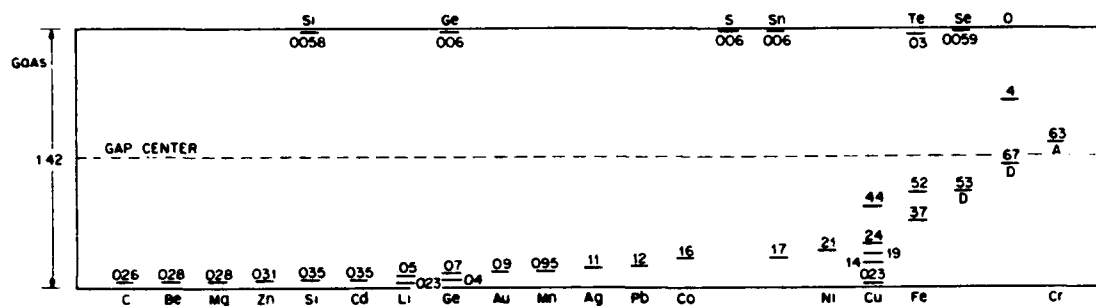


Figure 3. Ionization energies of various impurities and defects in GaAs (after Sze (86:21))

by Pantelides (66), who defines a level to be shallow if, $E_I \ll E_g$, and to be deep if, $E_I \approx E_g$, where E_g is the band-gap energy. In practice, for the wide band gap semiconductors, for example, GaAs and AlGaAs, energy states are typically referred to as being deep if $E_I \gtrsim 0.1$ eV.

It is also possible for a deep impurity to have multiple charge states. Although the nature of a donor and acceptor center is clear when dealing with shallow states, the situation is not the same for deep centers. However, the fact that the wave function of a localized state associated with a defect decays within a finite number of unit cells, led Shockley (82) to formulate an unambiguous definition of 'donor' and 'acceptor' in terms of occupancy of a given charge state: Positively charged states of an impurity are defined as donor states, and negatively charged states are defined as acceptor states, while neutral states bear no other distinctive name. Since electrical experiments typically measure the energy associated with the transition between successive charge states, it is more proper to speak of donor and acceptor transitions (57), the former occurring when a neutral impurity loses an electron or when a positively charged impurity gains or loses an electron, and the latter occurring when a neutral impurity gains an electron or when a negatively charged impurity gains or loses an electron.

2.2 Occupancy of Donor and Acceptor Levels

Any number of different centers can be present in a semiconductor. Further, any of these may have multiple charge states which appear in the band gap. Additionally, there may be excited states associated with any of these charge states. Look (57:244–250) has derived an expression for the occupancy, n_{klm} , of the m th excited level of the l th charge state of the k th center,

$$n_{klm} = \frac{N_k}{1 + \sum_{l', m' \neq l, m} (g_{kl'm'} / g_{klm}) \exp((E_{kl'm'} - E_{klm} - (l - l')E_F) / kT)}, \quad (1)$$

where N_k is the total concentration of the type k centers, E_F is the Fermi energy level, g_{klm} and E_{klm} are the degeneracy and energy of the (klm) state, respectively, k , is Boltzmann's constant, and T is the semiconductor's temperature in degrees Kelvin (K). Both the Fermi energy level and the energy of the (klm) state are measured with respect to the valence band maximum energy level, E_v .

The only unknown in this equation is the Fermi energy level, which is determined by requiring charge neutrality. The total positive and negative charges are given by

$$\text{positive charge} = p + \sum_{k, l=0, m}^{l=l_{Dk}} (l_{Dk} - l) n_{klm} \quad (2)$$

$$\text{negative charge} = n + \sum_{k, l=l_{Dk}+l_{Ak}}^{l=l_{Dk}+l_{Ak}} (l - l_{Dk}) n_{klm} \quad (3)$$

where the k th center has l_{Dk} donor levels and l_{Ak} acceptor levels. The electron and hole (n and p) concentrations are typically given by the Boltzmann approximation (86:17)

$$n = \frac{2(2\pi m_n^* kT)^{3/2}}{h^3} \exp(E_F - E_c) = N_C \exp((E_F - E_c) / kT) \quad (4)$$

$$p = \frac{2(2\pi m_p^* kT)^{3/2}}{h^3} \exp(-E_F) = N_V \exp(-E_F / kT), \quad (5)$$

where, h is Plank's constant, N_C and N_V are the conduction-band and valence-band density of states, respectively, m_n^* and m_p^* are the density-of-state effective masses of the valence band and conduction band, respectively, and E_c is the minimum conduction band energy level. Thus, equating the total negative charges to the total positive charges gives,

$$n = p + \sum_{k, l=0, m}^{l=l_{Dk}+l_{Ak}} (l_{Dk} - l) n_{klm}. \quad (6)$$

The Fermi energy level at a given temperature is determined by requiring this equality to hold.

Typically, there is either one dominant donor or acceptor species with a single charge state and no excited states in the band gap. The term 'dominant' implies that, at all temperatures, this center controls the position of the Fermi energy level, which remains more than a few kT away from every other center. Look (57:119) considered the situation in which a sample was dominated by a single donor, of concentration N_D , located at an energy E_D below E_c . This meant that the Fermi energy level was near this dominant center at all temperatures, and centers more than a few kT below E_F were always occupied with electrons, while states more than a few kT above E_F were always unoccupied. In this case, equation (6) reduces to

$$n + N_A^{net} = \frac{N_D}{1 + n/\Phi_D} \quad (7)$$

where

$$\Phi_D = \frac{g_{D0}}{g_{D1}} N_C \exp(-E_D/kT) \quad (8)$$

$$= \frac{g_{D0}}{g_{D1}} N'_C \exp(-\alpha_D/k) T^{3/2} \exp(-E_{D0}/kT), \quad (9)$$

$N'_C = 2(2\pi m_n^* k)^{3/2}/h^3$, and g_{D0} and g_{D1} are the degeneracies of the occupied and unoccupied states, respectively. Also, a linear dependence of the donor activation energy of the form $E_D = E_{D0} - \alpha_D T$ is allowed, where E_{D0} is the donor energy as $T \rightarrow 0$. Finally, N_A^{net} is a temperature-independent term representing the total charge due to the other acceptor or donor centers which are either above or below E_F . That is,

$$N_A^{net} = \sum_{k, E_{Ak} < E_F} N_{Ak} - \sum_{k, E_{Dk} > E_F} N_{Dk}. \quad (10)$$

A similar expression is obtained in the case of a p-type sample dominated by a single acceptor center of concentration N_A with an energy E_A above E_v . In this case, the charge neutrality relationship (equation (6)) yields

$$p + N_D^{net} = \frac{N_A}{1 + p/\Phi_A} \quad (11)$$

where

$$\Phi_A = \frac{g_{A1}}{g_{A0}} N'_V \exp(-\alpha_A/k) T^{3/2} \exp(-E_{A0}/kT), \quad (12)$$

$N'_V = 2(2\pi m_p^* k)^{3/2}/h^3$, and g_{A1} and g_{A0} are the degeneracies of the occupied and unoccupied states, respectively. Again, a linear dependence of the acceptor activation energy on temperature is assumed. That is, $E_A = E_{A0} - \alpha_A T$, where E_{A0} is the acceptor energy as $T \rightarrow 0$. The only difference between the form of equation (11) and that for the previous case of an n-type sample dominated by a single donor (equation (7)) is that the degeneracy ratios are inverted, and the conduction-band-effective density of states N'_C is replaced by the valence-band-effective density of states N'_V . Equations (7) and (11) show that measurement of the temperature-dependent electron or hole concentration may be used to obtain the donor or acceptor activation energies, but, only when these equations are valid. Overall, the steady-state behavior of centers giving rise to energy levels in the band gap has been described, allowing for the subsequent discussion of the rate at which electrons in the conduction band make transitions to unoccupied electron levels in the gap, or the rate at which electrons occupying these centers make transitions to holes in the valence band.

2.3 *Electrical and Optical Transitions at Deep Centers*

Sah (77) has summarized the mechanisms for charge transfer between the valence and conduction bands and the localized states within the band gap, as shown in Figure 4. In the four thermal transitions, energy balance is achieved by the absorption or emission of phonons. For example, in process (a), a conduction-band electron emits one or more phonons, and is thus captured by the unoccupied center. The inverse process (b) occurs when an electron in the center absorbs energy from the lattice (again phonons) to make a transition to the conduction band. The processes involving hole capture and emission are understood in terms of an electron level which is normally occupied and preferentially exchanges carriers with the valence band. Hole capture (c) occurs when an electron occupying a center emits phonons and transitions into an unoccupied valence band state. Likewise, when an electron in the valence band absorbs lattice energy and is promoted to the unoccupied center, a free carrier is generated in the valence band, and thus a hole is emitted (d). The optical processes are completely equivalent to the thermal processes with the exception that the phonon is replaced by a photon. That is, energy balance is achieved through the emission and absorption of photons. Finally, in the eight Auger processes, energy is conserved by the interaction with a third free particle, either a conduction band electron or a valence band hole. In this case, electron capture occurs with the excess energy either generating

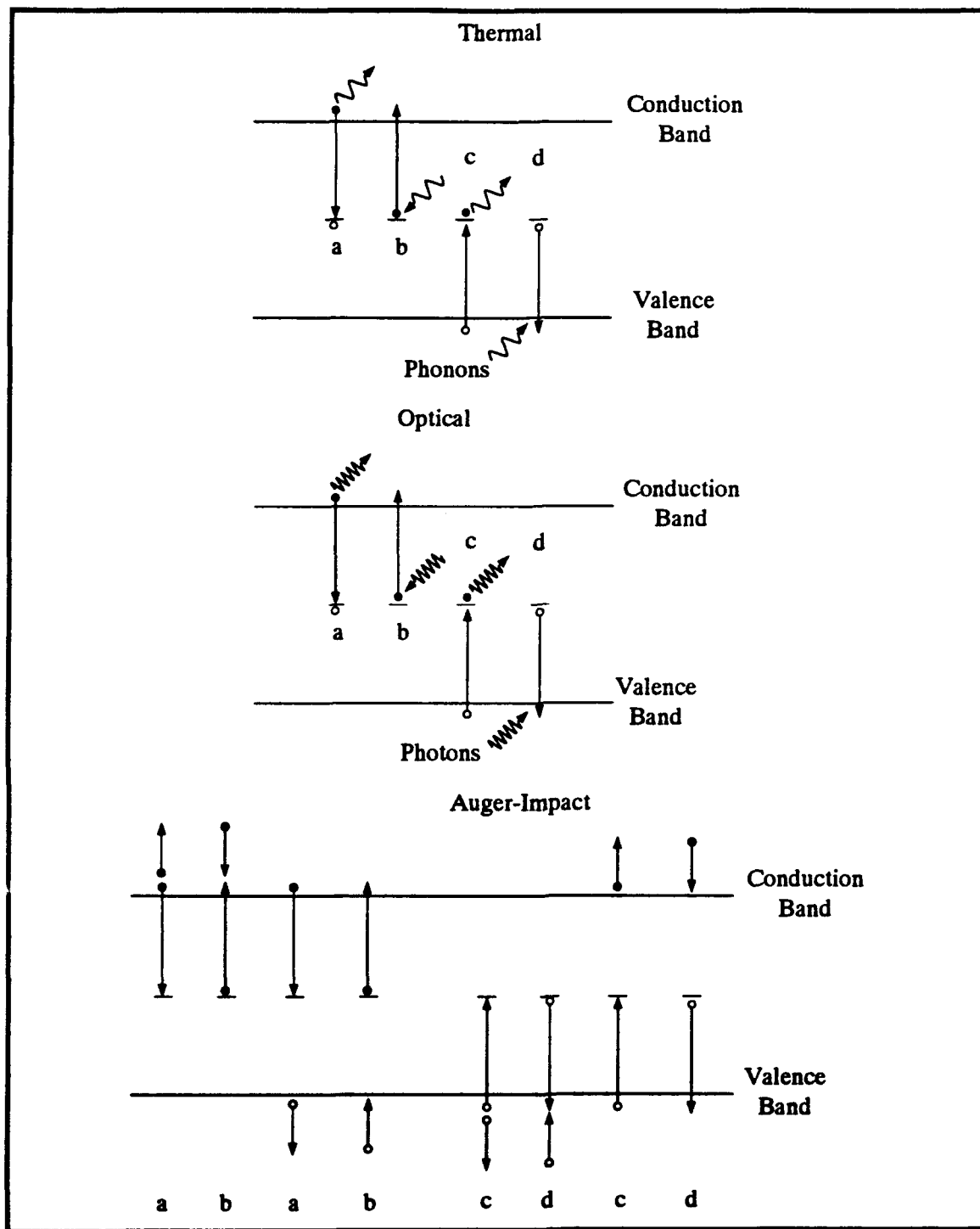


Figure 4. Sah's diagram showing the possible energy conserving mechanisms by which charges are exchanged between the conduction and valence bands and electron levels lying deep inside the band gap (77) (Processes a, b, c, and d designate electron capture, electron emission, hole capture, and hole emission, respectively.)

a hot electron or hole¹. Conversely, Auger-induced electron emission occurs upon impact of the filled center by an energetic electron or hole.

The rates at which these processes occur are typically written to the first-order involving the concentrations of free and bound particles. The electron and hole capture and emission rates are given by the sum of all of these processes (Table 1).

Table 1. Electron and hole capture and emission rates for thermal, optical, and Auger mechanisms.

(a)	electron capture	$(c_n^t + c_n^o + c_n^n n + c_n^p p) n p_T$
(b)	electron emission	$(e_n^t + e_n^o + e_n^n n + e_n^p p) n_T$
(c)	hole capture	$(c_p^t + c_p^o + c_p^p p + c_p^n n) p n_T$
(d)	hole emission	$(e_p^t + e_p^o + e_p^p p + e_p^n n) n_T$

In the electron and hole capture and emission equations in Table 1, e represents emission, and c represents capture. The superscript specifies the means of energy conservation for the coefficient, t for thermal, o for optical, and n if the third particle involved is an electron, or p if it is a hole. The subscript represents the particle being exchanged between the band and the deep state, with n for electrons and p for holes. n_T is the number of electrons occupying the deep center, and p_T is the number of unoccupied centers, or alternatively, the number of holes trapped at the center. Finally, the total number of deep centers, N_{TT} , is given by

$$N_{TT} = n_T + p_T. \quad (13)$$

Thermal capture rates are typically expressed as a product of the thermal capture cross section, σ_n^t or σ_p^t , and the mean thermal velocity of electrons or holes, v_n or v_p , that is,

$$c_n^t = \sigma_n^t v_n \quad (14a)$$

$$c_p^t = \sigma_p^t v_p. \quad (14b)$$

¹ One having a velocity much in excess of mean thermal velocity.

Similarly, optical emission rates for electrons and holes are given by the product of the photoionization cross section, σ_n^o or σ_p^o , and the photon flux Φ , that is,

$$e_n^o = \sigma_n^o \Phi \quad (15a)$$

$$e_p^o = \sigma_p^o \Phi. \quad (15b)$$

The thermal emission and capture rates depend upon each other since, in thermal equilibrium, the rate of capture must be equal to the rate of emission; that is,

$$e_n^t n_T = c_n^t n p_T \text{ or} \\ e_n^t = c_n^t n \frac{p_T}{n_T} \quad (16)$$

for electrons and

$$e_p^t = c_p^t p \frac{n_T}{p_T} \quad (17)$$

for holes. While these equalities apply strictly to thermal equilibrium, they are often assumed to hold for certain nonequilibrium conditions to determine the capture and emission coefficients. This assumption is valid as long as the perturbation which upsets the equilibrium conditions is applied, such that the free electrons and holes can redistribute themselves nearly instantaneously, and thus, maintain quasi-equilibrium. Equations (16) and (17) may be related to the parameters characterizing the deep level by making use of the Fermi distributions for n , p , n_T and p_T . The equilibrium electron and hole concentrations are given by the Boltzmann approximation in equation (2) for a nondegenerate semiconductor, while n_T is given by equation (7) and $p_T = N_{TT} - n_T$. Thus, the electron emission rate in equation (16) becomes

$$e_n^t = \frac{\sigma_n^t v_n N_c}{g} \exp(-(E_c - E_T)/kT), \quad (18)$$

where g is the degeneracy ratio. A similar expression is obtained for the emission rate for holes in equation (17); that is,

$$e_p^t = \frac{\sigma_p^t v_p N_v}{g} \exp(-(E_T - E_v)/kT). \quad (19)$$

Finally, the mean thermal velocity for electrons or holes ($v_{n,p}$) can be obtained from

$$\frac{1}{2} m_{n,p}^* v_{n,p}^2 = \frac{3}{2} kT. \quad (20)$$

Thus, the thermal emission rate for electrons or holes is given by

$$e_{n,p}^T = \frac{4\sqrt{6}\pi^{3/2}\sigma_{n,p}^T m_{n,p}^*}{g_{n,p}h^3} (kT)^2 \exp(-\Delta E_{n,p}/kT). \quad (21)$$

In this equation, the n subscript indicates electron traps, and the p subscript indicates hole traps. Thus, $\Delta E_n = E_c - E_T$ for electron traps, and $\Delta E_p = E_T - E_v$ for hole traps.

From equation (21), it is clear that if the capture cross section is independent of temperature, measuring the emission rate from the center as a function of temperature and forming a plot of

$$\ln(e_{n,p}/T^2) \text{ vs. } 1/kT, \quad (22)$$

will yield a straight line which has a slope equal to $\Delta E_{n,p}$. Furthermore, the intercept of this line with $1/kT = 0$ will yield, aside from a constant factor, the capture cross section for the center. This is referred to as an Arrhenius plot, and the straight line on the plot gives the 'signature' of the deep center.

In this chapter a background on the physical behavior of deep centers in semiconductors has been provided. While this review barely scratched the surface of the information available on deep centers, it gave a sufficient foundation for the remainder of this manuscript. Further details on the nature and behavior of shallow and deep centers in semiconductors may be obtained from the excellent works by Jaros (42) or by Lannoo and Bourgoin (55).

III. Characterization Techniques

In the preceding chapter, the various parameters characterizing deep centers in semiconductors were discussed. In this chapter, the common experimental methods used to measure these parameters will be reviewed. The electrical techniques used in the current study, namely, the Hall effect and Deep Level Transient Spectroscopy (DLTS), will be discussed in detail. Finally, a brief description of the photoluminescence system will be provided.

3.1 Hall Effect Measurements

Hall effect measurements will be performed using the standard van der Pauw technique (94). The advantage of this technique is that no physical dimension needs to be measured to calculate the sheet resistance or sheet-carrier concentration, although the depth of the layer must be known to obtain the volume resistivity and concentration. Furthermore, as shown in Figure 5, the sample may be virtually any shape as long as it is a flat, simply connected domain of uniform thickness with four point contacts along the periphery. Only the results of van der Pauw's analysis will be provided.

As shown in Figure 5, a current, I , is impressed between contacts (1) and (2), and a voltage, V_c , is measured between contacts (3) and (4). Next, the resistivity, $R_{ij,kl}$, can be defined as $R_{ij,kl} = V_{kl}/I_{ij}$, where the current enters contact i and leaves contact j , and $V_{kl} = V_k - V_l$. Therefore, the resistivity, ρ , of the sample whose thickness is d , with no externally applied magnetic field ($B = 0$) is given by

$$\rho = \frac{\pi d}{\ln 2} \left[\frac{R_{21,34} + R_{32,41}}{2} \right] f(Q) \quad (23)$$

where $f(Q)$ is a geometrical correction factor, and Q is the ratio of the resistances in equation (23), either $R_{21,34}/R_{32,41}$ or $R_{32,41}/R_{21,34}$, whichever is greater than or equal to unity. The geometrical correction factor is determined from the following transcendental equation,

$$\frac{Q-1}{Q+1} = \frac{f(Q)}{\ln 2} \operatorname{arccosh} \left(\frac{1}{2} \exp \left(\frac{\ln 2}{f(Q)} \right) \right). \quad (24)$$

The Hall mobility, μ_H , can be obtained from the configuration shown in Figure 5 b. It is given in terms of the Hall voltage, $V_{H42} = \rho \mu_H B I / d$, which is the difference in potential between

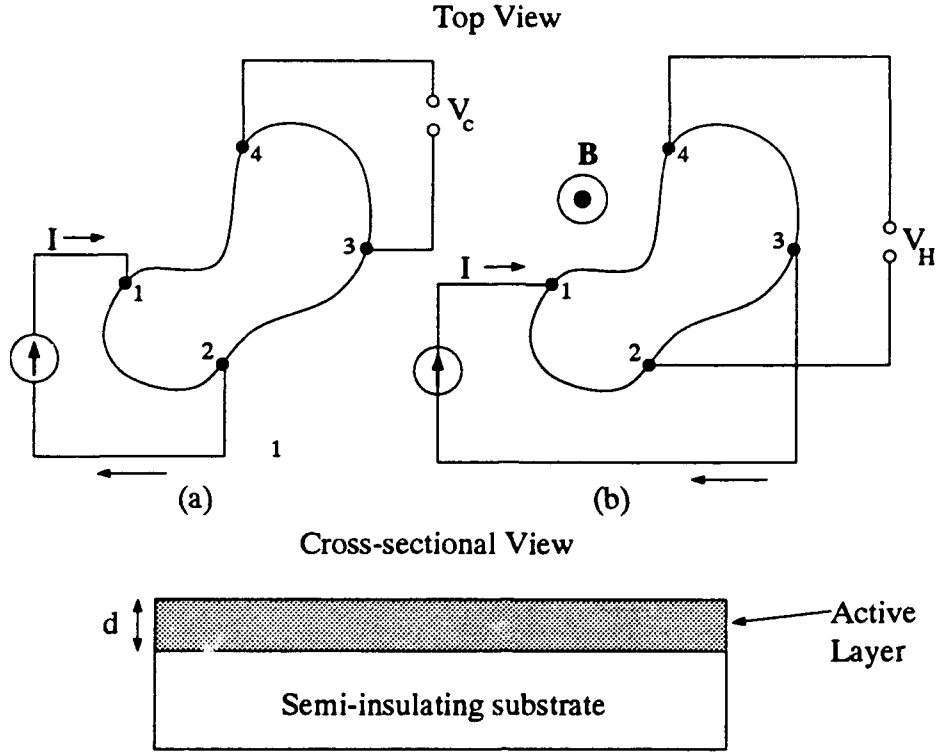


Figure 5. An arbitrarily shaped sample for van der Pauw measurements showing (a) resistivity configuration and (b) Hall effect configuration

contacts (4) and (2), with and without an applied magnetic field, $V_{H42} = (V_4 - V_2)_B - (V_4 - V_2)_0$, while a current, I , is impressed between contacts (1) and (3). The Hall coefficient is found by averaging V_{H42} and V_{H31} ; that is,

$$R_H = \frac{d}{B} \left[\frac{R_{31,42} + R_{42,13}}{2} \right]. \quad (25)$$

Finally, the measured Hall carrier concentration is given in terms of the Hall coefficient,

$$n_H = \frac{1}{qR_H}. \quad (26)$$

Hall effect measurements are simple to interpret for uniform substrates and for uniformly-doped films, while nonuniformly-doped layers require some special consideration. If the dopant density varies with film thickness, its resistivity and mobility will also vary with thickness. A Hall effect measurement gives the average resistivity, carrier concentration, and mobility. For instance, for a p-type layer of thickness d , with varying mobility $\mu_p(x)$ and carrier concentration

$p(x)$, Schroder (80:202) reported that the Hall sheet coefficient R_{Hs} , the sheet resistivity ρ_s , and the average Hall mobility $\langle\mu_H\rangle$ will be given by

$$R_{Hs} = \frac{\int_0^d p(x)\mu_p^2(x)dx}{q\left[\int_0^d p(x)\mu_p(x)dx\right]^2}, \quad (27)$$

$$\rho_s = \frac{1}{q\int_0^d p(x)\mu_p(x)dx}, \quad (28)$$

and

$$\langle\mu_H\rangle = \frac{\int_0^d p(x)\mu_p^2(x)dx}{\int_0^d p(x)\mu_p(x)dx}. \quad (29)$$

In order to determine the profiles of $p(x)$, the resistivity, $\rho(x)$, and $\mu_H(x)$, Hall effect measurements must be performed for varying thicknesses. This analysis is typically implemented using the differential Hall measurement technique, whereby chemical etching is used to remove thin layers while sequentially measuring the Hall coefficient. A second technique utilizes reverse biasing of a Schottky gate deposited on the surface of the van der Pauw structure to make portions of the conducting film electrically inactive. These techniques are addressed more thoroughly by Schroder (80:203), and they will not be dealt with further, since they will not be utilized in this research.

A block diagram of the automated Hall effect apparatus used in this investigation is given in Figure 6. This is the System 110 from Keithley, Inc. (45). With this arrangement, all configurations necessary for sheet resistivity and Hall voltage measurements are easily obtained under computer control, via the IEEE-488 interface. Electrical signals are carried by the center conductor of triaxial cables which have their inner shields maintained at the signal voltage by electrometers which are operated as unity-gain buffer amplifiers. This configuration minimizes cable charging effects and small leakage currents which become significant when measuring high-resistivity samples. These features, in combination with the use of a current source capable of regulating currents as small as 10^{-10} A, such as the Keithley model 220, allow the system to measure resistances up to $10^{12} \Omega$.

3.1.1 Temperature-Dependent Hall Effect Measurements The Hall effect system shown in Figure 6 is accompanied with a vacuum pump and a closed cycle helium refrigerator. This configuration facilitates the measurement of the carrier concentration, mobility, and resistivity at

Temperature-Dependent Hall Effect Measurements

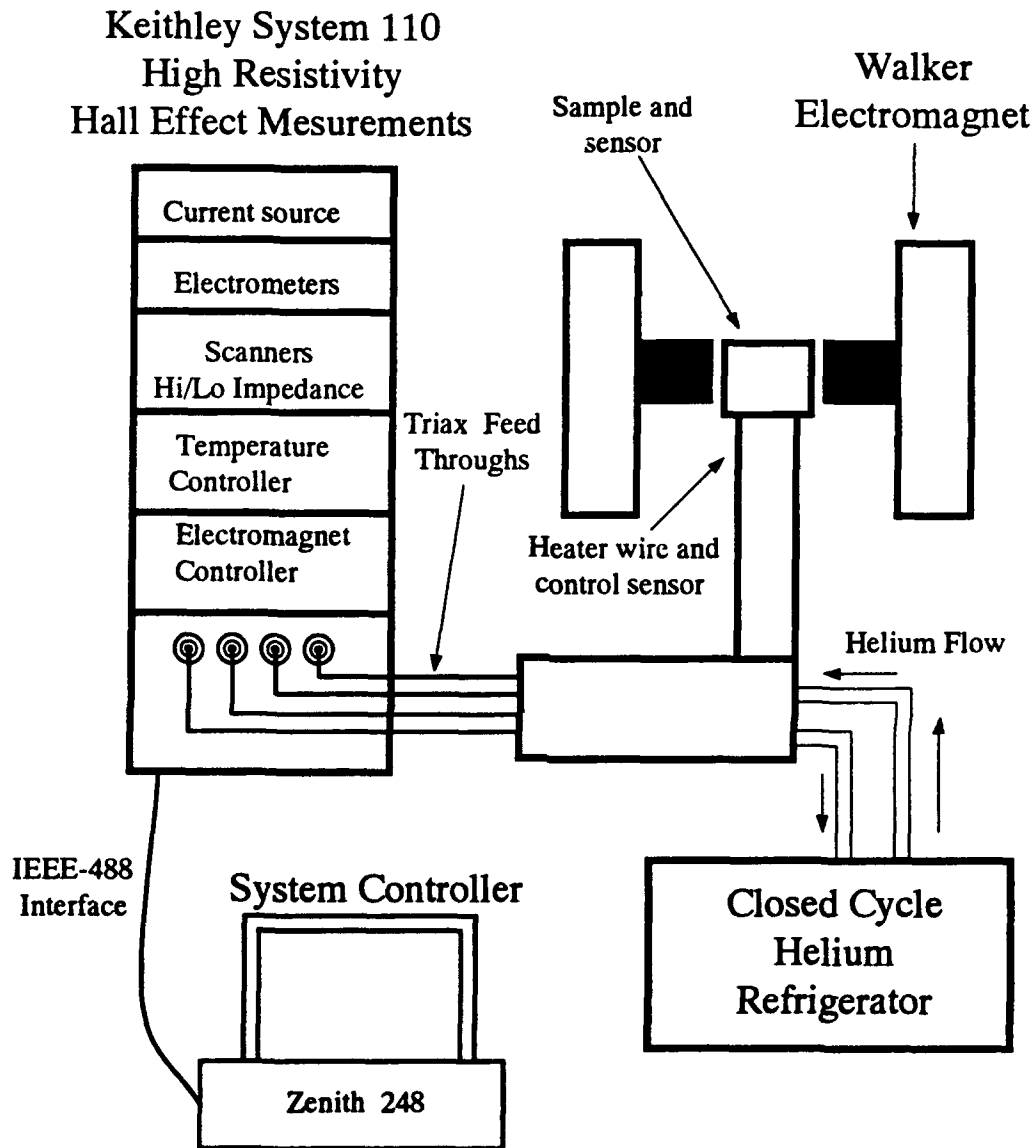


Figure 6. Schematic diagram of an automated Hall effect system used for high resistivity and temperature-dependent Hall effect measurements

any temperature between 8 and 325 K. The sample is mounted on a copper block at the end of the cold head. A heater wire at the base of the copper block allows the Lake Shore temperature controller to maintain a constant temperature while the Hall effect/sheet resistivity measurement is performed.

The two critical parameters of interest in the Temperature-Dependent Hall (TDH) effect measurements are the mobility and carrier concentration. Measurement of $\mu_H(T)$ contributes information on the type of scattering mechanisms. Look (57:74) gives the temperature dependencies of some of the typical scattering mechanisms, which include, defect, carrier-carrier, and lattice scattering (phonons). These scattering mechanisms will not be discussed further here since they will not be utilized for analysis of $\mu_H(T)$, which is acquired along with the temperature-dependent carrier concentration.

By measuring the electron or hole concentrations as a function of temperature, the donor or acceptor concentrations and activation energies may be determined. For instance, Figure 7 shows the temperature-dependent electron and hole concentrations, for an n-type $\text{Al}_{0.5}\text{Ga}_{0.5}\text{As:Si}$ sample and a p-type GaAs:Be sample. These temperature-dependent concentrations may be fit to the analytic expressions previously given for $n(T)$ and $p(T)$ in equations (7) and (11), respectively. These equations are nonlinear functions of the parameters characterizing the donor or acceptor centers, significantly complicating the procedure of fitting the temperature-dependent data to these equations. A general nonlinear technique proposed by Levenberg and Marquardt was used for this purpose. The Fortran version of this code was obtained from the book, Numerical Recipes (73). In the case of a p-type sample dominated by a single acceptor, there are four parameters which go into the fit:

N_A	the concentration of acceptors
N_D^{net}	the net unionized donor concentration above the Fermi level
E_{A0}	the energy of the acceptor with respect to the valence band maximum
$\frac{g_A}{g_{A0}} \exp(\alpha_A/k)$	the product of the degeneracy ratio and the exponentiated temperature dependence of the acceptor energy level

Since the concentration varies over logarithmic scales, the fitting algorithm will weigh the data at higher temperatures preferentially, and thus, the fit will not represent the data well at lower

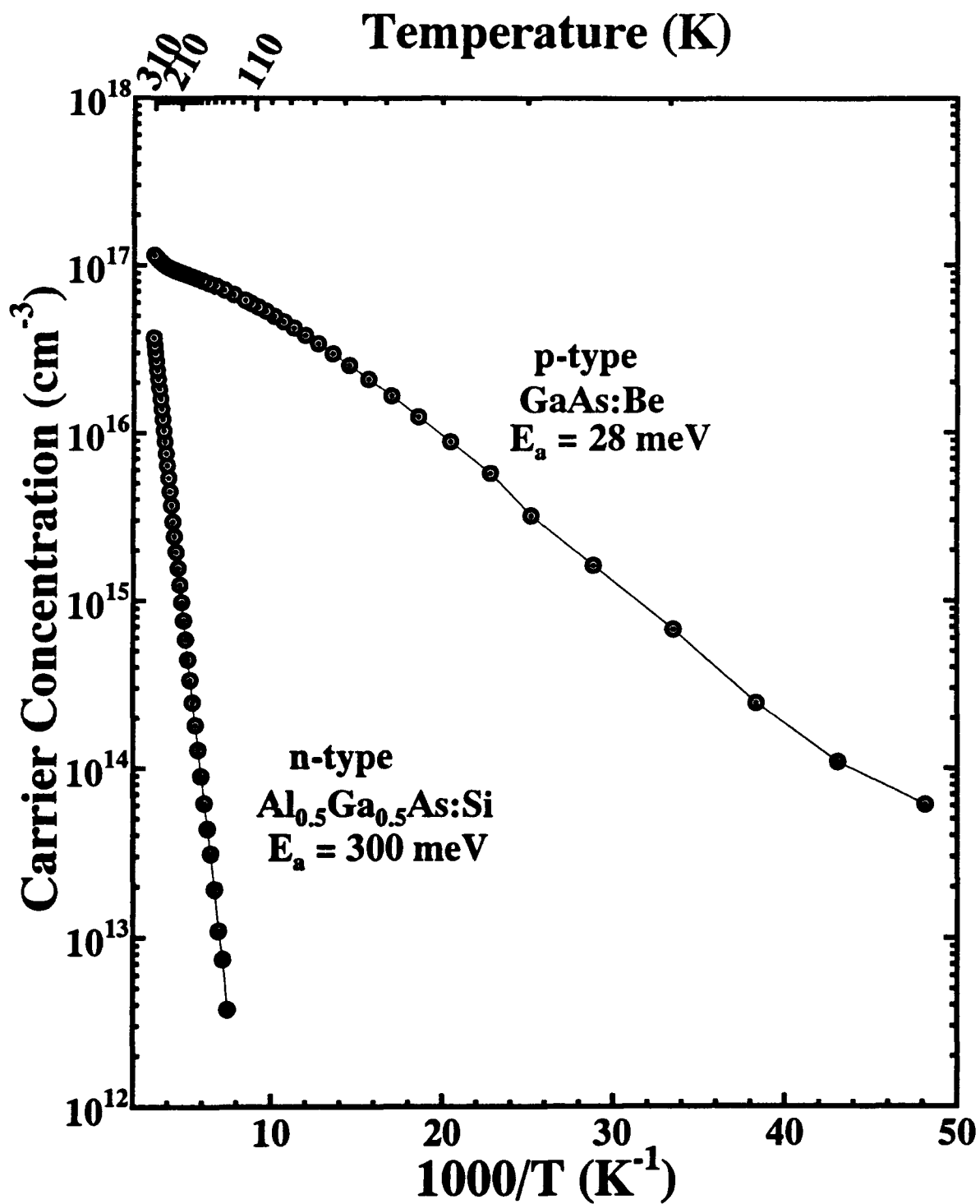


Figure 7. Temperature-dependent Hall effect data for a relatively deep Si donor in $\text{Al}_{0.5}\text{Ga}_{0.5}\text{As:Si}$ and a relatively shallow Be acceptor in GaAs:Be (Both samples were grown by molecular beam epitaxy.)

temperatures. However, the Levenberg-Marquardt technique works nicely when a proper weight is assigned to each point. This weighting is typically accomplished by dividing the measured concentration by a factor of 100, and assigning this number to an uncertainty associated with that concentration.

3.2 Capacitance Spectroscopy

In section 2.3, an expression was given for the temperature dependence of the thermal emission rate of trapped electrons or holes from a deep center. If the temperature-dependent emission rate can be measured, equation (21) will yield the activation energy and thermal capture cross section for the deep center. This section describes the means by which the thermal emission rate is measured.

From Figure 4 and Table 1, the concentration of electrons trapped at a deep center is governed by the following rate equation:

$$\frac{\partial n_T}{\partial t} = (a) - (b) - (c) + (d). \quad (30)$$

If the emission is occurring in the space-charge region of a p^+n junction or Schottky diode, then $n \approx 0$ and $p \approx 0$, and consequently $a = 0$ and $b = 0$. If, in addition, the measurements are carried out in darkness; i.e., $\Phi = 0$, the rate equation (equation (30)) is given by the following relationship:

$$\frac{\partial n_T}{\partial t} = -(e_n + e_p)n_T + e_p N_T \quad (31)$$

(with superscripts omitted, since all processes are now thermal). Since the rate equation is linear, the following solution is easily obtained:

$$n_T(t) = \exp(-(e_n + e_p)t) \left[\frac{N_T e_p}{e_n + e_p} + n_T(0) \right] + \frac{e_p N_T}{e_n + e_p}. \quad (32)$$

The initial trap concentration $n_T(0)$ is determined by the biasing of the diode at times prior to $t = 0$. For example, for a p^+n diode, a large concentration of holes and electrons will flow through the junction if it is forward biased. If this biasing condition is maintained to establish a steady state,

$$\frac{\partial n_T}{\partial t} = 0, \quad (33)$$

and equation (30) yields

$$n_T(0) = \frac{N_T(c_n n + e_p)}{c_n n + e_n + c_p p + e_p}. \quad (34)$$

During this period, the Auger-capture processes will dominate the thermal-emission processes, since the Auger terms are proportional to n or p . Thus, equation (34) becomes

$$n_T(0) = N_T \frac{c_n n}{c_n n + c_p p}. \quad (35)$$

Now, under high-injection conditions,

$$n \approx p \gg 0 \quad (36)$$

so that, finally

$$n_T(0) = N_T \frac{c_n}{c_n + c_p}. \quad (37)$$

In fact, identical arguments can be made for the concentration of holes trapped at the center during the injection portion of the biasing sequence, which yields

$$p_T(0) = N_T \frac{c_p}{c_n + c_p}. \quad (38)$$

If the center behaves primarily as an electron trap, then $c_n \gg c_p$, such that immediately after the pulse

$$n_T(0^+) \rightarrow N_T \quad (39)$$

$$p_T(0^+) \rightarrow 0, \quad (40)$$

or, in the case of a hole trap, with $c_p \gg c_n$, then

$$n_T(0^+) \rightarrow 0 \quad (41)$$

$$p_T(0^+) \rightarrow N_T. \quad (42)$$

Since, in general, electron traps are closer to the conduction band, it is expected that $c_n \gg c_p$, and the solution for the concentration of trapped electrons at the center, from equation (32), becomes

$$n_T(t) = N_T \exp(-e_n t). \quad (43)$$

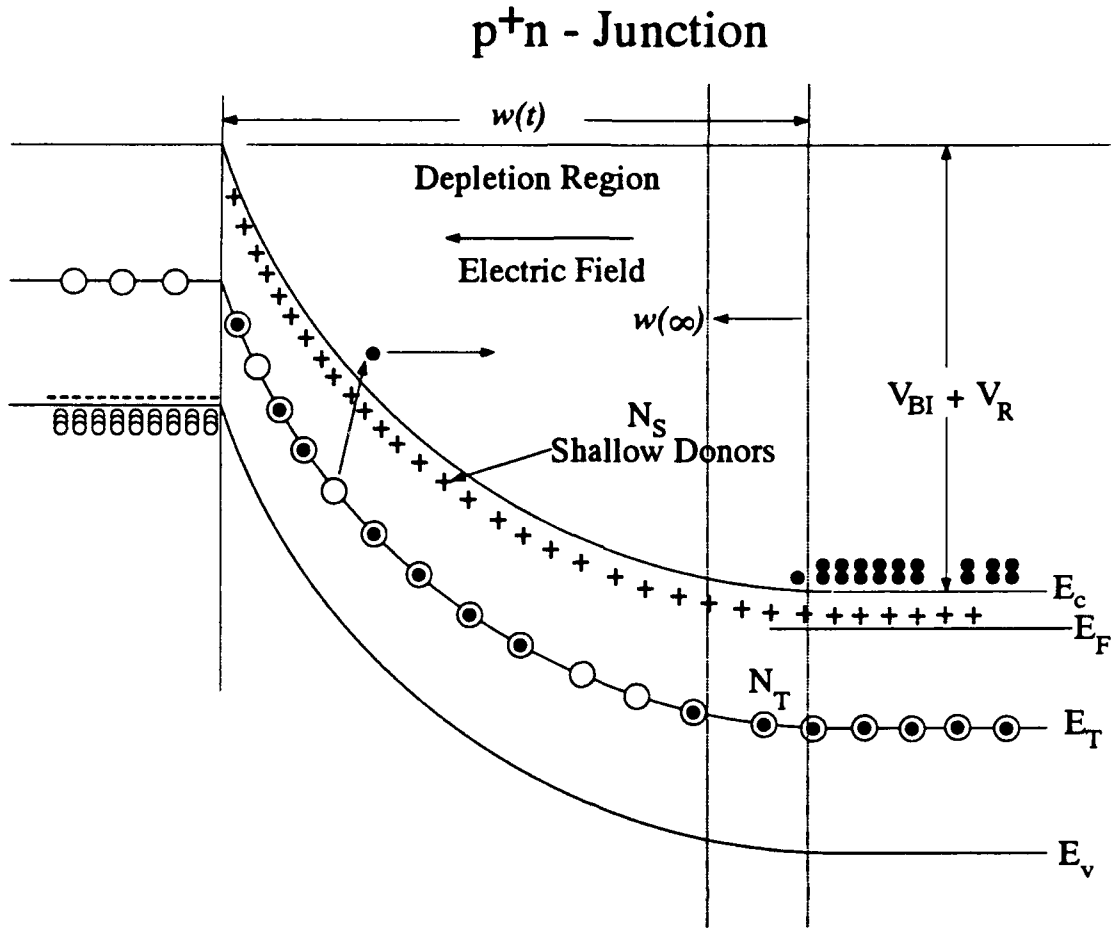


Figure 8. Emission of electrons trapped at centers located in the depletion region of a p⁺n junction

A rate equation similar to equation (31) may also be written for the trapped-hole concentration. For the case of a hole trap, $e_p \gg e_n$, and the solution for the trapped-hole concentration at a center acting as a hole trap becomes

$$p_T(t) = N_T \exp(-e_p t). \quad (44)$$

Figure 8 illustrates the basic means of measuring the time-dependent changes in the concentration of trapped holes or electrons. This figure shows a p⁺n junction with a built-in voltage, V_{BI} , and an applied reverse bias, V_R . There is a uniform concentration, N_S , of shallow donors in the n-type material below the rectifying junction. If these were the only impurities present, a double integration of Poisson's equation yields the width, w , of the space-charge

region (86:79,248)

$$w = \sqrt{\frac{2\epsilon_s}{N_S}(V_{BI} + V_R - nkT/q)}, \quad (45)$$

where ϵ_s is the permittivity of the semiconductor. For a Schottky diode, $n = 1$, and for a p⁺n junction, $n = 2$, and the depletion width may be determined indirectly by monitoring the high-frequency capacitance of the junction with area, A , which is given by

$$C = \frac{\epsilon_s A}{w} = \sqrt{\frac{q\epsilon_s N_S}{2(V_{BI} + V_R - nkT/q)}}. \quad (46)$$

However, as shown in Figure 8, there is also a uniform concentration N_T of deep centers acting as electron traps. At times $t < 0$, a forward bias is applied to the contact, which flattens the bands and allows electrons to flow into the junction and be captured by the electron traps. At $t = 0$, the reverse bias, V_R , is applied, and all traps in the space-charge region are occupied by electrons. For $t > 0$, electrons will be emitted from these centers in accordance with equation (43). Thus, the junction capacitance becomes time dependent

$$C(t) = \sqrt{\frac{q\epsilon_s(N_S - N_T \exp(-e_n t))}{2(V_{BI} + V_R - nkT/q)}}. \quad (47)$$

Furthermore, the square of the capacitance decays exponentially

$$C^2(t) = C^2(\infty) - \frac{N_T}{N_S} \exp(-e_n t) C^2(\infty). \quad (48)$$

Thus the trap concentration is related to the amplitude of the capacitance transient

$$N_T = -N_S \frac{C^2(0) - C^2(\infty)}{C^2(\infty)}. \quad (49)$$

For the usual case in which $N_T \ll N_S$, equation (48) can be expanded using the binomial theorem, so that the capacitance itself is exponential. That is,

$$C(t) = C(\infty) - \frac{N_T}{2N_S} \exp(-e_n t) C(\infty). \quad (50)$$

Thus, by measuring the capacitance transient and fitting it to an exponential decay, the concentration of deep levels and their emission rates at a given temperature can be determined. Finally, after measuring a sequence of capacitance transients at various temperatures and analyzing each for an exponential decay, an Arrhenius analysis may be used to determine the activation energy, $E_T = \Delta E_n$, and the thermal capture cross section for the trap, σ_n^t .

3.2.1 Majority and Minority Carrier Traps and Shape of the Capacitance Transient The amplitude of the capacitance transient in equation (50) is negative. This feature reflects the fact that the deep centers are considered as majority carrier traps; i.e., electron traps in an n-type material. A sequence of physical processes gives rise to the capacitance transient. That is, when electrons are trapped at centers in the n-type side of the space-charge region, the total (positive) ionized charge in this region is reduced. This situation causes an increase in the depletion width and a corresponding decrease in the junction capacitance. As the traps emit, the capacitance relaxes to its higher quiescent reverse-bias value. If instead, holes were introduced into the junction region, which were then captured by hole traps, there would initially be more positive charge in the junction, and this state would ultimately return to the shallow-dopant density as the holes are emitted into the valence band. This situation would result in a positive capacitance transient.

In the case of a Schottky junction formed on a p-type semiconductor, or similarly, for an n^+p junction, if the holes are trapped in the space-charge region of the p-type material, the total negative charge in this region will decrease. Thus, the depletion width will increase, and the capacitance will correspondingly decrease. As the hole traps emit, the capacitance will increase to its quiescent reverse-bias value. Arguments such as these lead to the conclusion that negative transients are associated with majority carrier traps, while minority carrier traps produce positive transients.

In the case of the Schottky contact on n-type material, the only way to introduce holes into the depletion region is via the intrinsic photoexcitation of electrons and holes. However, if measurements are performed on a p^+n junction, an applied-forward bias whose magnitude is larger than the built-in voltage will result in a large hole current flowing through the junction. This situation is referred to as a 'saturating injection pulse' or 'minority carrier injection pulse', and it is illustrated in Figure 9. The assumption is that during the pulse, $p \gg n$, and if a hole trap is present with $c_p \gg c_n$, then all these centers will have captured holes by the end of the pulse. This situation will produce a positive transient as the holes emit to the valence band after the reverse bias is established (or in other words, as valence-band electrons begin to occupy empty states below the Fermi energy level). In contrast, during the majority-carrier pulse, shown in Figure 10, the original reverse bias on the diode is reduced, or if a forward bias is applied,

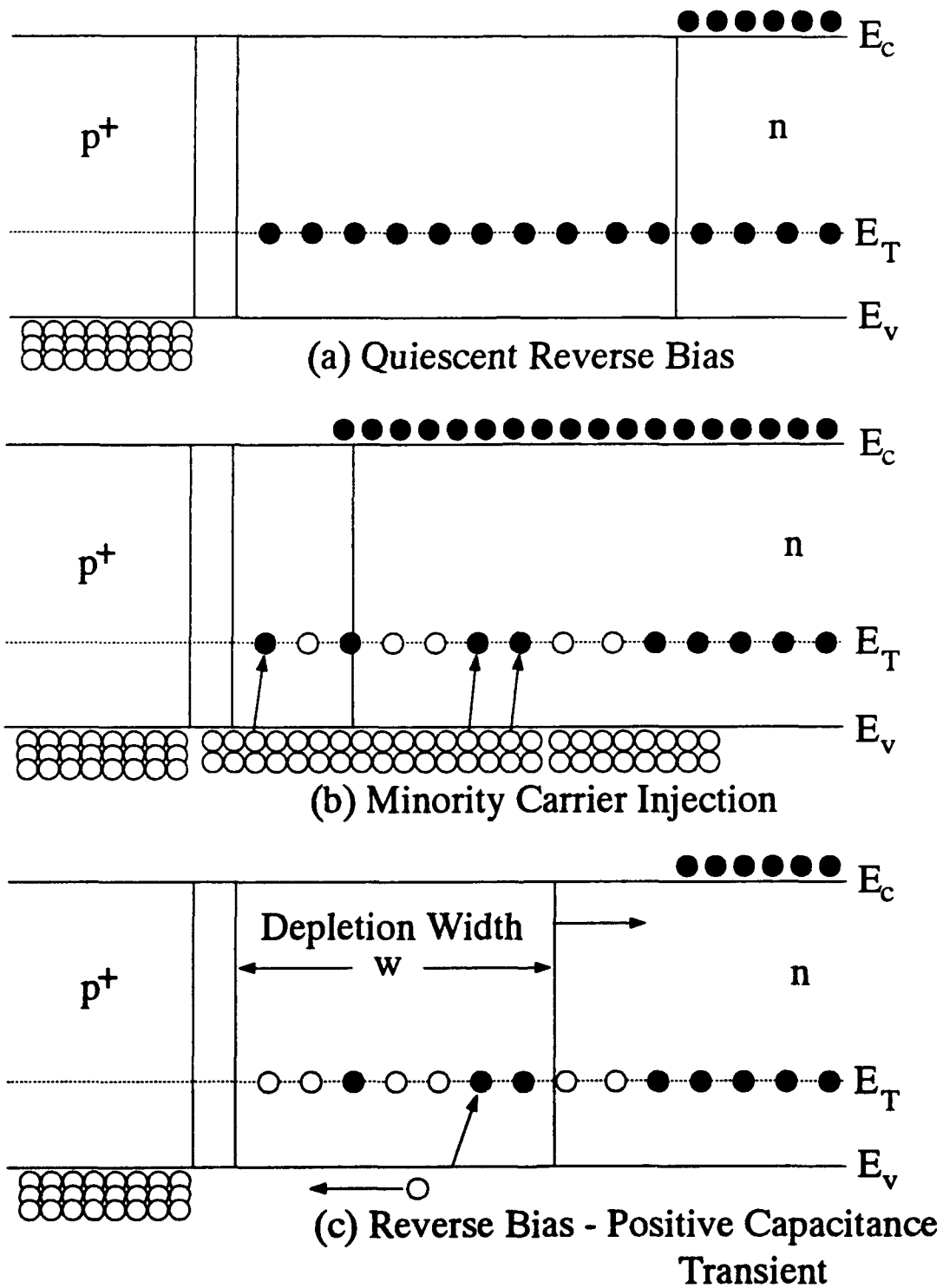


Figure 9. Saturation injection biasing sequence: (a) steady-state reverse bias, hole traps empty, (b) large forward bias, capture of holes, (c) original reverse bias reestablished, emission of holes, capacitance decreasing

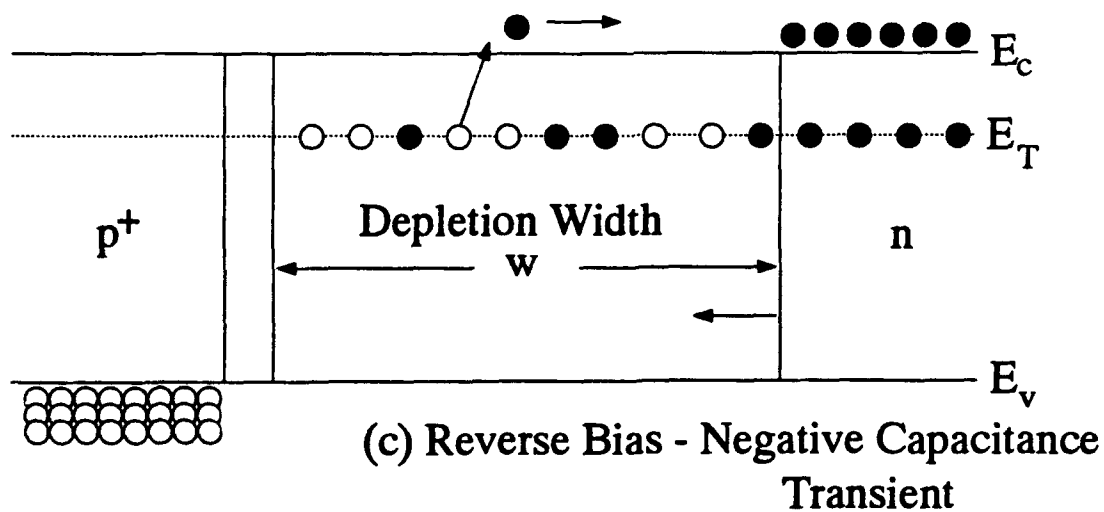
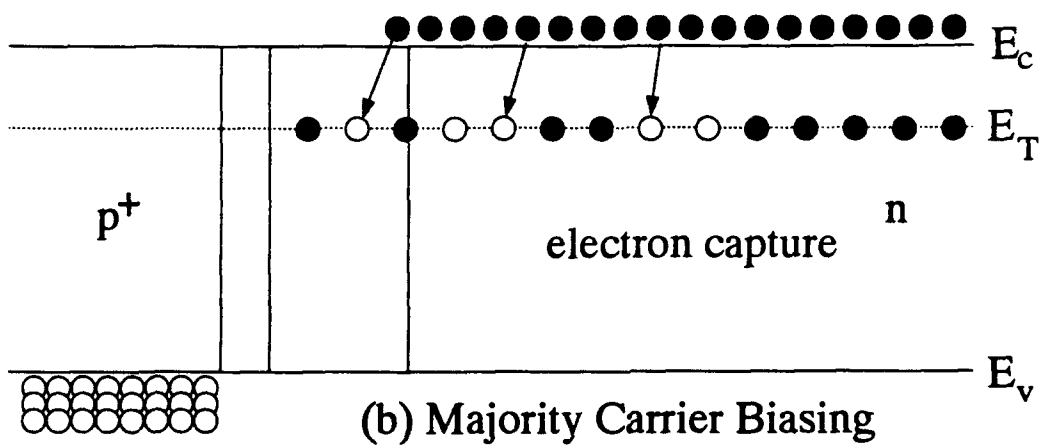
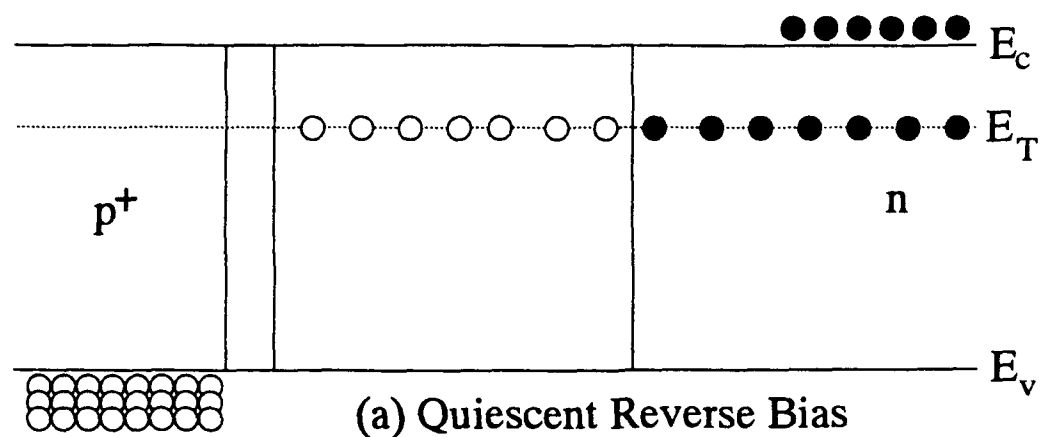


Figure 10. Majority-carrier biasing sequence: (a) steady-state reverse bias, electron traps empty, (b) reduced reverse bias with no hole injection, capture of electrons (c) original reverse bias reestablished, emission of electrons, capacitance increasing

its magnitude is chosen to be somewhat less than the built-in voltage, so that only electron traps (majority-carrier traps) can be charged.

The same type of measurements can be performed with an n^+p junction. With the negative terminal of the bias potential applied to the n^+ junction, a large forward bias (saturation injection biasing) will tend to inject electrons into the p -type side of the junction. The electrons will be captured by electron traps if they are present. The emission of these electrons, once the reverse bias has been established, will give rise to a capacitance transient with a positive amplitude. However, if during the pulsing sequence the forward bias does not exceed the built-in voltage, only holes will be introduced into the junction for capture by the hole traps. Thus, when the reverse bias is established, there will be a capacitance transient with a negative amplitude corresponding to the emission of holes from these centers. In general, during a saturating-injection pulse, minority carrier traps are observed, corresponding to positive transients, while during a majority carrier biasing sequence, only majority carriers traps are observed, corresponding to negative capacitance transients.

There are, however, exceptions to these simple rules for the shape of the capacitance transient. A donor center emits an electron to the conduction band, becoming positively charged. Likewise, an acceptor center emits a hole to the valence band, becoming negatively charged. Thus, a donor center gives rise to an electron trap, while an acceptor center acts as a hole trap. Unfortunately, under injection biasing, the shape of the capacitance transient does not always follow the rules stated above. This is due to the fact that during the injection pulse, both electrons and holes are flowing through the junction, and hence, either may be trapped at the center. Sah (78:777) has considered this situation in detail and showed that the shape of the capacitance transient for injection biasing is determined by comparing the ratio e_n^t/e_p^t to c_p^t/c_n^t . Sah considers both the p^+n and n^+p junction, and gives the shape of the capacitance transient, as shown in Figure 11, for the three conditions

$$(1) e_n^t/e_p^t > c_p^t/c_n^t$$

$$(2) e_n^t/e_p^t = c_p^t/c_n^t$$

$$(3) e_n^t/e_p^t < c_p^t/c_n^t$$

A donor center obeying condition (3) in a p^+n diode will give rise to a transient that has a positive amplitude. This situation occurs since condition (3) implies that $e_p^t c_p^t > e_n^t c_n^t$. Since the donor center is probably closer to the valence band, it is expected that $e_n^t > e_p^t$, which would

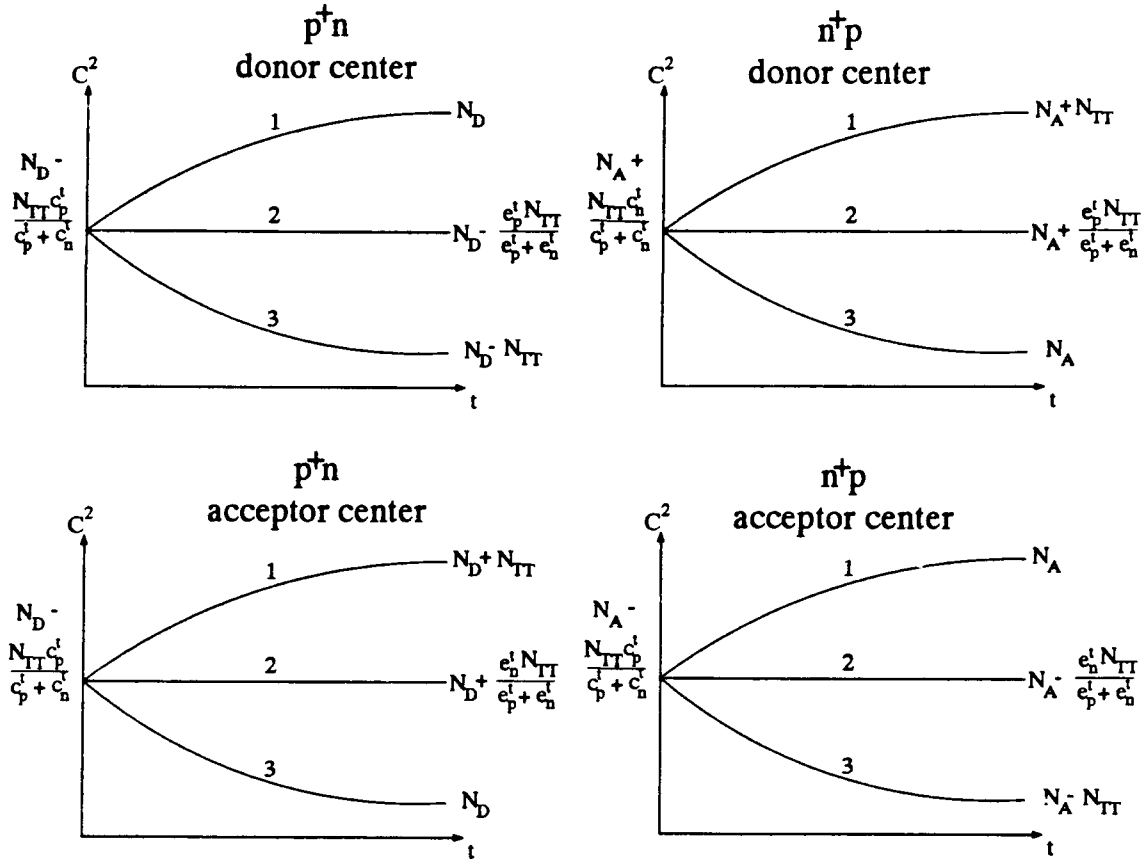


Figure 11. Capacitance transient shape for saturation injection biasing of p⁺n or n⁺p junctions, after Sah (78) (The cases are: (1) $e_n^t/e_p^t > c_p^t/c_n^t$, (2) $e_n^t/e_p^t = c_p^t/c_n^t$ and (3) $e_n^t/e_p^t < c_p^t/c_n^t$.)

require $c_p^t \gg c_n^t$. This characteristic is unusual for a donor center, which is expected to behave as an electron trap.

3.2.2 Deep Level Transient Spectroscopy When it was first recognized that space charge techniques could provide valuable information, such as trap concentrations and activation energies, high-speed waveform digitizers were not available. This led Lang (53) to introduce a technique known as Deep Level Transient Spectroscopy (DLTS), which is most easily explained with the aid of the diagram given in Figure 12. The capacitance transient is assumed to have an exponential decay at each temperature, as given in equation (50). Furthermore, equation (21) shows that as the temperature is increased, the emission rate of trapped charges will increase (and thus, the time constant, τ , will decrease). This situation is illustrated in Figure 12 for a sequence of capacitance

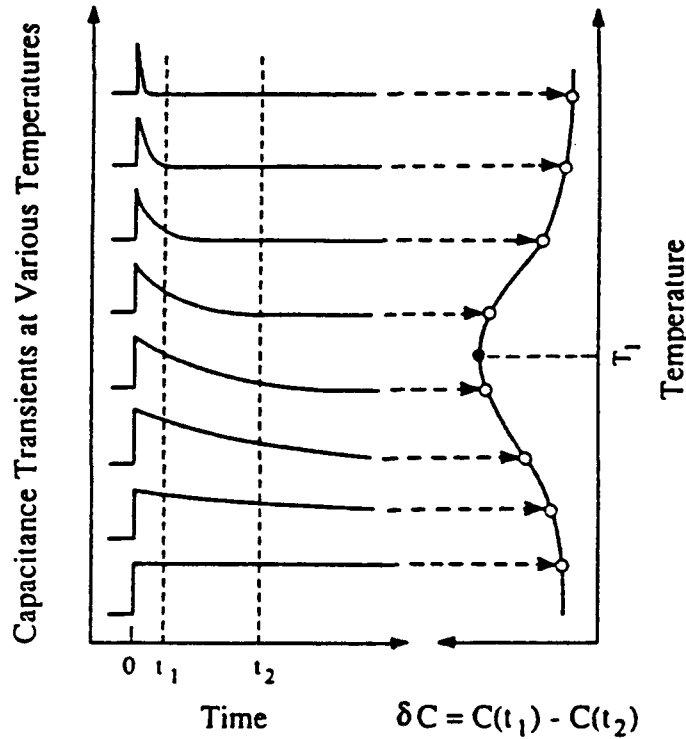


Figure 12. Rate-window concept developed by Lang (53)

transients with increasing temperatures. As the temperature T is continuously varied, the quantity $\Delta C(T) = C(t_1) - C(t_2)$, referred to as the DLTS signal, is generated. This difference signal is formed electronically with a double boxcar integrator, which has an integration window at t_1 and t_2 , with $t_2 > t_1$. At low temperatures, the time constant is much larger than t_2 , and hence $C(t_1) \approx C(t_2)$, and therefore, $\Delta C = 0$. On the other hand, at temperatures where $\tau \ll t_1$, $C(t_1) \approx C(t_2) \approx C(\infty)$, and once again, $\Delta C = 0$. Therefore, it is apparent that the DLTS signal will have a peak at some temperature between these two extremes. By differentiating the analytic function for the DLTS signal

$$\Delta C = \Delta C(0) \left(\exp \left(-\frac{t_1}{\tau} \right) - \exp \left(-\frac{t_2}{\tau} \right) \right) \quad (51)$$

with respect to τ , and equating the resulting expression to zero, the peak in the DLTS signal is found to occur when

$$\tau = \frac{t_2 - t_1}{\ln(t_2/t_1)}. \quad (52)$$

The times t_1 and t_2 are said to constitute a 'rate window' with emission rate given by the inverse of equation (52). The plot of ΔC vs T is known as a rate-window plot. If the decay is actually a single exponential as given by equation (50), the emission rate at the temperature of the peak in the DLTS signal is given by the inverse of equation (52). Hence, by choosing many different rate windows and performing a temperature scan with each, an Arrhenius analysis of T^2/ϵ_n vs. $1/kT$ can be implemented to determine the trap activation energy and capture cross section. Also, positive peaks on the rate-window plot are indicative of minority-carrier traps, while negative peaks are associated with majority-carrier traps. Finally, the amplitude associated with these peaks is proportional to the concentration of the center, as given by equation (50). Indeed, much information is contained in a rate-window plot. As an example, Figure 13 shows the rate-window plots for the EL2 defect in GaAs for three different rate windows. As the emission rate set by the rate window increases, the peak in the DLTS signal moves to higher temperatures.

3.2.3 Isothermal Transient Capacitance Measurements In the implementation of the standard DLTS technique, as proposed by Lang, a rate window is established, and the temperature is scanned from the lowest temperature of interest to the highest temperature. The temperature at which the DLTS signal peaks yields one data point for the Arrhenius plot. However, since at least two points are required for the Arrhenius analysis, and even more are desired for statistical purposes, several temperature scans must be performed. One way to avoid this inconvenience is to establish several simultaneous rate windows for the temperature scans. However, there is an even more serious problem that the standard DLTS technique cannot adequately handle; the DLTS analysis only considers the possibility that a single deep center is present. If a second deep center is present and emitting on a similar time scale as the first, the decay in the capacitance after the pulse-bias sequence will be given by a sum of the two exponentials. Furthermore, if a third center is present, the decay will be given by the sum of the three exponentials. In general, if N distinct centers are present, the decay in the squared capacitance is given by

$$C^2(t) = \frac{q\epsilon \left(N_d - \sum_{i=1}^N N_{T_i}(t) \right)}{2(V_{BI} + V_R - kT/q)}. \quad (53)$$

If a rate-window plot is made when such a situation arises, it is possible that the peaks originating from the various centers may overlap to such an extent that it is not possible to implement Lang's analysis or identify the temperature at which the peak occurs. For example, Figure 14

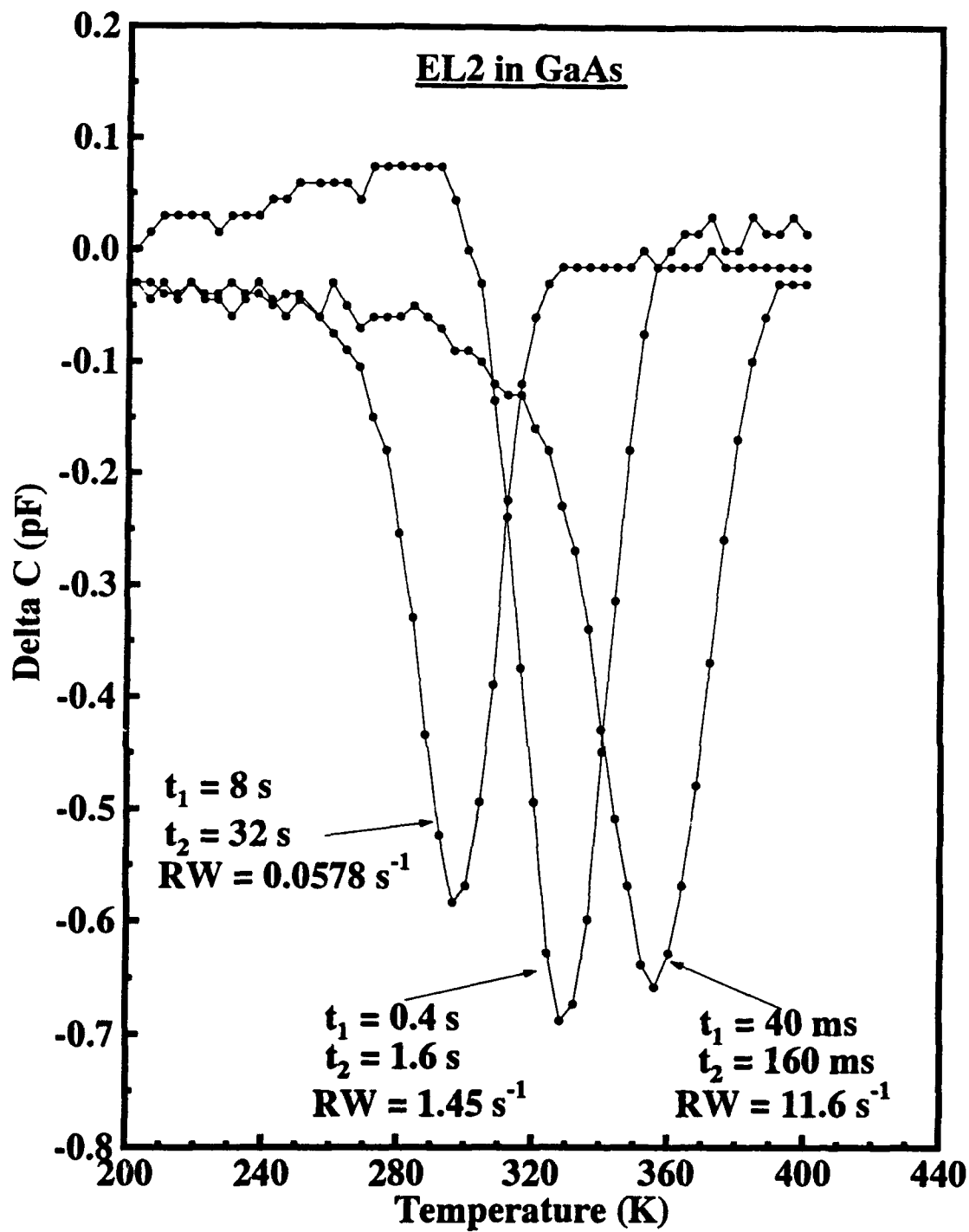


Figure 13. DLTS plots using different rate windows which show the response of the native EL2 defect in GaAs

shows various rate-window plots obtained using majority-carrier biasing on an n-type (Si-doped) $\text{Al}_{0.4}\text{Ga}_{0.6}\text{As}$ sample. The peaks observed in this sample are due to emission from the DX center, which is actually attributed to at least three closely-spaced levels. This figure shows that it would be very difficult to accurately obtain the peak positions for these three centers. Also, an attempt to utilize Lang's analysis would be subject to error, since the analysis was developed specifically for a single exponential decay.

A much better approach is to stabilize the temperature and digitally record the capacitance transient. This technique is referred to as Isothermal Transient Capacitance (ITCAP) measurements (40). If more than one deep center is present, the data may be analyzed for the multiexponential decay in equation (53). This technique has the added benefit that, for each temperature at which a transient is recorded, one point is obtained for the Arrhenius analysis. Thus, only one temperature sweep is required, although additional time will be required for temperature stabilization. The ITCAP technique is used to obtain information on deep levels in this investigation.

3.2.4 Experimental and Analytical Implementation Figure 15 shows the experimental arrangement used to implement the ITCAP measurements. The sample is mounted on a TO5 header which is placed in a fitted hole drilled into a copper block at the end of a Helitran liquid helium cryostat. The temperature of the system is lowered to approximately 20 K and stabilized. A Zenith-248 microcomputer is used to control the experiment via the IEEE-488 bus. The temperature is stabilized with the Lake Shore temperature controller, which monitors the sample temperature using a platinum resistance sensor. There are two such independent sensors, mounted on opposite sides of the sample block, and they typically agree to within 0.2 K.

Once the desired measurement temperature is stabilized, capacitance transient acquisition begins. A pulsing sequence is sent to the HP4280A C-meter, which uses the HP8112 pulser if the measurement time interval is less than 2 ms. The measurement is then initiated, and the resulting transient is stored in the HP4280A's internal buffer. After the transient acquisition is complete, the data is transferred from the C-meter to the Z-248 where it is written into a sequential file. Up to four different samples can be accommodated for one temperature scan, and each sample can be measured at a given temperature. The temperature is then incremented by a set interval,

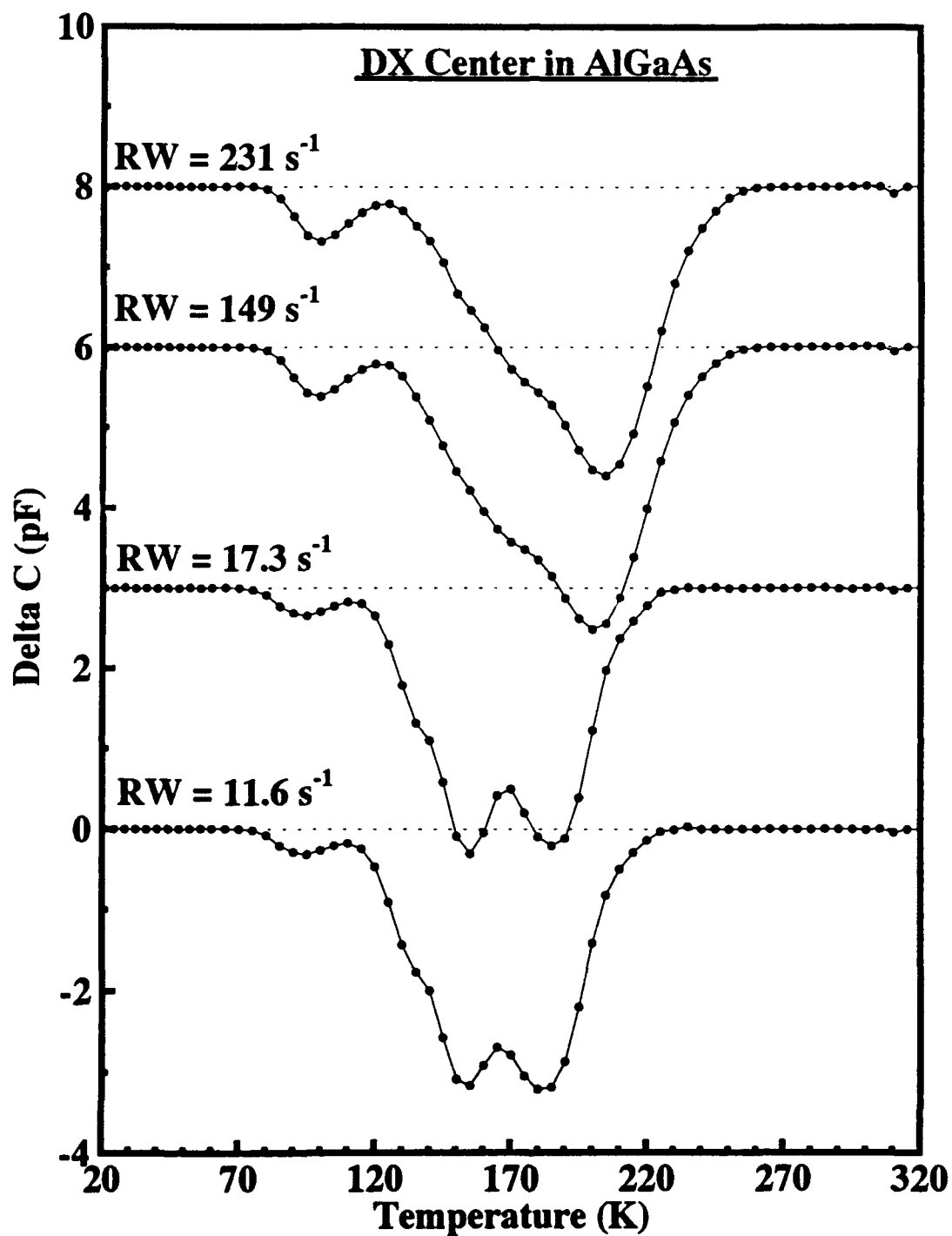


Figure 14. Rate-window plots for n-type $\text{Al}_{0.4}\text{Ga}_{0.6}\text{As}:\text{Si}$ sample showing the DX emission which consists of at least three centers (It is not possible to resolve these centers with the standard rate-window analysis.)

which is typically 4 K. This process is repeated until the temperature exceeds a specified value, typically not more than 425 K.

A sequence of transients is shown in Figure 16. These transients are due to electron emission from the EL2 center in n-type GaAs. The entire dynamic range of the HP280A C-meter is utilized by recording three separate capacitance transients. The relevant times for the three transients are:

- 200 points at 10 μ s intervals from 10 μ s to 2 ms
- 200 points at 2 ms intervals from 2 ms to 0.4 s
- 200 points at 0.4 s intervals from 0.4 s to 80 s.

By using 3 separate linear scales, time constants whose values span 7 orders of magnitude may be sampled. Thus, a fast transient can be acquired on the 2 ms time scale as well as a very slow transient on the 80 s time scale.

Once the entire temperature range is scanned, the data is transferred to a more powerful computer for analysis, typically a Sun SPARCstation 2. Although the rate-window plots are not analyzed using the technique of Lang, they are still generated because they provide a means for comparing various samples. That is, when a given rate window is selected, the DLTS peaks arising from the same center in different samples should coincide in temperature. Furthermore, the magnitude of the DLTS signal represents the concentration of the centers. The rate-window plots are numerically generated from the isothermal capacitance transients. In order for these plots to appear fairly continuous, as with a standard rate-window plot, transients are typically acquired at 2 K temperature intervals for temperatures below 80 K, and at 4 K intervals above 80 K. The rate-window plots are displayed with solid dots indicating the specific temperatures at which data was numerically generated from the isothermal capacitance transient.

The emission rates necessary for the Arrhenius plots are determined by fitting the transients to a multiexponential decay plus an offset. That is,

$$C^2(t) = C^2(\infty) + \sum_{i=1}^N A_i \exp(-t/\tau_i). \quad (54)$$

Appreciable difficulties are usually involved with fitting experimental data to equation (54). That is, since τ_i occurs in the exponent, equation (54) is a nonlinear function of the fitting parameters.

Isothermal Transient Capacitance System

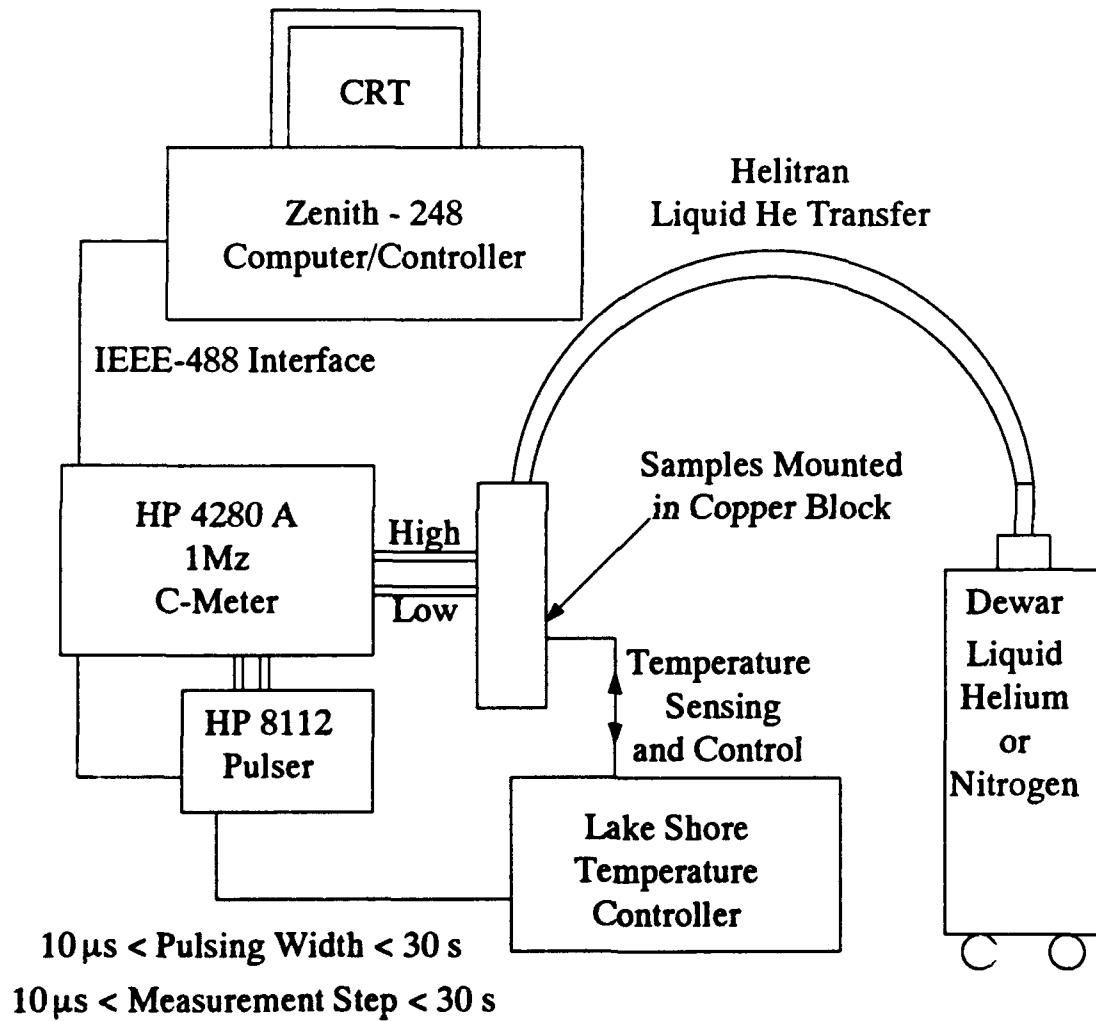


Figure 15. Experimental apparatus for performing the isothermal transient capacitance measurements

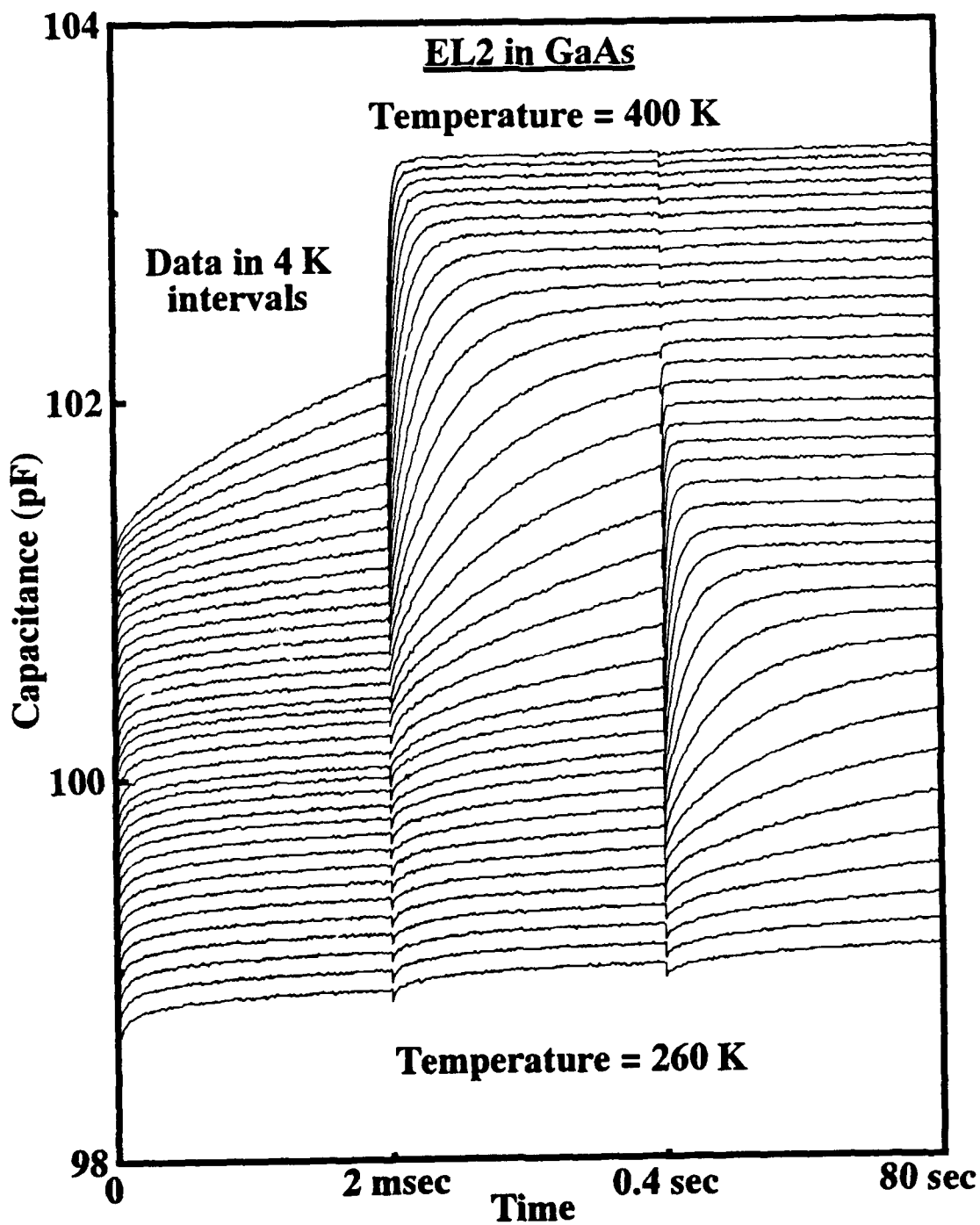


Figure 16. Sequence of transients arising from the EL2 defect in GaAs (Data is shown from 260 K to 400 K, in intervals of 4 K. Each transient is acquired on three separate linear scales, and analyzed for an exponential or multiexponential decay for subsequent Arrhenius analysis.)

Additionally, even when there is a single exponential decay ($N = 1$), if the transient does not level off to $C(\infty)$, it is not possible to determine the time constant by simply taking logarithms. Finally, in the general case of N levels, the number of exponentials in the decay must also be determined. Thus, the transient must be fit for $N = 1, 2, \dots$ transients, and a 'goodness of fit' criterion must be applied to determine the actual number of levels present.

Currently, the best technique available for fitting a multiexponential decay is the Method of Modulating Functions (MMF) that was proposed by Ransom et al. (75), which utilizes integration by parts to linearize the problem. Alternatively, a nonlinear least squares error minimization technique may be applied to fit equation (53) to the experimental data. In practice, what seems to work best is to use MMF to obtain a close approximation to all the parameters, followed by a nonlinear least squares error technique, such as that proposed by Levenberg and Marquardt, which is available in the book, Numerical Recipes (73).

3.2.5 Nonexponentiality There are many instances in which the capacitance transient or the square of the transient is not exponential. The foremost cause of nonexponentiality, that is, multiple thermally-active traps, has already been considered. A procedure for dealing with this case was proposed in the previous section. Unfortunately, nonexponentiality of the capacitance transient also occurs when the trap concentration is close to or exceeds the shallow dopant density, or when the trap has a field-dependent emission rate. While these two cases are less common than multiple thermally-active traps, they will be encountered later in the Results and Discussion chapter, and therefore they will be addressed here.

3.2.5.1 Large Trap Concentrations The effect of a large trap concentration relative to the shallow dopant density is illustrated using a single deep donor acting as an electron trap. A concentration, N_T , of these centers is located at an energy, E_T , below the conduction band minimum in an n-type material of shallow-dopant density, N_S , as shown in Figure 17. If the trap concentration is small compared to the shallow-dopant density ($N_T \ll N_S$), the junction capacitance after the trap charging pulse will be given by an exponential decay in time. This trap concentration is easily obtained from equation (50). Furthermore, the previous analysis suggested that even in the case when $N_T \sim N_S$, the quantity $C^2(t)$ will exponentially decay to a constant value, with the trap concentration given by equation (49). Bleicher and Lange (10) showed this

situation was also an approximation, which is valid only in the case of $N_T \lesssim 0.1N_S$, and that N_T is given by equation (49) only in the case of relatively shallow traps.

This second cause of nonexponentiality arises because the previous formulation of the time-dependent depletion width and capacitance neglected the fact that traps below the Fermi level, but still in the depletion region, will not emit, as shown in Figure 17. In this figure, the traps in the λ -region are always occupied. The length of the λ -region is independent of the applied potential, V_R , and is given by

$$\lambda = \sqrt{\frac{2\epsilon(E_F - E_T)}{qN_S}}. \quad (55)$$

The assumption that the emitting traps are distributed throughout the entire depletion region results in an over estimation of their concentration, since they are only distributed in the region $0 < x < w - \lambda$. Bleicher and Lange (10:377) have derived an expression for the trap concentration which corrects for this effect. That is,

$$N_T = N_S \frac{C^2(\infty) - C^2(0)}{C^2(0) \left(\sqrt{\frac{E_S}{qV_S}} C_\infty - 1 \right)^2}, \quad (56)$$

where

$$E_S = E_F - E_T, \quad (57)$$

and

$$V_S = V_{BI} + V_R. \quad (58)$$

The inverse of the denominator of equation (56) is a correction factor to the previously obtained expression for the trap concentration in equation (49), which assumed that the trap emission was contributed from the entire depletion region. Equation (56) shows that the correction factor is larger in the case of deeper traps, and it is smaller when the applied reverse bias is increased.

The nonexponential behavior of the capacitance transient occurs for the following reason. When the trapped charges which are above the Fermi energy level in the region $0 < x < w - \lambda$ emit, the depletion width w decreases, and the λ -tail, which is of fixed length, moves closer to the surface. Traps which were originally charged in the region $0 < x < w - \lambda$, and which have not yet emitted, will no longer emit if they have entered this new λ -region, which is continuously moving towards the surface. This behavior has the effect of enhancing the observed emission rate, causing it to appear faster. Bleicher and Lange have formulated an analytic expression for

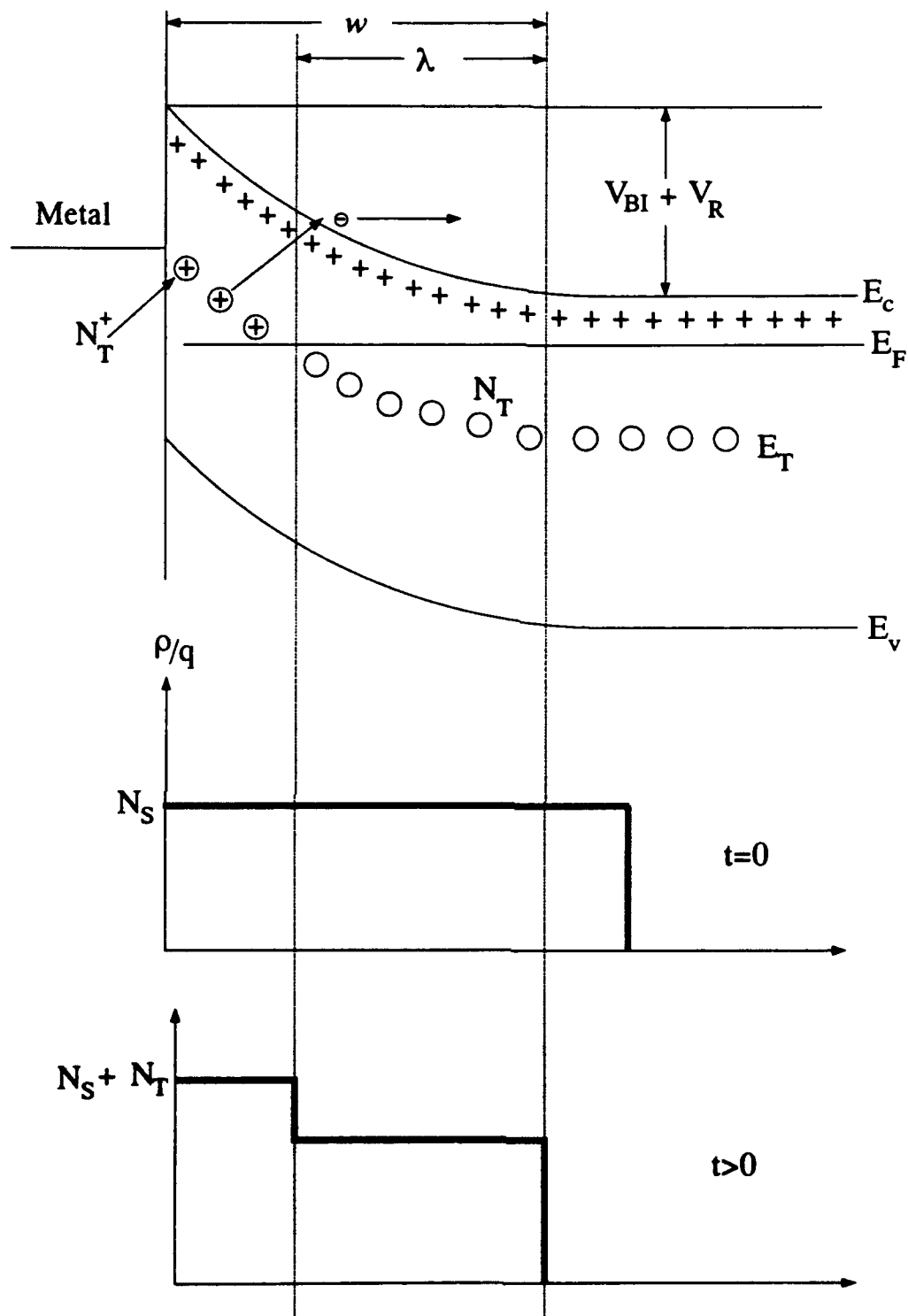


Figure 17. Schottky diode with a donor center acting as an electron trap showing the depletion width w , the λ -region, and the charge densities

the time-dependent capacitance of the Schottky diode (10:377) shown in Figure 17, which is valid for large concentrations of a single center. That is,

$$C(t) = \frac{C_0 \sqrt{qV_S/E_S}}{eV_S/E_S N_T - (1 - \exp(-e_n t))} \times \left\{ \sqrt{\frac{eV_S}{E_S} \left(\frac{N_S}{N_T}\right)^2 + \left(\frac{eV_S N_S}{E_S N_T} - \frac{N_S}{N_T}\right)(1 - \exp(-e_n t)) - (1 - \exp(-e_n t))} \right\}. \quad (59)$$

In order to assess the effect of a large trap concentration on the multiexponential analysis, a simulation was done by numerically generating a sequence of capacitance transients at different temperatures using equation (59), and an electron trap with $E_T = 0.3$ eV and $\sigma_n = 10^{-14}$ cm², in n-type material with a shallow dopant density of $N_S = 10^{16}$ cm⁻³. Figure 18 shows the simulated rate-window plots for various trap concentrations formed with a rate window of 29706 s⁻¹. This study shows that, as the trap concentration increases relative to the shallow-dopant density, the DLTS signal becomes broader, and its peaks shift to lower temperatures. This behavior is consistent with the prediction discussed above that required the observed emission rate to increase with increasing trap concentration. Furthermore, when the individual transients are analyzed with the multiexponential analysis, they are found to yield two exponential components. Figure 19 shows the Arrhenius analysis for the case in which $N_T = 0.9 N_S$. The nonexponential decay given by equation (59) has been fit with two transients. The Arrhenius analysis yields two fits with nearly parallel slopes or trap energies, but with somewhat different cross sections, as shown in Figure 19. This effect could mistakenly lead to the conclusion that the center being measured is composed of two distinct levels with nearly identical energies but different capture cross sections. In fact, this behavior has been observed for even the lowest trap concentration studied, $N_T = 0.02 N_S$. However, in this case, the relative magnitude of the secondary solution is drastically decreased as shown in Table 2, which gives the amplitude of both solutions, as well as the relative amplitude of the 'ghost solution' to the primary solution.

3.2.5.2 Field-Enhanced Emission When a defect lies in a region where there is an electric field, F , the trapped electron experiences the defect potential plus the perturbative potential, $-eFz$, where z is the electron's coordinate along the field (Figure 20). The defect potential reaches a relative maximum, E_m , at $z = z_m$. Such a potential can exhibit bound

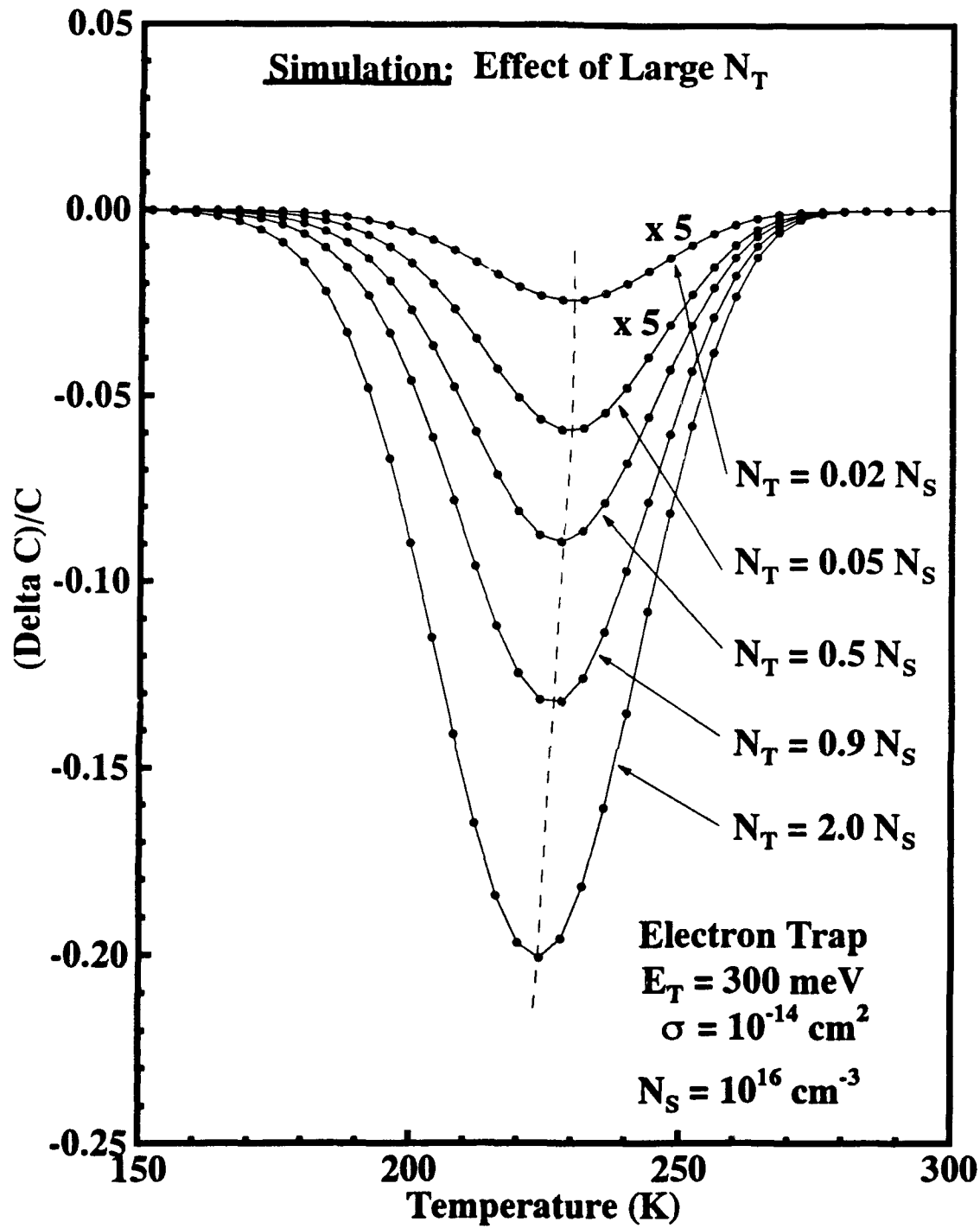


Figure 18. Simulated rate-window plots for an n-type GaAs Schottky diode with a shallow-dopant concentration of $N_S = 10^{16} \text{ cm}^{-3}$, a reverse bias of 2 V, and with various electron trap densities, N_T , for an electron trap with $E_T = 0.3 \text{ eV}$ and $\sigma_n = 10^{-14} \text{ cm}^2$

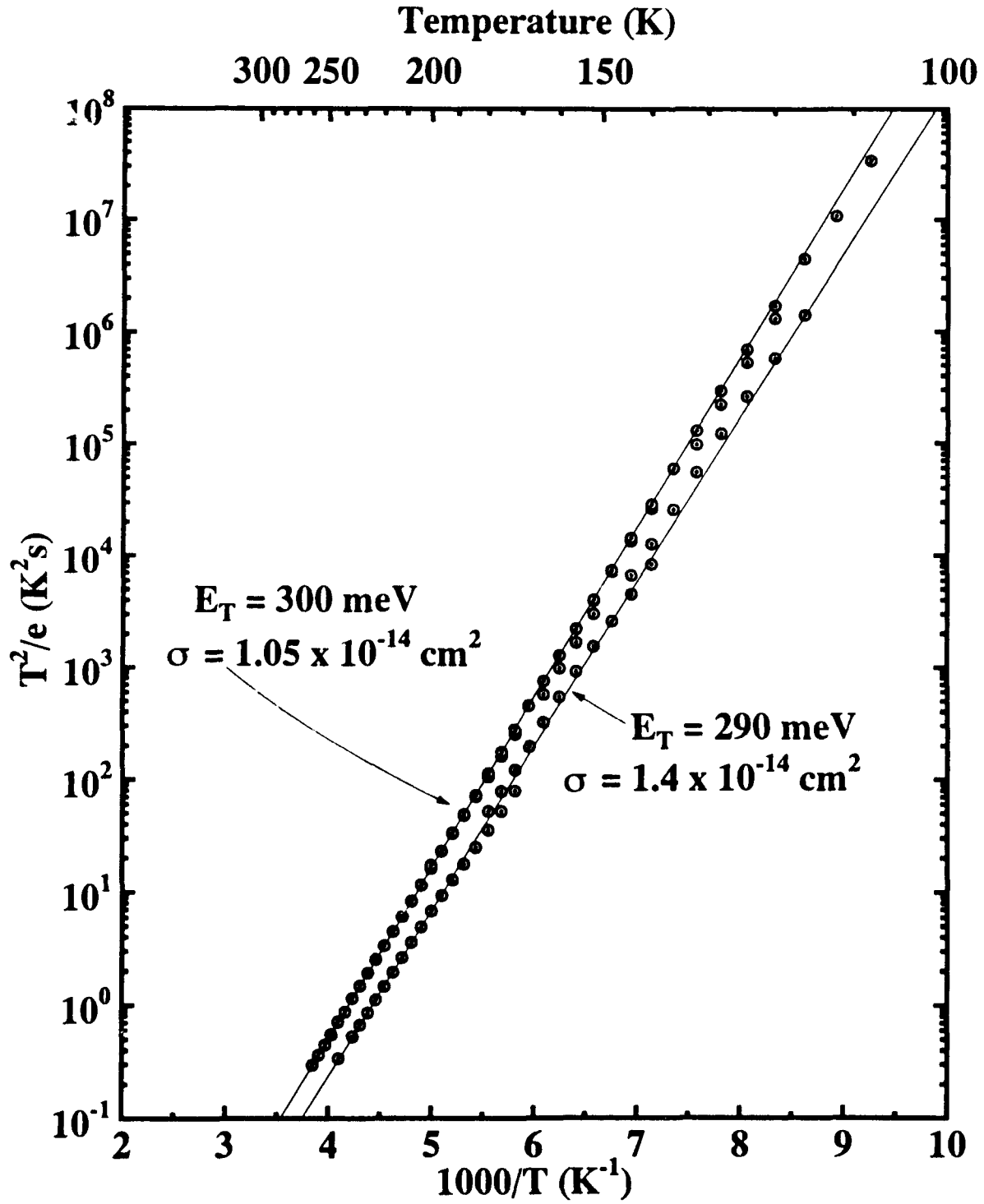


Figure 19. Arrhenius analysis of simulated capacitance transients using equation (59) for an n-type GaAs Schottky diode with a shallow dopant concentration of $N_S = 10^{16} \text{ cm}^{-3}$ and an electron trap density $N_T = 0.9 N_S$, with $E_T = 0.3 \text{ eV}$ and $\sigma_T = 10^{-14} \text{ cm}^2$

Table 2. Amplitudes of the two exponential components used to fit the nonexponential decay resulting from a simulation of the effect of large trap concentrations

N_T/N_S	A_1 (pF ²)	A_2 (pF ²)	$\frac{A_2}{A_1} \times 100$ (%)
0.02	-5.82	-0.0212	0.30
0.05	-14.3	-0.126	0.87
0.5	-125.9	-8.40	6.67
0.9	-207.4	-24.4	11.7
2.0	-375.0	-76.9	20.0

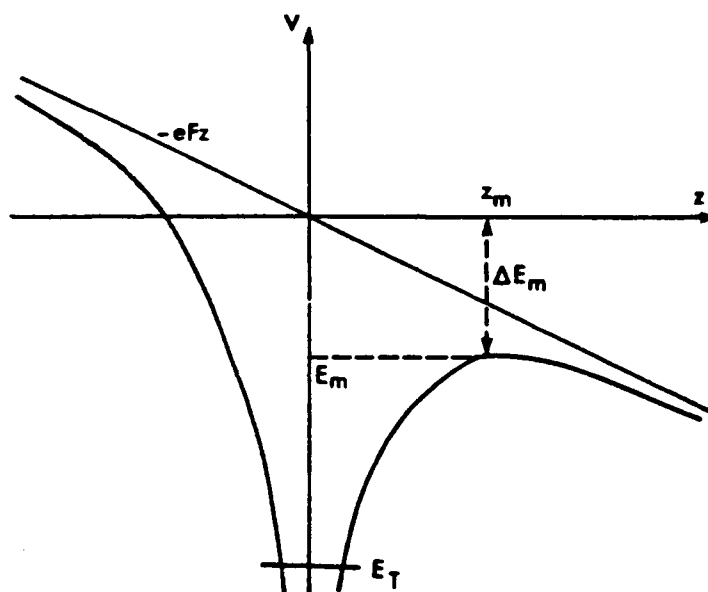


Figure 20. Poole-Frenkel field-enhanced emission, after Schroder (80)

states at energies lower than E_m , and it can exhibit a continuum of states for $E > E_m$, which can propagate toward: $z \rightarrow z_\infty$. For a weak electric field, the point z_m is relatively far from the defect site, and the energy, E_T , and the wave function, ψ_T , of the ground state are the same for $F = 0$. However, in cases where the electric field is significant, there is a finite probability for the defect electron to be thermally excited to states higher than E_m , causing the emission rate becomes (13:200)

$$e_n^t \propto \exp(-(E_T - \Delta E_m)/kT). \quad (60)$$

The effective lowering of E_m is thought to be significant only in the case of a coulomb potential, $V = -q/(4\pi\epsilon r)$, since this potential has a relatively long tail. Frenkel (31) found the quantities z_m and ΔE_m to be given by

$$z_m = \sqrt{\frac{q}{\epsilon F}}, \quad \Delta E_m = \sqrt{\frac{qF}{\epsilon}}. \quad (61)$$

With a typical value of $F = 10^5 \text{ Vcm}^{-1}$, these equations give $z_m \sim 100 \text{ \AA}$ and $\Delta E_m \sim 0.3 \text{ eV}$, which yield a significant enhancement of the emission rate.

The Poole-Frenkel theory for the field-enhanced emission from a coulomb center requires that the center be neutral when filled and charged when empty. A trap which is neutral when empty and charged when filled will not experience this effect because of the absence of the coulomb potential. Since the defects measured with the DLTS experiments are emitting in the depletion region of a diode, where there is an electric field, they are subject to the Poole-Frenkel field-enhanced emission. Field-enhanced emission may be confirmed experimentally in the DLTS experiment by increasing the reverse bias during the emission phase of the biasing sequence. If the DLTS peak for a given center moves to lower temperatures with increasing field strength, the center probably has a coulomb potential attributable to a nonneutral charge state of the unoccupied center.

Finally, the capacitance transients are nonexponential if field-enhanced emission is occurring due to the electric field varying continuously over the extent of the depletion region. It will have a maximum near the pn or metal-semiconductor junction and vanishes at the edge of the depletion width. Thus, the emission rate may vary continuously throughout the junction, making it very difficult to experimentally determine the lowering of the emission barrier, ΔE_m .

3.3 Optical Measurements

Photoluminescence (PL) measurements are the most common optical characterization technique for semiconductors. A theoretical discussion of optical transitions between the conduction band and valence band states, and between band states and localized levels in the gap, is given by Bebb and Williams (9). Furthermore, Williams and Bebb also provided an experimental review of the transitions observed in GaAs (99). Therefore, these transitions will not be explicitly reviewed here.

A schematic diagram of the experimental apparatus used to perform the PL measurements is given in Figure 21. It consists of a 20-W Ar-ion laser, which lases at 488 nm and 514 nm. In the PL experiment, this laser is typically operated near its minimum power, and the total output power in the 3 mm diameter beam is usually maintained at a constant value of 150 mW. This gives an irradiance of approximately 2000 mW/cm². PL measurements are usually performed at the lowest possible temperature because the many band-edge emissions, as well as RE emissions, are quenched at higher temperatures. Therefore, the sample is typically maintained at 4 K by a continuous flow of liquid He stored in a Dewar above the sample chamber. Prior to excitation of the semiconductor, the intensity of the laser beam is modulated to allow phase-sensitive detection of the resulting luminescence.

The optical emissions from the sample exit the cryostat window and are collected by focusing optics which image the emissions onto the entrance slit of a 3/4-m Spex spectrometer. In the spectrometer, they are dispersed with a 600 line/mm grating blazed at 1.2 μ m, and then they are directed to the exit slit, where they generate a current in a Ge-PIN photodiode operated at 77 K. This electrical signal is detected by the lock-in detector and digitized by an A-to-D board interfaced to a Zenith-248 computer. A spectra is acquired by setting the spectrometer in a forward-scanning mode, and then activating a sequence of digitizing measurements.

The wavelengths indicated by the spectrometer dial are in error by as much as 50 Å. Accordingly, the true wavelengths are determined by calibration with Ar and Kr spectral lamps. The measured wavelength is converted to the true wavelength using a third-order polynomial fit of the true vs. measured wavelengths. Calibration for intensity is not as simple. Calibration factors to correct the intensity of spectra recorded with different spectrometer slit widths were determined by comparing the detector response to a fixed input signal while varying slit widths. However, no attempt was made to correct for the spectral response of the grating/detector, although the spectral response of the system to a 1000 °C blackbody was determined, as shown in Figure 22.

This chapter has given a summary of three of the most common characterization techniques applied to semiconductors. Hall effect measurements may be used to determine if an impurity or defect introduced into a semiconductor yields donor or acceptor states, or how these imperfection centers affect the mobility of free electrons or holes. The temperature dependence of the electron or hole concentration, as measured by the Hall effect, may yield the concentration of donor or acceptor centers as well as the energetic location of these centers in the band gap. Centers

Photoluminescence (PL) Photoluminescence Excitation (PLE)

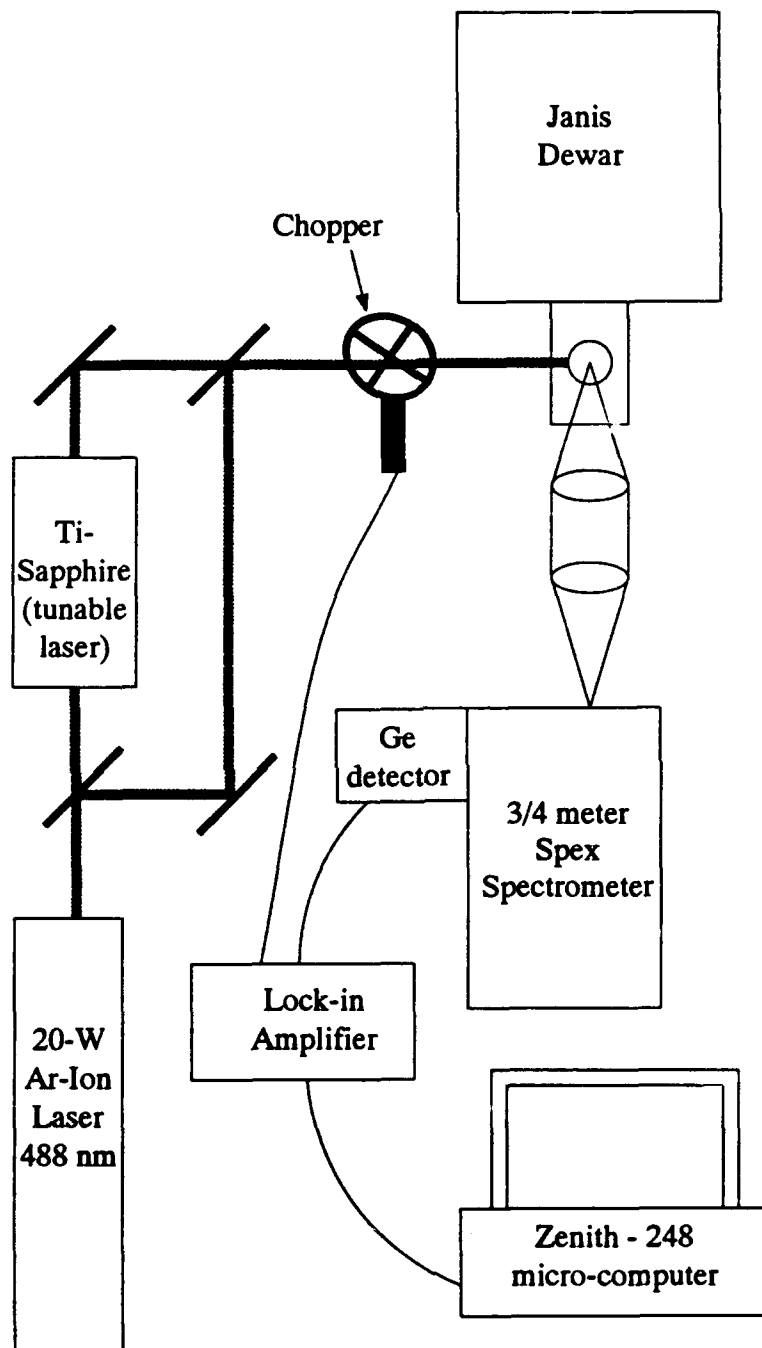


Figure 21. Photoluminescence (PL) apparatus for measuring optically active transitions

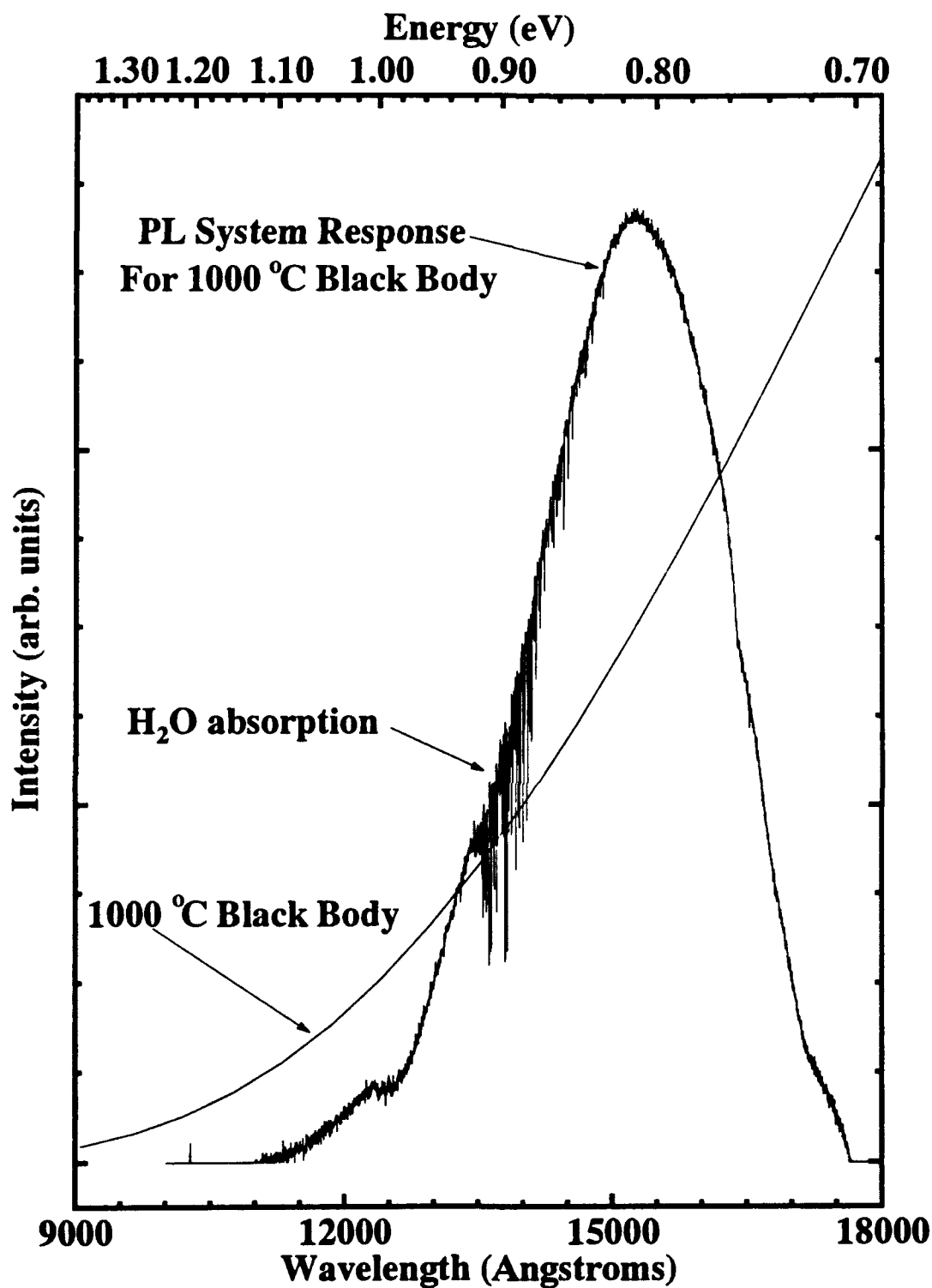


Figure 22. Response of the grating and detector combination in the experimental configuration in Figure 21 relative to a 1000 °C blackbody

with energy levels greater than ~ 150 meV from the band edge require transient capacitance measurements for a satisfactory characterization. This non-equilibrium technique can yield the concentration of the centers, their energetic positions with respect to the band edges, and their probability for capturing electrons or holes. Finally, photoluminescence measurements of semiconductors can be used to characterize the optical transitions which occur between band states, between band states and levels in the band gap, or between excited levels and lower lying levels associated with the atomic-like core states of impurities.

IV. Sample Preparation and Growth

Er-doping of the GaAs and AlGaAs samples in the current study was performed using two different techniques, ion implantation and Molecular Beam Epitaxial (MBE) growth. In the former technique, the dopant atom is ionized and accelerated to large kinetic energies which implant it into the semiconductor. Unfortunately, this doping process causes severe damage to the crystal structure, requiring a high-temperature treatment to anneal the damage. In the MBE technique, the Er atoms are introduced during epitaxial growth, and thus, they do not cause massive damage to the crystal structure, but may result in the formation of different Er centers compared to those in Er-implanted material. Each of these techniques has both beneficial and detrimental aspects which will be discussed in this chapter. Additional sample preparation required for the fabrication of the pn diodes will also be addressed.

4.1 Ion Implantation

In the ion-implantation technique, the desired dopant atom is ionized, mass selected, and then accelerated to high kinetic energies, which carry it into the substrate (Figure 23). The process begins when a source of dopant atoms, either gaseous or solid, is ionized, typically with an electron beam. These ions are then passed through a mass spectrometer to select the desired dopant atoms from the impurities. The undesired impurities are further screened by passing the ion beam through slits which form the entrance to the acceleration tube. Once in this tube, the selected ion is accelerated to the desired implant energy. The ion beam of fixed diameter is then scanned across the target substrate with sawtooth voltages applied to x- and y-deflection plates. This situation produces a uniform fluence across the entire target.

As the ion enters the substrate, it suffers numerous nuclear collisions and coulombic interactions with the host atoms, thereby dissipating its kinetic energy and eventually coming to rest. There are two contributions to the rate S at which the ion loses energy. These are the electronic, $S_e(E)$, and nuclear, $S_n(E)$, stopping powers, where E is the continually decreasing kinetic energy of the ion as measured along its path. The electronic component of the stopping power is attributed to the interaction of the electronic clouds surrounding the dopant and target atoms, and it constitutes the dominant energy dissipating mechanism for dopant atoms which are lighter than the target atoms. On the other hand, the nuclear stopping power, which is due to the

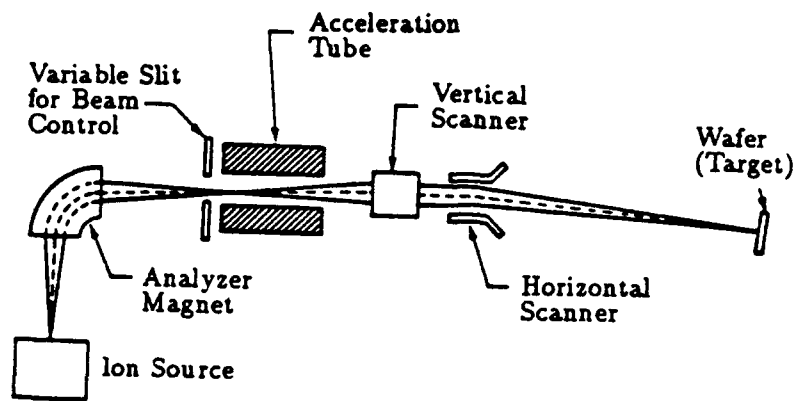


Figure 23. Typical ion implantation apparatus (after Böer(12))

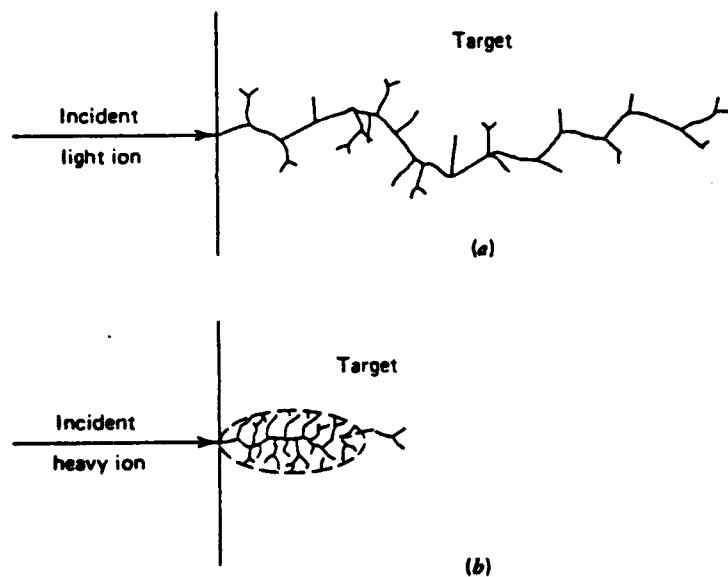


Figure 24. Damage resulting from a light or heavy implanted ion (after Ghandi (34))

impact of atomic nuclei, is the dominant energy-loss mechanism for implanted atoms which are much heavier than the target atoms. As shown in Figure 24, heavier atoms are more likely to generate an amorphous region where the crystal structure has been completely destroyed.

Table 3. Projected ranges and straggles for the RE ions and implant energies used in this investigation (after Pomrenke (69))

Ion	Atomic number	Energy (keV)	R_p (Å)	ΔR_p (Å)
	Mass number			
Pr	59	390	957	387
	141			
Nd	60	1000	2260	707
	144			
Er	68	1000	1862	658
	166			

The depth from the surface to which the impurity ion finally comes to rest, R , is calculated by integrating the energy loss along the path of the implanted atom. That is,

$$R = \int_0^{E_0} \frac{dE}{S_e(E) + S_n(E)}, \quad (62)$$

where E_0 is the kinetic energy of the ion at the surface. In the case of an amorphous material, the distribution of implanted atoms, $N(x)$, is given by the theory of Linhard, Sharff, and Schiott (LSS). The analytic form is given by the Gaussian function (12:981),

$$N(x) = \frac{\Phi}{2\pi\Delta R_p} \exp \left\{ -\frac{1}{2} \left(\frac{x - R_p}{\Delta R_p} \right)^2 \right\}, \quad (63)$$

where Φ is the ion fluence or dose, x is the measured distance from the surface, R_p is the projected range, and ΔR_p is the projected straggle.

When implantation is performed into a crystal lattice, the ions may channel along crystallographic axes. In this case, the energy loss may be much less than otherwise expected, resulting in a much deeper implant, or a distribution which is nearly Gaussian except for a long tail. In order to avoid this, the beam and crystal axis are typically misaligned by 7° to 11° , so that the crystal appears amorphous.

More sophisticated Monte Carlo simulation techniques have also been developed to give improved accuracy relative to the original LSS theory. Further discussion is given by Pomrenke (69:44), who used these techniques to obtain R_p and ΔR_p for the REs and implant energies used in this investigation. These are listed in Table 3. Also, the Gaussian distributions for the three

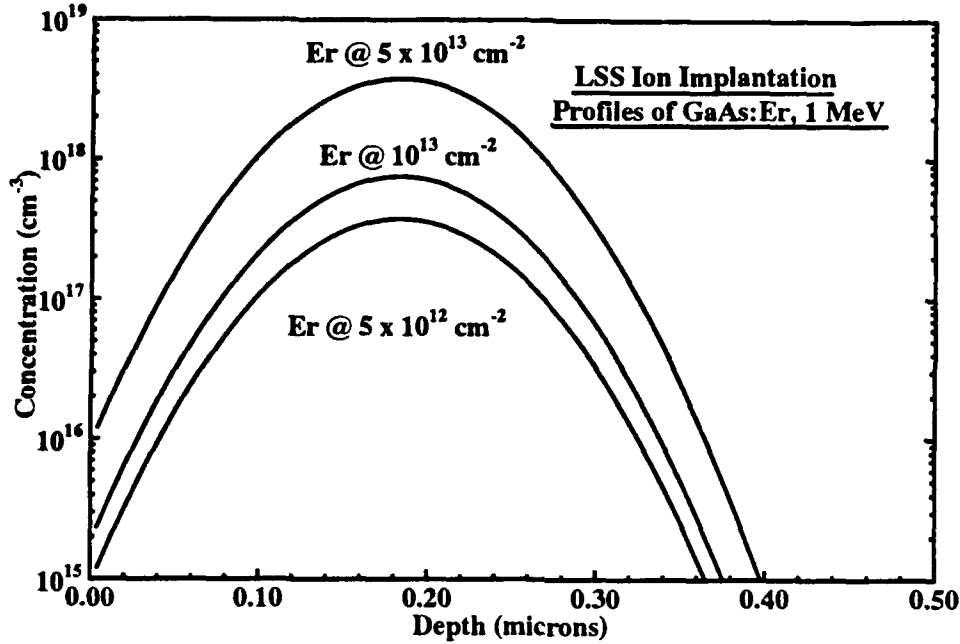


Figure 25. Theoretical LSS distributions for the Er atoms in GaAs after implantation of the given fluences at an energy of 1 MeV

Er fluences used in this work, $\Phi_{\text{Er}} = 5 \times 10^{12}$, 10^{13} , and $5 \times 10^{13} \text{ cm}^{-2}$, each implanted at 1 MeV, are shown in Figure 25.

As shown in Figure 24, ion implantation is always accompanied by the production of radiation damage along the path of the implanted ion. For the lighter ions, $S_e(E)$ dominates until the end of the path, where $S_n(E)$ becomes comparable, resulting in displaced host atoms. However, for heavier implanted atoms, $S_n(E)$ dominates at all energies. Consequently, there are atomic displacements along the entire path of the ion. If the implant fluence is sufficiently high, a volume of amorphous material is generated. The critical ion fluence required to displace all atoms in the lattice may be calculated if the energy required to displace a single atom, E_d , is known. The critical fluence is given by

$$\Phi_c \approx N_0 E_d R_p / E_0, \quad (64)$$

where there are N_0 atoms per unit volume in the target material, and E_0 is the energy of the incident beam (12:989). For GaAs, the average of the Ga and As displacement energies is 9 eV (8:368), and $N_0 = 4.4 \times 10^{22} \text{ cm}^{-3}$. Therefore, for Er implanted at 1 MeV into GaAs,

$\Phi_c = 7.5 \times 10^{12} \text{ cm}^{-2}$. This value is near the minimum Er fluence used in this investigation, and thus, virtually all of the unannealed Er-implanted samples are expected to be amorphous or nearly so.

To restore the crystal structure, the implanted samples are subjected to a high-temperature annealing treatment, which involves heating the sample to temperatures between 700 °C and 1000 °C. Since the implanted region of the crystal is essentially amorphous, the annealing process may be thought of as an epitaxial growth of the implanted region, with the substrate acting as a seed crystal.

The annealing performed in this study of Er-doped GaAs was carried out with the Rapid Thermal Annealing (RTA) technique. This method was found to result in more intense Er-related emissions (70) compared to the conventional furnace annealing technique. The GaAs sample is placed between two clean polished Si wafers to limit As evaporation from the sample's surface during the high-temperature anneal. This configuration is positioned on a 3-inch diameter silicon substrate which is housed in a sealed-quartz container. Nitrogen or forming gas flows through this container for several minutes to displace oxygen and moisture, and then high-intensity tungsten lamps are energized. The radiant energy penetrates the quartz container and is absorbed by the silicon wafer. The temperature of the silicon wafer, as measured by a thermocouple mounted on its underside, typically approaches the setpoint within 15 seconds. When the temperature is within 50 degrees of the setpoint, a temperature controlling loop is engaged. After a typical overshoot of 10 °C, the controller maintains the substrate's temperature to within ± 3 °C of the setpoint. When the annealing period has elapsed, the tungsten lamps are shut off, and the temperature of the Si substrate cools very rapidly, typically at rates greater than 50 °C/s for temperatures above 600 °C.

4.2 MBE Growth

Other Er-doped GaAs and AlGaAs samples characterized during this research were produced by the molecular beam epitaxial growth technique. This technique may be naively thought of as a refined form of vacuum evaporation. The molecular beams are produced by evaporation or the sublimation of heated solid or liquid sources in crucibles, which impinge on a substrate, resulting in the growth of epitaxial layers. The actual growth mechanisms are discussed in more detail by Stradling and Klipstein (85:39-44).

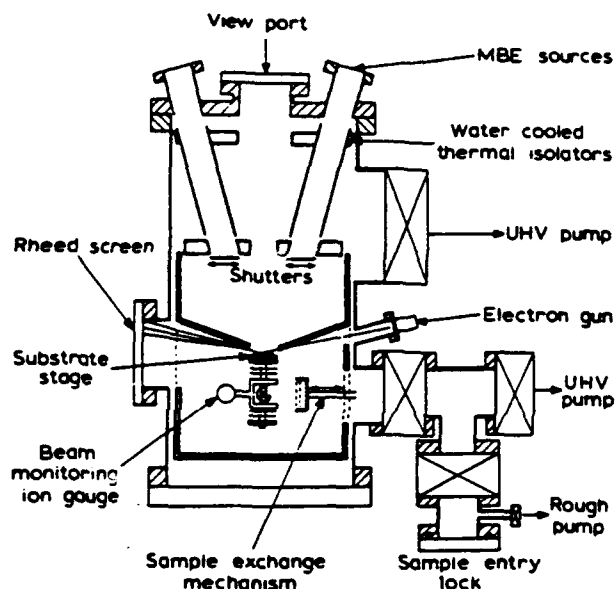


Figure 26. Molecular beam epitaxial growth system (after Stradling (85))

A schematic of a conventional solid source MBE apparatus is shown in Figure 26. The system shown is similar to the Varian-360 MBE apparatus, operated by the Air Force Solid State Electronic Research Directorate, which was used to grow the Er-doped GaAs and AlGaAs studied in this investigation. Solid arsenic and gallium sources are placed in their separate crucibles, which are maintained at a desired temperature using a temperature controller and a thermocouple sensor. The crucibles, known as Knudsen cells, are designed with a small recessed orifice from which the material effuses. This arrangement allows an equilibrium vapor pressure to be established in the cell. The effusion flux is governed by the vapor pressure of the material in the cell, which typically has an Arrhenius-type dependence on temperature, $\Phi = \Phi_0 \exp(-E_A/kT)$. Thus, the rate at which a species reaches the substrate's surface can be well established. The growth of GaAs is typically carried out at pressures of 10^{-6} Torr, which corresponds to a growth rate of about 1 monolayer per second. However, when the Ga and As shutters are closed and block these molecular beams, the background pressure should drop to UHV conditions (typically, 10^{-11} Torr). This situation facilitates the growth of high-purity layers.

Additional molecular sources may be added to provide n-type or p-type doping capabilities. Common dopants used to obtain n-type and p-type material are Si and Be, respectively. Furthermore, in this investigation an Er source was also added. The Er-doping density vs. cell temperature was calibrated by growing Er-doped GaAs layers as shown in Figure 27 a. Also

Figure 27 b shows that the Er-doping density follows the Arrhenius expression,

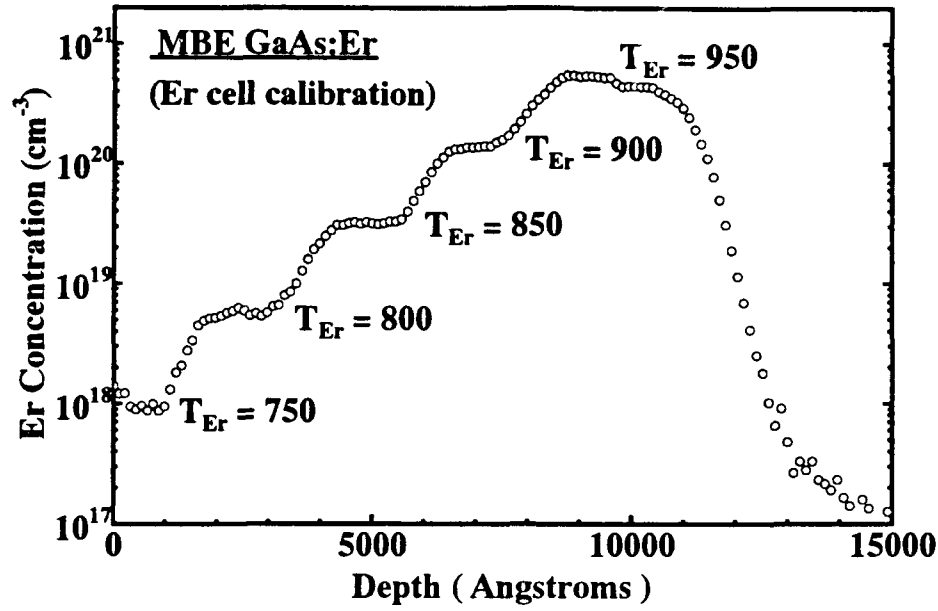
$$[\text{Er}] = 1.18 \times 10^{31} \exp(-1.95 \text{ eV}/kT). \quad (65)$$

Other group III or V species may be added in order to grow alloys. For instance, with the addition of an Al source, Er-doped $\text{Al}_x\text{Ga}_{1-x}\text{As}$ alloys, GaAs/AlGaAs superlattices, or quantum well structures are achievable. Such structures may be used to tune electron kinetic energies into resonance with the $^4I_{15/2} \rightarrow ^4I_{13/2}$ transition in the Er^{3+} -4f shell.

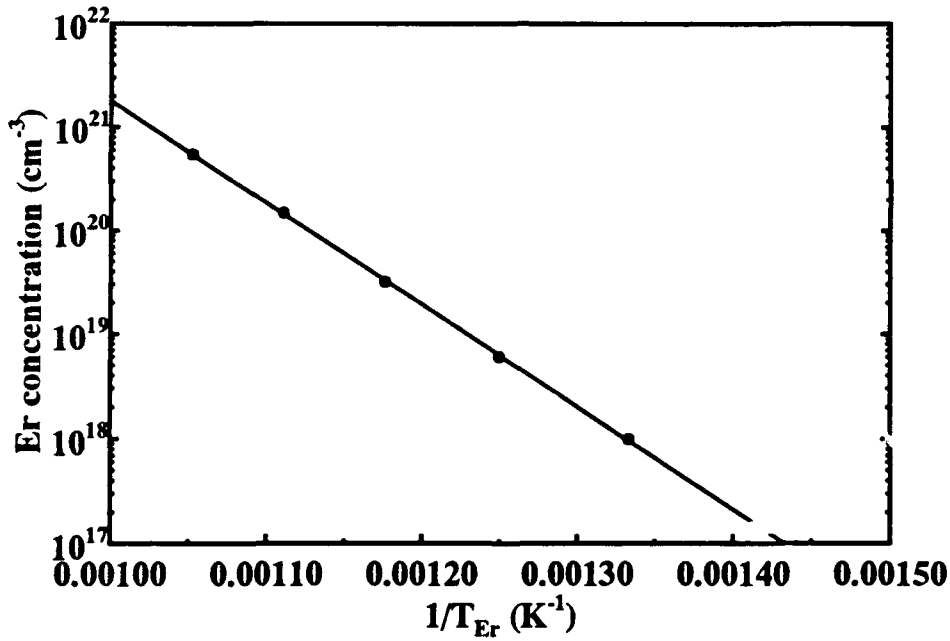
4.3 Ion Implantation vs. MBE Growth

The study of Er-related centers in GaAs will be greatly enhanced by the acquisition of GaAs samples doped with Er, both by ion implantation or during MBE-growth. Primarily, the extent to which the characterization of these two materials produces similar experimental observations leads to the conclusion that these common properties are attributable to Er-doping and, more specifically, to common Er centers. On the other hand, since these two doping techniques are very different, the Er may form completely different centers in each material, which show different optical and electrical behavior. In the following section, the advantages and disadvantages associated with each of these Er-doping techniques will be discussed.

The ion-implantation technique may be used to dope Er in a wide variety of samples with just one implant. For instance, for the implantation accomplished in this research, various substrates, including n-type, p-type, semi-insulating, GaAs and AlGaAs, were mounted on the same target for a single implantation. Conversely, with the MBE technique, each sample was independently grown. For example, if an n-type sample was desired, a GaAs:Er,Si sample would have to be grown. Furthermore, to study the effect of Er and Si co-doping in GaAs, the control sample GaAs:Si must also be grown. Thus, with the ion-implantation technique, a variety of samples can be synthesized very quickly. Finally, the MBE technique is superior for doping compared to ion implantation in all respects, except for possibly one; that is, a greater variety of species can be co-implanted with Er compared to those species which can be co-doped during MBE growth. Some species have a vapor pressure too high to be used effectively in the MBE, while others may not be available in a solid or liquid source.



(a)



(b)

Figure 27. Calibration of Er source for the growth of Er-doped GaAs and ⁷⁵AsGaAs structures by MBE, showing (a) Er-concentration profile for growths at various Er-cell temperatures and (b) Arrhenius analysis of the temperature-activated dopant density $[Er] = 1.18 \times 10^{31} \exp(-1.95 \text{ eV}/kT)$.

However, when considering the variety of sample structures each technique is capable of producing, the MBE technique is by far, superior. For example, an Er-doped layer of arbitrary thickness can be grown by the MBE technique. Since the typical growth rates are $1\text{ }\mu\text{m/hour}$, a $5\text{ }\mu\text{m}$ thick layer would require 5 hours of growth time. On the other hand, a $5\text{ }\mu\text{m}$ thick Er-implanted layer may require an implanter capable of producing energies in excess of 20 MeV, which probably does not exist. Such thick layers are necessary for some characterization techniques, such as electron paramagnetic resonance (EPR) and absorption measurements. Also, with MBE growth, the Er concentration can be readily varied over several orders of magnitude by simply varying the temperature on the Er-effusion cell. However, in the ion-implantation technique, increasing the Er-doping density by one order of magnitude requires an implantation time which likewise becomes one order of magnitude longer. Furthermore, other characterization techniques or device structures require detailed doping profiles. In the MBE technique, the Er doping, or shallow donor or acceptor doping, may be essentially controlled to within one monolayer by the opening and closing of the proper effusion cell shutter. Also, heterostructure layers may be grown to generate electrons which have kinetic energies resonant with the Er-4f transitions.

4.4 Formation of p^+n and n^+p Junctions

DLTS measurements can be performed on n-type or p-type substrates by forming Schottky diodes on Er-implanted and control substrates. Alternatively, p^+n or n^+p diodes will be formed for both the DLTS as well as the injection luminescence measurements to be performed. The p^+ and n^+ layers were formed by implanting Mg and Si, respectively, with a fluence of 10^{14} cm^{-2} and an implant energy of 40 keV. Figure 28 shows the LSS distributions for these Si and Mg implants in GaAs. It also shows the uniform Si-doping for the n-type substrate 02-PR-1748, with $[\text{Si}] = 5 \times 10^{15}\text{ cm}^{-3}$, and the uniform Zn-doping for the p-type substrate 3B-PR-840, with $[\text{Zn}] = 4 \times 10^{16}\text{ cm}^{-3}$, which are both used extensively in this research. The p^+n and n^+p junctions formed by the Mg and Si implantation into these two substrates are identified in the figure. Finally, the LSS distribution for the 1 MeV Er implant at a fluence of 10^{13} cm^{-2} shows that the peak of the Er distribution is in the junction region. Thus the DLTS measurements performed on these diodes will detect any Er-related deep centers or native defects caused by Er implantation. Also, carrier injection should produce a large overlap of electrons and holes near

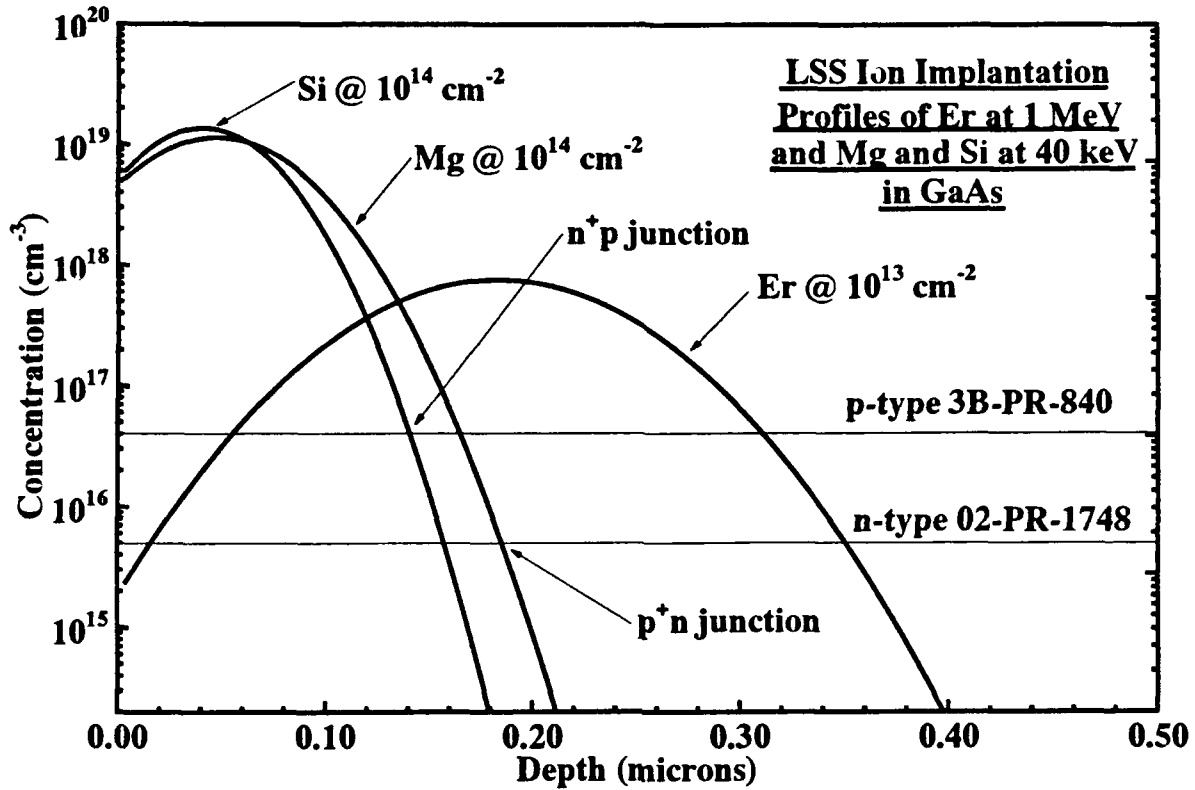


Figure 28. LSS distributions for Mg and Si ions implanted in GaAs with a fluence of 10^{14} cm^{-2} at an energy of 40 keV (These implants are used to form p^+ or n^+ layers, respectively, for the formation of p^+n and n^+p diodes.)

the peak in Er concentration, leading possibly to Er-4f electroluminescence.

The p^+n and n^+p diodes with the Er implant, as well as the control samples, are then rapid thermal annealed, and mesa diodes are formed using photolithography. The mesa etch is typically 0.5 to 1 μm in order isolate the highly-doped top contact from the opposite carrier type conductivity region where the traps are measured. The mesa consists of a disc 538 μm in diameter. Ohmic contacts are formed on the n-type GaAs or AlGaAs by a sequential deposition of Ni/Ge/Au (50 Å, 200 Å, and 5000 Å thicknesses, respectively), and on the p-type material with a sequential Au/Zn/Au (50 Å, 250 Å, and 5000 Å thicknesses, respectively) deposition, followed by a furnace alloy at 425 or 375 °C, respectively, for 30 seconds. A small disc, large enough for wire bonding, is utilized for the contact on the top of the mesa. This arrangement permits electroluminescence from a forward-biased junction to exit from the largely uncovered

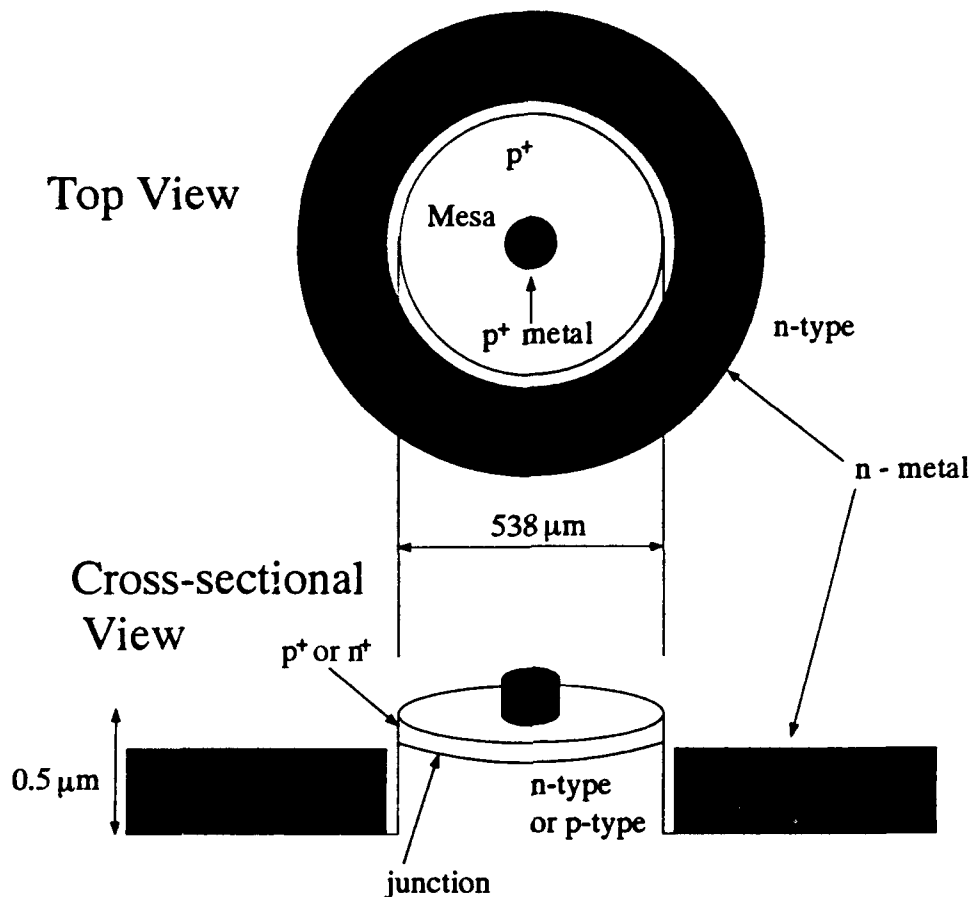


Figure 29. Dimensions and structure of the p^+n or n^+p mesa diodes fabricated using photolithography for DLTS and electroluminescence measurements

surface region. The contact for the opposite side of the junction covers the whole etched region. A sketch of the diode is given in Figure 29.

After the fabrication processes are completed, the samples are sawed into 2×2 die. For DLTS measurements, one of these die, yielding 4 diodes, is mounted on a 10-pin TO5 header with ultrasonic wire bonding electrically connecting the pins and the p -type or n -type ohmic contacts. For electroluminescence measurements, 2 die are mounted on a 16-pin flat package. This yields a total of 8 diodes, which are connected in parallel in order to maximize the electroluminescent area.

In this chapter, the means of Er-doping of GaAs and AlGaAs samples have been reviewed, that is, doping by ion implantation and during MBE-growth. Each technique has advantages and disadvantages, and it is important to determine the conditions under which each yields the strongest Er^{3+} -4f emissions. This investigation will be aided by studying both types of Er-doped

materials. The Er may form the same centers in each material, and thus, exhibit similar electrical or optical behavior. Alternatively, different Er centers may be formed in each material, with each manifesting a unique behavior.

V. Properties of Rare Earth Elements in III-V Semiconductors

5.1 Introduction

In this chapter, the optical and electrical properties of the rare earth (RE) atoms will be reviewed. First, their electronic configurations will be discussed with special attention devoted to the unfilled 4f-shell. The terms in the Hamiltonian relevant to this shell will be considered in detail. This background will provide an understanding of the important characteristics attributed to the RE atoms in semiconductors, such as the temperature-independent 4f-4f transition energy and linewidth, the narrow atomic-like linewidths associated with these transitions, and finally, the contraction of the RE radius with increasing atomic number.

As discussed in the introduction, it is paramount to the proper design and optimization of optoelectronic devices to understand the electrical behavior of RE atoms in III-V compounds. At the present time, there has only been a sparse amount of electrical measurements performed on GaAs:RE, or for that matter, any III-V:RE. In fact, most studies have involved only the use of photoexcitation techniques (PL measurements), which have the benefit of requiring a minimal amount of sample preparation. Yet any devices which utilize the RE 4f-4f transitions will almost certainly rely on electrical excitation. Thus, it is crucial to understand the electrical behavior of the RE impurities. Accordingly, a review of the electrical measurements performed on III-V semiconductors doped with REs will be given in the second section of this chapter.

An important goal in the current study is to gain an understanding of the relationship between the electrical properties of the Er-doped semiconductor and the excitation and quenching mechanisms of Er-4f luminescence. Thus, in the final section of this chapter, the previous work relating to the excitation mechanisms of RE-4f shells in semiconductors will be reviewed. The most complete work performed for III-V:RE has been for InP:Yb, in which the electrical characterization was crucial to the inception of a model for the excitation and quenching of the 4f luminescence associated with the Yb^{3+} ion.

5.2 Rare Earth Elements

The lanthanides, or rare earth (RE) elements, are the elements following lanthanum in the periodic table in which fourteen 4f electrons are successively added to the lanthanum configuration. The filling of the 4f shell begins with cerium (Ce), which has an outer configuration $5s^2 5p^6 4f^1 5d^1 6s^2$, and ends with ytterbium (Yb), whose configuration is $5s^2 5p^6 4f^{14} 5d^1 6s^2$. The valence electronic configuration of lanthanum and the RE elements (as well as several other important elements) are given in Table 4. The RE atoms occur as doubly- or triply-charged ions in solids, with all of the 5d and 6s electrons removed, and the 4f shell is only partially occupied.

The eigenstates of the 4f shell are determined by solving the Schrödinger wave equation with the appropriate Hamiltonian, which considers the most important interactions,

$$H = H_0 + H_{e-e} + H_{so} + H_{cf}. \quad (66)$$

The various terms in this expression are given in order of decreasing significance. H_0 is the zeroth order term which considers only kinetic energy of the electrons and their electrostatic interaction with the partially shielded nuclear charge. H_{e-e} is a further correction representing the electrostatic repulsion between electrons. H_{so} accounts for the interaction of each electron's spin with its orbital angular momentum. Finally, H_{cf} represents the influence of external electric fields. In the zero order approximation, the Hamiltonian is given by

$$H = H_0 = \sum_{i=1}^{i=N} (p_i^2/2m - Z_{eff}q^2/(4\pi\epsilon_0 r_i)), \quad (67)$$

where p_i is the momentum of the i th electron of mass m , which is located at a radial distance, r_i , from the nucleus, and which experiences a coulombic attraction from Z_{eff} positive charges. The 4f electrons are considered to move in a radially-symmetric attractive coulombic field produced by Z_{eff} positive-point charges, given by the nuclear charge less the 54 electrons in the completed xenon-like shell. At this level of approximation, the electrostatic repulsion between the 4f electrons and the influence of their spins are disregarded. Consequently, all 4f electrons are independent of each other, and the energy cannot depend on the relative orientation of their orbits. The state of a given 4f electron is characterized by four quantum numbers, n , l , m_l , and m_s , where the usual interpretation associated with the single electron hydrogen atom, is attributed

Table 4. Important properties of the rare earth atoms in the order of increasing atomic number (Included are the valence configuration of the free atom, its electronegativity, and ionic radius in the 3+ oxidation state, as reported by Cotton and Wilkinson (21:45,103,1052). Other important metallic elements are given for comparison.)

Atomic Number	Name	Symbol	Atomic Valence	Electronegativity (\sqrt{eV})	RE ³⁺ Radius (Å)
57	Lanthanum	La	5d6s ²	1.08	1.061
58	Cerium	Ce	4f ¹ 5d ¹ 6s ²	1.06	1.034
59	Praesodymium	Pr	4f ³ 6s ²	1.07	1.013
60	Neodymium	Nd	4f ⁴ 6s ²	1.07	0.995
61	Promethium	Pm	4f ⁵ 6s ²	1.07	0.979
62	Samarium	Sm	4f ⁶ 6s ²	1.07	0.964
63	Europium	Eu	4f ⁷ 6s ²	1.01	0.950
64	Gadolinium	Gd	4f ⁷ 5d6s ²	1.11	0.938
65	Terbium	Tb	4f ⁹ 6s ²	1.10	0.923
66	Dysprosium	Dy	4f ¹⁰ 6s ²	1.10	0.908
67	Holmium	Ho	4f ¹¹ 6s ²	1.10	0.894
68	Erbium	Er	4f ¹² 6s ²	1.11	0.881
69	Thulium	Tm	4f ¹³ 6s ²	1.11	0.869
70	Ytterbium	Yb	4f ¹⁴ 6s ²	1.06	0.858
71	Lutetium	Lu	4f ¹⁴ 5d6s ²	1.14	0.848
Other important elements					
13	Aluminum	Al	3s ² 3p ¹	1.61	0.50
31	Gallium	Ga	4s ² 4p ¹	1.81	0.62
49	Indium	In	5s ² 5p ¹	1.78	0.81

to each of these symbols. In a configuration of N electrons, the principal quantum number n and orbital angular momentum l are specified for each electron, but m_l and m_s can assume all possible values. The degeneracy of the configuration of N equivalent 4f electrons is given by the binomial coefficient $\binom{14}{N}$.

When electrostatic repulsion between electrons in the 4f configuration is taken into con-

sideration, the Hamiltonian is given by

$$H = H_0 + H_{e-e} = H_0 + \sum_{i>j}^{i=N} q^2 / (4\pi\epsilon_0 r_{ij}), \quad (68)$$

where r_{ij} is the distance between the i th and j th electron. This additional interaction separates the $\binom{14}{N}$ degenerate states. That is, linear combinations of the original states given by the four quantum numbers n , l , m_l , and m_s , are used to obtain new groupings of degenerate states which are now characterized by the quantum numbers L , S , M_L , and M_S . L and S are the total-orbital and spin-angular momenta, respectively, and, M_L and M_S are their projections onto the z -axis (i.e., $M_L = L \cos(\theta)$). These states, which are referred to as the LS terms, are $(2L + 1)(2S + 1)$ -fold degenerate.

For heavier atoms, such as the REs, the interaction between the spin and orbital angular momenta, H_{so} , must also be considered. This interaction is typically understood as a radially-dependent coupling of the magnetic moment associated with the electron spin \vec{s}_i and the magnetic field associated with the electron's orbital angular momentum \vec{l}_i , and is typically given as

$$H_{so} = \sum \zeta_i(\vec{r}) \vec{l}_i \cdot \vec{s}_i, \quad (69)$$

where $\zeta_i(\vec{r})$ accounts for the radial dependence of this interaction. The spin-orbit coupling splits the LS terms into states which are eigenfunctions of the total angular momentum $J = L + S$, and its projection onto the z -axis, m_J . Each J level, known as a J -multiplet, is $(2J + 1)$ -fold degenerate. For a given LS term, the lowest lying J -multiplet is determined by Hund's rules (2:650). Furthermore, the total angular momentum J can take on integral values between $|L - S|$ and $L + S$ (2:651). Thus, in accordance with Hund's first two rules, the Er^{3+} core with a $4f^{11}$ configuration has a ground state with $L = 6$ and $S = 3/2$. Also, according to Hund's third rule, the Er^{3+} core has a lowest lying multiplet of $J = L + S = 15/2$. This spin orbit level is denoted by $^4I_{15/2}$ in accordance with the standard spectroscopic notation $^{2S+1}L_J$. The other multiplets of the 4I term of Er^{3+} are $^4I_{13/2}$, $^4I_{11/2}$, and $^4I_{9/2}$, in order of increasing energy. Their respective energies above the ground state, as reported by Dieke (25:134), are approximately 0.80, 1.25, and 1.54 eV.

Finally, the last term in the Hamiltonian, H_{cf} , accounts for the effect of external electric fields which act to further break the $(2J + 1)$ -fold degeneracy associated with a given J -multiplet. In a semiconductor, the electric field is attributed to the ligand atoms composing the crystal

structure, and thus, it is referred to as the 'crystal field'. The symmetry group of the crystal field will be the same as the symmetry group associated with the RE site in the crystal. The methods of group theory are typically invoked to describe the states resulting after this last perturbation is considered. For instance, if the Er^{3+} atom occupies a site with low symmetry (i.e., little or no symmetry), then the 16 degenerate levels of the ground state $^4I_{15/2}$ become 8 distinct doubly-degenerate levels. On the other hand, if the Er occupies a site of tetrahedral symmetry, T_d , consistent with the Er occupying a substitutional position in the GaAs lattice, the methods of group theory reveal that the 16 degenerate levels are now grouped into 5 distinct levels, one of Γ_6 , one of Γ_7 , and three of Γ_8 character (6:2804), where Γ_6 , Γ_7 , and Γ_8 are irreducible representations of the cubic-lattice structure. Thus, by merely counting emission lines, the site location of the RE in the crystal lattice may possibly be inferred.

The magnitude of the crystal-field splitting associated with the 4f states of the RE atoms is very small, typically 10 meV, compared to the relatively large spin-orbit splitting, which is on the order of 1 eV. This characteristic of the 4f energy levels has been discussed previously in the introductory chapter, where it was attributed to the shielding of the 4f shell by the 5s and 5p electrons. This behavior is illustrated in Figure 30, which shows the square of the 4f, 5s, 5p, and 6s wave functions of Gd^{3+} , obtained using Hartree-Fock calculations (25:64). This plot demonstrates that the 4f orbitals of the RE ions are largely inside the 5s and 5p orbitals. In addition to the relatively small splitting of a given J-multiplet, this shielding also acts to isolate the 4f shell from the effects of crystal vibrations (phonons) which would otherwise tend to broaden these atomic levels. Thus, the 4f-4f transitions in RE ions tend to maintain atomic like linewidths and stable transition energies, independent of crystal temperature.

When interpreting the behavior of the RE atoms in III-V hosts, it is critical to understand that the RE^{3+} ionic radius actually decreases with increasing atomic number, as demonstrated in Table 4. This anomalous behavior, known as the "lanthanide contraction" phenomenon, can be understood on the basis of an incomplete shielding of one electron by another in the same subshell. As the atomic number increases from La to Lu, the nuclear charge and number of 4f electrons increases by one at each step. The shielding of one 4f electron by another is imperfect due to the shape of the orbitals. Thus, at each increase, the effective nuclear charge experienced by each 4f electron increases, causing a reduction in the size of the entire 4f shell. The accumulation of these successive contractions is known as the total lanthanide contraction.

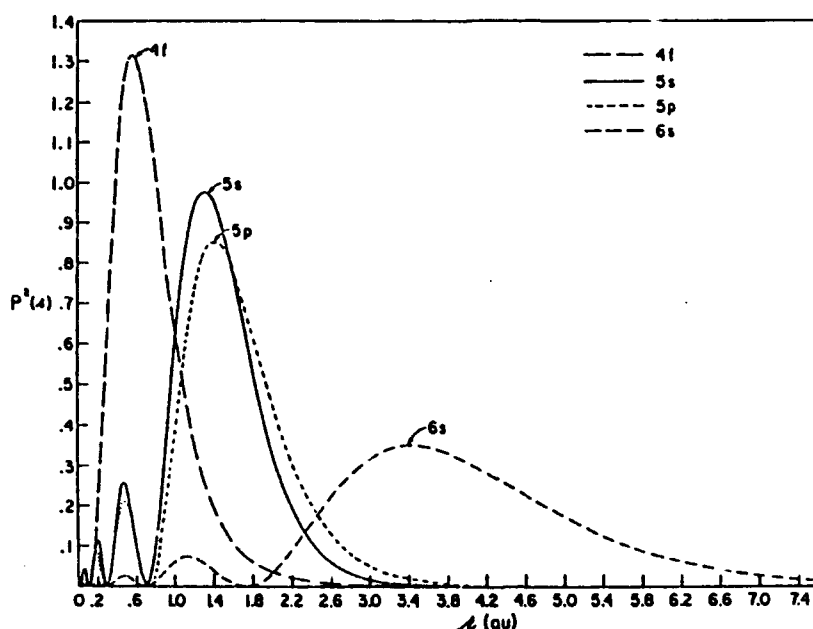


Figure 30. Square of the radial wave functions for the 4f, 5s, 5p, and 6s orbitals of the Gd^{3+} ion obtained using Hartree-Fock calculations (after Dieke (25:64))

5.3 Electrical Properties of RE-Doped III-V Compounds

5.3.1 Donor or Acceptor Behavior The REs have an electronic configuration of $[\text{Pd}]4f^n5s^25p^66s^2$. This is essentially the configuration for an element of group IIA of the periodic table. Thus, a RE atom substituting for a group III atom might be expected to act as a single acceptor, or as a triple acceptor on a group IV site. However, if an additional electron from the 4f shell is ionized, the RE atom in the configuration $4f^{n-1}5s^25p^6$ would act as an isoelectronic impurity on a cation site, with the $6s^2$ electrons and this last 4f electron transferring into bonding orbitals. The same configuration on an anion site would lead to a double acceptor. For instance, ytterbium in the trivalent state has the configuration $4f^{13}5s^25p^6$, and so on the cation site it acts electrically as a neutral acceptor, A^0 , with its hole highly localized in the 4f shell. Conversely, ytterbium in the A^- state would have a closed 4f shell. Therefore, aside from ytterbium, it should be possible to observe luminescence from both the trivalent (A^0) and the divalent (A^-) state of

the acceptors. However, no 4f-4f luminescence of the divalent state of RE ions in semiconductors have been observed (27:125), indicating a definite preference for the RE^{3+} configuration.

Aside from this observation, early theoretical and electrical measurements revealed conflicting evidence as to the actual state of the RE ion in a III-V semiconductor. Theoretical calculations carried out by Hemstreet (36) using a full-relativistic version of the X- α -scattered wave cluster method indicate that the Yb should act as a single acceptor with a hole ionization energy level located approximately 0.26 eV above the valence band edge. These calculations were performed with a 17-atom cluster consisting of Yb substituting on an indium site, surrounded by 4 phosphorus atoms and the 12 next nearest indium atoms. Hemstreet's calculations provided a theoretical basis for the p-type conductivity observed by Körber (48) for Liquid Phase Epitaxial (LPE) InP:Yb. However, using temperature-dependent Hall effect measurements, Körber found the activation energy of the $(3+/2+)$ transition to be only 45 meV.

In contrast, Yb-doped InP samples grown by Metalorganic Chemical Vapor Deposition (MOCVD) have shown n-type conductivity (93:977). Uwai (93:978) suggested that the p-type conductivity observed in LPE-grown InP:Yb was caused by unintentionally incorporating p-type impurities rather than the Yb itself. It is known that commercially available RE metals often have large concentrations of Zn or Mg impurities. This information also explains the relatively low hole ionization energy measured by Körber. Electron Spin Resonance (ESR) experiments (52) also support this claim since they reveal that the Yb^{3+} occupies a site of tetrahedral symmetry, and that the Yb^{2+} acceptor level is not found in the band gap.

5.3.2 Deep States in III-V:RE Little attention has been given to the study of deep levels occurring in RE-doped III-V materials. The most notable work was performed by Whitney et al. (98), who performed DLTS and temperature-dependent Hall effect measurements on Yb-doped, MOCVD-grown InP. They found an acceptor-like electron trap located 30 meV below the conduction band edge. The concentration of this center was found to be nearly equal to the Yb concentration for Yb doping in the range of 10^{14} to 10^{18} cm $^{-3}$, indicating that this level is due to a Yb center, as opposed to a native defect due to Yb incorporation. While these measurements were performed with Schottky diodes on n-type material, Whitney et al. also investigated possible hole traps by fabricating p $^+$ n junctions. Saturating injection pulses revealed no hole traps present in their epilayers.

A possible model for the 30 meV level involves charge transfer leading to the $\text{Yb}^{3+}/\text{Yb}^{2+}$ transition. However, this explanation seems doubtful due to the screening of the $5s^2$ and $5p^6$ electrons. A better explanation might be that the Yb^{3+} acts as an isoelectronic trap due to a distortion of the lattice and a difference in electronegativities between In^{3+} and Yb^{3+} .

Lambert et al. (51) performed temperature-dependent Hall effect measurements on bulk-grown $\text{InP}:\text{Yb}$ and concurs with Whitney's measurements by finding a 30 meV electron trap. They also performed temperature-dependent Hall effect measurements on $\text{InP}:\text{Er}$ and found a similar behavior to $\text{InP}:\text{Yb}$, except that the electron trap was found to be 60 meV below the conduction band edge. On the other hand, it appears that not all III-V:RE combinations give such shallow centers. For instance, Taguchi et al. (88) found that Yb-doped, MOCVD-grown GaAs manifested an electron trap between 0.5 and 0.7 eV below the conduction band edge, but unlike $\text{InP}:\text{Yb}$, they discovered no shallow centers.

Besides the effect on the electrical properties of the crystal, a knowledge of the RE-related deep centers is also important since they may be related to the excitation or nonexcitation of the RE-4f shell. For instance, Lambert proposes that the 30 meV electron trap may be involved in the efficient excitation of the Yb^{3+} -4f shell, since the PL intensity increases strongly as the temperature is lowered. At low temperatures, all of these electron traps would be filled. Excitons bound at these traps could then recombine and directly transfer their energy to the RE. On the other hand, Taguchi claims that the depth of the Yb center in GaAs is likely to be responsible for the absence of Yb-4f photoluminescence in GaAs. That is, the energy difference between the trap level and either the bottom of the conduction band or the top of the valence band is insufficient to provide the 1.24 eV necessary to excite the Yb^{3+} -4f shell.

5.3.3 Donor Gettering or Purification by REs The direct-gap semiconductors InP and its alloy InGaP are of interest for their possible application as avalanche photodiodes, phototransistors, and p-i-n diodes. This material system has a spectral response in the 1.0 to 1.7 μm region, and therefore, like Er-doped semiconductors, is of interest for applications in fiber-optic communications. Due to the high vapor pressure of phosphine, it is difficult or impossible to grow these compounds using the MBE technique. However, the liquid phase epitaxial (LPE) growth technology is a promising alternative. Unfortunately, the primary difficulty experienced with LPE is focused on the preparation of pure crystals, due to the unavoidable presence of such

residual impurities as silicon, oxygen, and carbon, which are present in the sapphire and graphite cassettes which contain the melt.

Bagraev et al. (3:49) was the first to observe that RE-doping can significantly reduce these impurities, with the RE-atom acting as a scavenging agent to purify these materials. Specifically, the free electron concentration in the undoped material has been reduced by up to 2 orders of magnitude, and the 77 K mobility has been enhanced by a factor as large as 5. This effect was observed for InP and GaInP while doping 0.01% atomic concentration of Yb or Gd. Electron concentrations were reduced from, typically, 10^{15} cm^{-3} to $5 \times 10^{13} \text{ cm}^{-3}$, and the 77 K Hall mobilities were enhanced from 21,000 to 102,000 $\text{cm}^2/\text{V} \cdot \text{s}$. Bagraev attributed these results to the high chemical reactivity of the REs, which formed electrically neutral compounds with the group VI impurity O, and group IV impurities C and Si. This interaction prevents the formation of shallow donors which are combinations of Si_xC_y , Si_xO_y , and C_xO_y .

Gettering effects, or n to p-type conversion, has also been observed by Bantien (6) for Er-doped into LPE GaAs. Undoped substrates show an n-type conductivity of 10^{15} cm^{-3} . However, light Er doping (< 0.01 atomic %) resulted in p-type concentrations ranging from $5 \times 10^{14} \text{ cm}^{-3}$ to 10^{15} cm^{-3} . Near-band-edge PL measurements of the material with no Er doping showed emissions due to the bound exciton at a neutral donor (D^0, X) as well as donor-acceptor-pair (DAP) transitions due to residual C and Si acceptors, $(\text{D}^0, \text{A}^0)_{\text{C}}$ and $(\text{D}^0, \text{A}^0)_{\text{Si}}$. For the Er-doped substrate, a drastic decrease in (D^0, X) , and $(\text{D}^0, \text{A}^0)_{\text{C}}$ with a corresponding increase in the free-to-bound transitions $(\text{e}, \text{A}^0)_{\text{C}}$ and $(\text{e}, \text{A}^0)_{\text{Si}}$ occurred. This indicated that the conversion from n- to p-type material is due to the decrease in donor concentration, as opposed to compensation by the RE acting as an acceptor.

Raczynska (74) also uses PL in conjunction with Hall effect measurements to confirm that purification of LPE-grown InP by Yb is due to donor gettering. He doped Yb in varying concentrations ($0 \rightarrow 1000 \text{ ppm}$) into InP and observed a gradual conversion to p-type conductivity, as well as a conversion from a donor-bound exciton (D^0, X)-dominant transition to an acceptor-bound exciton (A^0, X)-dominant emission.

More recently, Wu (102) has reported the decrease in electron-carrier concentration for Er-doped InGaAsP material by up to two orders of magnitude relative to the undoped material, with a corresponding narrowing of the band edge emissions from approximately 45 meV to

only 6 meV. He also revealed that, when doping by more than 0.32 wt. %, the surface has a fairly rough morphology, which may be due to extensive deposits of erbium hydride and oxide. Wavelength-dispersive x-ray spectrometry analysis indicated that the higher Er doping also tended to change the composition of the $\text{Al}_x\text{Ga}_{1-x}\text{As}_y\text{P}_{1-y}$, possibly due to the formation of microparticles of ErAs or ErP, demonstrating that the utility of the REs in the purification of the LPE material is unlimited.

5.4 *Excitation Mechanisms*

In order to optimize the fabrication of optoelectronic devices, it necessary to understand the mechanisms responsible for the RE intracenter atomistic excitations. Conversely, luminescence quenching mechanisms, which divert crystal energy away from the 4f shell or cause nonradiative deexcitation of the excited RE, are also of interest. Before work began on RE-doped III-V compounds, much work had already been done on RE-doped II-VI compounds, since with their larger band gaps, these semiconductors could possibly transfer energy to higher energy 4f states, leading to 4f-4f transitions in the visible wavelengths. A recent review article by Boyn (15:29) addressed the modes of excitation observed in these materials. Excitation spectroscopy of the internal RE 4f transitions revealed several possible mechanisms for RE excitation. Among these are:

- (a) **direct excitation** of the 4f shell, which is characterized by very sharp lines ≈ 0.1 meV, occurring between the transition energy and the band gap. These lines are very weak due to the low 4f-4f oscillator strengths.
- (b) **excitation of impurity states external to the 4f shell** followed by nonradiative energy transfer to the 4f shell. This excitation occurs in the same spectral range as (a) but is characterized by broad bands, typically 0.1 to 0.6 eV wide. These processes are due to donor-acceptor pairs (DAP) or sensitizing centers.
- (c) broad bands also observed around the band gap E_g attributed to **energy transfer from free excitons or electron-hole pairs**.

Although much less work has been done in III-V materials, there is evidence that the same type of processes are occurring.

Ennen et al. (28) have furnished the only report of direct excitation of a RE in a III-V semiconductor. They performed PL and photoluminescence excitation (PLE) measurements

on Er-doped MBE-grown GaAs using a tunable color center laser (KCl:Ti^+). Eight lines were observed in PL, and seven sharp lines in the PLE spectrum, all near $1.54 \mu\text{m}$. This number of lines is indicative of an Er-related center with lower than cubic symmetry (T_d). Most other researchers investigating the excitation of REs in III-V semiconductors attribute excitation to mechanisms (b) and (c), where the excitation energy is coupled into the 4f shell by fairly localized crystal states, i.e., by DAPs or excitons.

Kasatkin (44) was the first to address the excitation mechanism of REs in III-V compounds by measuring the excitation spectra of the Yb^{3+} -4f and DAP emissions in GaP:Yb and InP:Yb. In GaP he found that the excitation spectra of Yb^{3+} -4f emissions exactly mirrored the excitation spectra of the DAP for excitation in the range of 2.3 to 2.6 eV. Furthermore, this behavior did not deviate with a Yb^{3+} concentration up to $5 \times 10^{17} \text{ cm}^{-3}$.

Similar results were obtained for InP:Yb. However, in this case, excitation spectra in the region 1.40 to 1.42 eV depended strongly on N_{DAP} , the concentration of donor-acceptor pairs. When $N_{\text{DAP}} \gg N_{\text{Yb}}$, there is a strong quenching of the DAP luminescence and a corresponding increase in the intensity of the Yb^{3+} -4f emissions. An increase in Yb concentration to 10^{17} cm^{-3} resulted in a complete quenching of the DAP spectrum. Furthermore, when $N_{\text{Yb}} \gg N_{\text{DAP}}$, the Yb^{3+} -4f luminescence excitation spectrum was virtually identical to the DAP spectrum of InP without Yb doping.

These measurements indicated that the DAPs participated in the intracenter atomistic excitation of the Yb^{3+} ion, and that the process was much more effective for InP:Yb than for GaP:Yb. Kasatkin proposed an Auger process in which energy released by the nonradiative recombination of the DAP was transferred via the coulomb interaction with the Yb^{3+} -4f shell, as well as to a nearby charge carrier at a donor or acceptor, which was excited into the appropriate band. Finally, quenching of the DAP luminescence in InP:Yb (and the nonquenching in GaP) was explained by showing that the cross section for the above Auger process was at least two orders of magnitude higher in InP:Yb than in GaP:Yb, due to the Yb^{3+} -4f transition being more nearly resonant with the InP band gap.

Zakharenkov and Kasatkin (107) examined the effect of shallow-dopant density on the efficiency of the intracenter Yb^{3+} -4f luminescence in InP, and they found that the Yb^{3+} -4f luminescence increased steadily up to an electron density of $2 \times 10^{17} \text{ cm}^{-3}$, but then was sharply

quenched. The excitation of the Yb^{3+} -4f emissions showed the same behavior that was observed by Kasatkin, independent of electron concentration. Further the excitation spectra of a free-to-bound transition of energy $h\nu = 1.37 \text{ eV}$ was quenched as the Yb concentration increased, and as Yb^{3+} -4f luminescence increased in intensity, with the maximum quenching occurring at the same electron concentration where the Yb^{3+} -4f luminescence was maximized. The excitation region where quenching occurred, 1.40 to 1.42 eV, corresponded to absorption and emission of bound excitons. Thus, in addition to the DAP-excitation mechanism proposed by Kasatkin, excitation may also be attributed to the diffusion of excitons to Yb^{3+} ion complexes. However, the nature of the Yb^{3+} ion complexes was unknown until the measurements of Whitney et al. (98) revealed that Yb in InP manifested a 30 meV isoelectronic electron trap.

The most recent and comprehensive model for the Yb^{3+} -4f-shell excitation in InP has been proposed by Takahei (90) who utilized the 30 meV acceptor-like electron trap. Above-band-gap excitation generates electron-hole pairs. The electrons are subsequently trapped at the 30 meV Yb^{3+} center, which becomes negatively charged and has a potential attractive to holes. Thus, a free hole is attracted to this center, forming a bound exciton, which then nonradiatively decays and transfers its energy to the Yb^{3+} -4f shell. The excited-4f shell either radiatively or nonradiatively decays, making the transition $^2F_{5/2} \rightarrow ^2F_{7/2}$, with the energy appearing as a 1.24 eV photon or with the energy being returned to the crystal (phonon), respectively.

Takahei proposed that the nonradiative quenching of the excited-4f shell may occur along two paths. First, after the excitation, the Yb^{3+} ($^2F_{5/2}$) may also capture an electron. The energy of the 4f shell may be transferred to this trapped electron in a localized Auger process, sending the electron deep into the conduction band. This argument assumes that, since the 4f shell is well shielded from the ligands, the first excited state of Yb^{3+} ($^2F_{5/2}$) and the ground state Yb^{3+} ($^2F_{7/2}$) give rise to essentially the same 30 meV electron trap. In the second quenching mechanism, the energy in the Yb^{3+} -4f shell is transferred back to the crystal lattice, either by lifting a valence band electron to the Yb-related 30 meV electron trap or by generating an electron-hole pair. Takahei showed that the band-edge emissions of the Yb-doped InP samples increased with temperature, while the undoped InP samples decreased, which is indicative of the back-transfer process.

For excitation at energies below the free exciton energy, E_{ex} , Yb^{3+} -4f emissions were detected for heavily Yb-doped InP, but not for lightly Yb-doped InP. Takahei (89) found that the 30 meV electron trap may be utilized to explain this behavior. First, electrons at shallow acceptors

are excited to the conduction band, from which they are captured into the 30 meV electron traps. These trapped electrons recombine with the holes at acceptors with the simultaneous excitation of the Yb-4f shell. This process is possible only for heavily Yb-doped materials, as opposed to lightly Yb-doped samples, since, in the former case, there is a smaller average separation between the Yb ions and acceptors. This model is also consistent with the work of Körber and Hangleiter (48) who have measured PLE spectra in n- and p-type LPE InP:Yb, and they have only observed below E_{ex} excitation in samples with a large concentration of acceptors.

The excitation of the Er^{3+} -4f shell in GaAs and AlGaAs may be attributed to similar mechanisms as have been observed for Yb in InP. Yet, there is an important difference to be noted for these two systems. For Yb^{3+} , the exciting transition $^2F_{7/2} \rightarrow ^2F_{5/2}$, requires 1.24 eV, while the InP band gap is 1.42 eV. However, the Er^{3+} transition $^4I_{15/2} \rightarrow ^4I_{13/2}$ requires only 0.805 eV of the 1.52 eV GaAs band-gap energy. Obviously, the Yb^{3+} -4f transition is nearly resonant with E_g in InP, while the Er^{3+} -4f transition is far from resonance with E_g in GaAs. Thus, an excitation process of the Er^{3+} -4f shell in GaAs must also account for the dissipation of roughly 0.7 eV.

This background chapter has provided a review of the behavior of rare earths in III-V semiconductors. The material studied the most extensively by previous researchers was Yb-doped InP. In this material the Yb was found to predominantly occupy a cation (In) site and gave rise to a very shallow isoelectronic electron trap, through which the excitation of the Yb^{3+} -4f shell proceeds. On the other hand, Yb in GaAs was found to yield a deep electron trap, which was thought to be responsible for the lack of Yb luminescence observed in this material. Thus, when REs in III-V semiconductors must be considered on a case by case basis. Similarly, Er incorporation in GaAs and AlGaAs may give rise to shallow or deep levels, or possibly levels which are in the bands, and thus are not readily observable. Excitation of the Er^{3+} -4f shell may proceed through any of these levels. These issues will be addressed in the following chapter.

IV. Results and Discussion

6.1 Introduction

The results obtained in this study will be presented, in sequence, beginning with the most easily obtained and most valuable parameters, such as the Er atomic distributions, Er diffusion during annealing or growth, and the fundamental changes manifested in the substrate's electrical conductivity due to Er incorporation. Subsequently, the more complex findings will be discussed, including the types of centers the Er atoms form in GaAs and AlGaAs, and the electron levels these centers introduce, either deep within the bandgap or closer to the band edges. Most importantly, the role of these centers in the excitation of the Er-4f shell will be explored.

In the first section, **Erbium Doping and Electrical Behavior**, the nature of the Er distribution resulting from Er-doping either by ion implantation or MBE growth will be discussed. More specifically, the as-implanted Er distributions, as well as the nature of diffusion in both the implanted and MBE material will be covered. Additionally, the effect of Er-doping on the electrical conductivity of the GaAs or AlGaAs host substrate will be explored. Using the Hall effect and CV measurements, the resulting substrate's electrical conductivity and carrier distributions after Er-doping and annealing treatments will be examined. The primary focus will be to determine whether Er-doping, by either ion implantation or during MBE growth, introduces shallow donor or acceptor levels that manifest large and readily observable effects on the substrate's electrical conductivity, or on the other hand, if it introduces deeper states, which tend to act as compensating centers. Another possibility is that neutral centers are formed due to shallow donor complexes with Er, as has been previously reported (6).

In the next section, **The Effect of Er on Deep States in GaAs and AlGaAs Obtained by DLTS Measurements**, the emphasis will be focused on discussing possible deep states introduced by ion-implantation damage, and states most likely due directly to Er-related centers. The effect of Er-doping on deep states existing in the substrate prior to implantation, such as the EL2 defect in GaAs and the DX center in AlGaAs, will also be addressed.

The third section, **Annealing Studies and Excitation Mechanisms of Er in GaAs and AlGaAs**, deals with an investigation of the formation of certain optically-active, Er-related centers after annealing the Er-implanted substrate at different temperatures. The intensity of the Er-4f

emissions and near-band-edge PL will be correlated with the electrical behavior of the Er-doped layer.

In the final section, **Electroluminescence from Er-Doped GaAs**, the cumulative results obtained in the preceding sections will be used to explore possible reasons for relatively weak electroluminescence from Er-doped GaAs.

6.2 *Erbium Doping and Electrical Behavior*

Prior to attempting in-depth electrical and optical measurements on Er-doped layers, it is prudent to examine the distribution of ions in the Er-doped region by Secondary Ion Mass Spectrometry (SIMS) measurements. The as-implanted Er distributions were measured to assess the actual Er distribution and the effects of Er ion channelling (during implantation). Further, the Er distributions were measured after annealing treatments to assess the effect of Er diffusion.

Initially, when introducing Er in GaAs or AlGaAs, it is critical to examine the effect it has on the electrical conductivity of the substrate. If the substrate is semi-insulating (SI), it is essential to determine if the introduction of Er causes p-type or n-type electrical conductivity, thereby introducing acceptors or donors, respectively. Further, if the substrate is conducting, it is necessary to determine if Er-doping makes it less conductive by introducing a compensating center or deep trap, or possibly by forming neutral complexes of the shallow dopant atoms and Er atoms. It is expected that differing results will be obtained from the MBE-grown material and the ion-implanted material, as these two technologies represent vastly different doping techniques. The extent to which the results overlap between these two doping techniques will allow the common properties to be attributed to distinct Er-related centers.

6.2.1 *Ion-Implanted Material* SIMS measurements were performed on the Er-implanted substrates to compare the actual Er distribution with the one predicted by the LSS theory. These measurements were also implemented for the purpose of calibrating the SIMS apparatus so that the Er distributions in the MBE samples could be accurately determined. Once the relative sensitivity factor of the Er ion in the GaAs matrix has been determined, the MBE effusion cells can be calibrated. Figure 31 shows the as-implanted Er distribution for the high and low Er implant fluences, 5×10^{12} and $5 \times 10^{13} \text{ cm}^{-2}$, both at 1 MeV implant energy, as well as their distributions

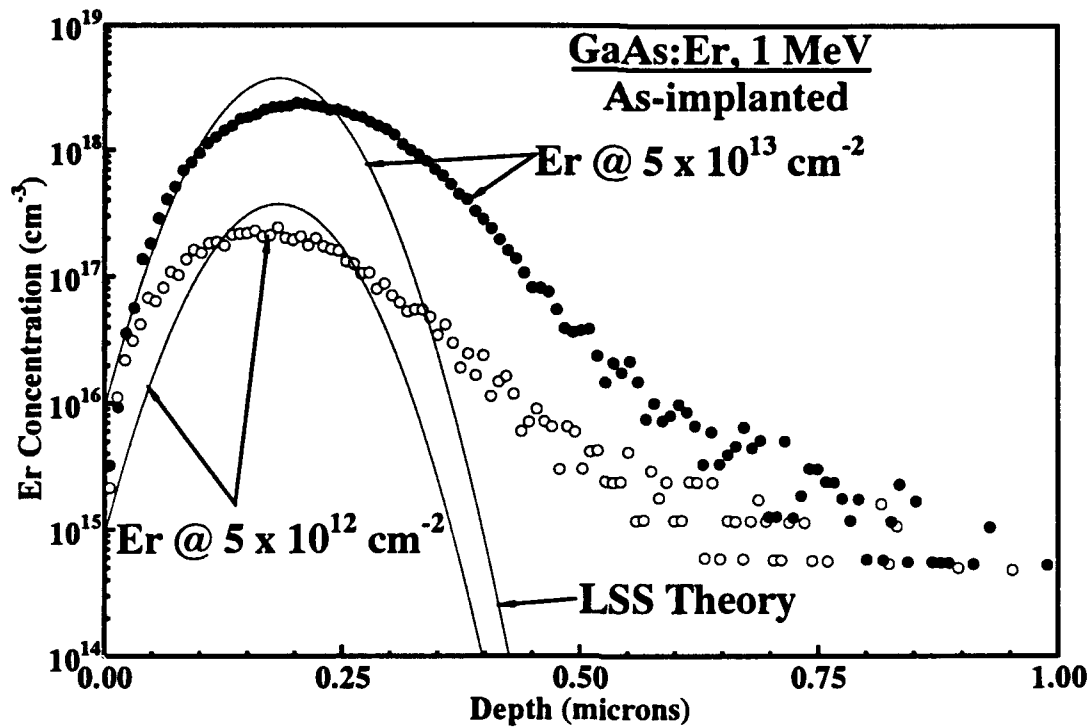


Figure 31. SIMS measurement of the as-implanted Er distributions in a GaAs substrate for Er fluences of $\Phi_{\text{Er}} = 5 \times 10^{12}$ and $5 \times 10^{13} \text{ cm}^{-2}$ at an energy of 1 MeV (The theoretical LSS distributions are shown as solid lines.)

predicted by the LSS theory. The resolution of the measurement was roughly 10^{15} cm^{-3} , which is sufficient to clearly show that the Er distribution has a much longer tail than expected, probably due to a small degree of ion channeling during implantation. Otherwise, the projected range and straggle seem to be close to the theoretical predictions (larger by approximately 10 and 20%, respectively). Furthermore, the shapes of the two profiles are very similar, indicating that the distribution does not depend upon the Er fluence.

SIMS measurements were also performed on Er-implanted substrates after rapid thermal annealing at various temperatures to assess the effect of diffusion. Figure 32 shows the Er distribution in a GaAs substrate after annealing the substrate which was implanted with an Er fluence of $\Phi_{\text{Er}} = 5 \times 10^{13} \text{ cm}^{-2}$ at an energy of 1 MeV. The three measurements shown in the figure are the as-implanted Er distribution, the Er distribution after an RTA at 750 °C for 15 seconds, and the Er distribution after an RTA at 850 °C for 15 seconds. The latter two annealing

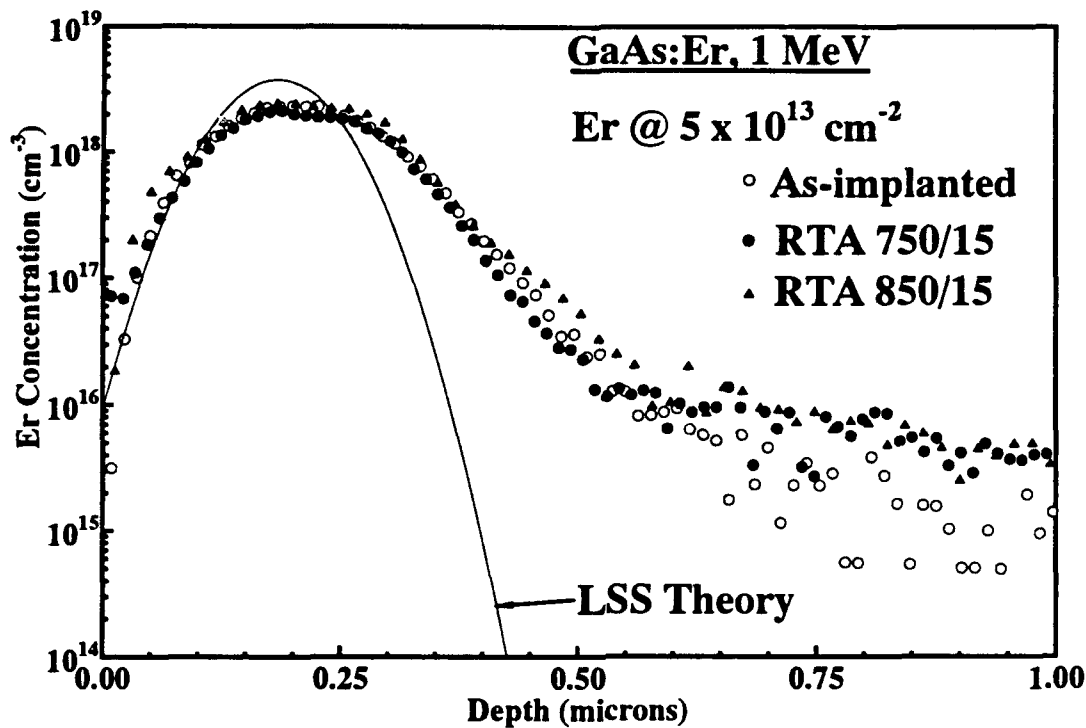


Figure 32. SIMS profiles of Er in GaAs after a 1 MeV implant with a fluence of $\Phi_{\text{Er}} = 5 \times 10^{13} \text{ cm}^{-2}$ for the as-implanted substrate after an RTA of 750 °C for 15 seconds, and after an RTA of 850 °C for 15 seconds

conditions were chosen because the Er-related emissions at 1.54 μm were found to be most intense at 750 °C for 15 seconds, and almost totally quenched at 850 °C for 15 seconds. The Er distribution of both annealed samples shows a slight depression in the center, indicating a slight Er redistribution. Although the overall diffusion of the Er is rather small, as is expected for the RTA technique, both annealing conditions shown in Figure 32 produced a tail that is much longer compared to the as-implanted sample. This tail has an Er concentration of $\approx 10^{16} \text{ cm}^{-3}$, which is an order of magnitude larger than the background.

Table 5 summarizes the results of the room-temperature Hall effect measurements for samples implanted with three Er fluences of $\Phi_{\text{Er}} = 5 \times 10^{12}$, 1×10^{13} , and $5 \times 10^{13} \text{ cm}^{-2}$, all with an energy of 1 MeV, into n-type, p-type and semi-insulating substrates. All samples were annealed at 750 °C for 15 seconds. The most significant finding was that the Er-doping tends to make the semi-insulating substrate slightly more conducting with increasing dose, but, in general, leaves the substrate semi-insulating. In the n-type substrates, the electron concentration

Table 5. Effect of Er doping on semi-insulating (SI), n-type, and p-type GaAs substrates as determined by room temperature Hall effect measurements (All samples were annealed at 750 °C for 15 seconds using the RTA method.)

Substrate	Er dose (cm ⁻²)	ρ (Ω -cm)	μ (cm ² /Vs)	N_s (cm ⁻²)	n- or p-type (cm ⁻³)	ΔN_s (%)
02-PR-1748 n-type Si-doped t=3 μ m	-	0.198	6655	1.42×10^{12}	4.74×10^{15} ⁿ	0
"	5×10^{12}	0.281	6399	1.04×10^{12}	3.47×10^{15}	-26.7
"	1×10^{13}	0.285	5565	1.18×10^{12}	3.94×10^{15}	-16.8
"	5×10^{13}	0.274	6398	1.06×10^{12}	3.56×10^{15}	-24.8
3B-PR-840 p-type Zn-doped t=3 μ m	-	0.448	346.8	1.21×10^{13}	4.02×10^{16} ^p	0
"	5×10^{12}	0.495	245.3	8.58×10^{12}	2.86×10^{16}	-28.8
"	1×10^{13}	0.377	758	6.57×10^{12}	2.19×10^{16}	-45.5
"	5×10^{13}	0.489	314.8	1.21×10^{13}	4.05×10^{16}	0.7
L2-728 SI undoped t=500 μ m	-	2.57×10^7	4824	2.52×10^6	5.04×10^7 ⁿ	0
"	5×10^{12}	-	-	1.41×10^7	-	
"	1×10^{13}	1.37×10^7	1612	1.41×10^7	2.83×10^8	460
"	5×10^{13}	3.4×10^6	830	1.11×10^8	2.22×10^9	4400

was consistently reduced by approximately 25% of the substrate's initial value. In the p-type material, a large reduction in the hole concentration occurred with the two lower fluences, but with the sample implanted with an Er fluence of 5×10^{13} cm⁻², the p-type conductivity returned to the initial substrate value.

The primary difficulty with these measurements was that the Hall effect yields the average carrier concentration in the substrate, or the average concentration in the entire conducting layer, if the conducting layer is grown on a semi-insulating substrate. Thus, the reduction in the electron concentration in the n-type substrate may be interpreted as a total n-type carrier removal only

in the region of the implant. This behavior would indicate that the implant and post-annealing diffusion of the Er would extend approximately $0.75\text{ }\mu\text{m}$ into the substrate. This conclusion may be a reasonable interpretation, since it is supported by the SIMS results depicted in Figures 31 and 32. While it is possible to profile active carrier concentrations with the Hall effect method using repeated layer removal by chemical etching (differential Hall measurements), this technique was not pursued since capacitance voltage (CV) profiles provided similar information.

Figure 33 shows the CV profiles for the same three Er fluences and the same n-type substrate that was used in Table 5. These profiles were obtained on p^+n junctions formed by first implanting Er, and then implanting magnesium ions, and finally, annealing at $825\text{ }^\circ\text{C}$ for 12 seconds, as discussed in section 4.4. The actual depth in Figure 33 was measured from the junction, which was about $0.15\text{ }\mu\text{m}$ below the substrate's surface as shown in Figure 28. Also shown with the CV profiles is the SIMS profile for Er at a fluence of $5 \times 10^{13}\text{ cm}^{-2}$ after annealing at $850\text{ }^\circ\text{C}$ for 15 seconds. Certainly the lower carrier region extended deeper into the sample as the Er dose increased. Taken together, these measurements indicate that both the long tail and the Er diffusion contributed to the extended region of depleted carriers. Thus, the speculation from the Hall effect data regarding the severe electron depletion in the region of the Er implant is confirmed.

The same results were observed with a substrate with a much higher carrier concentration. Figure 34 shows the reduction in the carrier concentration for substrate 02-PR-3714, which has a nominal free electron concentration of $3 \times 10^{17}\text{ cm}^{-3}$. This reduction was induced by Er implantation at a fluence of $5 \times 10^{12}\text{ cm}^{-2}$. In this case, the Er concentration did not completely overwhelm the Si doping, as was the case in Figure 33. Instead, the free electron concentration was reduced by approximately 35% with Er doping.

Using the same p-type substrate 3B-PR-840 that was characterized by the Hall effect in Table 5, n^+p diodes were fabricated by low energy Si implantation for each of the 3 standard Er implant doses listed above. The implanted substrates were annealed at 825°C for 15 seconds prior to fabricating the diodes. Only the results from the lowest Er dose of $5 \times 10^{12}\text{ cm}^{-2}$ are presented in Figure 35, because the diodes fabricated with the two higher doses showed poor current-voltage (IV) characteristics. For the two higher dose samples, the Er probably prevented the formation of a well-defined junction by reducing the n-type carrier concentration in the region of the Si implant. However, in the case of the $5 \times 10^{12}\text{ cm}^{-2}$ implant, sufficient

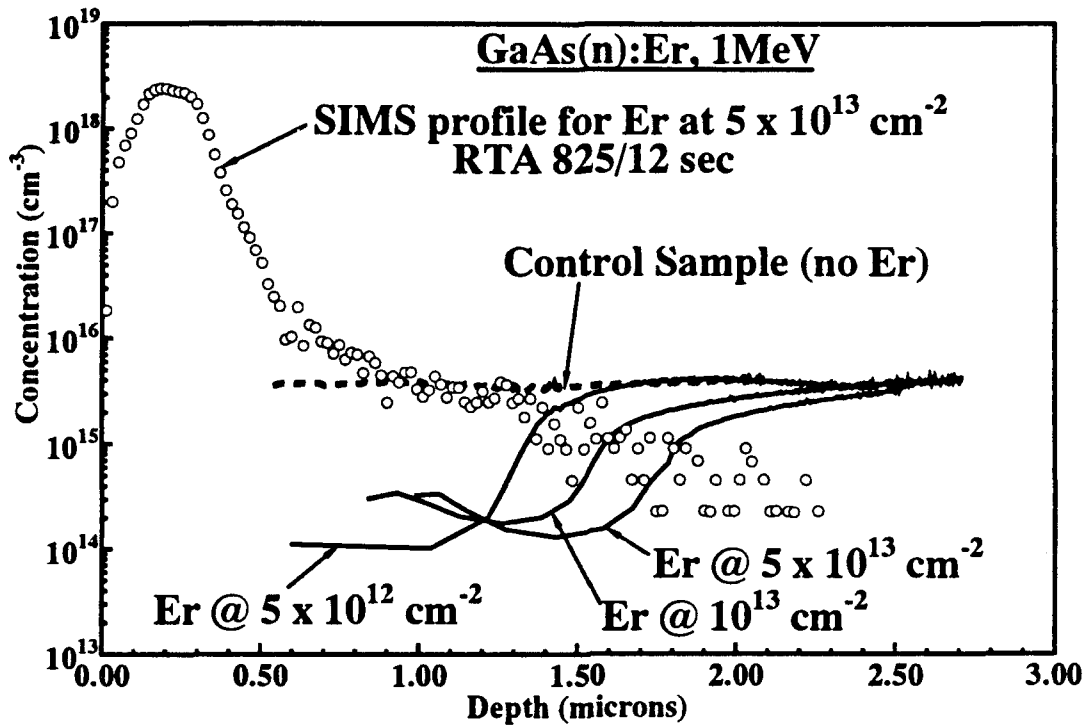


Figure 33. Capacitance-voltage (CV) carrier profiles for an n-type substrate implanted with Er at fluences of $\Phi_{\text{Er}} = 5 \times 10^{12}$, 1×10^{13} , and $5 \times 10^{13} \text{ cm}^{-2}$, each with an energy of 1 MeV and each annealed at 825 °C for 12 seconds

active carriers were left to form the junction. The CV profiles were typically carried out with a small initial positive voltage, typically 0.5 V, in order to probe as close to the junction as possible. The sudden drop in the carrier concentration at the beginning of the carrier profile was a result of electrical conduction through the junction during the initial positive part of the bias voltage sweep. It does not represent the actual carrier concentration; instead it is indicative of the position of the junction. In fact, the shift of the carrier profile of the Er-doped sample from 0.1 to 0.15 μm into the substrate indicates that a significant part of the depletion region exists on the n-type side of the junction. This is justification for the above claim that Er was reducing the n-type carrier concentration in the Si-implanted region. Further, the hole concentration of the Er-implanted samples was comparable to the value of the substrate, consistent with the Hall effect measurements in Table 5. In order to bolster these results, the hole concentration was also measured using a Schottky diode formed on the same substrate, with Er-implanted at a fluence of

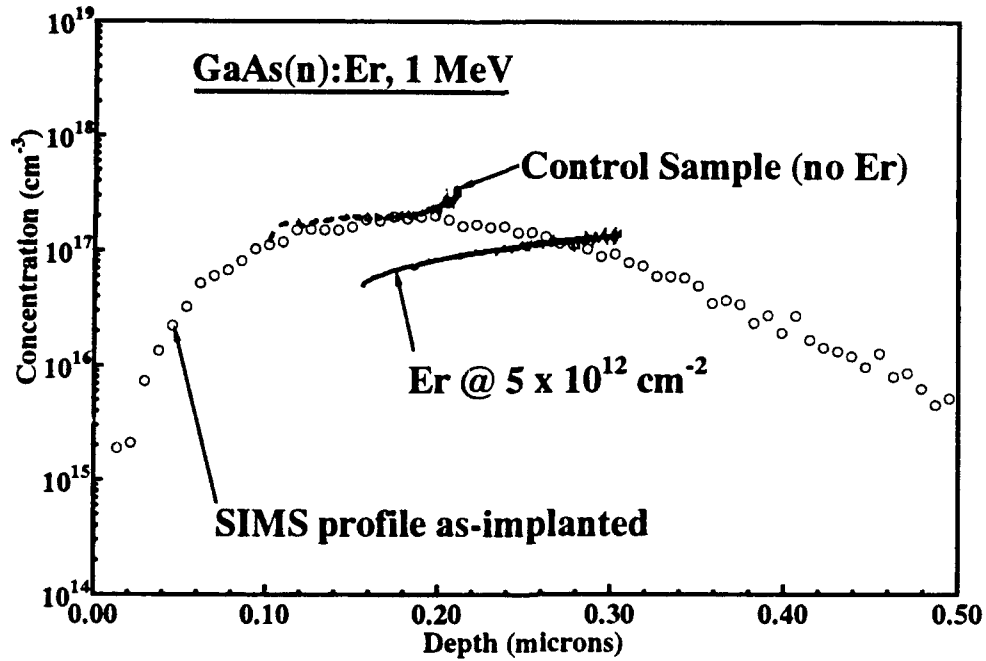


Figure 34. CV carrier profiles for Er implanted at a fluence of $\Phi_{\text{Er}} = 5 \times 10^{12} \text{ cm}^{-2}$ and with an implant energy of 1 MeV into an n-type GaAs substrate with $n \approx 3 \times 10^{17} \text{ cm}^{-3}$

$\Phi_{\text{Er}} = 10^{13} \text{ cm}^{-2}$, which was annealed at 900 °C for 15 seconds (Figure 35). Again, the carrier concentration was slightly higher than the substrate's initial value.

Figure 36 shows the temperature-dependent hole carrier concentration and resistivity that was measured using the Hall effect on the p-type GaAs substrate 3B-PR-840 with and without the $\Phi_{\text{Er}} = 5 \times 10^{13} \text{ cm}^{-2}$ Er implant. As the temperature decreases, the resistivity of the control sample increases by roughly one order of magnitude relative to the Er-implanted sample. Since the Hall mobilities of both samples were nearly the same in this temperature range, this effect was primarily due to the relative increase in the hole carrier concentration of the Er-implanted sample compared to the substrate, indicating the presence of additional acceptors.

The opposite effect was observed in the n-type GaAs substrate 02-PR-1748 with the same Er fluence and energy as indicated in Figure 37. The electron concentration of the substrate changed little with temperature. This behavior is thought to be due to the formation of an impurity band, which occurs when the shallow donor or acceptor concentration becomes sufficiently large

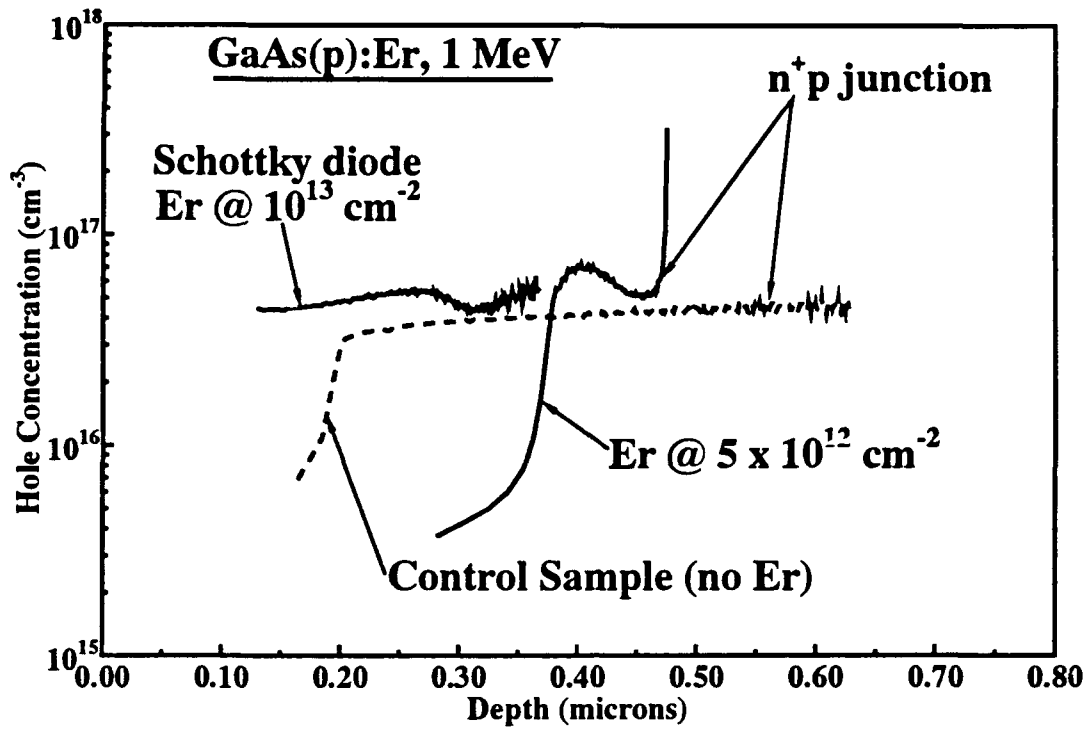


Figure 35. CV carrier profiles for an Er implant at a fluence of $\Phi_{\text{Er}} = 5 \times 10^{12} \text{ cm}^{-2}$ implanted into a p-type GaAs substrate with $p \approx 4 \times 10^{16} \text{ cm}^{-3}$.

to allow electrons, or holes, respectively, to hop from one donor or acceptor impurity to another. The effect is more pronounced for shallower centers. That is, the onset of impurity banding is observed at lower impurity concentrations. Thus, in n-type GaAs, where the donors are typically 6 meV from the conduction band, the impurity banding is typically observed after donor concentrations are approximately 10^{15} cm^{-3} . In contrast, for acceptors with typical activation energies of 30 meV, the impurity band formation does not occur until the acceptor concentrations have exceeded 10^{17} cm^{-3} (57:113–115).

The electron concentration in the Er-doped sample as a function of temperature, however, remains much smaller than in the control sample. This behavior indicates the presence of compensating centers, possibly the same centers that are giving rise to the additional hole concentration in the p-type substrate.

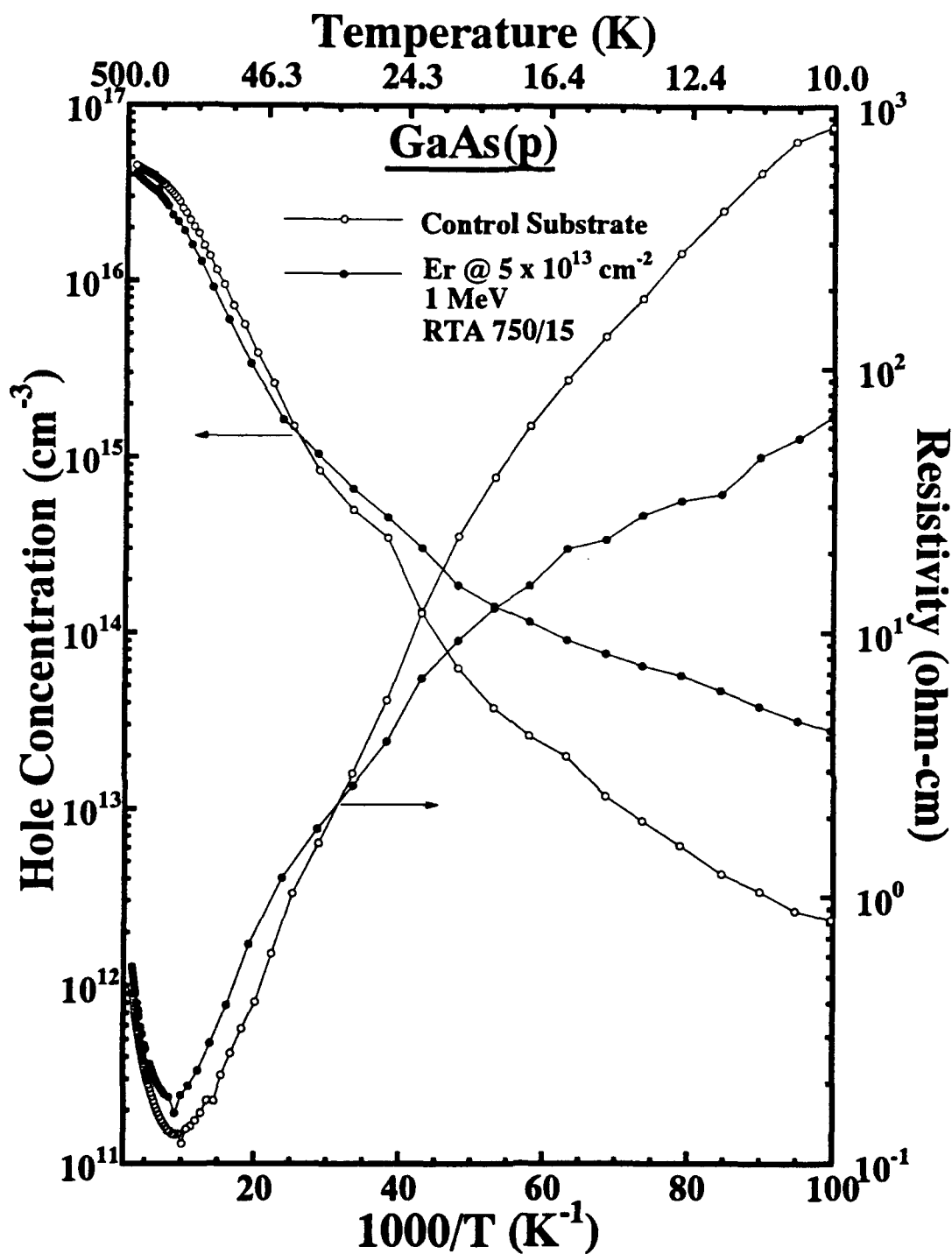


Figure 36. Temperature-dependent hole concentration and resistivity of a p-type substrate with no treatment, and the same substrate implanted with Er at a fluence of $\Phi_{\text{Er}} = 5 \times 10^{13} \text{ cm}^{-2}$ and at an energy of 1 MeV, and annealed at 750 °C for 15 seconds (Solid symbols represent the Er-doped sample.)

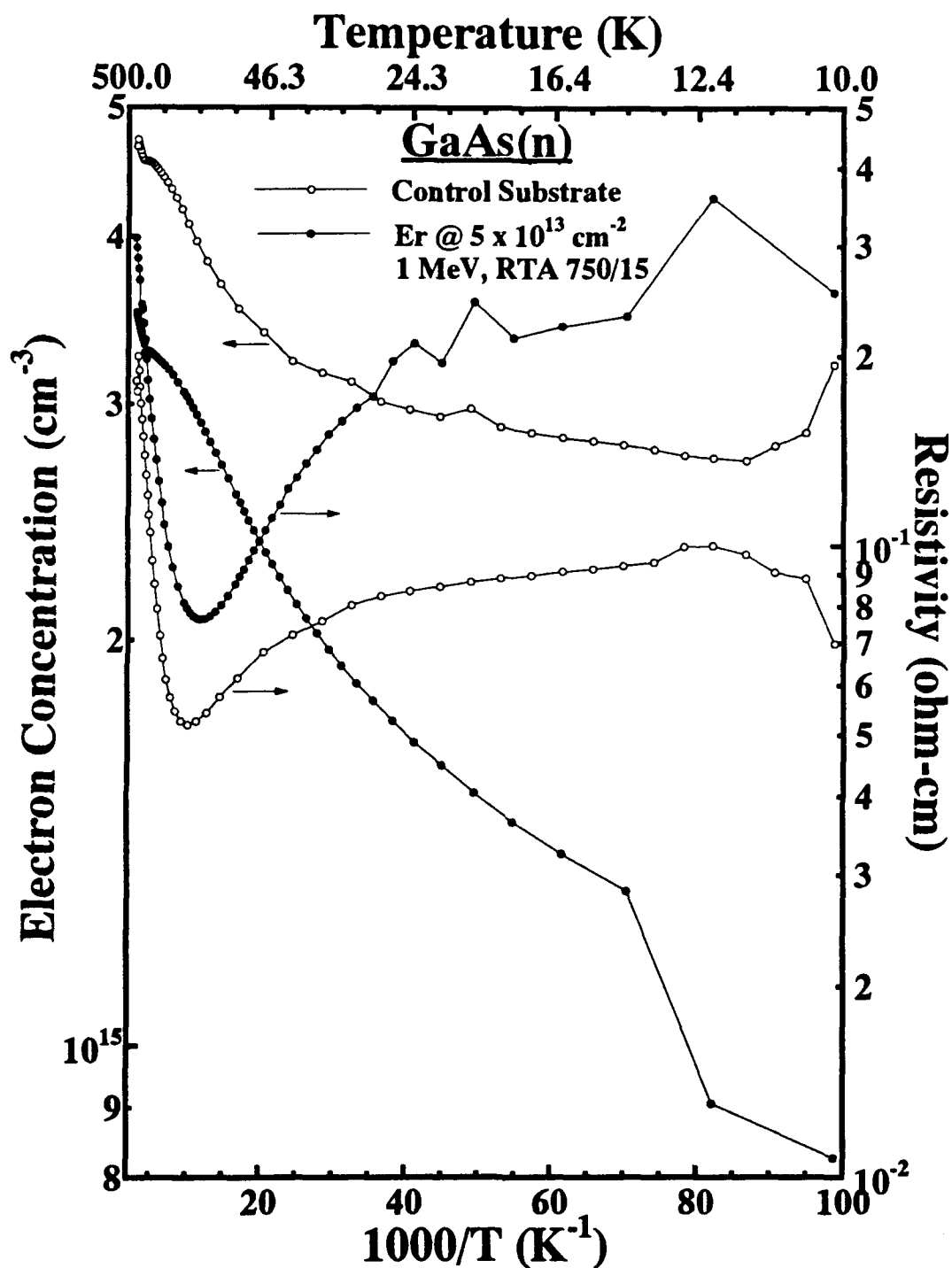


Figure 37. Temperature-dependent electron concentration and resistivity of an n-type substrate with no treatment, and the same substrate implanted with Er at a fluence of $\Phi_{\text{Er}} = 5 \times 10^{13} \text{ cm}^{-2}$ and an energy of 1 MeV, and annealed at 750 °C for 15 seconds (Solid symbols represent the Er-doped sample.)

6.2.1.1 Effect of Er on $Al_xGa_{1-x}As$ Substrates Room temperature Hall effect measurements were also performed on $Al_xGa_{1-x}As$ substrates for $x = 0, 0.1, 0.2, 0.3$ and 0.4 , with Er implanted at the same three fluences discussed above, each at an energy of 1 MeV . Table 6 shows the effect of Er on the substrate after annealing at $750\text{ }^\circ\text{C}$ for 15 seconds. All substrates showed n-type conductivity even though they were reported as 'undoped' by the crystal grower (Epitronix Inc.). A representative of this company suggested that the electrical conductivity could be due to virtually any of the common shallow donors, such as Te, Sn, Ge, and Si. Therefore, the substrates were submitted for SIMS analysis, which showed Si to be the only shallow donor impurity present at concentrations large enough to give rise to the observed carrier concentration.

The results strongly indicate that the reduction in the free electron concentration was not as pronounced as in the case of n-type GaAs. In fact, for many of the measurements performed on $Al_xGa_{1-x}As$, the sample implanted with Er showed higher electron concentrations than the substrates. This characteristic possibly indicates that Er was acting as a donor in AlGaAs.

In order to explore the implant region further, p^+n diodes were formed by Mg implantation in the same substrates with a thermal anneal at $825\text{ }^\circ\text{C}$ for 12 seconds. Figure 38 shows the resulting CV profiles. The profile for the $Al_{0.1}Ga_{0.9}As:Er$ sample appears to show the same n-type carrier concentration reduction that was manifested by the GaAs substrates. However, for all other Er-implanted $Al_xGa_{1-x}As$ substrates, with $x = 0.2, 0.3$, and 0.4 , the CV profiles revealed an electron distribution which was even more uniform than that of the control sample, which was implanted only with Mg. Since the carrier concentration in the Er-implanted AlGaAs substrates increased only to the substrate value, it is likely that the Er was not necessarily acting as a donor, but instead was reducing or compensating for defects associated with the implantation damage and annealing treatment. This effect occurred only for $x \geq 0.2$ (the Al mole fraction where the Si donor begins to depart from the Γ band and become a deep donor).

For the semi-insulating substrates, the implanted Er did not introduce free carriers. This affect is attributed to the shallow depth of $0.5\text{ }\mu\text{m}$ that increased to a depth of $0.75\text{ }\mu\text{m}$ by diffusion during the high-temperature annealing treatment (Figure 32). Further, due to the depletion of carriers at the surface by a typical surface potential of $V_{BS} = 0.6\text{ eV}$ (18:646), any free carriers introduced within this shallow region were immobilized in surface states and were not detected

Table 6. Effect of Er-doping on $\text{Al}_x\text{Ga}_{1-x}\text{As}$ substrates as determined by room-temperature Hall effect measurements

Substrate	Er dose (cm^{-2})	ρ ($\Omega\text{-cm}$)	μ (cm^2/Vs)	N_s (cm^{-2})	n- or p-type (cm^{-3})	ΔN_s (%)
02-PR-966 $\text{Al}_{0.1}\text{Ga}_{0.9}\text{As}$ n-type undoped $t=5 \mu\text{m}$	-	0.0277	3672	3.07×10^{13}	ⁿ 6.14×10^{16}	-
"	5×10^{12}	0.0292	3641	2.94×10^{13}	5.88×10^{16}	-4.0
"	1×10^{13}	0.0323	3248	2.98×10^{13}	5.96×10^{16}	-2.9
"	5×10^{13}	0.0430	2149	3.38×10^{13}	6.77×10^{16}	10.2
02-PR-895 $\text{Al}_{0.2}\text{Ga}_{0.8}\text{As}$ n-type undoped $t=5.5 \mu\text{m}$	-	0.0195	2311	7.62×10^{13}	ⁿ 1.38×10^{17}	-
"	5×10^{12}	0.0219	2286	6.86×10^{13}	1.25×10^{17}	-9.9
"	1×10^{13}	0.0230	2261	6.60×10^{13}	1.20×10^{17}	-13.3
"	5×10^{13}	0.0226	2165	7.03×10^{13}	1.28×10^{17}	-7.7
02-PR-1034 $\text{Al}_{0.3}\text{Ga}_{0.7}\text{As}$ n-type undoped $t=5 \mu\text{m}$	-	0.0334	2350	3.98×10^{13}	ⁿ 7.96×10^{16}	-
"	5×10^{12}	0.0369	2093	4.05×10^{13}	8.10×10^{16}	1.7
"	1×10^{13}	0.0350	2239	4.38×10^{13}	8.76×10^{16}	10.1
"	5×10^{13}	0.0309	2219	4.55×10^{13}	9.10×10^{16}	14.4
02-PR-1037 $\text{Al}_{0.5}\text{Ga}_{0.5}\text{As}$ n-type undoped $t=5.5 \mu\text{m}$	-	0.0927	2219	1.65×10^{13}	ⁿ 3.00×10^{16}	-
"	5×10^{12}	0.0981	2205	1.59×10^{13}	2.89×10^{16}	-3.0
"	1×10^{13}	0.116	1698	1.74×10^{13}	3.17×10^{16}	5.8
"	5×10^{13}	0.105	1964	1.66×10^{13}	3.02×10^{16}	0.8

by the Hall effect measurements. The free surface depletion depth, l_s , is given by (18:646)

$$l_s = \left[\frac{2\epsilon\epsilon_0(V_{BS} - kT/q)}{q(N_D - N_A)} \right], \quad (70)$$

where N_D and N_A are the concentrations of donor or acceptor impurities, respectively. This equation can be used to calculate the minimum carrier concentration the Er implant must induce

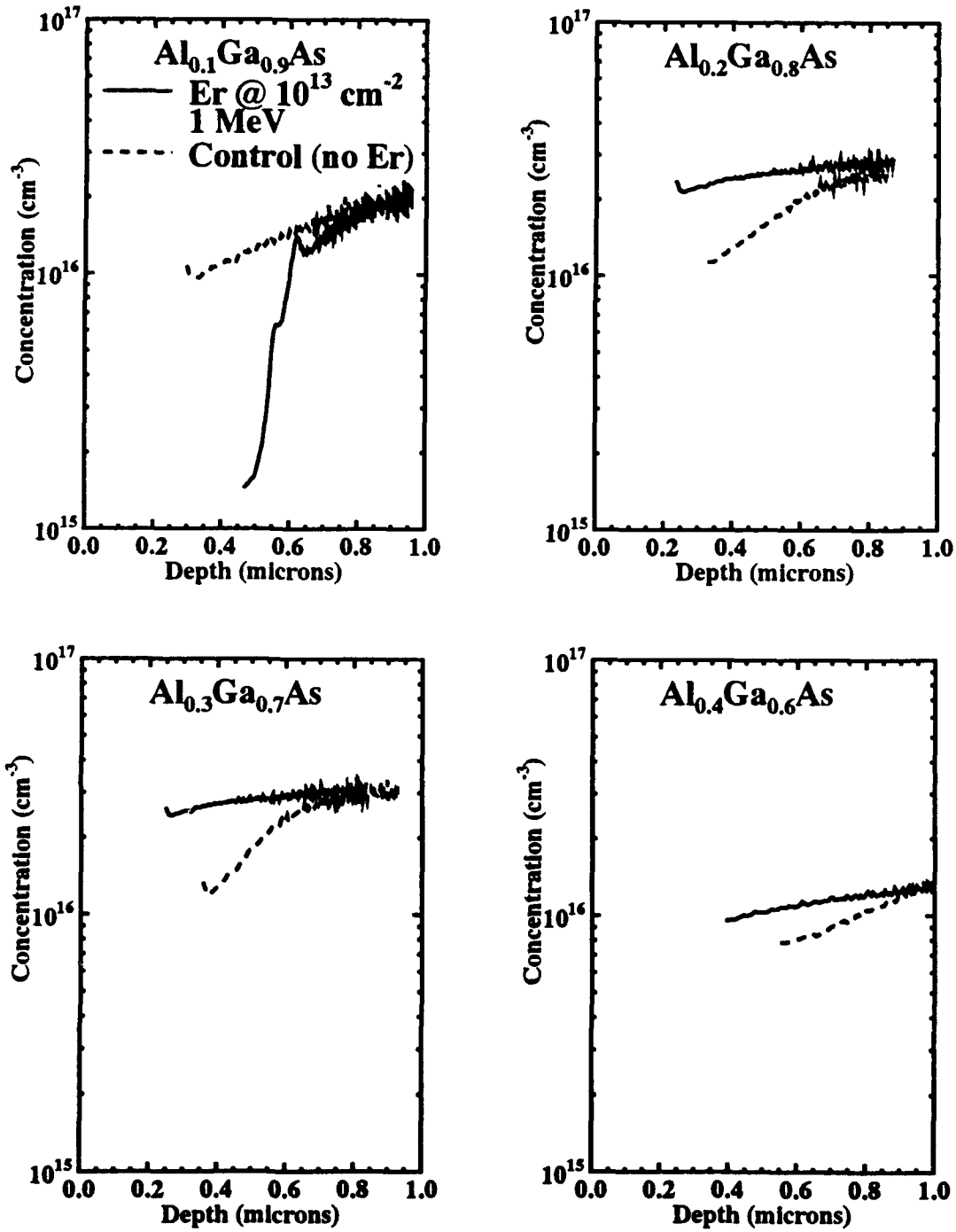


Figure 38. CV profiles of p⁺n diodes showing the effect of Er on the n-type carriers in AlGaAs, with Al mole fraction $x = 0.1, 0.2, 0.3$, and 0.4 , and with Er implanted at a fluence of $\Phi_{\text{Er}} = 10^{13} \text{ cm}^{-2}$ at an energy of 1 MeV (The dashed lines represent the carrier concentration in the control sample and the solid lines give the carrier concentration in the Er-implanted sample)

to be detected. Taking $l_s = 0.15 \mu\text{m}$, which corresponds roughly to the maximum of the implant depth, and $V_{BS} = 0.6 \text{ eV}$, the implant must give rise to roughly $4 \times 10^{16} \text{ cm}^{-3}$ carriers. Since the Er may give rise to deeper acceptors or donors which are not fully ionized at room temperature, it becomes difficult to observe any induced carriers in the Er-implanted material. Thus, the optimal sample structures for Hall effect measurements are thick, uniformly-doped layers of GaAs:Er. These structures may be attained by the Molecular Beam Epitaxy (MBE) growth technique.

6.2.2 Er-Doped, MBE-Grown GaAs and AlGaAs A variety of Er-doped samples were grown by Molecular Beam Epitaxy (MBE) for electrical and optical characterization (29). Initial studies revealed that the Er-related $1.54 \mu\text{m}$ emissions were much stronger in the Er-doped $\text{Al}_x\text{Ga}_{1-x}\text{As}$ substrates compared to the GaAs substrates. Figure 39 shows the Er PL for MBE-grown GaAs:Er, $\text{Al}_{0.33}\text{Ga}_{0.67}\text{As}$, and $\text{Al}_{0.5}\text{Ga}_{0.5}\text{As}$ doped with $[\text{Er}] = 6 \times 10^{18} \text{ cm}^{-3}$, $6 \times 10^{18} \text{ cm}^{-3}$, $1.5 \times 10^{19} \text{ cm}^{-3}$, respectively. Since MBE-grown $\text{Al}_x\text{Ga}_{1-x}\text{As}$:Er produced more intense Er-4f emissions than GaAs:Er, growth of $\text{Al}_x\text{Ga}_{1-x}\text{As}$:Er was preferred over GaAs:Er. Thus, a substrate temperature growth study as well as an Er concentration study were performed on AlGaAs, but not on GaAs. However Er-doped GaAs samples were grown with various Er concentrations, and they were additionally co-doped with Si donors and Be acceptors. The actual chronological sequence of the MBE growths is reflected in the sample number, beginning with x005.

The Er effusion cell was calibrated by SIMS measurements, as shown previously in Figure 27, by growing the Er-doped layers at a low substrate temperature of 300°C to assure that all the Er atoms incident on the surface were actually incorporated. A structure was then grown with Er doped in a square wave structure at substrate temperatures, T_s , ranging from 660°C to 500°C , in order to determine incorporation efficiency and to assess the effect of diffusion during growth. The SIMS measurements shown in Figure 40 demonstrate that the Er concentration was independent of T_s in this range, and it was approximately equal to the value from the Er-vapor pressure data (29:870), indicating a 100% Er-incorporation efficiency for $T_s < 660^\circ\text{C}$. The steepness of the $[\text{Er}]$ profile between the GaAs:Er and GaAs layers was reduced at high T_s values, suggesting a thermally activated diffusion mechanism. (The first Er-doped layer nearest to the substrate was $\text{Al}_{0.5}\text{Ga}_{0.5}\text{As}$.) Figure 40 clearly shows that the diffusion was greater in this material.

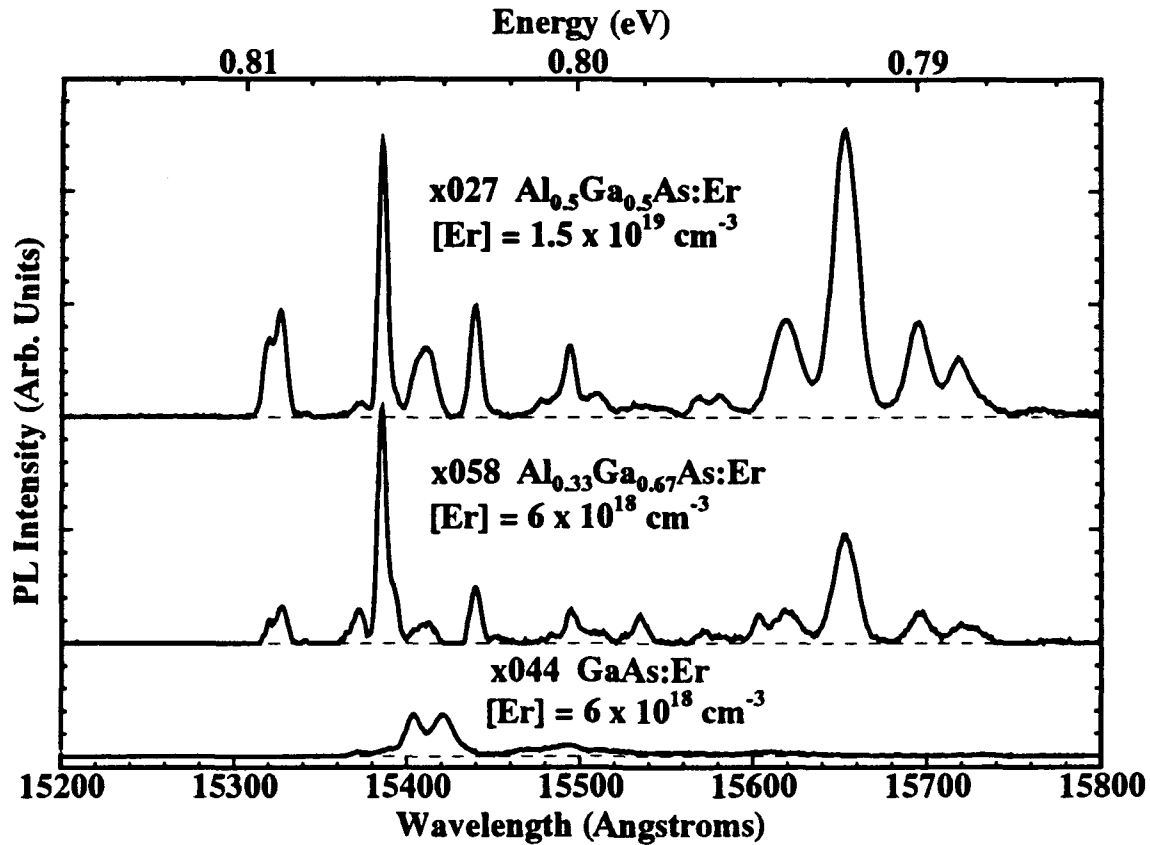


Figure 39. PL measurements of sample x044 GaAs:Er, x058 Al_{0.33}Ga_{0.67}As:Er, and x027 Al_{0.5}Ga_{0.5}As:Er with a nominal Er-doping of $[Er] = 6 \times 10^{18} \text{ cm}^{-3}$, $6 \times 10^{18} \text{ cm}^{-3}$, and $1.5 \times 10^{19} \text{ cm}^{-3}$, respectively

After growth of 200 nm of GaAs:Er at 500 °C, T_g as ramped to 300 °C as the GaAs:Er growth continued. The presence of the spike in $[Er]$ implies that Er migrated to the surface during growth, and finally, it was completely incorporated upon reducing T_g from 500 to 300 °C. Integration of the spike gives approximately $1.4 \times 10^{14} \text{ cm}^{-2}$, which translates to an average separation of approximately 85 Å between Er atoms on the surface. With such a high Er surface concentration, it is highly probably that any incident species will encounter an Er atom during growth and possibly incorporate it as a complex. In fact, Er may form different centers in GaAs and in AlGaAs grown by MBE when compared to the result obtained with Er implantation, by virtue of this growth mode, and further, the electrical and optical characteristics may be quite different for materials prepared by these two techniques.

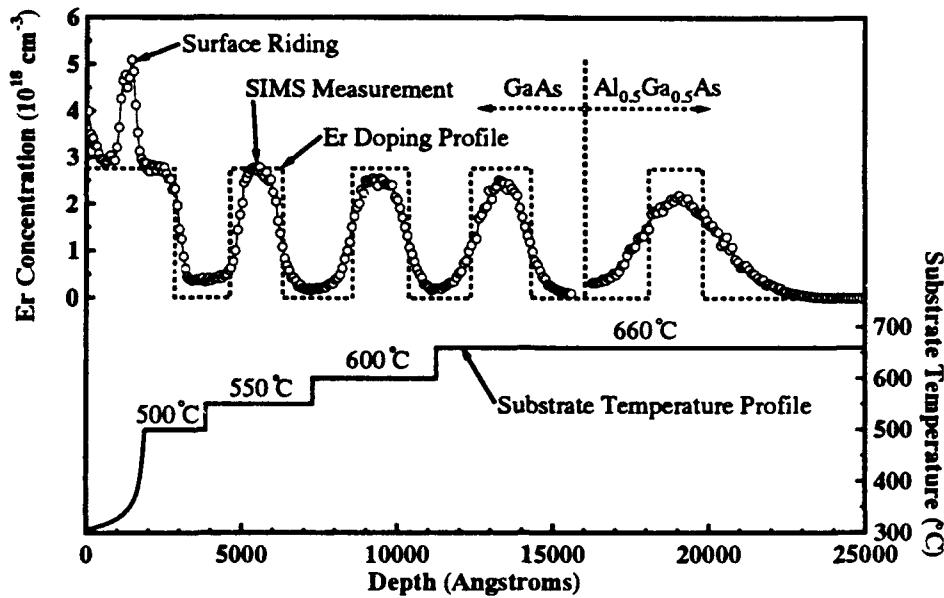


Figure 40. Effect of the GaAs substrate temperature on the Er-incorporation efficiency as well as Er diffusion and “surface riding” during the MBE growth of GaAs:Er with $[Er] \approx 3 \times 10^{18} \text{ cm}^{-3}$

Table 7 shows the results of the Hall effect measurements on a sequence of Er-doped GaAs samples with an Er concentration of approximately $6 \times 10^{18} \text{ cm}^{-3}$ grown on SI substrates with different orientations, each with Er-doped layers $1.5 \mu\text{m}$ thick. These samples consistently showed a p-type conductivity with hole concentrations in the mid-to-low 10^{16} cm^{-3} range. Temperature-dependent Hall effect measurements were performed on sample x0452d, and the results are presented in Figure 41. The free hole concentration was least-squares fitted to equation (11) for a single acceptor level, yielding an acceptor concentration of $N_A = 1.0 \times 10^{17} \text{ cm}^{-3}$, a net donor concentration of $N_D^{\text{net}} = 3.0 \times 10^{16} \text{ cm}^{-3}$, and an activation energy of $E_A = 98.3 \text{ meV}$, as well as a degeneracy ratio of $\frac{g_A}{g_{AO}} e^{\alpha_0} = 0.5$. At first, this result was very promising, since the Er occupying an As site is expected to act as a double acceptor. Similarly, using a self-consistent X- α scattered wave calculation, Hemstreet predicted that Yb on an In site in InP could introduce a single acceptor level at approximately 260 meV above the valence band. However, it is also possible that this conductivity was generated by contamination from the MBE apparatus or source materials. Common contaminants from the MBE consist of CO and CO₂ from the effusion cells, or possibly H₂O or other contaminants on the stainless steel frame, as

Table 7. GaAs:Er layers grown by MBE on different substrate orientations which consistently show p-type conductivity (This p-type conductivity is due to Mn contamination in the Er source.)

Substrate	Er concentration (cm ⁻³)	ρ (Ω -cm)	μ (cm ² /Vs)	N_a (cm ⁻²)	n or p-type (cm ⁻³)
x044 <100> GaAs:Er t=1.5 μ m	6×10^{18}	2.26	202.8	2.04×10^{12}	^p 1.36×10^{16}
x044 <211> GaAs:Er t=1.5 μ m	6×10^{18}	1955	73.38	6.54×10^9	^p 4.36×10^{13}
x044 <111> GaAs:Er t=1.5 μ m	6×10^{18}	1.625	199.8	4.70×10^{12}	^p 3.13×10^{16}
x045 <100> GaAs:Er t=1.5 μ m	6×10^{18}	0.703	213.9	6.23×10^{12}	^p 4.15×10^{16}
x045 <100> GaAs:Er t=1.5 μ m	6×10^{18}	0.703	213.9	6.23×10^{12}	^p 4.15×10^{16}
x045 6°<100> 111B GaAs:Er t=1.5 μ m	6×10^{18}	0.788	174.4	6.83×10^{12}	^p 4.55×10^{16}
x045 2°<100> 111B GaAs:Er t=1.5 μ m	6×10^{18}	0.614	250.9	6.09×10^{12}	^p 4.06×10^{16}
x045 6°<100> 1111 GaAs:Er t=1.5 μ m	6×10^{18}	0.646	245.5	5.85×10^{12}	^p 3.9×10^{16}

well as any contaminants in the Ga, As, or Er solid sources. The observation that the growth of undoped pure GaAs yielded only semi-insulating layers eliminated all possible sources of contamination except for the Er source. Table 8 is a list of contaminants in the source provided by the supplier. From Figure 3, the energy level 98.3 meV listed above is close to that reported for the manganese (Mn) acceptor. Ilegems et al. (41:3060) have performed temperature-dependent Hall effect measurements on GaAs doped with Mn by MBE, and they have found that Mn acts as a single acceptor with an activation energy of 97 meV. In addition, they have correlated a deep luminescence band at 113 meV below the band edge with the presence of this acceptor.

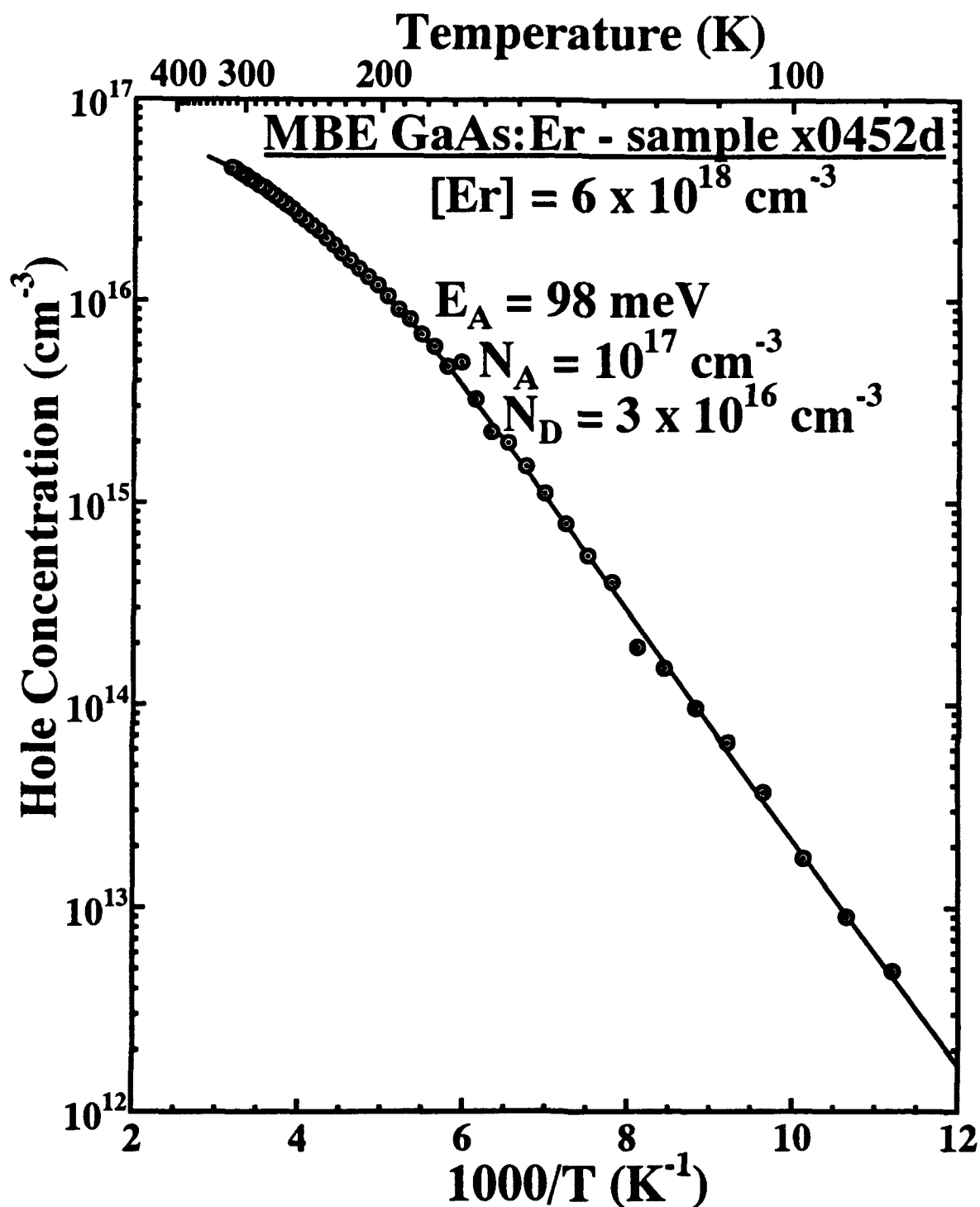


Figure 41. Temperature-dependent Hall effect measurements on the MBE-grown, Er-doped GaAs samples x045 2°<100> 111B and x0452d (Room-temperature measurements are given in Table 7.)

Table 8. Metallic contaminants in the MBE Er source in parts-per-million (ppm) as measured by the supplier, Rare Earth Products, using X-ray fluorescence spectrometry

Contaminant	Concentration (ppm)
Aluminium	50
Calcium	4
Copper	20
Iron	7
Manganese	15

This band, has four distinctive distinct peaks at 1.406 eV, 1.396 eV, 1.372 eV, and 1.340 eV (41:3061), which are due to the recombination of a conduction-band electron with a hole bound at the Mn acceptor, the corresponding transverse acoustic phonon replica, and the two longitudinal optical phonon replicas, respectively. Figure 42 shows the band edge and the deep 113 meV band occurring in MBE sample x051, which exhibits the peaks observed by Ilegemes. In addition, SIMS measurements performed on a sample with this room temperature p-type conductivity have revealed a Mn concentration of approximately $8.6 \times 10^{16} \text{ cm}^{-3}$, which agrees with the Hall Effect measurements. Thus, the p-type conductivity exhibited by some of the MBE-grown GaAs samples is almost certainly due to Mn contamination from the MBE source. Shortly after the p-type conductivity appeared in the Er-doped MBE-grown samples, the Er-related PL at $1.54 \mu\text{m}$ disappeared, and this characteristic was found by SIMS measurements to be due to the absence of Er in the sample (i.e., source depletion). After the source was replenished and the $1.54 \mu\text{m}$ emissions returned, Mn-related emissions were no longer observed, as seen in Figure 42 for MBE sample x102, consisting of $1 \mu\text{m}$ of GaAs:Er with $[\text{Er}] = 1.3 \times 10^{18} \text{ cm}^{-3}$. In addition, sample x102 clearly shows the sharp Er-related $1.54 \mu\text{m}$ emissions. Therefore, it appears that Mn contamination should not normally be a problem during MBE growth since Mn contamination occurs when the Er is depleted and only contaminants remain.

Further MBE-grown, Er-doped GaAs samples did, however, show p-type behavior. Sample x105, $1 \mu\text{m}$ of GaAs:Er with $[\text{Er}] = 1.3 \times 10^{18} \text{ cm}^{-3}$, had a room-temperature hole concentration of $3.4 \times 10^{13} \text{ cm}^{-3}$. The temperature-dependent hole concentration, as measured by Hall effect measurements, is shown in Figure 43. The temperature-dependent hole concentration for the

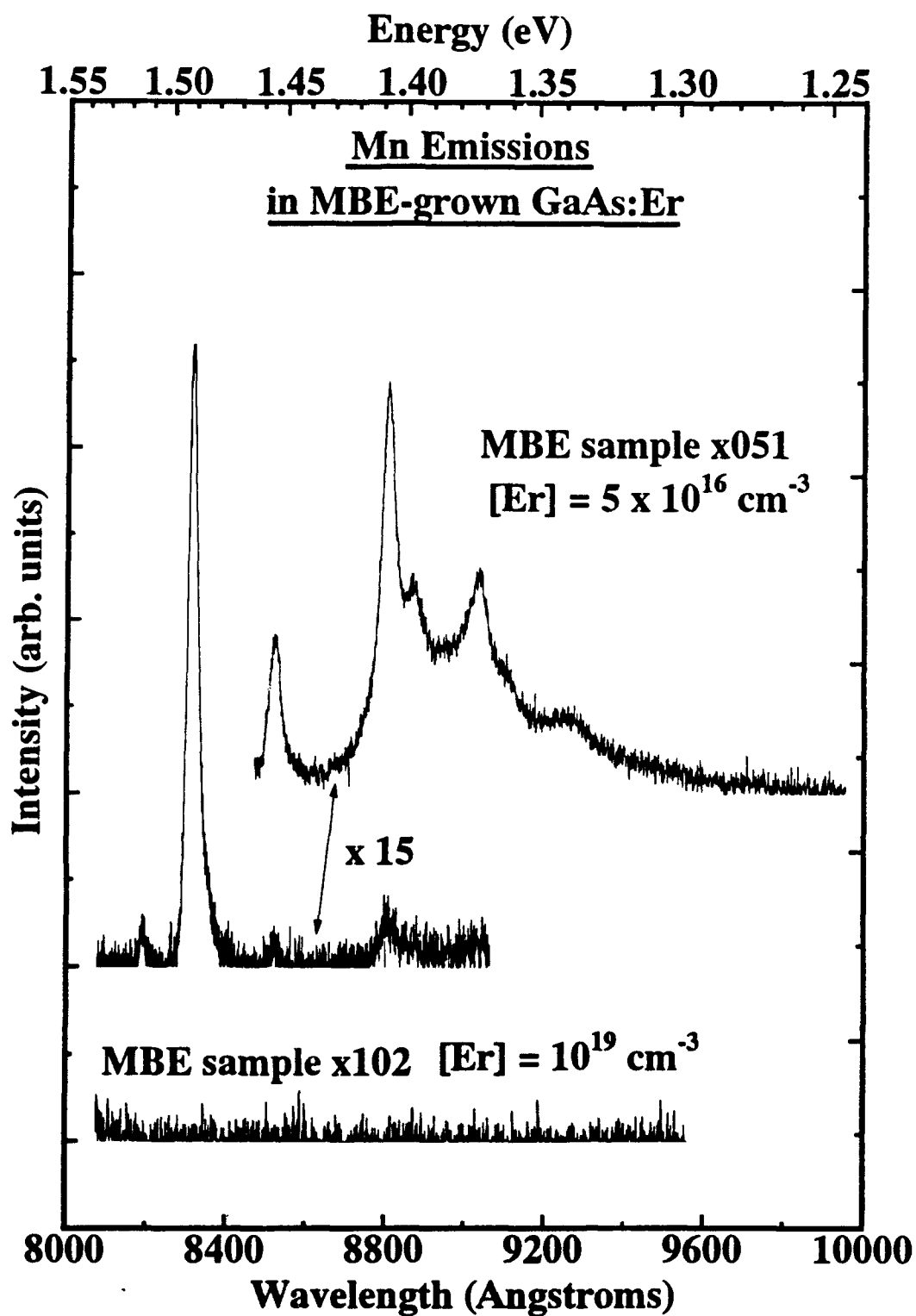


Figure 42. Band-edge luminescence of GaAs:Er samples (Sample x051 shows the presence of Mn-related donor-acceptor and conduction-band-acceptor recombination. Sample x102, which shows no Mn emissions, was grown after the Er source was replenished.)

sample x0452d is repeated to show that there is indeed a different center giving rise to this p-type behavior. Analysis of the data yields an activation energy for this much deeper center of $E_A = 340 \pm 15$ meV. Unfortunately, the concentration of this center cannot be determined from the Hall effect measurements, since the concentration must begin to level-off at higher temperatures before the fitting routine can extract this parameter. In fact, of all the parameters for the single acceptor fit, only the activation energy can be determined.

Overall, implantation of Er into n-type $\text{Al}_x\text{Ga}_{1-x}\text{As}$ substrates with $x \geq 0.2$ has little effect on the carrier concentrations. For MBE-grown, Er-doped AlGaAs layers, a much higher concentration of Er can be incorporated into the AlGaAs than with ion implantation. A sequence of $\text{Al}_{0.5}\text{Ga}_{0.5}\text{As}$ structures with varying Er concentrations was grown as shown in Figure 9. Table 10 summarizes the electrical properties of the MBE-grown $\text{Al}_{0.5}\text{Ga}_{0.5}\text{As}$ layer co-doped with Si at $2 \times 10^{18} \text{ cm}^{-3}$ and with Er at varying concentrations. For the MBE material, Er tends to make the material semi-insulating, as in the case of the ion-implanted GaAs layer. Similarly, the same AlGaAs:Er layers without Si co-doping were semi-insulating, indicating that for the $\text{Al}_{0.5}\text{Ga}_{0.5}\text{As}$ samples, the 340 meV level observed in the GaAs:Er layer, referred to above, has either moved into the bands, or it has moved deeper into the band gap, where it is not contributing carriers at room temperature.

6.2.3 Summary and Discussion The distribution of Er atoms in ion-implanted GaAs was close to that predicted by the LSS theory. However, for both the high and low fluences used in the ion-implantation study, the Er shows a longer tail than that predicted by the LSS theory. This is due either to ion channelling or to inadequacies in predicting the stopping power for such heavy ions. Additionally, the SIMS measurements showed measurable diffusion of the as-implanted distribution during the RTA anneals at both 750 and 850 °C for 15 seconds. However, this diffusion was less than would be expected for conventional oven anneals (12:990). Zhao (109:278) measured the diffusion of Er in GaAs at 600 °C and found a thermally-activated diffusion dependency, $D = D_0 \exp(-\Delta E/kT)$, with $D_0 = 5.0 \times 10^{-14} \text{ cm}^2/\text{sec}$ and $\Delta E = 0.3 \text{ eV}$. The activation energy of the diffusion coefficient was similar to that of copper in GaAs, suggesting that interstitial type diffusion dominates. However, the pre-exponential factor for Cu gives it a much larger absolute diffusion constant. Since the Er^{3+} ion has a radius of 0.88 Å, and the Cu^{2+} ion has a radius of 0.92 Å, the Er atom probably diffuses interstitially in the 3+ oxidation state.

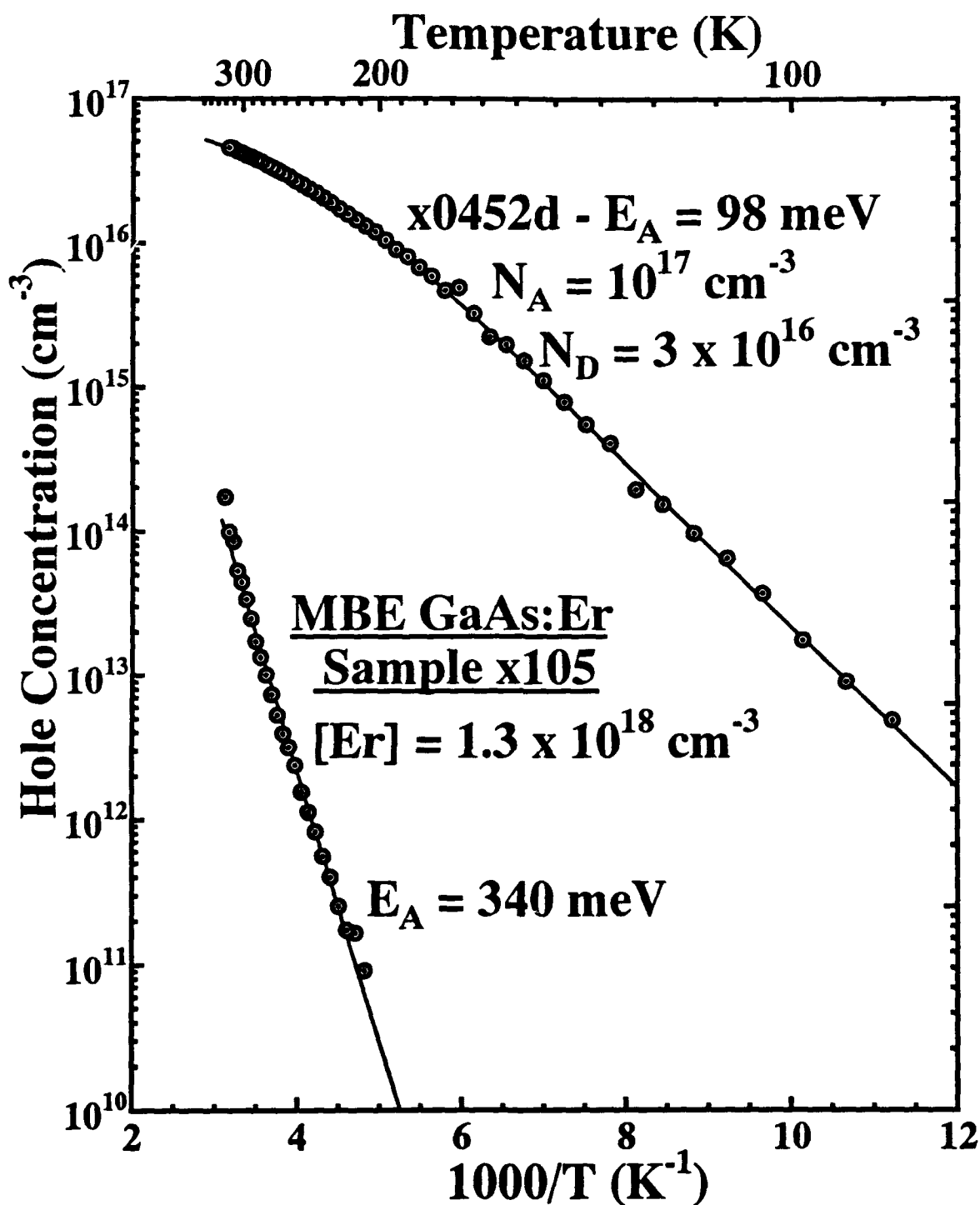


Figure 43. Temperature-dependent Hall effect measurements of the MBE-grown GaAs sample x105 grown after the Er cell was replenished (The measurements for samples x0452d and x045 2° <100> 111B are repeated to demonstrate that the p-type conductivity in x105 is related to a much deeper center.)

Table 9. Sample structures grown for the Er concentration study

$1\mu\text{m of Al}_{0.5}\text{Ga}_{0.5}\text{As:Er}$ $[\text{Er}] = 1.7 \times 10^{17}, 2.7 \times 10^{18}, 1.5 \times 10^{19}, 4.6 \times 10^{19}, 2 \times 10^{20}\text{cm}^{-3}$ $[\text{Si}] = 2 \times 10^{18}\text{cm}^{-3}$
$1\mu\text{m of Al}_{0.5}\text{Ga}_{0.5}\text{As:Er}$ $[\text{Er}] = 1.7 \times 10^{17}, 2.7 \times 10^{18}, 1.5 \times 10^{19}, 4.6 \times 10^{19}, 2 \times 10^{20}\text{cm}^{-3}$
SI-GaAs substrate

Table 10. Room-temperature Hall effect measurements on MBE-grown $\text{Al}_{0.5}\text{Ga}_{0.5}\text{As:}(\text{Er}+\text{Si})$ with $[\text{Si}] = 2 \times 10^{18}\text{cm}^{-3}$, and various Er concentrations

Substrate	Er concentration (cm^{-3})	ρ ($\Omega\text{-cm}$)	μ (cm^2/Vs)	N_s (cm^{-2})	n or p-type (cm^{-3})
x025 t=1 μm	2×10^{20}	6144	5985	3.4×10^7	ⁿ 1.7×10^{11}
x026 t=1 μm	4.6×10^{19}	5.97×10^4	3614	5.8×10^6	ⁿ 2.9×10^{10}
x027 t=1 μm	1.5×10^{19}	7.53	68.93	2.41×10^{12}	ⁿ 1.21×10^{16}
x028 t=1 μm	2.7×10^{18}	2.07	98.68	6.11×10^{12}	ⁿ 3.05×10^{16}
x028 t=1 μm	1.7×10^{17}	1.44	114.3	7.57×10^{12}	ⁿ 3.78×10^{16}

Although the Er-diffusion has not been quantified, Figure 32 shows that the Er implant diffuses more or less uniformly towards the surface and towards the substrate, also indicating interstitial diffusion. If vacancy-related diffusion were dominating, the implant would preferentially diffuse towards the surface, since, in this region, there is more implantation damage. Pomrenke measured the distributions of Pr, Er, Tm, and Yb in as-implanted InP and, after a conventional furnace annealing at 750 °C for 10 minutes (69:199, 155, 178, 137), he found that Pr, Er, and Th preferentially diffused towards the surface with a decreasing tendency (magnitude decreasing in this order), while Yb diffused into the substrate. Considering the rare earth contraction with

increasing atomic number, as illustrated in Table 4, this seems to indicate that for REs of larger ionic radii, vacancy-related diffusion is more likely.

Minor diffusion was also observed in Er-doped GaAs layers grown by MBE, as shown in Figure 40. Diffusion of the Er^{3+} ion was enhanced in AlGaAs as compared to GaAs, which was expected, since the lattice constant is slightly larger in AlGaAs as compared to GaAs.

Additionally, SIMS measurements performed on the Er-doped GaAs substrates show that all of the Er incident on the surface was incorporated, independent of the substrate's temperature(29). This behavior has recently been independently verified by Poole et al. (72:123). In addition, SIMS measurements also revealed that a relatively large amount of Er migrated to the surface during growth at temperatures above 500 °C, indicating that Er may form complexes with any incident species, such as Si donors, or possibly with other Er atoms. Poole(72) recently revealed by Transmission Electron Microscopy (TEM) that Er in MBE GaAs at 580 °C essentially has a solubility limit of $[\text{Er}] = 7 \times 10^{17} \text{ cm}^{-3}$. Above this concentration, Er was incorporated primarily as nearly spherical micro-precipitates which possess a cubic (NaCl) structure. This observation is consistent with the chemical composition of ErAs.

Er implanted into semi-insulating GaAs substrates seems to leave the material semi-insulating, at least for annealing using the RTA technique with temperatures in the 750 to 825 °C range with an annealing time of 15 seconds. Again, the failure to detect any change in electrical conductivity may be related to the effect of surface and interface depletion. However, in the case of MBE samples, where thick, uniformly-doped layer growth is possible, this is not expected to be a significant complication. For GaAs:Er layers otherwise undoped, the introduction of Er at a concentration of $[\text{Er}] = 1.3 \times 10^{18} \text{ cm}^{-3}$ results in p-type conductivity which arises from an acceptor level with $E_A = 340 \text{ meV}$. MBE-grown GaAs samples with lesser Er doping did not show this center. It was not possible to determine the concentration of this center. However, at room temperature, it gave rise to a hole concentration of only $3.4 \times 10^{13} \text{ cm}^{-3}$, which would be difficult to detect in the ion-implanted material. Therefore, this center may also occur in the implanted material. Other shallow acceptor behavior with $E_A = 98.3 \text{ meV}$ was confirmed to be due to Mn contamination from the Er source.

In the Er-implanted n-type substrates, the introduction of Er significantly reduced the electron concentration in the region of the implant. The same effect was also observed in

MBE-grown GaAs:Er co-doped with Si. There are several possible causes for this effect:

- a. In both materials, the Er may have formed neutral complexes with donor atoms since REs tend to getter shallow donors, as discussed in section 5.3.3.
- b. In both materials, the 340 meV acceptor center observed in the MBE material may have acted as compensating center.
- c. In both materials, there may have been other deep Er-related compensating centers that were so deep that they could not readily be detected by temperature-dependent or room-temperature Hall effect measurements.
- d. The carrier reduction in the ion-implanted material may have been caused by compensation from damage-related centers which were still present after the anneal.
- e. Finally, in the MBE-grown material, the effect may also have been due to the introduction of deep centers as a result of the formation of micro-precipitates of ErAs.

There have been many reports on the gettering effect or removal of shallow donors by REs in III-V semiconductors. Bagraev first reported this effect for LPE-grown Yb and Gd-doped InP and InGaAs (3). Other researchers have observed drastic reductions in the free electron concentration (108; 7; 102) and donor-related, band-edge emissions, such as, donor-acceptor pairs and donor bound excitons (6; 74). The last two references were reports on donor gettering by Yb and Er, respectively, in GaAs. However, all of these reports have been for RE's doped into the semiconductor during LPE or bulk Czochralski growth, and there has been no report of this behavior in ion-implanted or MBE-grown material.

According to Masterov (62:386), in a recent review of rare earth elements in III-V semiconductors, the actual purification mechanism is not well understood. Some researchers have attributed the purification to chemical reactions of the rare earths with accidental impurities in the liquid phase, with the resultant compounds remaining in the flux and not entering the solid phase. Others have hypothesized that the complexes formed from rare earths and nonmetal impurities are incorporated into the growing crystal or epitaxial film, and are electrically neutral. Masterov cites several Soviet reports (5; 35; 7) which support the former position. For instance, Baranskii (7) measured the electrophysical properties of GaP:Yb epitaxial films and found that the Hall mobility versus temperature, $\mu(T)$, remains substantially unaffected relative to the undoped substrate, indicating that the impurity complexes are not captured by the epitaxial films. However,

others support the latter position. For instance, a comparison of the mobilities of electrons in GaAs:(Yb+Sc) films led Voronina (96) to conclude that there were microinclusions of rare earths and other nonmetals formed in these RE-doped samples. Finally, Zakharenkov (108) examined the purification effectiveness of various REs in InP, concluding that, due to the rare earth contraction, the best elements for purification are those at the end of the series. For example, a Yb atom can either fit nicely on the cation site or can remain free to form a complex with an impurity if present during growth. According to Masterov, either of these two views may be valid, depending upon the growth technique, rare earth elements, and compound semiconductors utilized.

In the present study, it was clear that Er ions were present in the ion-implanted material. If the Er and Si ions were forming electrically neutral complexes, then upon annealing a uniformly Si-doped substrate (implanted with Er), the Si profile would tend to redistribute itself to the Er-implant profile. To investigate this possibility, SIMS measurements were performed on GaAs substrates with a uniform Si doping of 10^{18}cm^{-3} and Er-implanted with a fluence of $\Phi_{\text{Er}} = 5 \times 10^{13}\text{cm}^{-2}$ at an energy of 1 MeV, and annealed at 850 °C for 15 seconds. There were no detectable changes in the Si profile. This measurement by itself is not conclusive since the Er is expected to diffuse faster than Si. However, the Er diffusion was approximately the same in this heavily Si-doped substrate as was observed previously in the undoped substrate shown in Figure 32. If the Er were forming complexes with the Si, then Er diffusion would be substantially inhibited. Thus, the Er and Si atoms do not appear to have formed complexes.

For further evidence supporting the above conclusion, Er-implanted, Si-doped $\text{Al}_x\text{Ga}_{1-x}\text{As}$ substrates with $x \geq 0.2$ did not exhibit a reduction in the shallow donor profiles. Unexpectedly, the CV profiles of the Er-implanted $\text{Al}_x\text{Ga}_{1-x}\text{As}$ substrates revealed a donor concentration near the region of the Er implant that was closer to the substrate value than was the case for the control substrates which had no Er implant. Once again, donor gettering is refuted, since this process is not expected to be strongly dependent on the alloy parameter. It seems more likely that the effect was related to the presence or absence of deep levels in the ion-implanted material as well as their relative positions with respect to the band edges as the alloy parameter, x , changes. Chand (17:4486), reported that the deep level referred to as the DX center in Si-doped $\text{Al}_x\text{Ga}_{1-x}\text{As}$ was due to states associated with the Si donor. For $x \leq 0.2$ the donor level followed the Γ band and remained fairly shallow. However, for $x > 0.2$, the dominant donor energy level with respect to

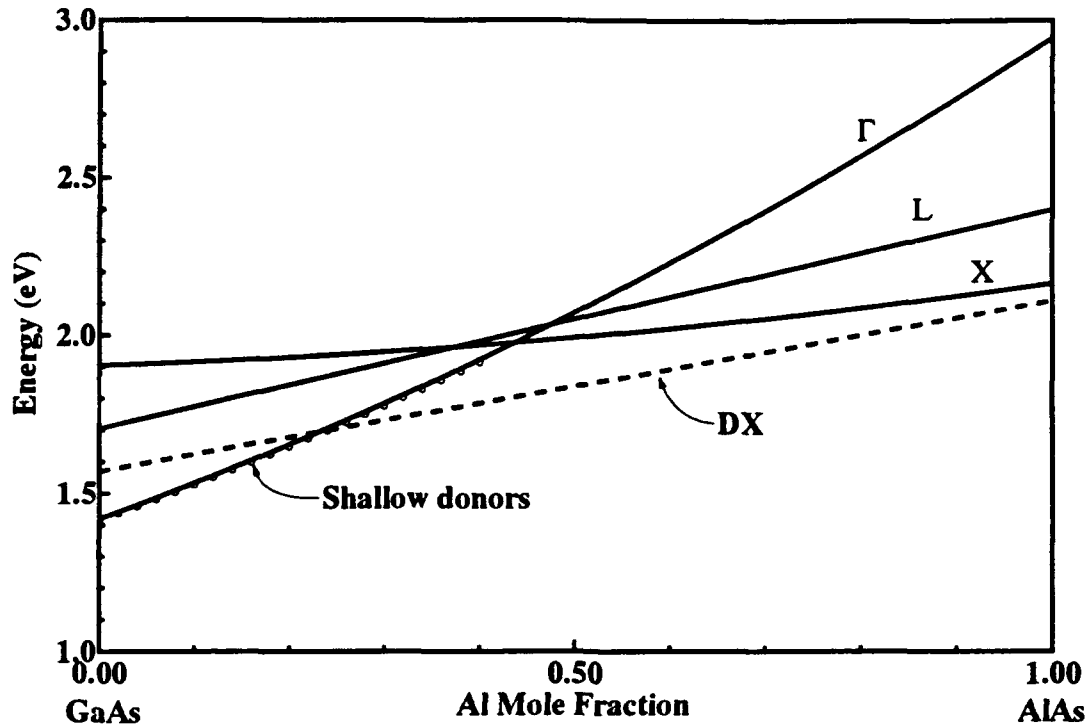


Figure 44. Variation of the Γ , L, and X conduction bands, and the dominant Si donor level, that is, the DX center, with Al mole fraction x

the valence band edge increased linearly, and it can be described by

$$E_d \approx 0.54x + 1.57 \text{ eV}. \quad (71)$$

At $x \sim 0.2$, the dominant donor level begins to follow the L band minima, indicating that for $x > 0.2$, the donor level associated with the L band minima dominates the conduction process, even though the Γ band valley is still the conduction band minimum, as shown in Figure 44. With increasing x , the donor begins to follow the X minima, and has a depth of 57 meV from this band in AlAs. The maximum depth of the DX center is 160 meV near the direct-indirect band gap crossover at $x \sim 0.48$. At this point it cannot be conclusively established that the sudden disappearance of the carrier reduction in $\text{Al}_x\text{Ga}_{1-x}\text{As:Er}$ is related to the depth of the Si donor levels. In fact, if any Er-related deep centers were responsible for the carrier reduction via compensation, the variation in their activation energies relative to the bands could also have caused this effect. However, it appears likely from this data that the Er is not forming complexes with the Si in the Er-implanted material.

With the MBE material, similar to LPE or bulk growth, there is a phase discontinuity at which growth takes place. In the present study, a large mobile concentration of Er available on the surface during growth was free to form complexes with any species arriving at the surface. As shown in Figure 9, sample x026 consisted of 2 μm thick layer of $\text{Al}_{0.5}\text{Ga}_{0.5}\text{As:Er}$ with $[\text{Er}] = 4.6 \times 10^{19} \text{cm}^{-3}$, and during growth of the top half of this structure, the Si shutter was opened and Si was co-doped at $2 \times 10^{18} \text{cm}^{-3}$. SIMS measurements on this sample revealed that there was no discontinuity in the Er-distribution at this interface. Therefore, Si does not affect the incorporation of Er. Further, Poole has observed that Er doping at various concentrations ranging from 5×10^{17} to $3 \times 10^{19} \text{cm}^{-3}$ does not affect Si incorporation at a uniform Si doping of 10^{17}cm^{-3} . No conclusions regarding whether or not Er and Si are forming complexes can be made; however, if they are in fact forming complexes, these complexes are being incorporated into the substrate. Therefore, Er and Si co-doping cannot reduce the electron concentration in the MBE material by preventing the incorporation of shallow donors.

Unlike the Er-implanted samples, co-doping of Er and Si in AlGaAs during MBE growth strongly reduces the electron concentration, as shown in Table 6. This finding is fairly consistent with the results obtained from the ion-implanted material, since the most drastic drop in electron concentration occurs for $[\text{Er}] \gtrsim 2 \times 10^{19} \text{cm}^{-3}$, and doping at this concentration was not possible by ion implantation. This effect may be due to compensation by the formation of ErAs micro-precipitates acting as deep centers and, therefore, may not be related to Er-Si complexes. The data, however, is inconclusive.

If the carrier reduction in GaAs is not caused by donor-gettering, which appears likely in the case of the ion-implanted material, it may be due to other possible causes (b-e) listed above. For instance, (b) the 340 meV acceptor level may act as a compensating center. If this level is due to an isolated Er center, it may also be found in the ion-implanted material. The proposed mechanisms (b-e) are discussed in the next section, which analyzes the results obtained by the DLTS measurements of the deep levels introduced in Er-doped GaAs either by MBE growth or ion implantation.

6.3 *Effect of Er on Deep States in GaAs and AlGaAs Obtained by DLTS Measurements*

The results discussed in the previous section were incomplete because, although the Hall

effect and CV measurements can reveal the presence of deep compensating centers, they do not always give their concentration and activation energy, and never provide the capture cross section of the electrons or holes at these centers. Thus, CV measurements, and especially the temperature-dependent Hall effect measurements, have limited applicability. First, in order to determine the concentration of the center, the level giving rise to the p-type or n-type conductivity must be fairly shallow in order to be fully ionized at reasonable temperatures (350 K). This limitation generally requires an activation energy of $\lesssim 150$ meV. For instance, Figure 43 illustrates that a full fit is possible for the Mn impurity in GaAs. However, it is only possible to obtain the activation energy for the deep center giving rise to the p-type conductivity in sample x105. Furthermore, the analysis becomes much more complicated when more than a single donor or acceptor is controlling the Fermi energy level (56).

As with any experimental technique, there are limitations involved when applying the DLTS technique. However, these limitations are much less confounding than those for the Hall effect. DLTS will yield trap concentrations, activation energies, and capture cross sections for centers located up to 1 eV from a band edge. Thus, DLTS yields significant information which is not readily attainable from Hall effect measurements.

Er-implanted n-type and p-type GaAs were measured by DLTS in order to determine whether the deep centers formed upon Er-incorporation were related to complexes with shallow donors or acceptors. The effect of the Er-incorporation on native defects, such as EL2 in GaAs and the DX center in AlGaAs, was also examined. These centers have been extensively studied, and their microscopic nature is better understood than any of the other centers in these materials. In some instances they can dominate the electrical behavior of the material. DLTS measurements were also performed on GaAs crystals doped with Er during MBE growth for several reasons. First, if this material yields the same centers as in the ion-implanted material, they can be attributed to Er-related centers as opposed to incidental centers caused by ion-implantation damage, or centers formed due to the MBE growth process. Secondly, MBE is the growth technique of choice for most current research, and it can be used to obtain a much wider range of Er-doping densities than is available with ion implantation. Additionally, substrate temperature, As₂ or As₄ flux, Ga flux or growth rate, and Er flux may be adjusted in an attempt to maximize the concentration of optically active Er centers. Finally, with the MBE technique, it is possible to grow heterostructure optoelectronic devices such as Er-doped double heterostructure lasers (95)

or the step impact electroluminescent device proposed by Lozykowski (59). Thus, by using DLTS, the basic electrical behavior of Er in MBE material can be better understood, which may be beneficial for future device applications.

6.3.1 DLTS Measurements on Ion-Implanted GaAs The one-sided junctions, p^+n or n^+p , necessary for the DLTS measurements, were formed by high-dose, low-energy Mg or Si ion implantation, respectively, into the Er-implanted substrates as described in section 4.4. Figure 45 shows the numerically-generated rate-window plots for samples with Er-implanted into the n-type GaAs substrate 02-PR-1748, with $n = 5 \times 10^{15} \text{cm}^{-3}$. The measurements are shown for all three Er fluences, as well as for the control sample, which had only the Mg implant. All samples were rapid thermal annealed at 825 °C for 12 seconds.

The rate window was formed with $t_1 = 10 \mu\text{s}$ and $t_2 = 8 t_1 = 80 \mu\text{s}$, which yielded a rate window of 29706 s^{-1} . Additionally, the normalized DLTS signal, $\Delta C/C$, where $\Delta C = C(t_1) - C(t_2)$, and $C = C(t_2) \approx C(\infty)$ is roughly the offset capacitance, since from equation (50) the trap concentration is approximately given in terms of the shallow doping density, N_S , and $\Delta C/C$,

$$N_T = -2N_S(C(0) - C(\infty))/C(\infty) \approx -2N_S\Delta C/C. \quad (72)$$

Thus, $\Delta C/C$ vs. T allows for a more direct comparison of the deep level concentration in the various samples. The measurements shown in Figure 45 were obtained with a minority carrier (hole) injection pulsing sequence of 1.5 V forward bias, followed by a reverse bias of typically 1 V. Several peaks are labelled from (a) through (k) on this plot for easy reference, and they will be referred to interchangeably as peaks or centers, since the peaks are caused by deep centers.

Figure 45 primarily exhibits positive peaks. Since the deep levels which give rise to these signals were being detected in n-type material, these positive peaks represent minority carrier traps or hole traps. The activation energy and capture cross sections for levels (a) – (k) are reported in Table 11.

The center which occurs at the lowest temperature, peak (a), has a rather small concentration of $N_T = 1.0 \times 10^{14} \text{cm}^{-3}$, and a very shallow activation energy of approximately 35 meV. Such a small activation energy is characteristic of a shallow acceptor. However, a shallow acceptor would be expected to have an even smaller capture cross section than was observed for this center

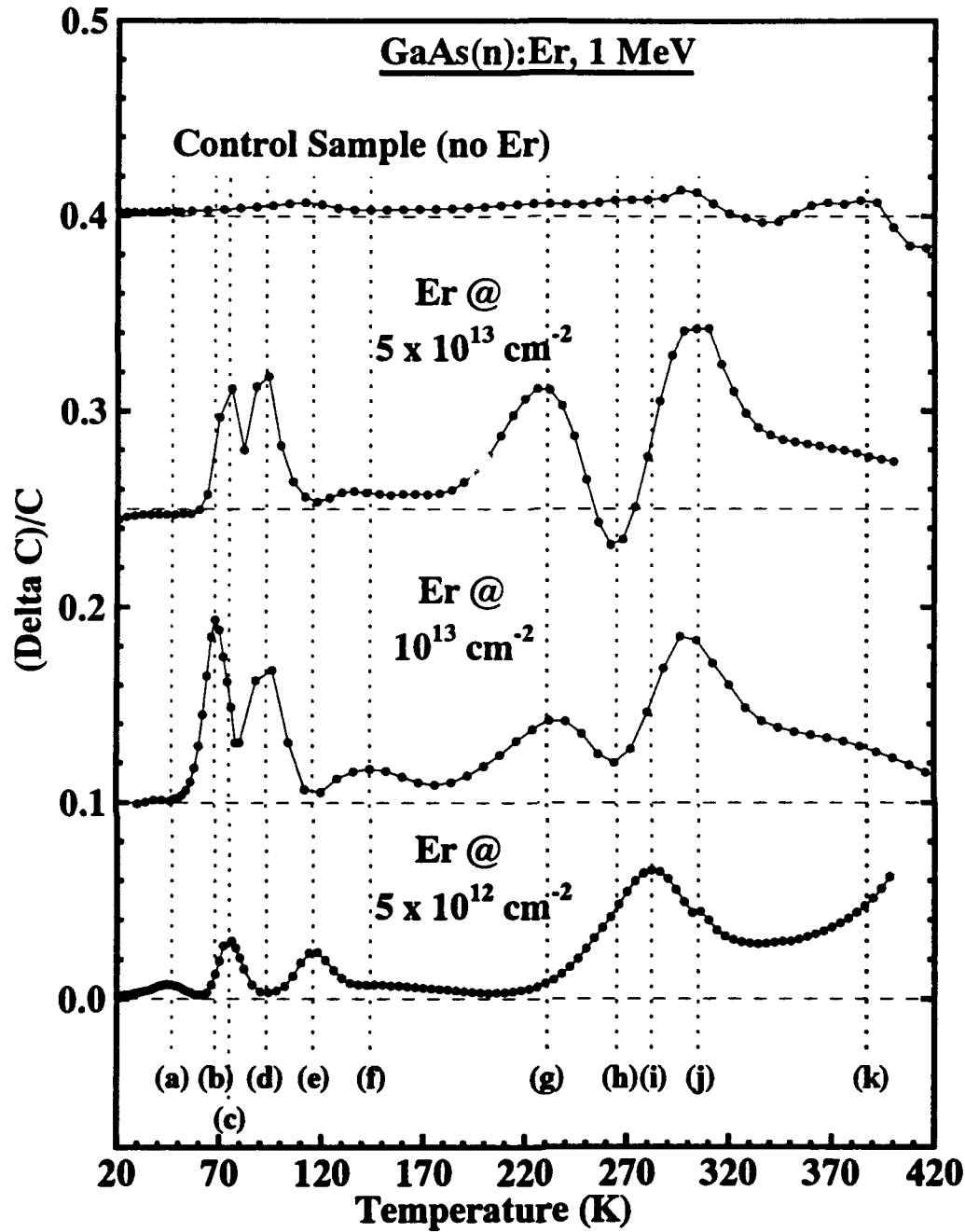


Figure 45. Rate-window plots showing the effect of the Er implants with fluences of $\Phi_{\text{Er}} = 5 \times 10^{12}$, 10^{13} , and $5 \times 10^{13} \text{ cm}^{-2}$, and an ion energy of 1 MeV on n-type GaAs substrates (All data was obtained using minority carrier injection biasing, and the various peaks are identified for discussion in the text. The rate window is 29706 s^{-1} .)

Table 11. Activation energies and thermal capture cross sections for the various centers measured in this work

Center/Peak	Activation Energy $E_T - E_v$ (meV)	Capture Cross Section (cm ²)
a	35 ± 3	3×10^{-17} $\approx 5.3 \times 10^{-17} \approx$ 9×10^{-17}
b	96 ± 3	5.8×10^{-15} $\approx 1 \times 10^{-14} \approx$ 1.8×10^{-14}
c	78 ± 10	2×10^{-17} $\approx 1.8 \times 10^{-16} \approx$ 1.5×10^{-15}
d	probably the same center as e	
e	150 ± 4	2.3×10^{-15} $\approx 3.5 \times 10^{-15} \approx$ 5×10^{-15}
f	poor fit - possibly several centers	
g	345 ± 7	6×10^{-17} $\approx 8.5 \times 10^{-17} \approx$ 1.2×10^{-16}
i	395 ± 7	1.2×10^{-15} $\approx 1.9 \times 10^{-15} \approx$ 2.8×10^{-15}
j	447 ± 4	1.8×10^{-15} $\approx 2.2 \times 10^{-15} \approx$ 2.8×10^{-15}
k	540 ± 8	5.3×10^{-16} $\approx 7.7 \times 10^{-16} \approx$ 1.1×10^{-15}

with $\sigma_p = 5 \times 10^{-17} \text{cm}^{-2}$. This level was only observed in the lowest dose of the implants, and it was not observed in the control sample. This information implies that the formation of this center was due to the introduction of Er, and that it may possibly be inhibited by implantation damage, since more implantation damage occurred with the two higher doses.

The remaining peaks in the low temperature region of the spectra, (b-f), seem to shift among the various samples. For peaks (b) and (c) in the sample implanted with Er at a fluence of $\Phi_{\text{Er}} = 5 \times 10^{12} \text{cm}^{-2}$, peak (c) at $T \approx 75 \text{ K}$ is dominant. However, in the sample implanted with Er at a fluence of $\Phi_{\text{Er}} = 10^{13} \text{cm}^{-2}$, peak (b) at $T \approx 68 \text{ K}$ is dominant, although on

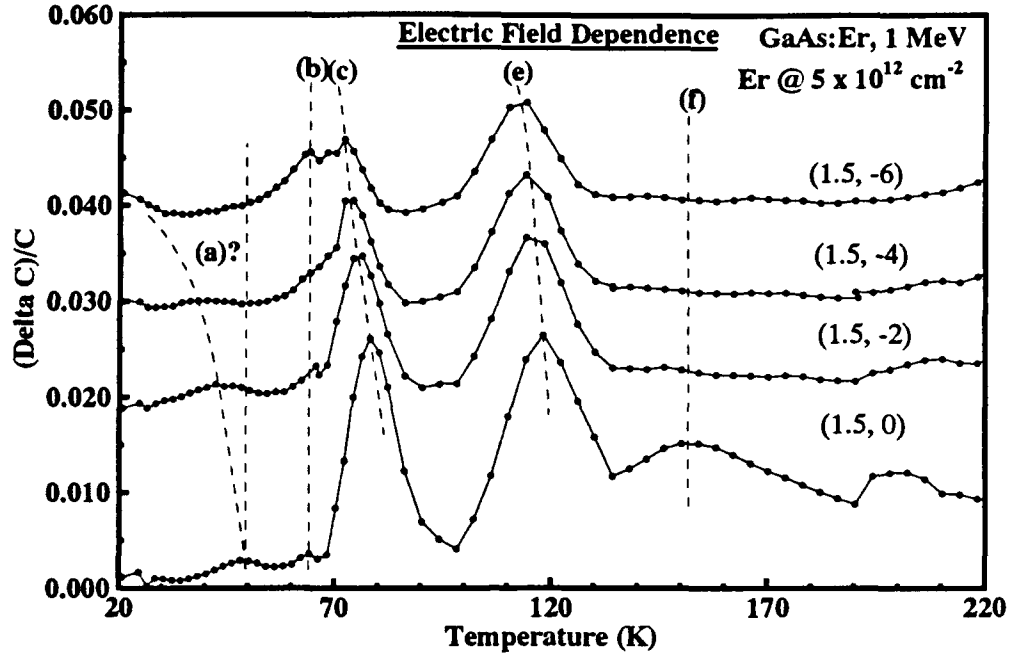


Figure 46. Electric field dependence of the low temperature peaks observed in the n-type GaAs samples implanted with Er at a fluence of $\Phi_{Er} = 5 \times 10^{12} \text{ cm}^{-2}$ and at an energy of 1 MeV (The rate window is 29706 s^{-1} .)

an expanded scale, this peak reveals a shoulder near 75 K. Finally, for the sample implanted with Er at a fluence of $\Phi_{Er} = 5 \times 10^{13} \text{ cm}^{-2}$, it appears that both peaks (b) and (c) are present in comparable concentration, with peak (c) slightly dominating. Two distinct possible physical mechanisms could give rise to the observed shifting. First, levels (b) and (c) might be due to the same center, and the differences in the activation energy or peak position in the rate-window plot can be interpreted as being due to field-enhanced emission from this center. The second possibility is that there are two distinct centers, one with a peak at 68 K and the other with a peak at 75 K. In order to resolve this question, a bias-dependent study was performed on the $\Phi_{Er} = 5 \times 10^{12} \text{ cm}^{-2}$ sample.

Figure 46 shows the rate-window plot for four different biasing conditions on the n-type GaAs sample with $\Phi_{Er} = 5 \times 10^{12} \text{ cm}^{-2}$. All four measurements were performed on the same sample with a forward bias pulse of 1.5 V, and the measurement bias was 0, -2, -4, and -6 V. In addition, Figure 47 shows the CV profile for this sample along with the depletion width for each of the measurement bias values. Figure 46 shows that two distinct levels are present.

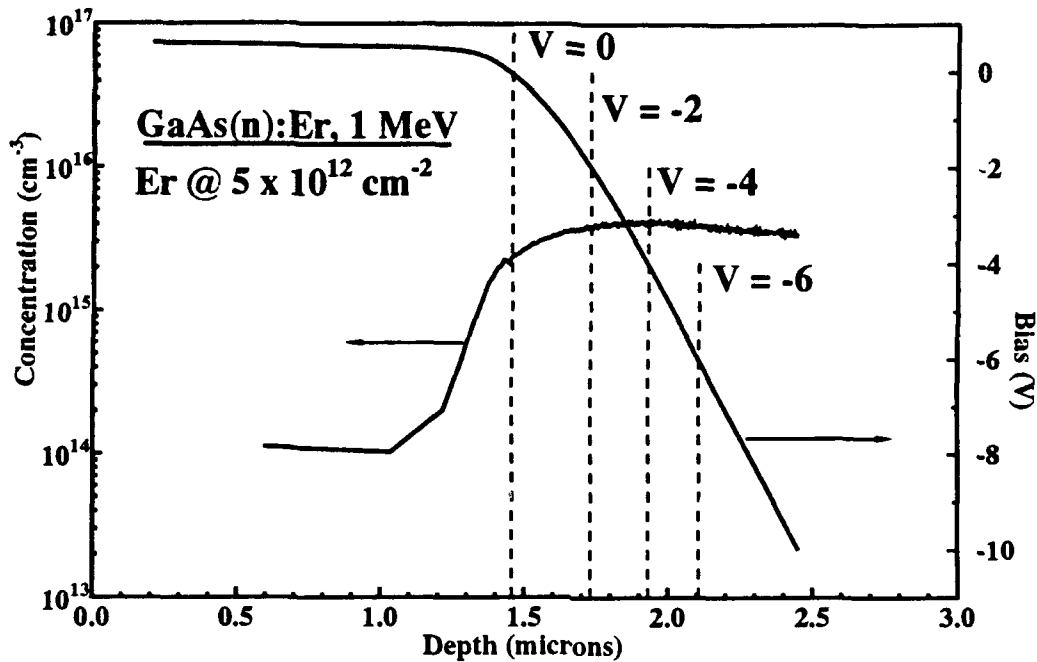


Figure 47. Depletion width vs. applied bias for the various DLTS measurements shown in Figure 46

Furthermore, the higher temperature peak, (c), has a large field-enhanced emission rate, while the lower energy peak, (b), apparently has no field dependence. Peak (c) moves from approximately 78 K for the (1.5,0) bias state to 72 K for the (1.5,-6) bias state, while peak (b) remains fixed at 63 K. According to the conventional understanding of Poole-Frenkel field-enhanced emission, this indicates that the center (b) is neutral when empty, and that the center (c) is charged when empty. Thus, center (c) has a coulomb-like potential which is strongly influenced by an applied field. Figure 46 also shows that the concentration of the center associated with peak (b) increases with reverse bias, while that associated with peak (c) decreases. By comparison with Figure 47, it is clear that peak (b) is associated more with the extremities of the Er implant, and peak (c) is associated more with the peak region of the Er implant, suggesting that center (c) is due to Er-related ion-implantation damage, while center (b) is possibly due to an isolated Er center formed during Er diffusion into the substrate.

Peak (e) seems to follow the same trend as peak (c) with a field-enhanced emission, although slightly less pronounced. It moves from 118 to 113 K, and it also follows the same trend, but with smaller signals as the reverse bias increases. Thus, center (e) also appears to be related to

implantation damage. Finally, peak (f) shows up only for the smallest reverse bias state. It is a very broad peak, and the transients giving rise to it do not clearly show a single activation energy. It is, therefore, likely to be due to emission from a set of related centers with slightly different energies, such as clusters of unannealed damage-related centers near the front of the Er implant.

Figure 46 also shows peak (a) moving to lower temperatures with increasing field, possibly indicating field-enhanced emission. However, this cannot be conclusively established for several reasons. First, this center has a very small concentration, making it difficult to determine whether or not there is actually more than one center present. Secondly, it seems unlikely that the peak would shift so much. Further, for the (1.5,-4) biasing sequence, the DLTS signal is virtually gone, but reappears for the (1.5,-6) biasing sequence at very low temperatures. This emission at low temperatures in the highest reverse bias state is probably due to an artifact related to conduction through the diode. However, it does appear that this level also decreases in concentration with depletion width, even faster than the center (c).

In Figure 45, peak (e) is observed for the lowest Er fluence, $\Phi_{Er} = 5 \times 10^{12} \text{ cm}^{-2}$, but it is absent in the two higher Er fluences, $\Phi_{Er} = 10^{13} \text{ cm}^{-2}$ and $\Phi_{Er} = 5 \times 10^{13} \text{ cm}^{-2}$, while the opposite behavior applies to peak (d). Thus, the center (e) appears to be converted into center (d) for higher Er implantation fluences. However, peak (d) has an unnatural shape, and the transients which give rise to this center actually have emission rates which are decreasing with increasing temperature, as shown in Figure 48. This behavior is contrary to that expected for the normal thermally-activated emission from a deep center, given in equation (21), and it is probably related to incomplete capture at this center. This behavior is due either to the presence of a very large concentration of center (e) or possibly to a temperature-dependent cross section of the center. In fact, Yu et al. (104:533) have reported a level similar in energy to that corresponding to peak (e) which has a temperature-dependent cross section consistent with capture by a multiphonon emission process. Specifically, they found the capture cross section to be

$$\sigma = \sigma_{\infty} \exp(-E_{\infty}/kT) = 7.1 \times 10^{-15} \text{ cm}^{-2} \exp(-50 \text{ meV}/kT). \quad (73)$$

They also reported an activation energy for hole emission of 130 meV. The activation energy of the capture cross section is subtracted from the measured energy to obtain the true depth of the level, 80 meV. According to Yu, this is the first acceptor level of the Ga antisite defect, Ga_{As} , and hole emission corresponds to the transition $\text{Ga}_{As}^0 \rightarrow \text{Ga}_{As}^{-1}$.

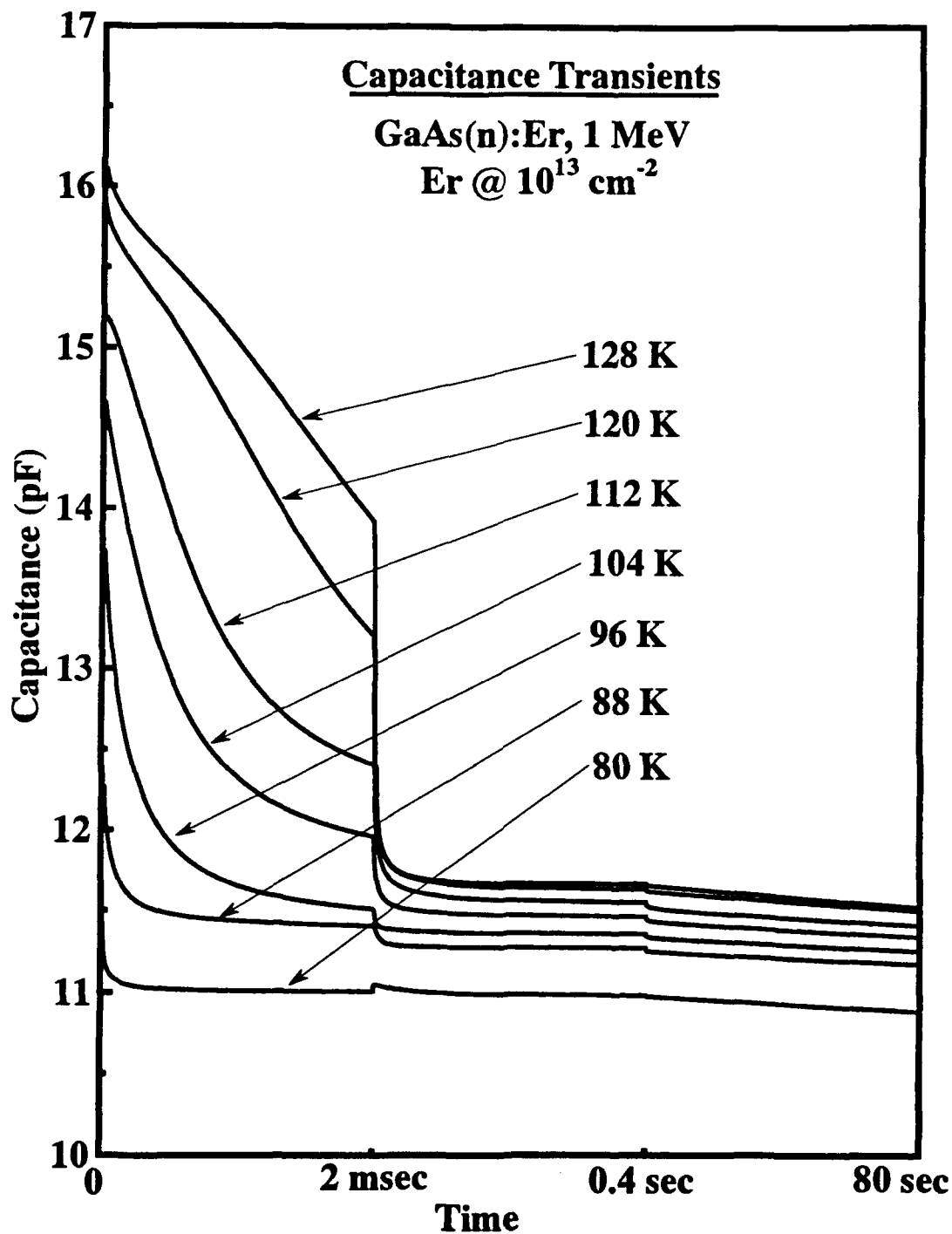


Figure 48. Capacitance transients recorded between 80 and 128 K for the n-type GaAs substrate 02-PR-1748, with Er-implanted at a fluence of $\Phi_{\text{Er}} = 10^{13} \text{ cm}^{-2}$ and at an energy of 1 MeV (The transients have an increasing time constant with temperature, indicating incomplete capture at a deep center.)

For the higher temperature peaks in Figure 45, there are at least four other hole traps present in the n-type, Er-implanted substrates corresponding to peaks (g), (i), (j), and (k), and possibly one electron trap corresponding to peak (h). DLTS measurements were performed on the same n-type substrates implanted with the RE praseodymium (Pr), instead of Er, to clarify the nature of these centers. Figure 49 shows a rate-window plot for samples with a Pr fluence of $\Phi_{Pr} = 10^{13}$ and $5 \times 10^{13} \text{ cm}^{-2}$ implanted at an energy of 390 keV and annealed at 825 °C for 12 seconds. The rate-window plots for all three Er fluences are repeated for comparison. The concentration of the deep levels in the Pr-implanted samples was much less than in the Er-implanted samples, and consequently, the rate-window plots for the Pr samples were multiplied by a factor of 10 so that they could be compared directly with the Er-implanted samples. Peaks (c), (e), (i), and (j) are clearly seen in both the Er and Pr-implanted samples. Thus, these centers are not due to the chemical nature of the implanted impurity, but are probably due to the influence of the implantation process on the crystal structure. That is, they are most likely due to unannealed native defects caused by the ion-implantation process. On the other hand, peaks (b) and (g) do not appear in the rate-window plot for the Pr-implanted sample. Figure 45 also shows that the concentration of (g) increases with increasing Er fluence. Further, the activation energy measured for the (g) center is approximately 345 meV, which is in agreement with that measured in the Er-doped MBE sample x105 by temperature-dependent Hall effect measurements. Based upon these three observations, it seems likely that this level is due to an Er-related center. Likewise, the center (b), which is not observed in the Pr-implanted sample, is probably not related to ion-implantation damage.

There also appears to be a peak in the Pr-implanted samples close to the peak (a) observed in the Er-implanted samples. However, the concentration of this center is at least one order of magnitude smaller than that associated with center (a) in the Er-doped sample. Analysis of the capacitance transients did not yield an acceptable Arrhenius behavior in this region. Furthermore, the low-temperature peak in the Pr-implanted sample seems to be part of a broad band, extending from 20 K to as high as 220 K. This peak is possibly due to a set of related centers which are closely-spaced in energy.

The activation energies and capture cross sections of the hole traps (e) and (j) are similar to those reported for copper (Cu) impurities in GaAs as reported by Mitonneau et al. (64:667). In order to explore the possibility that these centers were related to copper impurities, DLTS

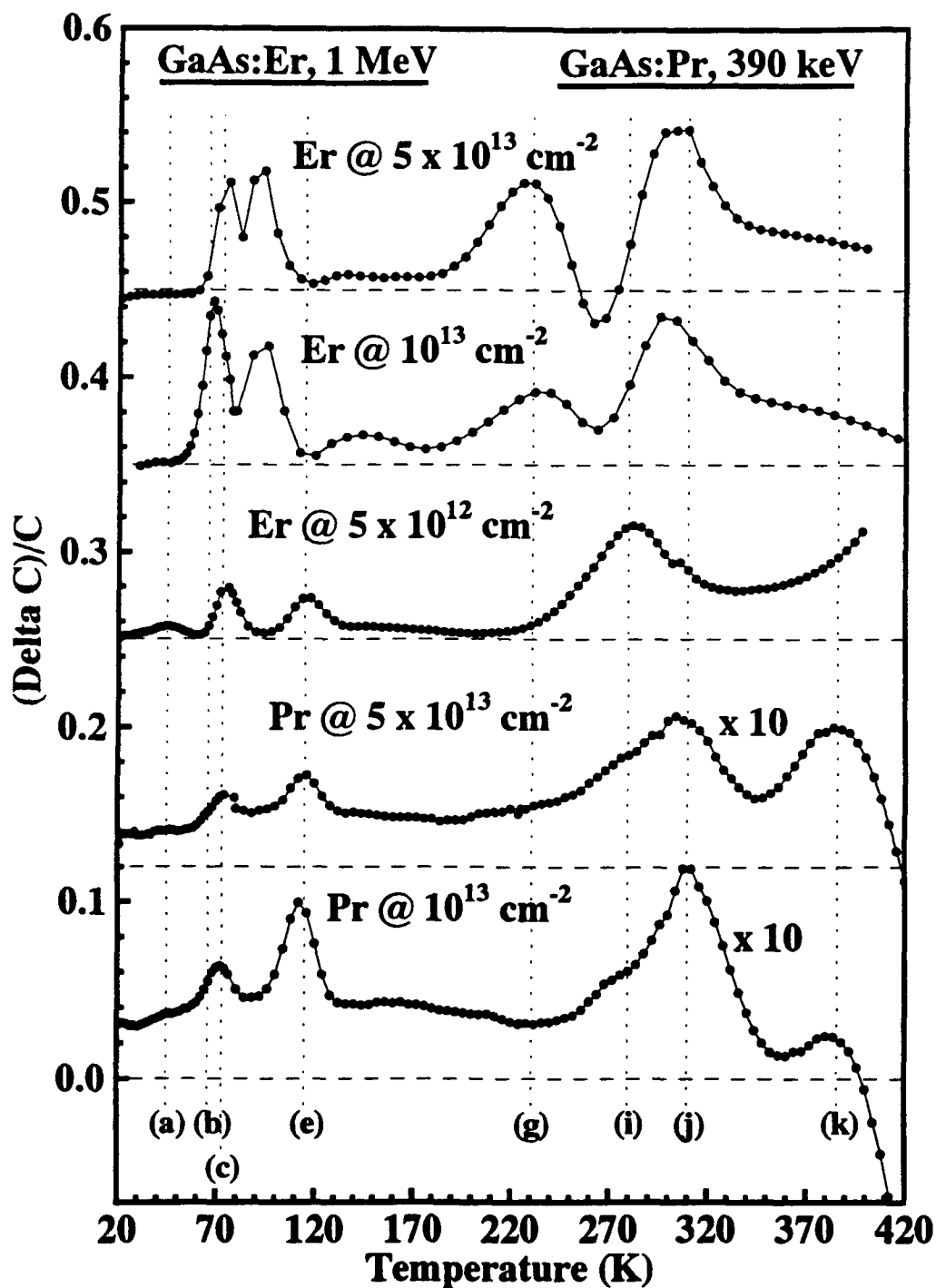


Figure 49. DLTS spectra for Er implants in n-type GaAs at the indicated fluence and an energy of 1 MeV, as well as Pr implants in n-type GaAs at 390 keV (Common peaks represent centers which are most likely due to ion-implantation damage. The rate window is 29706 s^{-1} .)

measurements were performed on GaAs implanted with copper. Since Cu impurities were known to give hole traps, the Cu implantation was performed on the p-type substrate 3B-PR-840. The Cu was implanted with a fluence of $\Phi_{\text{Cu}} = 5 \times 10^{13} \text{ cm}^{-2}$ at 370 keV. (The LSS theory gives a peak concentration of $[\text{Cu}] = 2.7 \times 10^{18} \text{ cm}^{-3}$ at $0.176 \mu\text{m}$ with a straggle of $0.075 \mu\text{m}$.) The sample was annealed at 825°C for 15 seconds, and Schottky diodes were fabricated for the DLTS measurements. Figure 50 shows the rate-window plot obtained with majority-carrier biasing. The negative peaks represent hole traps. For comparison, Figure 50 also shows the previous results for the high and low Er fluences implanted into the n-type substrate that are reproduced from Figures 45 and 46. The positive signals are indicative of hole traps in the n-type samples, since injection biasing was used in that case. Two hole traps are present in the Cu-implanted sample, designated Cu1 and Cu2. The activation energies and capture cross sections for these centers are given in Table 12, which also shows the levels Lang and Logan (54), and Mitonneau et al. (64) considered to be related to Cu, Fe and other native midgap hole traps.

Peak Cu1 does not align well with center (e). However, in the rate-window plot for the sample measured under the highest reverse bias state (Figure 46), the concentration of center (b) increased relative to center (c) with reverse bias. This was thought to be due to a higher concentration of this defect in the extremities of the implant. Figure 50 shows that Cu1 aligns very well with peak (b). In addition to the overlap of their DLTS signals, these two centers have a similar activation energy, near 100 meV (Tables 11 and 12). Furthermore, the activation energies and capture cross sections for these two centers are probably more uncertain than is indicated in Tables 11 and 12. In the case of center (b), this uncertainty is due to the emission rate being very similar to center (c), and, as well, to the generally small concentration of center (b). Also, in the Cu-implanted sample, Cu1 has a very large concentration, which makes the transients nonexponential and, therefore, the analysis is subject to error. Center (b) has higher concentrations for larger reverse biases, indicating a higher concentration of this center in the substrate compared to the implanted region. Thus, center (b) may be the Cu-related center Cu1.

Comparing the second Cu-related center with the higher-temperature peaks in Figure 50, peak Cu2 in the Cu-implanted sample does not align well with any of the other peaks in the Er-implanted GaAs, although it apparently has a similar activation energy relative to center (i) of approximately 395 meV. Figure 51 shows the Arrhenius plot for center Cu2 in the Cu-implanted GaAs sample. The signature for center HB4, attributed to a Cu-related center by Lang (54),

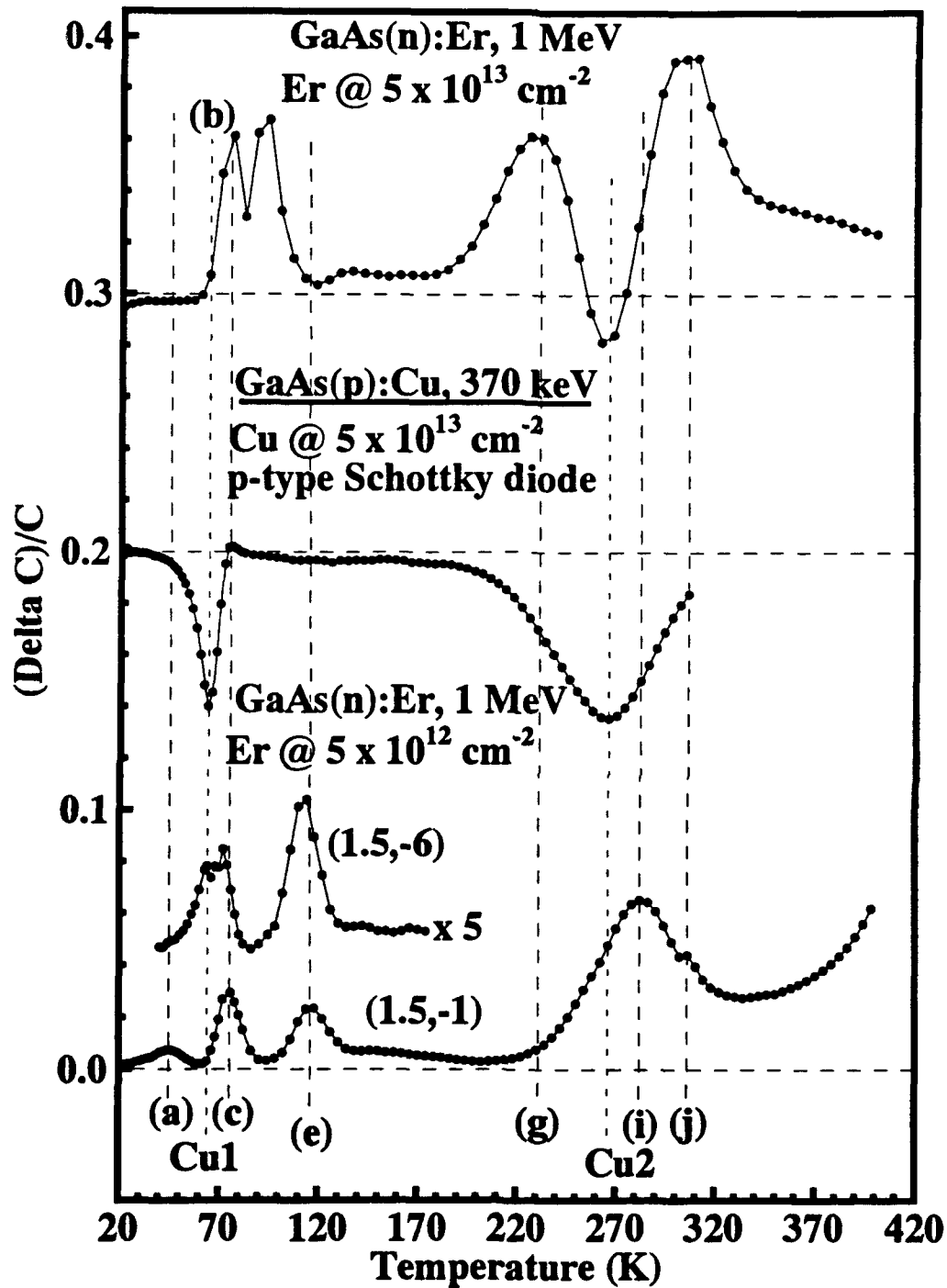


Figure 50. DLTS measurement of p-type Schottky diodes GaAs:Cu with Cu implanted at a fluence of $\Phi_{\text{Cu}} = 5 \times 10^{13} \text{ cm}^{-2}$ and at an energy of 370 keV, using majority carrier biasing, and DLTS measurements performed on the n-type GaAs Er-implanted samples with the high and low Er fluences using injection biasing on p⁺n diodes (The rate window is 29706 s^{-1} .)

Table 12. Activation energies and capture cross sections for mid-gap hole traps in GaAs as measured in this investigation and as reported by Lang, et al. (54) and Mitonneau, et al. (64)

Center/Peak Treatment	Activation Energy (meV)	Capture Cross Section (cm ²)
The following centers measured during this research		
Cu1 Cu - implanted	116 ± 8	$\begin{matrix} 1.7 \times 10^{-12} \\ \approx 7 \times 10^{-12} \approx \\ 2.7 \times 10^{-11} \end{matrix}$
Cu2 Cu-implanted	395 ± 5	$\begin{matrix} 3 \times 10^{-15} \\ \approx 5 \times 10^{-15} \approx \\ 7 \times 10^{-15} \end{matrix}$
⁽ⁱ⁾ Er and Pr implanted	395 ± 7	$\begin{matrix} 3 \times 10^{-15} \\ \approx 1.9 \times 10^{-15} \approx \\ 7 \times 10^{-15} \end{matrix}$
^(j) Er and Pr implanted	447 ± 5	$\begin{matrix} 1.8 \times 10^{-15} \\ \approx 2.3 \times 10^{-15} \approx \\ 2.8 \times 10^{-15} \end{matrix}$
^(k) MOCVD - as-grown Er and Pr implanted	540 ± 8	$\begin{matrix} 5.3 \times 10^{-16} \\ \approx 7.7 \times 10^{-16} \approx \\ 1.1 \times 10^{-15} \end{matrix}$
The following centers measured by Lang and Logan (54)		
unnamed Cu-doped LPE	140	not given
HB3 Fe-doped LPE	520	3.4×10^{-16}
HB4 as-grown LPE	440	3.4×10^{-14}
HB5 as-grown LPE	400	2.2×10^{-13}
The following centers measured by Mitonneau et al. (64)		
HL3 Fe-diffused VPE	590	3.0×10^{-15}
HL4 Cu-diffused VPE	420	3.0×10^{-15}
HL5 as-grown VPE	410	9.0×10^{-14}

as well as the signatures for centers (i) and (j), are also shown. The temperature-dependent emission of center Cu2 is closer to the behavior of HB4 that was observed by Lang, especially at the higher temperatures, compared to the behavior of centers (i) and (j). However, it is possible

that center (i) is actually the Cu₂ center, due to their similar activation energies, as well as the fact that center (i) has a fairly uncertain capture cross section (Table 12). The fit for (i) was obtained from the Pr-doped sample which had overlapping centers (i) and (j), thus, contributing additional uncertainties to their respective fits.

DLTS measurements were also performed on the p-type GaAs substrate 3B-PR-840 implanted with Er at a fluence of $\Phi_{\text{Er}} = 5 \times 10^{12} \text{ cm}^{-2}$ and an energy of 1 MeV. In this case n⁺p diodes were formed by Si ion implantation. The same annealing conditions of 825 °C for 12 seconds were used for consistency. As explained in the previous section, suitable diodes could be formed only for this lowest Er fluence, since for higher Er fluences, the n⁺ implant was not effective due to the reduction in the free electron concentration. Figure 52 shows the rate-window plots for the p-type and n-type GaAs with $\Phi_{\text{Er}} = 5 \times 10^{12} \text{ cm}^{-2}$ as well as the control p-type sample which only had the n⁺ Si implant. The measurements for the p-type samples were carried out with a majority carrier biasing sequence, so that essentially only holes were swept into and out of the junction. The negative signals appearing for these samples indicate the presence of majority carrier hole traps in the p-type material. Centers (b), (c) and (i) also appear as hole traps in the Er-implanted p-type substrate, indicating that these centers are also not related to an Er complex with Si or Zn. Figure 52 also reveals that centers (a) and (g) are not observed in the p-type Er-implanted material. For (g), this is a consistent result, since it was not observed in the n-type samples at this fluence. On the other hand, the non-occurrence of center (a) indicates that it may be related to an Er-Si complex. However, this conclusion would be premature since center (a) also has a small concentration in the n-type sample. Thus, since it does not appear in the p-type sample, it could be related to the higher shallow-doping in this sample with $p = 4 \times 10^{16} \text{ cm}^{-3}$, which is comparable with $n = 5 \times 10^{15} \text{ cm}^{-3}$ in the n-type sample. The capacitance transients are already small in magnitude and close to the limit of the resolution for the capacitance meter for the n-type sample. For the same concentration of this defect in the p-type sample, the transients are approximately one order of magnitude smaller and, therefore, not detectable. Thus, it is not possible at this point to formulate a conclusion as to whether or not the (a) center is also seen in p-type material.

Center (k) is seen clearly in the p-type, ion-implanted sample, as well as the p-type control sample, and it is either due to a native defect or to an impurity which is already present in the material before Er implantation. Lang (54) found a center with a similar signature and directly

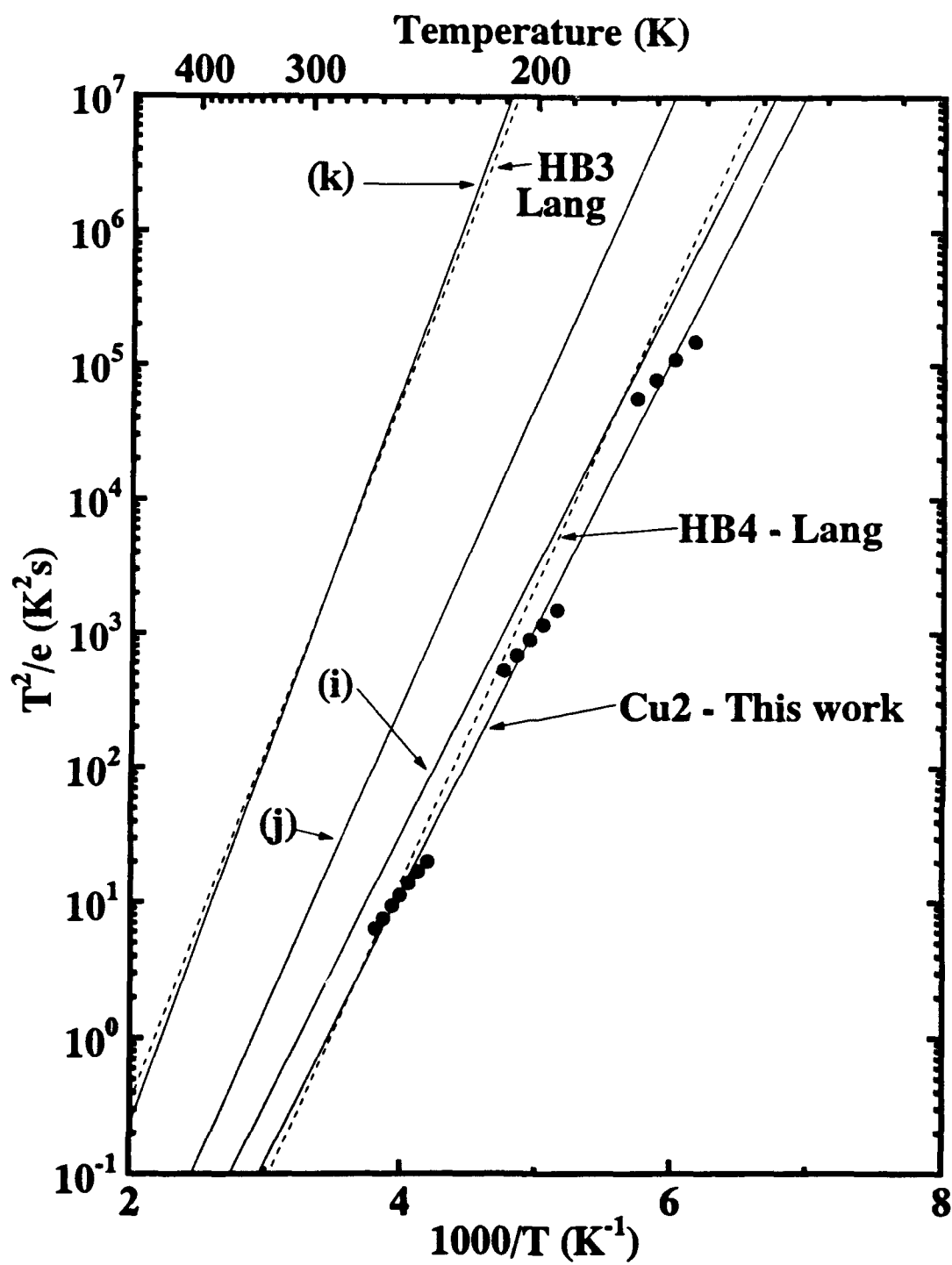


Figure 51. Arrhenius plots for centers Cu2, (i), (j) and (k) in GaAs from the current work (HB3 and HB4 were measured by Lang (54) and attributed to Fe and Cu impurities, respectively.)

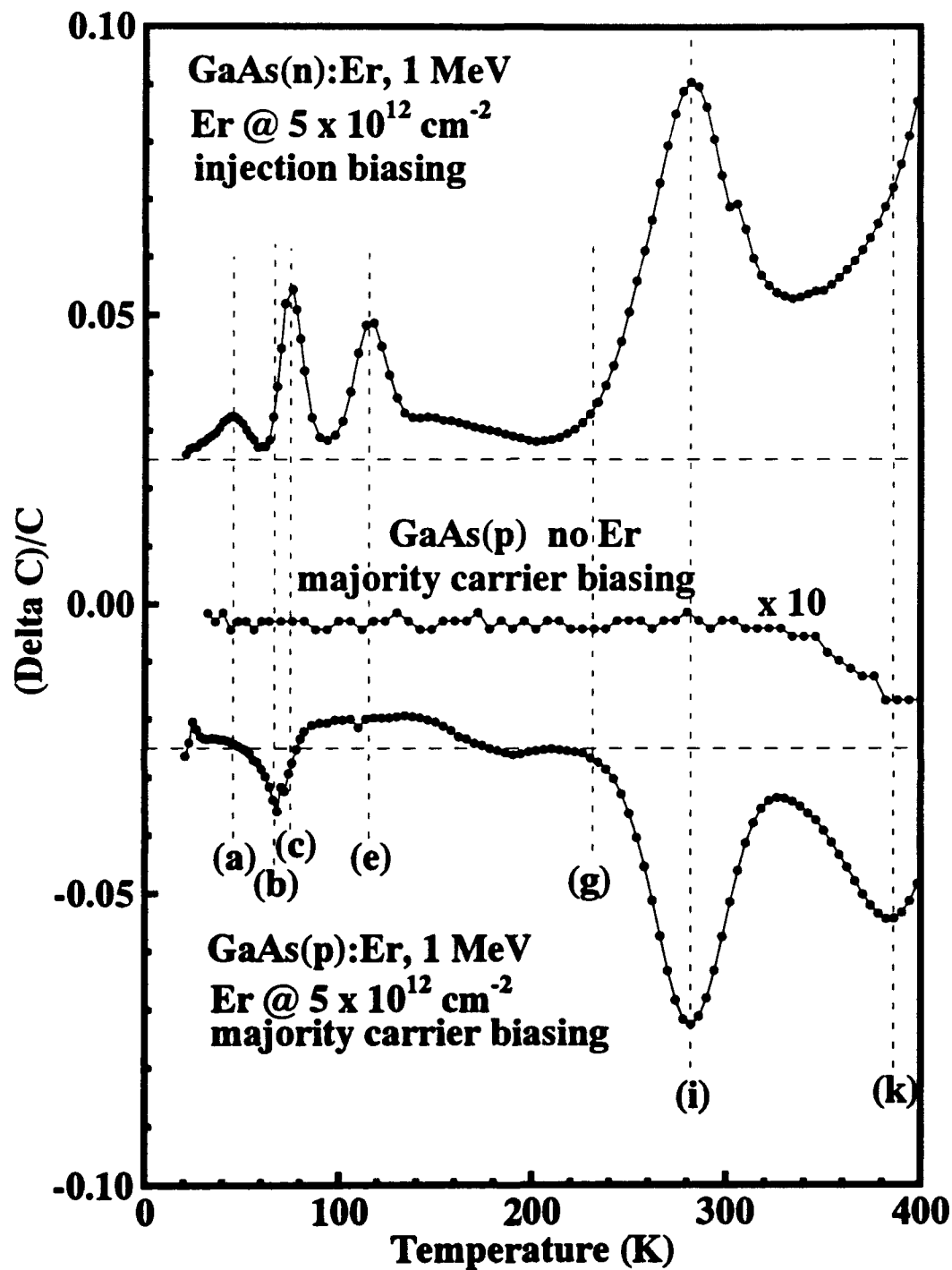


Figure 52. Rate-window plots for the p-type GaAs substrate with Er implanted at a fluence of $\Phi_{\text{Er}} = 5 \times 10^{12} \text{ cm}^{-2}$ and at an energy of 1 MeV, and a p-type control sample with no Er implant (The measurement for the n-type sample with the same Er fluence is shown for comparison. The rate window is 29706 s^{-1} .)

correlated it with the concentration of Fe doped into LPE GaAs (designated as level HB3 in Table 12). The Arrhenius behavior of center (k) and HB3 are almost identical, as shown Figure 51. Figures 49 and 52 illustrate that the Pr implantation as well as the Er implantation seem to enhance the concentration of this center, indicating that it is probably due to a complex of Fe and some native defect, which is enhanced by implantation damage.

The Arrhenius plots showing the temperature-dependent emission of the hole traps (a)-(k) are shown in Figures 53 and 54. Figure 53 shows the results for the shallower traps (a) – (e), while Figure 54 shows the behavior of the deeper traps (g) – (k). In Figure 53, centers (b) and (c) had a similar Arrhenius behavior, and their combined emissions yielded a double exponential decay. The data for center (c) is plotted with open circles to distinguish it from the data due to center (b).

In Figure 54, the data for centers (i) and (j) was taken from the analysis of the Pr-implanted sample in which centers (i) and (j) were present, but the center (g), attributed to Er, was absent. Furthermore, as seen from Figure 49, the concentration of these damage-related centers is much less than that in the Er-implanted samples. This resulted in a more reliable Arrhenius analysis for these centers. However, in the case of the Er-implanted samples, the concentration of both damage-related centers (i) and (j) are very large. For instance, $\Delta C/C \sim 0.1$ for these centers in the samples with Er implanted with fluences of $\Phi_{Er} = 10^{13}$ and $5 \times 10^{13} \text{cm}^{-2}$. Such a large concentration of deep levels makes the capacitance transients nonexponential and broadens the DLTS signals in the rate-window plots, making it difficult to obtain an accurate Arrhenius analysis for center (g). The Arrhenius analysis was further complicated since center (g) emitted with time constants similar to centers (i) and (j). For the Arrhenius behavior of center (g), the data was taken from the single exponential analysis of the capacitance transients obtained from the sample with Er implanted at a fluence of $\Phi_{Er} = 5 \times 10^{13} \text{cm}^{-2}$, since the concentration of (g) appears to be the largest for this Er fluence. While the analysis indicates that this center is shallower than centers (i) and (j), it is clearly not well separated from these centers. Therefore, the activation energy and capture cross section for center (g) listed in Table 11 may be more erroneous than is indicated in the table. In order for the analysis to accurately determine the parameters for center (g), a sample is needed in which only center (g) is present, or one in which centers (i) and (j) have a much smaller concentration.

Thus far, Er has only given rise to hole traps in GaAs, and they have been verified with injection biasing on Er-implanted p^+n junction diodes. In order to check for the presence of

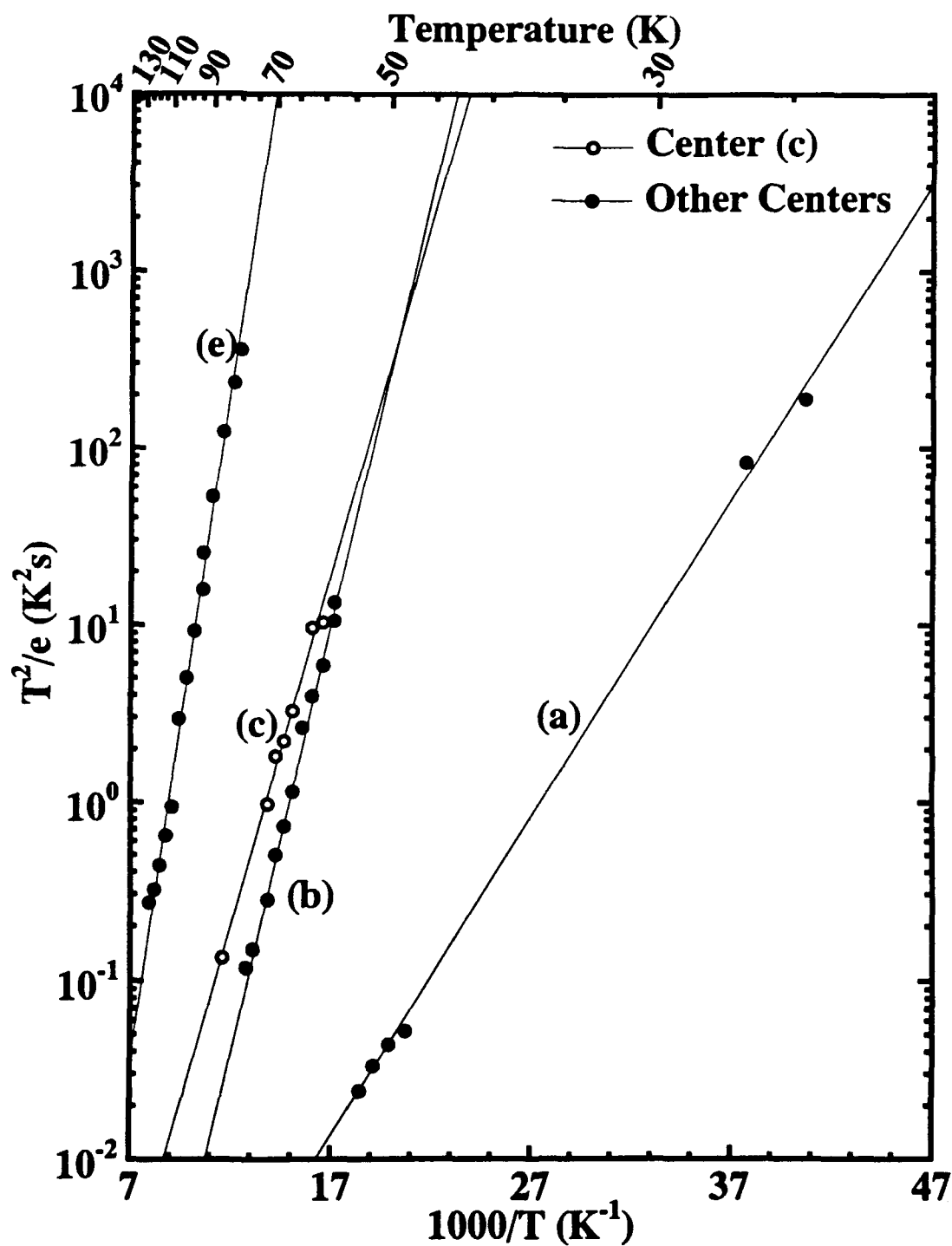


Figure 53. Arrhenius analysis for hole traps (a) — (e) occurring in Er-implanted GaAs (The data for center (c) is plotted with open circles.)

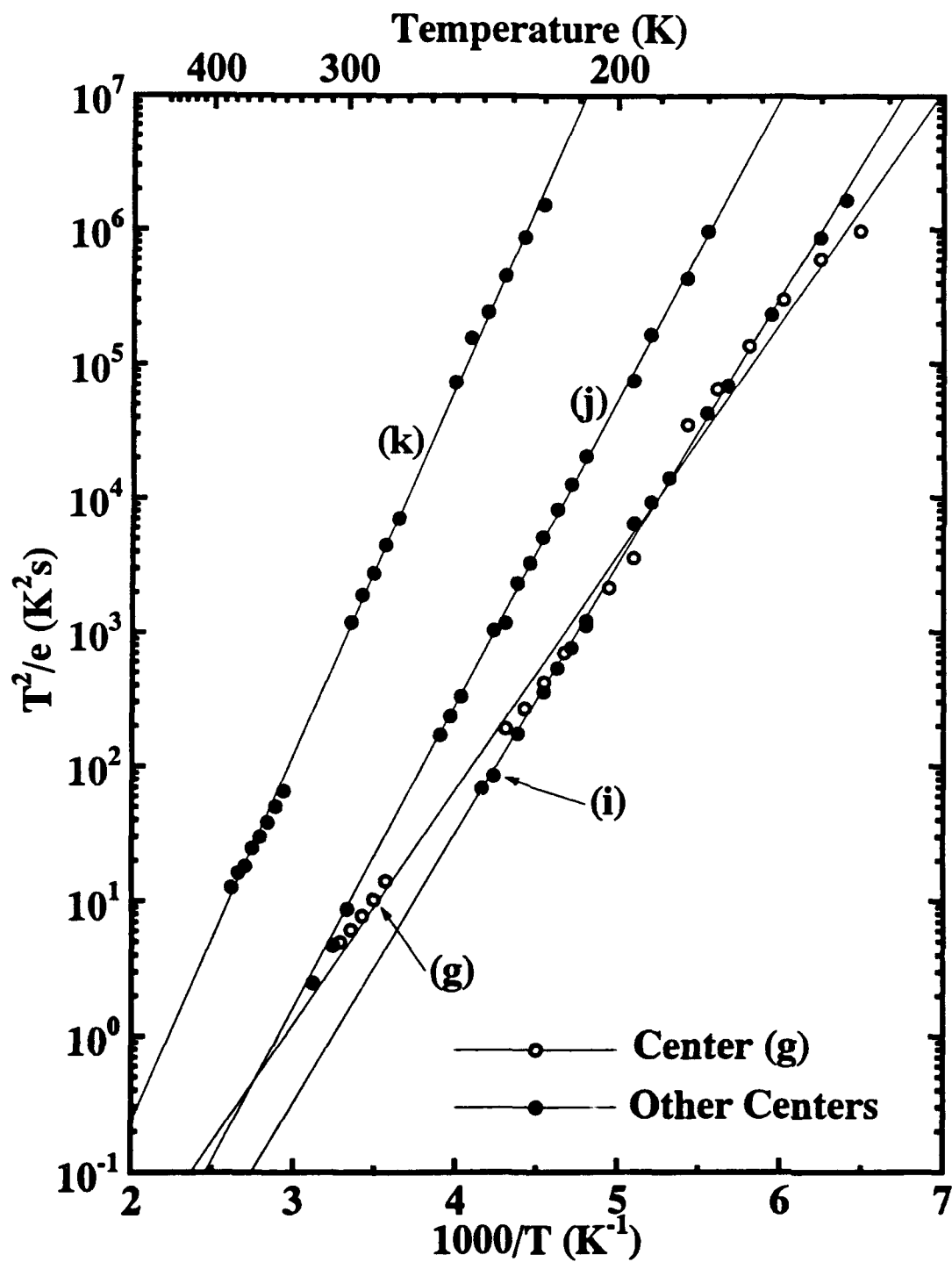


Figure 54. Arrhenius analysis for hole traps (g) — (k) occurring in Er-implanted GaAs (The data for center (g) is plotted with open circles.)

Er-related electron traps, DLTS measurements were performed on these samples using majority-carrier biasing. These measurements were typically performed with a biasing sequence of (1,-1), so that the bands were flattened as much as possible without the introduction of a large hole current through the junction. The rate-window plots for all three Er fluences in the n-type substrate 02-PR-1748 are shown in Figure 55. These rate-window plots were formed with a relatively slow rate window of 0.742 s^{-1} , because the observed electron traps were somewhat deeper in energy than the hole traps. This rate window was formed by taking $t_1 = 0.4 \text{ sec}$, and $t_2 = 8t_1 = 3.2 \text{ sec}$. Three main electron traps appear in these samples, which are labelled (l), (m), and (n) in Figure 55. The activation energy and capture cross section of these traps are given in Table 13. Also listed are the activation energies and capture cross sections for the electron traps with similar energies. The parameters for EL2, the major deep electron trap found in GaAs, is obtained from the review article by Martin et al. (61:192). The parameters for M3, which is a less well known metastable trap found only in n-type MOCVD-grown samples, are obtained from Buchwald et al. (16:1008). The Arrhenius behavior of all of these centers is demonstrated in Figure 56, showing that EL2 and M3 correspond closely with the electron traps (l) and (n), respectively, observed in this investigation. Both of these centers are observed in the control sample, as well as in the Er-implanted layers. Therefore, they are thought to be due to impurities or defects native to this material. However, centers (l) and (n), or M3 and EL2, behave differently with respect to increasing Er fluence. The concentration of (l) or M3 increases drastically with increasing Er fluence, while that of (n) or EL2 decreases with increasing Er fluence, until it is less than that of the substrate for $\Phi_{\text{Er}} = 5 \times 10^{13} \text{ cm}^{-2}$. Furthermore, the behavior of the EL2 or center (n) is somewhat more complicated, since for the lowest Er fluence, it seems to change into the slightly deeper level (m).

6.3.2 DLTS Measurements on Er-Implanted $\text{Al}_x\text{Ga}_{1-x}\text{As}$ DLTS measurements were performed on Er-implanted n-type $\text{Al}_x\text{Ga}_{1-x}\text{As}$ substrates with an Al mole fraction $x = 0, 0.1, 0.2, 0.3$, and 0.4 . CV profiles of these substrates were shown previously in Figure 6. Figure 57 shows the rate-window plots for these substrates with Er implanted at a fluence of $\Phi_{\text{Er}} = 10^{13} \text{ cm}^{-2}$ and at an energy of 1 MeV and annealed at 825°C for 15 seconds. These samples were measured using an injection-biasing sequence. Measurements were also made on the unimplanted control samples, which are shown with dashed lines in the figure. The measurements for the Er-implanted GaAs sample have been multiplied by a factor of 0.5, because the carrier concen-

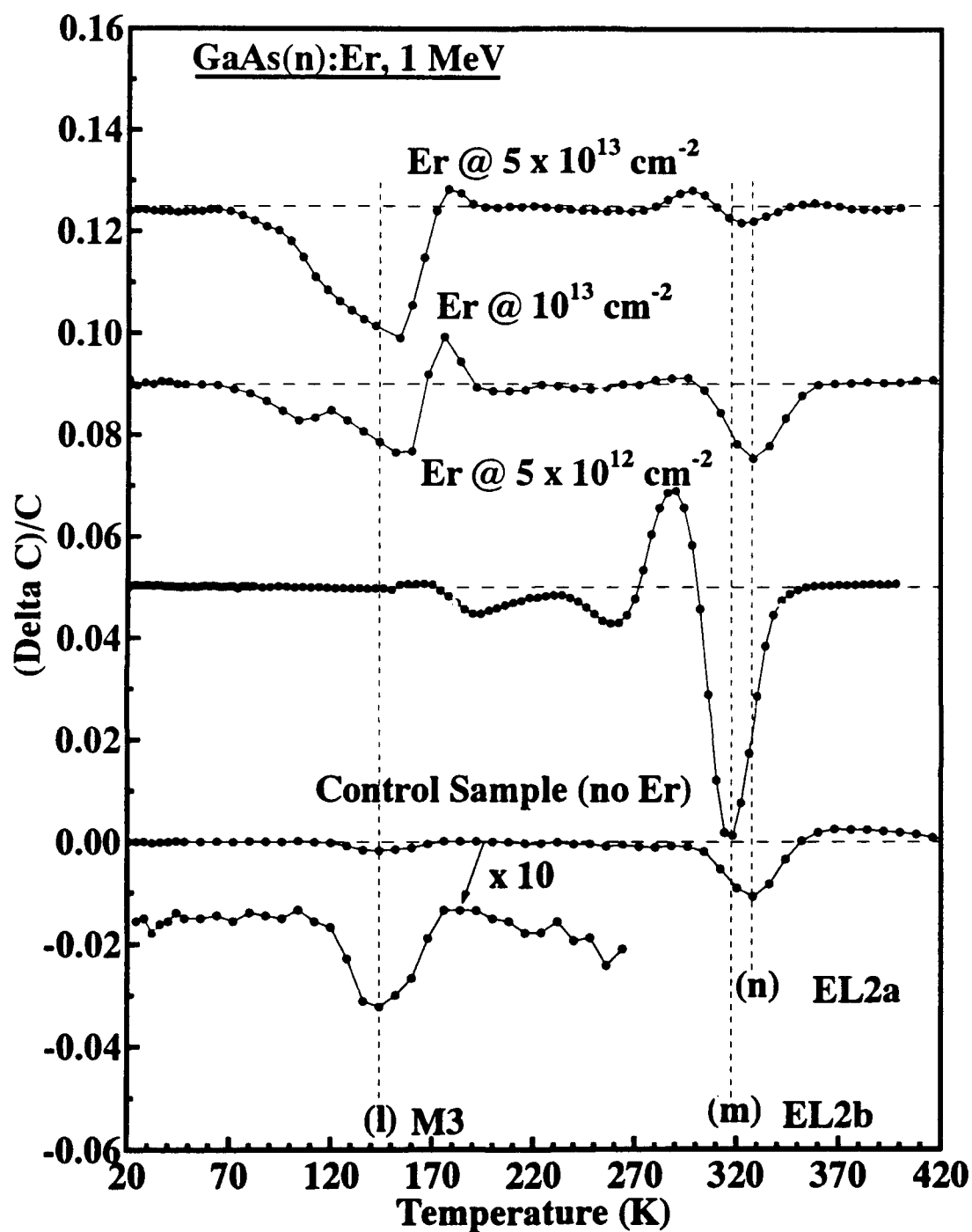


Figure 55. DLTS measurements using majority carrier biasing on p⁺n GaAs diodes for different Er fluences, as well as for the control sample which was not implanted with Er (The rate window is 0.742 s^{-1} .)

Table 13. Electron traps found in the n-type MOCVD-grown GaAs substrate 02-PR-1748 as well as in the Er-implanted GaAs substrates

Center/Peak Treatment	Activation Energy $E_c - E_T$ (meV)	Capture Cross Section (cm ²)
The following centers measured during this research		
l n-type MOCVD	613 ± 8	4.1×10^{-14} $\approx 5.3 \times 10^{-14} \approx$ 6.9×10^{-14}
m n-type MOCVD	840 ± 5	8.0×10^{-13} $\approx 9.5 \times 10^{-13} \approx$ 1.1×10^{-12}
n n-type MOCVD	785 ± 7	2.9×10^{-14} $\approx 3.6 \times 10^{-14} \approx$ 4.5×10^{-14}
The following center measured by Buchwald et al. (16)		
M3 n-type MOCVD	610 ± 10	3.3×10^{-14}
The following information obtained from the review by Martin et al. (61)		
EL2	830	2×10^{-13}

tration in this substrate was $n = 5 \times 10^{15} \text{cm}^{-3}$, while in the AlGaAs layers, it was approximately twice as large, $n = 10^{16} \text{cm}^{-3}$. Therefore, by multiplying the GaAs:Er signal by 0.5, all deep level concentrations become directly comparable. For an Al mole fraction of $x = 0.1$, the concentrations of deep levels are roughly the same as in the GaAs sample. However, all peaks are not present, and some have shifted to the right, which corresponds to the centers moving deeper into the band gap. For the $x = 0.2$ and $x = 0.3$ Al mole fractions, a drastic decrease in the concentration of the deep centers has occurred. Even those centers which have been attributed to ion-implantation damage have disappeared in these samples. Finally, an electron trap with a very large concentration is observed in the samples with an Al mole fraction of $x = 0.4$. This signal is due to the DX center, which, as mentioned above, is due to an isolated Si_{Ga} , and it is a deep

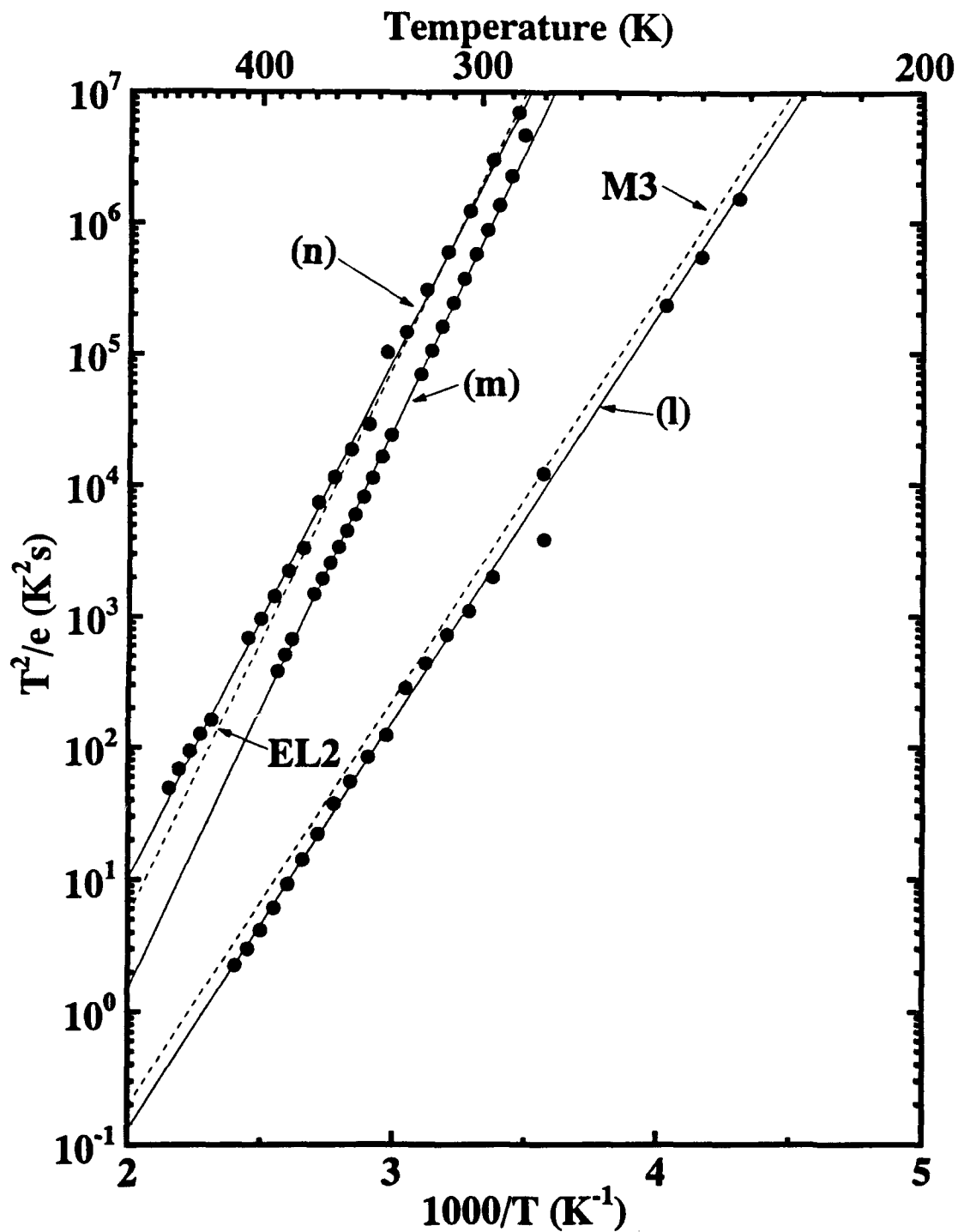


Figure 56. Comparison of the Arrhenius behavior for electron traps (l), (m), and (n) found in this work, as well as M3 and EL2 obtained, respectively, from Buchwald (16) and Matrin (61)

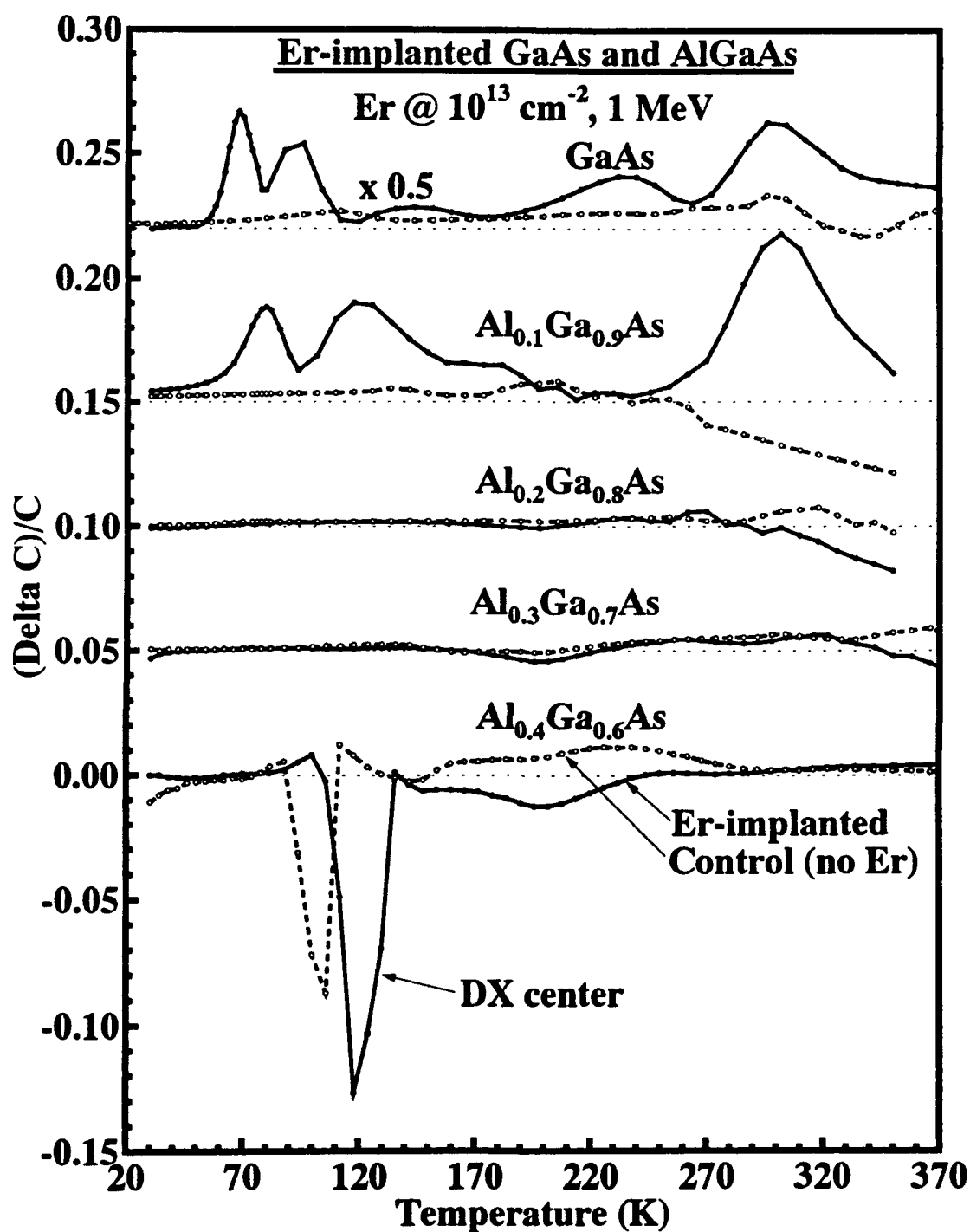


Figure 57. Rate-window plots using injection biasing for n-type $\text{Al}_x\text{Ga}_{1-x}\text{As}:\text{Er}$ for $x=0, 0.1, 0.2, 0.3$, and 0.4 with Er implanted at a fluence of $\Phi_{\text{Er}} = 10^{13} \text{ cm}^{-2}$ and at an energy of 1 MeV as well as control samples, which are shown with dashed curves (The rate window = 29706 s^{-1} .)

donor for $x \gtrsim 0.2$. The signal from the DX center in the Er-doped sample is shifted somewhat relative to the control sample, but has approximately the same concentration. The concentration of the DX center is near its maximum for $x = 0.4$, illustrating how readily it is observed in this sample, but not as easily observed in the samples with $x = 0.2$ or $x = 0.3$. Since the DX center is an electron trap, it should be measured in the n-type material with majority carrier biasing instead of injection biasing.

The rate-window plots using majority carrier biasing for $x = 0.2, 0.3$, and 0.4 (Figure 58) show that the introduction of Er in AlGaAs does not affect the concentration of the DX center. Since the DX center involves the deep donor Si_{III} , Er is clearly not diffusing to the Si and forming neutral complexes in AlGaAs. The diffusion coefficient of Er in GaAs is similar to or even less than that of Er in AlGaAs, further preventing the formation of Er-Si complexes in GaAs:Er. Thus, the n-type carrier removal observed in Er-implanted GaAs is not due to the gettering mechanism, but it is probably due to compensation by the large concentration of unannealed, ion-implantation damage centers, and/or isolated Er deep centers.

While Figure 57 shows a significant reduction in the concentration of deep centers, it does not take into account the possibility that these centers may be moving deeper into the band as the Al mole fraction increases. If this were the case, the deeper centers would not be readily observable with the fast rate window of 29706 s^{-1} used for the measurements shown in Figure 57. Therefore, a rate-window plot was constructed using the same samples and injection biasing sequence described above, but with an emission rate of 0.742 s^{-1} . Figure 59 shows that for GaAs:Er, and $\text{Al}_{0.1}\text{Ga}_{0.9}\text{As:Er}$, hole traps appear in the Er-implanted layers which are absent in the control samples.

Further, since the DLTS signal is moving towards higher temperatures, the deep centers are moving deeper into the band gap with increasing Al mole fraction. That is, these centers are moving away from the valence band and towards the conduction band. However, for the $x=0.3$ and $x=0.4$ samples, there is an electron trap present in the Er-implanted layers, but it is absent in the control substrate. As the Al mole fraction increases, this peak moves towards lower temperatures. Thus, this electron trap is becoming shallower or moving towards the conduction band as the Al mole fraction increases. That is, this electron trap is moving from a position deeper in the band gap towards the edge of the conduction band. Finally, for the sample with Al mole fraction of $x=0.2$, there are no peaks observed in the Er-doped substrate or in the control

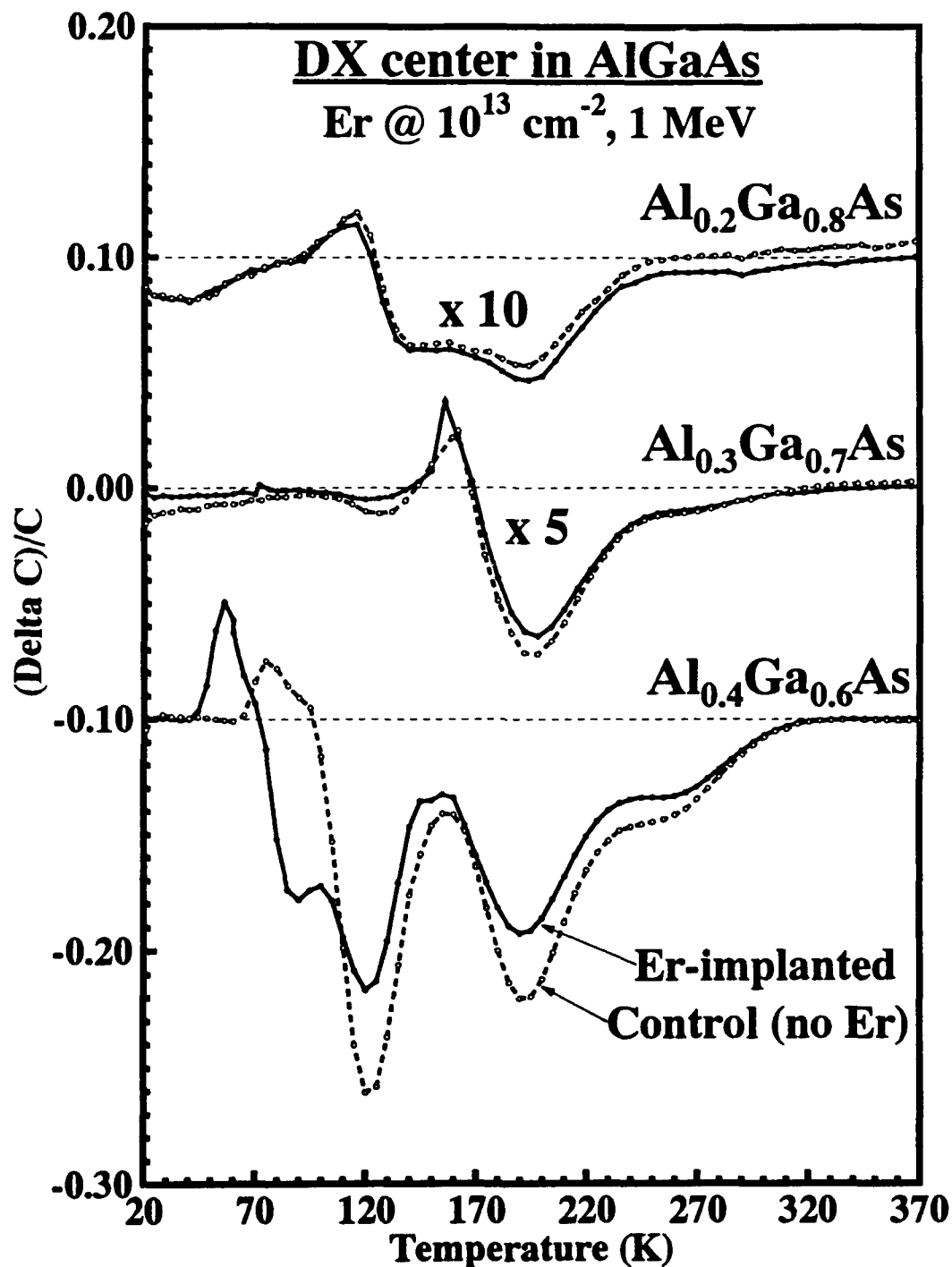


Figure 58. Rate-window plots using majority carrier biasing for n-type $\text{Al}_x\text{Ga}_{1-x}\text{As}:\text{Er}$ for $x = 0.2, 0.3$, and 0.4 with Er implanted at a fluence of $\Phi_{\text{Er}} = 10^{13} \text{ cm}^{-2}$ and an energy of 1 MeV, as well as control samples, which are shown with dashed curves (The deep level observed is the DX center. The rate window used is 29706 s^{-1} .)

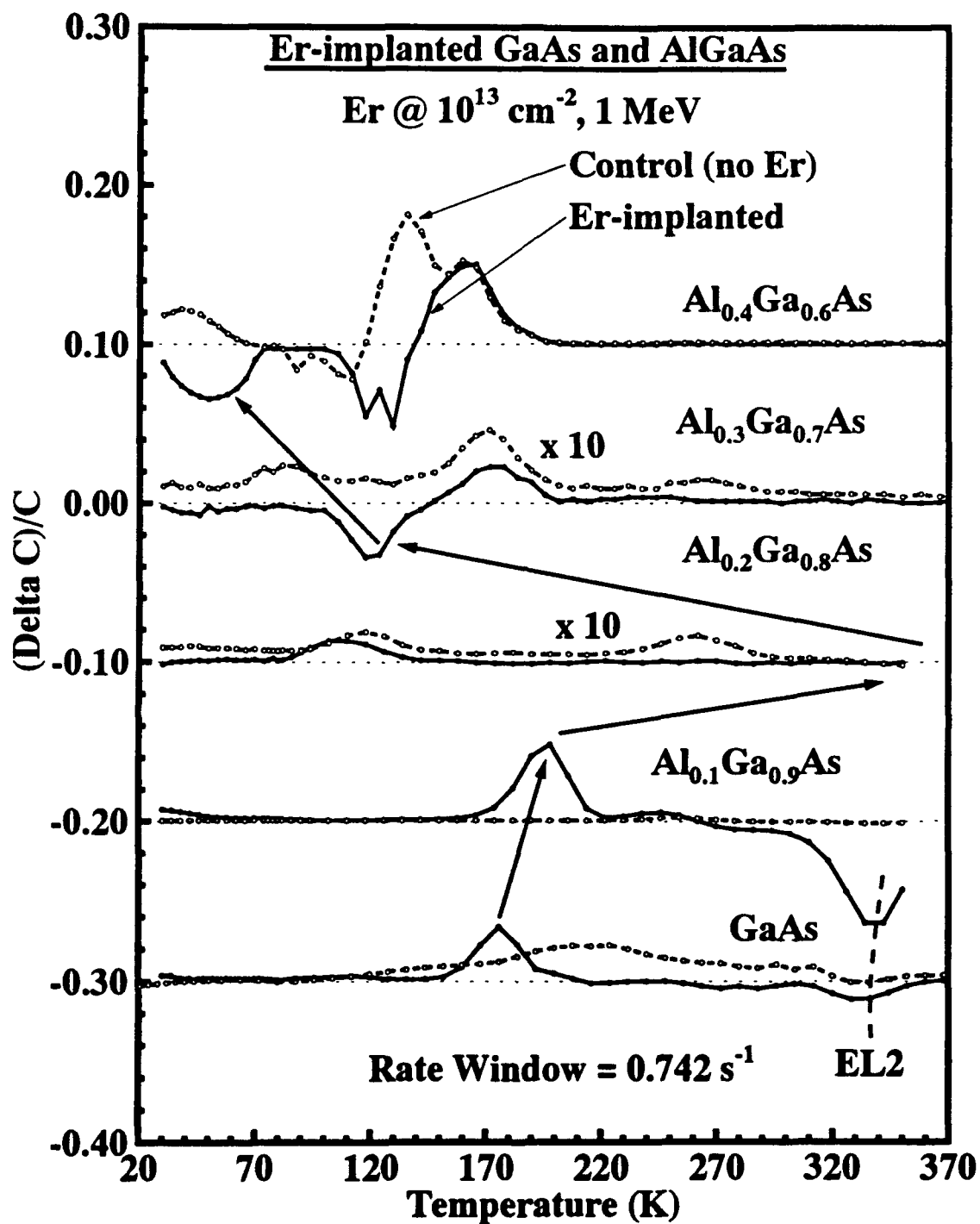


Figure 59. Rate-window plots using injection biasing for n-type $\text{Al}_x\text{Ga}_{1-x}\text{As}:\text{Er}$ for $x = 0, 0.1, 0.2, 0.3$, and 0.4 with Er implanted at a fluence of $\Phi_{\text{Er}} = 10^{13} \text{ cm}^{-2}$ and at an energy of 1 MeV, as well as control samples, which are shown with dashed curves (The rate window is 0.742 s^{-1} .)

substrate. A possible explanation for this behavior of conversion from hole to electron traps is that all these levels correspond to the same center which is acting as a hole trap in GaAs. As the Al mole fraction increases to $x=0.1$, this center (hole trap) moves deeper into the gap away from the valence band. For $x=0.2$, the center (hole trap) is so deep that it is undetectable with the rate window used and the temperature range being scanned. For $x=0.3$, the level has crossed the center of the gap and is now acting as an electron trap, while continuing to move closer to the conduction band for $x=0.4$, where it now has an even shallower activation energy for electron emission.

6.3.3 DLTS Measurements on MBE-Grown, Er-Doped GaAs Several Er-doped GaAs samples were grown by MBE for DLTS measurements. These samples were either heavily or lightly Er-doped, with $[Er] = 4.6 \times 10^{19}$ or $5 \times 10^{16} \text{ cm}^{-3}$.

Table 14 shows the MBE structures grown for the lightly Er-doped samples. These samples were grown with an intentionally small, constant Er-dopant level and varying shallow donor and shallow acceptor concentrations, to investigate whether Er-doped layers grown at low Er concentrations would result in the Er atom preferentially occupying a specific lattice site, giving rise to a corresponding deep center. Further, a small concentration was chosen to avoid the reduction in free electrons observed for the higher Er-doping densities. The nominal shallow doping was varied from one order of magnitude below, to one order of magnitude above, the nominal Er-doping level. This was accomplished in order to attain a maximum sensitivity to deep levels in the event that their concentrations were lower than, comparable to, or greater than the Er-doping density. If the concentration of deep centers were lower than the Er-doping density, the sample with a shallow doping of $5 \times 10^{15} \text{ cm}^{-3}$ would give the best DLTS results. However, if the deep level concentration were similar in concentration to the Er-doping density, the sample with the highest shallow doping of $5 \times 10^{17} \text{ cm}^{-3}$ would give the best DLTS results. Also, if the Er were tending to form complexes with Si or Be, the DLTS signals resulting from these centers would increase with increasingly shallower concentrations.

The DLTS measurements on these samples revealed fairly low concentrations of deep levels, independent of the Si and Be doping, and thus, the Er is probably not forming complexes with Si or Be, which are the most common n- and p-type dopants in MBE-grown GaAs. Therefore, only the samples with the lowest electron or hole concentrations will be discussed. Figure 60

Table 14. Structures for the lightly Er-doped MBE-grown GaAs, consisting of n^+p and p^+n junction diodes with Er in the n-type or p-type material, respectively (The nominal Si and Be dopant concentrations are shown along with the measured free carrier concentrations determined from the CV profiles)

n^+ :
0.15 μm of GaAs:Si, $[\text{Si}] = 10^{19} \text{ cm}^{-3}$, no Er
p
1 μm of GaAs:Er, $[\text{Er}] = 5 \times 10^{16} \text{ cm}^{-3}$ and
$[\text{Be}] = 5 \times 10^{15} \text{ cm}^{-3}$, $p = 2.0 \times 10^{16} \text{ cm}^{-3}$ in x048
$[\text{Be}] = 5 \times 10^{16} \text{ cm}^{-3}$, $p = 1.0 \times 10^{17} \text{ cm}^{-3}$ in x047
$[\text{Be}] = 5 \times 10^{17} \text{ cm}^{-3}$, $p = 5.7 \times 10^{17} \text{ cm}^{-3}$ in x046
SI substrate

p^+ :
0.15 μm of GaAs:Si, $[\text{Si}] = 10^{19} \text{ cm}^{-3}$, no Er
n
1 μm of GaAs:Er, $[\text{Er}] = 5 \times 10^{16} \text{ cm}^{-3}$ and
$[\text{Si}] = 5 \times 10^{15} \text{ cm}^{-3}$, $n = 1.2 \times 10^{16} \text{ cm}^{-3}$ in x051
$[\text{Si}] = 5 \times 10^{16} \text{ cm}^{-3}$, $n = 1.4 \times 10^{17} \text{ cm}^{-3}$ in x049
$[\text{Si}] = 5 \times 10^{17} \text{ cm}^{-3}$, $n = 6.2 \times 10^{16} \text{ cm}^{-3}$ in x050
SI substrate

shows the rate-window plot for samples x048 and x051. The biasing conditions are shown next to the DLTS plot for each measurement, with the first number indicating the pulsing voltage and the second number indicating the measurement bias. A shallow hole trap is observed in sample x051 with injection biasing, while sample x051 exhibits no deep levels under majority carrier biasing. Sample x048 shows a hole trap under both majority carrier and injection biasing. This observation is a consistent result, since under injection biasing, holes are still flowing through

the junction. The peaks agree well with the peak (a) measured in the n-type GaAs substrate 02-PR-1748 implanted with $\Phi_{\text{Er}} = 5 \times 10^{12} \text{ cm}^{-2}$ at 1 MeV, which is repeated in Figure 60 for comparison.

MBE sample x009b was also grown for DLTS with a high Er-doping density of $[\text{Er}] = 4.6 \times 10^{19} \text{ cm}^{-3}$ (Table 15). Unfortunately, at the time this sample was grown, there was no p-type dopant loaded in the MBE, and so in order to form a p^+n junction, a $0.15 \mu\text{m}$ layer at the surface was left undoped for Mg implantation. In addition, this sample was grown with an n^+ layer without Er co-doping so that ohmic contacts could be easily formed. The sample was implanted with Mg at a fluence of $\Phi_{\text{Mg}} = 10^{14} \text{ cm}^{-2}$ and at an energy of 40 keV for the p^+ contact. Mesa diodes were fabricated after annealing at 825°C for 12 seconds or at 750°C for 15 seconds.

Figure 61 shows the rate-window plots for the two annealing conditions. The rate-window plot for the ion-implanted sample with $\Phi_{\text{Er}} = 5 \times 10^{13} \text{ cm}^{-3}$ is included for comparison. Under both annealing conditions, the MBE samples revealed the same center (g) that was observed in the ion-implanted samples, with an activation energy of approximately 345 meV. However, for the sample which was annealed at 750°C for 15 seconds, a hole trap with a very large concentration was formed at roughly 100 to 150 meV above the valence band. In fact, as shown in Figure 61, the concentration of this center was at least an order of magnitude larger than the (g) center observed in the sample annealed at 825°C . Due to the large magnitude of the concentration, the activation energy and capture cross section cannot be accurately determined. The obvious conclusion drawn from these measurements is that between the two annealing temperatures of 750 and 825°C , a center acting as a hole trap, which has a very large concentration, dissociates. This center does not correlate well with any of those previously measured in the ion-implanted samples, and so it may be unique to the MBE growth process.

6.3.4 Summary and Discussion Overall, the DLTS measurements presented in this section indicate that GaAs doped with Er either by ion implantation or during MBE growth, two hole traps are consistently found, one at 35 meV, and the second at 345 meV above the valence band. Additionally, other hole traps observed in Er-doped GaAs, which are probably not directly related to Er-centers or Er-complexes, may be due to impurities or native defects, either already present in the substrate, or incorporated along with the Er. They may be caused by

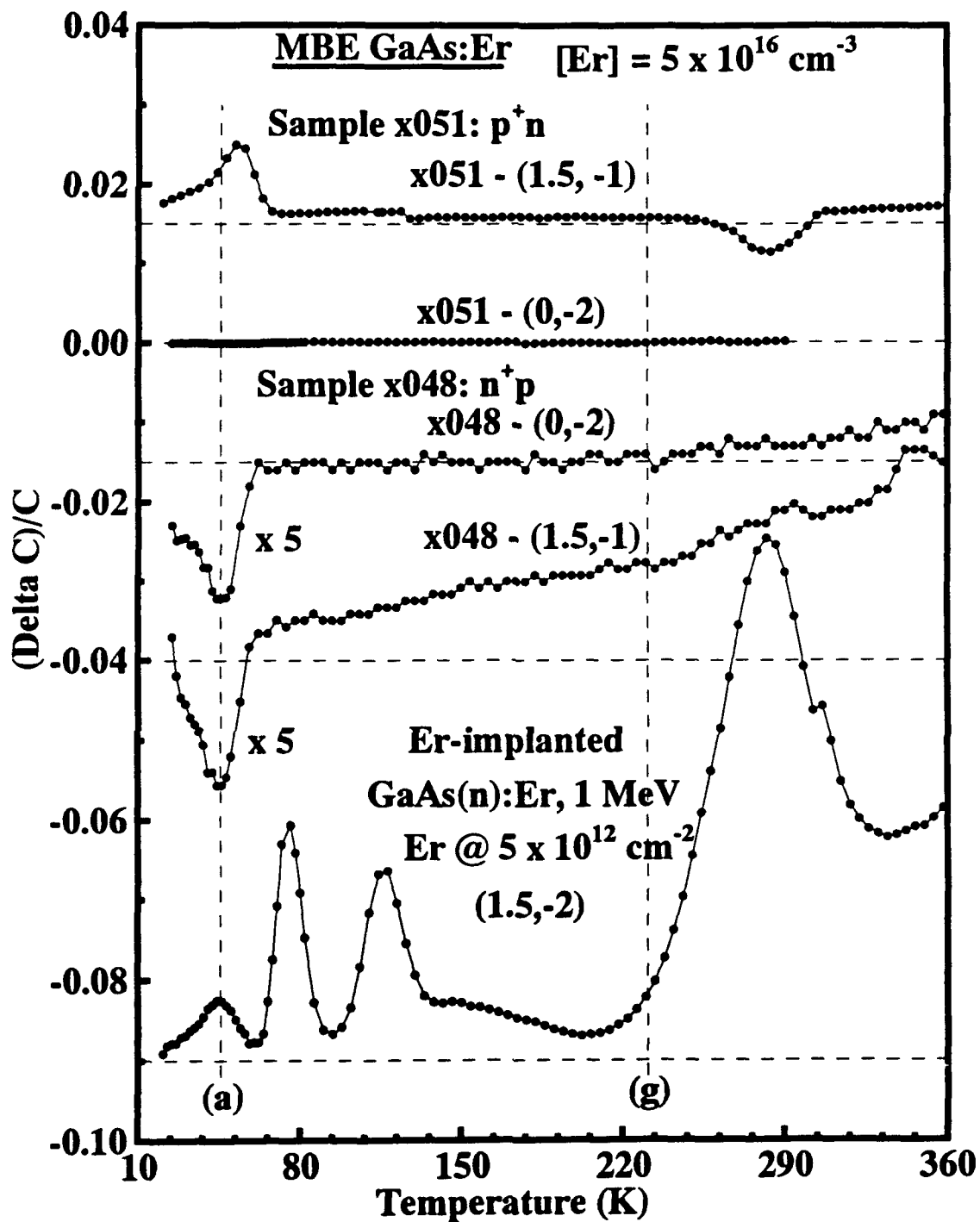


Figure 60. Rate-window plots for MBE-grown GaAs samples x048 and x051 (The measurements are shown for injection biasing and majority carrier biasing. The DLTS measurements for the injection sequence on the n-type GaAs substrate 02-PR-1748 implanted with Er at a fluence of $\Phi_{\text{Er}} = 5 \times 10^{12} \text{ cm}^{-2}$ and at an energy of 1 MeV is shown for comparison.)

Table 15. Structure for the Er-doped MBE-grown GaAs sample x009b; heavily Er doped

p^+ : 0.15 μm of GaAs, no Er to be implanted with $\Phi_{\text{Mg}} = 10^{14} \text{ cm}^{-2}$ at 40 keV
n 2 μm of GaAs:Er $[\text{Er}] = 4.6 \times 10^{19} \text{ cm}^{-3}$, $[\text{Si}] = 2 \times 10^{18} \text{ cm}^{-3}$
n^+ : 1 μm of GaAs:Si, no Er $[\text{Si}] = 10^{19} \text{ cm}^{-3}$

Er-doping or by the processing techniques. For the ion-implanted samples, this is mainly due to the effect of damage to the crystal resulting from the Er implantation process and the subsequent annealing which gives rise to several centers which primarily act as hole traps. In the case of the MBE material, the only other center observed with an appreciable concentration is a trap which has a very large concentration, and it is probably related to the solubility limit in Er in GaAs.

6.3.4.1 Er-Related Centers in GaAs While all deep levels reported in Er-doped samples (and absent in control samples) are related to Er incorporation, they do not necessarily involve an electron transition localized at an Er atom in the semiconductor; that is, an Er-related center. In the ion-implanted material, these centers may be related to damage or annealing treatments. In the MBE material, a specific center may be related to the growth conditions. However, if a center is observed in Er-doped GaAs prepared by ion implantation, as well as in MBE Er-doped GaAs, it is almost certainly related to a transition occurring at an Er atom occupying a specific lattice site, or at an Er atom forming a complex with a native crystal defect. There were two such Er-related centers observed in this study, and both were hole traps.

The first was a very shallow level located 35 meV above the valence band, which only appears to represent a small fraction of the Er doping. This center has not only been observed in n-type GaAs substrates implanted with Er, but also in both n-type and p-type MBE-grown

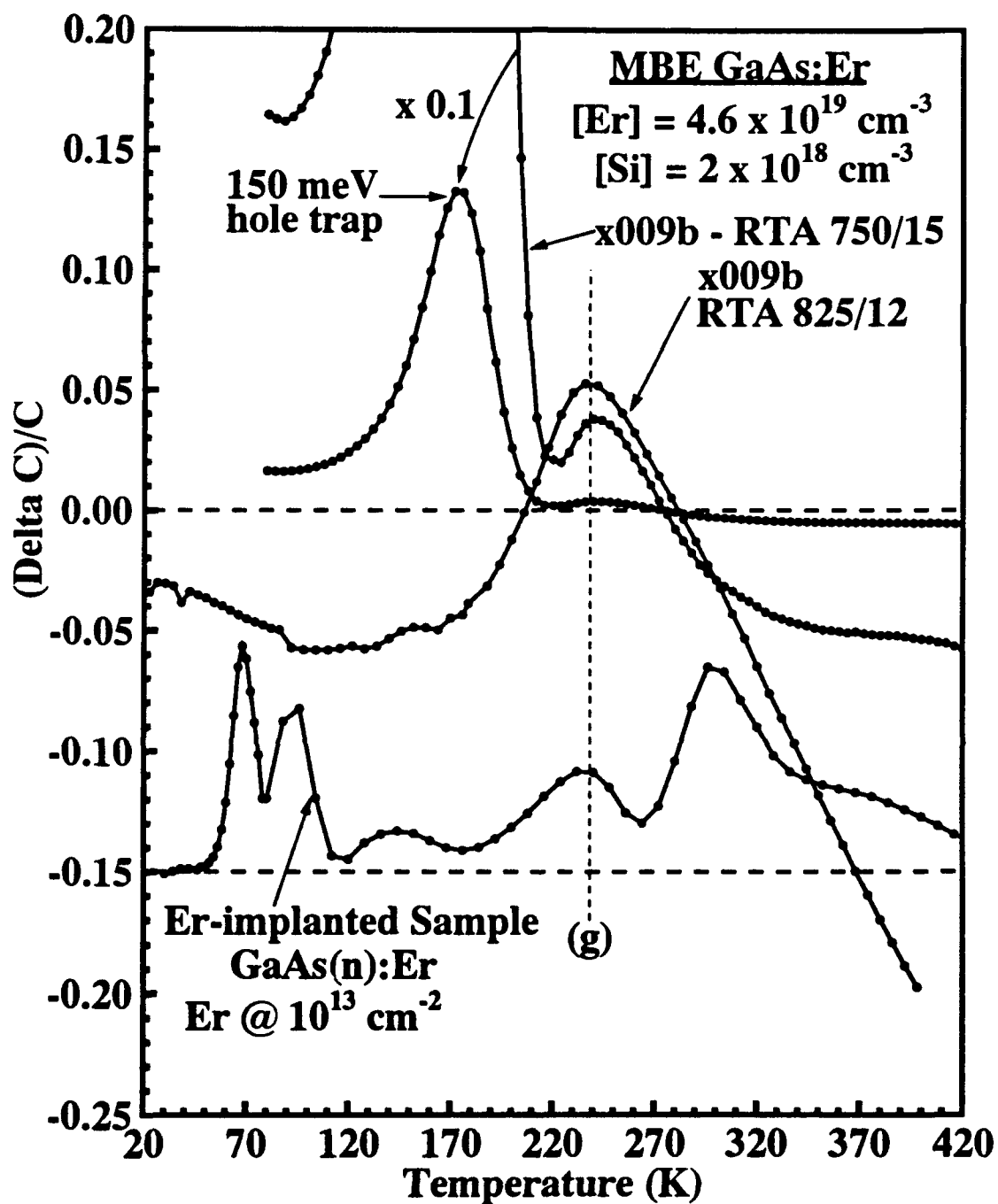


Figure 61. Rate-window plots for the MBE-grown GaAs sample x009b with $[Er] = 4.6 \times 10^{19} \text{ cm}^{-3}$ and annealed either at 750 °C for 15 seconds or at 825 °C for 12 seconds; and for the ion-implanted GaAs sample with Er implanted at a fluence of $\Phi_{Er} = 10^{13} \text{ cm}^{-2}$ and at an energy 1 MeV, all under injection biasing conditions (The rate window is 29706 s^{-1} .)

GaAs lightly doped with Er. However, it has not been observed in non-Er doped control samples. Based upon this observation, it is almost certainly attributable to an Er-related center. Further, since it is observed in both n-type and p-type material, it does not appear to be related to an Er-Si or Er-Be complex. The center has been observed only with relatively small Er-doping densities ($[Er] \lesssim 5 \times 10^{17} \text{ cm}^{-3}$). For instance, in the ion-implanted material, it has been observed only for the sample with Er implanted at a fluence of $\Phi_{Er} = 5 \times 10^{12} \text{ cm}^{-2}$, and not for the two higher fluences of $\Phi_{Er} = 10^{13}$ and $5 \times 10^{13} \text{ cm}^{-2}$, indicating that the damage associated with the ion-implantation process may be interfering with the formation of this center. This center was also detected in the Er-doped MBE-grown GaAs with an Er doping density of $[Er] = 5 \times 10^{16} \text{ cm}^{-3}$, but not with $[Er] = 4.6 \times 10^{19} \text{ cm}^{-3}$, where the 345 meV center dominates.

The very shallow depth of this center is characteristic of an isoelectronic center, which can only weakly bind a free carrier. Various authors have reported that Yb and Er are acting as isoelectronic centers in InP. Whitney et al. (98), using both DLTS and temperature-dependent Hall effect measurements, have reported that Yb doping in InP during MOCVD growth gives rise to a 30 meV electron trap. They claim there is a one-to-one correspondence between the concentration of this level and the Yb-doping density, for dopant concentrations between $[Yb] = 10^{14}$ and $5 \times 10^{18} \text{ cm}^{-3}$. They attribute this center to an isoelectronic 'acceptor-like' electron trap formed by Yb_{In} . Lambert et al. (51), using temperature-dependent Hall effect measurements, confirmed the results of Whitney for Yb in InP, and they also measured a 60 meV electron trap in Er-doped InP, which they attributed to an isoelectronic electron trap. While these authors found that REs were creating a potential attractive for electrons in the InP material, others have suggested that an isoelectronic center may introduce a potential which can attract both electrons or holes. For instance, Seghier et al. (81), using admittance spectroscopy, found that Yb introduces an electron trap in n-type InP at a level 29 meV below the conduction band, while in p-type InP, Yb gives rise to a hole trap located 50 meV above the valence band.

Thus, the 35 meV center seems to be due to an Er atom occupying a Ga site (Er_{Ga}) and acting as an isoelectronic center. However, there are some important differences between the shallow center in GaAs:Er and the isoelectronic trap associated with Yb_{In} in InP. For instance, unlike the case of Yb in InP, Er in GaAs was found to introduce these shallow centers in much smaller concentrations than the Er-doping density. This is, perhaps more a characteristic of the Er atom itself as opposed to the crystal, since Lambert et al. (51) found that the concentration of 60

meV centers in InP:Er was approximately 2% of the Er-doping density for $[Er] = 10^{19} \text{ cm}^{-3}$. The most striking difference between the electrical behavior of Er_{Ga} reported here, and the previous measurements of Yb and Er in InP, is that while the Yb_{In} and Er_{In} yield predominantly electron traps in InP, the Er_{Ga} center has a similar binding energy in the Er-doped GaAs, but it binds a hole instead of an electron.

Bound states associated with an isoelectronic impurity are quite rare. Isoelectronic traps have been found only when the impurity atom is either very large (for example, GaP:Bi and InP:Bi), or very small (for example, GaP:N and ZnTe:O), compared to the host atom (4). That is, only much larger or much smaller atoms can produce an impurity potential strong enough to bind a free carrier. Experimental evidence has not shed much light on the binding mechanisms of isoelectronic traps except for providing evidence for a strong electron-phonon interaction. Based upon observations of this interaction in various systems (ZnTe:O, GaP:N, GaP:Bi), Hopfield et al. (39) claim that an isoelectronic impurity will bind either an electron or a hole according to the 'electronegativity rule': An isoelectronic impurity may bind a hole (electron) only if its electronegativity is smaller (larger) than that of the host atom it replaces. Using the appropriate values in Table 4, Er has an electronegativity of 1.11 by Pauling's method (21:100), which is smaller than the value of 1.81 for Ga. Therefore, the electrical behavior of Er_{Ga} in GaAs is consistent with the empirical rule proposed by Hopfield. Yet, this rule has limited applicability, since it also predicts that Yb_{In} in InP will act as a hole trap given that the electronegativity of Yb is 1.06 and that of In is 1.78. While Yb_{In} has exhibited the tendency to attract holes, Seghier (81:983-984) estimates it is roughly one order of magnitude more likely for Yb_{In} to capture an electron, as it is to capture a hole. Thus, a more careful consideration of the nature of the isoelectronic impurity potential is in order.

In the case of a substitutional impurity with the same valence state as the host atom: it replaces, the impurity potential is given by Jaros (42:222) as

$$V_{imp} = V_{core} + V_{scr} + V_{latt}, \quad (74)$$

where V_{core} is attributed to the difference between the bare core potential of the impurity and the host atom, and this potential is, therefore, confined to the atomic radius of the larger of the two atoms. Additionally, V_{scr} represents the change in electronic potential due to the rearrangement of the valence band electrons in the vicinity of the impurity, and it is generally limited to the first

nearest neighbor. Finally, V_{latt} is a potential expressing the effects of the strain field occurring when a large impurity replaces a smaller host atom.

When V_{core} is large, then $V_{scr} + V_{latt}$ is also large, but in the negative sense, so as to partially cancel V_{core} . For instance, Faulkner (30) was the first to conduct a theoretical study of the isoelectronic trap formed by N_P in GaP. In this treatment, V_{imp} was given only by V_{core} , which was taken to be the difference in the atomic pseudopotentials of nitrogen and phosphorous. Faulkner found that the resulting impurity potential was attractive to electrons, had a range of about 0.5 \AA , and produced a bound state in the gap with a depth of about 1 eV. This value was approximately 2 orders of magnitude larger than the experimentally observed value. Reasonable agreement was obtained only after scaling the potential by a factor of 0.5. Phillips (68) generalized Faulkner's results to all other isoelectronic systems by showing that if V_{imp} is assumed to be given only by the difference in atomic pseudopotentials, then, in all cases, the binding energy is on the order of 1 eV. Since, in general, experimental evidence shows the binding energy to be two orders of magnitude smaller, Phillips suggested that the lattice deformation around the impurity was of critical importance. A deeply-bound state like those calculated by Phillips and Faulkner would correspond to an extremely localized charge distribution, which would act on nearby nuclei to produce a strong relaxation in the lattice, giving a large V_{latt} . The valence electrons around the nuclei would also readjust themselves to give a large V_{scr} term. Phillips estimated that these new terms compensated for the binding forces due to the core difference, and thus, greatly reduced the binding energy.

Baldereschi (4) carried the analysis further by incorporating more terms into the impurity potential. He took V_{core} to be given by the difference in core pseudopotentials, including the spin-orbit contributions, which are more important for heavy impurities. Additionally, this potential was screened by V_{scr} using the dielectric function which represents the local electron density. Baldereschi observed that within a given isoelectronic sequence, the atomic pseudopotentials were generally deeper for the lighter atoms compared to the heavier atoms. This relationship implies that if the host atom is replaced by a heavier (lighter) atom, the impurity potential will be attractive to holes (electrons). Further, for a given isoelectronic sequence, the electronegativities decrease with heavier elements (4:85). Therefore, if the isoelectronic impurity is heavier (lighter) than the atom it replaces, then it is likely to be less (more) electronegative relative to the host atom, and consequently, it will be attractive to holes (electrons). Thus, Baldereschi presented a

theoretical foundation for the electronegativity rule. In addition, he pointed out that the relativistic effects due to spin-orbit coupling can considerably modify the impurity potential, especially in the case of a heavy impurity. These relativistic corrections vanish if the impurity wave function is spherically symmetric. Therefore, corrections are expected for hole traps with wave functions that are mainly p-like, but not for electron traps with wave functions that are mainly s-like. Thus, Baldereschi found (4:87) that the spin-orbit interaction increased the hole binding energy, and was indeed more significant for heavier atoms. For example, for GaP:As and GaP:Sb, the spin orbit contribution to the impurity potential is approximately 20%, while for GaP:Bi it is 40%.

Contrary to these authors, Allen (1:85) claimed that in the majority of cases where there is a significant impurity potential, V_{latt} and the effects of spin-orbit interaction will be the dominant terms. Allen closely examined atomic pseudopotentials and found that, aside from the elements in the first row of the periodic table, within a group, the pseudopotentials are very similar. Thus, if other terms of the impurity potential are also small, the center may act to scatter carriers, but it will not produce a bound state. This situation applies to most of the isoelectronic centers, and it accounts for the sparseness of the observation of isoelectric centers. An impurity from the first row of the periodic table has a pseudopotential substantially different from that of the other members of the group, except for the case of Be. In fact, due to the lack of many core electrons, the use of the pseudopotential in this case is a poorer approximation. However, it is clear that the first row elements have a narrower but usually deeper potential. Depending upon which of these attributes is dominant, the impurity will attract electrons and repel holes or vice versa. Also, a heavy atom replacing a lighter one can attract a carrier associated with the valence band edge whose degeneracy has been lifted by spin-orbit coupling. Within the tetrahedrally coordinated semiconductors, the valence band is usually split, but the conduction band is not, and thus, the holes are attracted to a heavy atom, while electrons are not. In other classes of materials, for instance, the II-VI compounds with two degenerate bands, the isoelectronic impurity may create a potential which is simultaneously attractive to both holes and electrons. Finally, an impurity potential which differs in size from the host atom will produce a strain field in its vicinity. A degenerate band edge is split by this shear in such a manner that an attractive potential is felt by a carrier at the band edge. Further, this result is independent of the charge of the carrier or whether the impurity is larger or smaller than the host atom. Thus, in GaP, where both the conduction and valence bands are degenerate, the strain field is attractive to both holes and electrons.

The electronegativity rule has failed to give a consistent picture of whether a rare earth ion will bind a hole or an electron when occupying a cation site in a III-V semiconductor. That is, Er_{In} and Yb_{In} in InP yield electron traps, while Er_{Ga} in GaAs produces a hole trap. In all of these cases, the electronegativity rule predicts that the RE_{III} should produce a hole trap. These results are partly in agreement with the theory proposed by Allen. Specifically, based upon the ionic radii listed in Table 4, the Er^{3+} ion is 42 % larger than the Ga^{3+} ion, while the Yb^{3+} and Er^{3+} ions are only approximately 6% larger than the In^{3+} ion. Therefore, Er_{Ga} in GaAs is much more likely to form a hole trap by virtue of the fact that it produces a more significant strain field than does Er_{In} or Yb_{In} in InP.

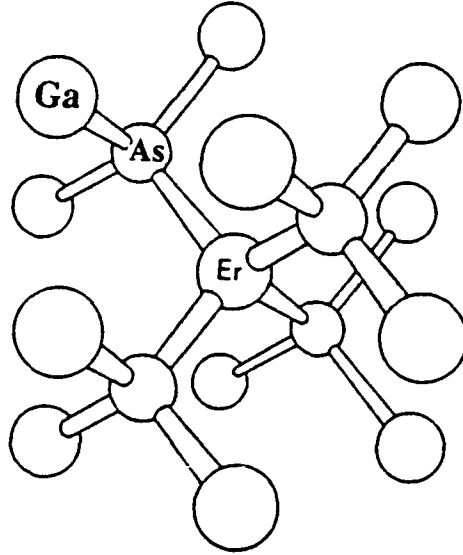
Another possible cause for Er giving rise to hole traps is that it has a higher angular momentum ground state, $J = 15/2$, while $J = 7/2$ for Yb in the ground state. Thus, the spin-orbit interaction would be approximately twice as large for Er as for Yb. However, Er_{In} has been observed to give rise to a 60 meV electron trap in InP which is even deeper than the 30 meV electron trap given by Yb_{In} in InP. Thus, the spin-orbit interaction is probably not as important for the rare earths as is the strain effect.

Apparently the theory of Allen does not predict why Yb and Er in InP yield isoelectronic electron traps. In fact, neither the theory of Allen nor that of Baldereschi addresses this point. Allen's prediction was that, aside from elements of the first row of the periodic table, an isoelectronic impurity from the same group as the element being replaced has essentially the same pseudopotential, and so it will not give rise to a deep state. However, the REs essentially form their own group, and therefore, they would not have a comparable pseudopotential to the group III atoms. Similarly, when Baldereschi formulated his theoretical explanation for the electronegativity rule, he was comparing elements in the same group of the periodic table. It seems likely that in the case of Yb and Er in InP, since they are approximately the same size as In, the difference in core potentials between the impurity and host will dominate V_{imp} . The substantially different pseudopotential of the RE as compared to that of the group III element apparently causes them to behave as electron traps. On the other hand, for the case of the REs in GaAs, where the RE atom is roughly 40% larger than the Ga atom, the substantial contribution to V_{imp} should be given by the strain field; i.e., V_{latt} . According to the theory of Allen, this potential should be attractive only to holes, since only the valence band is degenerate in GaAs. In the present study, the observation that Er_{Ga} in GaAs yields a 35 meV hole trap is consistent with

this interpretation. Similarly, DLTS measurements performed by Taguchi et al. (88:3391) on GaAs:Yb also agree with this interpretation. Schottky diodes were formed on n-type, Yb-doped MOCVD-grown GaAs, and majority carrier biasing was conducted, allowing only the detection of electron traps. Unlike InP:Yb, these measurements did not detect a shallow isoelectronic electron trap, but only a very deep electron trap between 0.5 and 0.7 eV. Unfortunately, these researchers did not check for the presence of shallow hole traps in this material, which could have been done by performing optical DLTS measurements on the Schottky diodes. Optical pulsing would generate holes, which would then be available for capture. Nevertheless, these results are consistent with the present interpretation of V_{imp} , since shallow electron traps were not observed.

A more accurate view of RE isoelectronic centers should also take into account the 4f-core levels. For instance, Robbins and Dean (76:516) discussed two situations in which the isoelectronic RE can give rise to a hole attractive potential. The first occurs when the highest filled electron level of the RE^{3+} core lies within the band gap. In this case, an approaching hole may be captured directly into the core so that it becomes a RE^{2+} ion. A second case, considered more likely for the RE atoms, occurs when the highest filled electron level of the RE^{3+} core is resonant with the valence band, but has an empty electron level lying in the gap. Since this higher level excited configuration possesses a filled core level in the gap, then by analogy with the previous case, it will also produce a potential attractive to holes. Hence an admixture of the excited state configuration and the ground-state configuration could introduce a short-range potential attractive to holes. In fact, the electrostatic perturbation produced by the approaching hole may itself cause this required configurational admixture to generate this hole-attractive potential. Because this potential arises in a higher order approximation, it is expected to produce a much shallower level compared to the previous case.

This interpretation of the RE core contribution to the isoelectronic impurity potential fits well with recent numerical calculations of an isolated Er_{Ga} in GaAs by Saito and Kimura (79). Using a self-consistent, local-density-functional DV-X α cluster calculation with a cluster of 17 atoms (Figure 62), the one-electron 4f-levels were found to appear just above the valence band (they do not give hard numbers). Such localized levels lying just inside the band gap could give rise to the hole-attractive potential specified by Robbins and Dean. Alternatively, even if their calculations are off slightly and the highest filled 4f electron level is actually resonant with the valence band, then their second model may be more applicable. However, this latter model



ErAs₄Ga₁₂

Figure 62. ErAs₄Ga₁₂ cluster used in the local-density-functional DV-X α cluster calculations by Saito and Kimura (79)

would predict a center which may appear to be dependent upon the free hole concentration. In fact, this model may reflect the situation for the isolated Er_{Ga} center, since in the present study, the (a) center has a much smaller concentration, as measured by DLTS, than would otherwise be expected. That is, a relatively large fraction of the Er atoms should occupy Ga sites and act as isoelectronic centers.

The second hole trap, center (g), has a much larger concentration and an activation energy of approximately 345 meV. This trap has been observed in n-type, Er-implanted GaAs as well as in n-type GaAs:Er by MBE growth. Also, p-type conductivity was observed in an MBE GaAs:Er sample with $[Er] = 1.3 \times 10^{18} \text{ cm}^{-3}$. Temperature-dependent Hall effect measurements indicated the presence of a single acceptor level located 342 meV above the valence band. This center was observed at higher Er concentrations ($[Er] \gtrsim 10^{18} \text{ cm}^{-3}$), both in the ion-implanted material and in the MBE-grown material. In the ion-implanted material, the 340 meV center was observed for only the two higher Er fluences of $\Phi_{Er} = 10^{13}$ and $5 \times 10^{13} \text{ cm}^{-2}$, which have Er peak concentrations of 7.6×10^{17} and $3.8 \times 10^{18} \text{ cm}^{-3}$, respectively, but not in the lowest Er fluence of $\Phi_{Er} = 5 \times 10^{12} \text{ cm}^{-2}$, which has an Er peak concentration of about $3.8 \times 10^{17} \text{ cm}^{-3}$. Similarly,

DLTS measurements of the MBE GaAs-doped sample with $[Er] = 4.6 \times 10^{19} \text{ cm}^{-3}$, showed the presence of this center, which was not observed for samples with $[Er] = 5 \times 10^{16} \text{ cm}^{-3}$.

Results for heavily Er-doped GaAs may be correlated with Rutherford backscattering (RBS) measurements performed on Er-implanted GaAs and Er-doped MBE-grown GaAs. Kozanecki et al. (49) performed RBS measurements on GaAs substrates implanted with Er at a fluence of $\Phi_{Er} = 10^{15} \text{ cm}^{-2}$ and an energy of 150 keV. These samples were annealed at temperatures between 700 and 1000 °C. For the lower annealing temperatures, the Er atoms were displaced from their substitutional positions on the $\langle 100 \rangle$ row towards the middle of the $\langle 110 \rangle$ channel. As the annealing temperature was increased, the Er atoms monotonically approached their substitutional positions. In fact, after annealing at 1000 °C for 30 seconds, only 3% of the Er atoms were displaced from the $\langle 100 \rangle$ row. Kozanecki attributed the tendency of the Er atom to occupy an interstitial position, Er_i , to the high chemical reactivity of the Er atom and its tendency to break the Ga-As bonds and form ErAs. The M-V bond lengths were much different in these two compounds. That is, the Er-As bond (0.28 nm bond length) was much larger than the Ga-As bond (0.24 nm bond length). However, only a 1.6% mismatch occurred in the lattice constants of GaAs and ErAs due to the differences in the coordination of these two compounds, with the Ga being 4-fold coordinated in a tetrahedral zinc blend structure, and the Er being 6-fold coordinated in a cubic NaCl structure. The mismatch existed only along the $\langle 100 \rangle$ direction. Thus, Er apparently did not occupy the same lattice position as Ga. Due to the 6-fold coordinated structure, Er was displaced in the $\langle 110 \rangle$ direction. As the annealing temperature was increased, the Er atoms moved to substitutional positions, indicating that the Er was occupying tetrahedral lattice sites in GaAs. Kozanecki also measured the Er-4f PL as a function of annealing temperature, and found it to be completely extinguished upon annealing at 1000 °C for 30 seconds, where most of the Er atoms are substitutional, indicating that this center is not optically active.

Galtier et al. (32) have performed similar RBS measurements in GaAs:Er grown by MBE with $[Er] = 6 \times 10^{18} \text{ cm}^{-3}$. These researchers measured 86% of the channeling along the $\langle 100 \rangle$ direction, but only 69% along the $\langle 110 \rangle$ direction, indicating that although the majority of the Er is incorporated into substitutional positions, a significant fraction occupies tetrahedral and octahedral interstitial lattice sites.

These measurements are all consistent with DLTS results obtained in this investigation. First, an Er_i center was expected to form a much deeper level than an Er_{Ga} causing much less of

a disruption in the crystal lattice. Secondly, the formation of ErAs compounds was more likely with higher Er concentrations, since the presence of Er in second-nearest neighbor positions is expected to enhance the formation of the ErAs precipitates. Thus, for lower Er-doping densities, the Er is probably more likely to occupy Ga sites in a tetrahedral structure, giving relatively shallow isoelectronic traps, or center (a). In the ion-implanted material, this center has been observed only in the Er-implant with the smallest fluence, $\Phi_{\text{Er}} = 5 \times 10^{12} \text{ cm}^{-2}$, and it is absent for the two higher Er fluences, $\Phi_{\text{Er}} = 10^{13}$ and $5 \times 10^{13} \text{ cm}^{-2}$. Similarly, in the MBE samples, the isoelectronic center was observed only in the sample with $[\text{Er}] = 5 \times 10^{16} \text{ cm}^{-3}$, and it has not been detected for the highly Er-doped samples with $[\text{Er}] = 4.6 \times 10^{19} \text{ cm}^{-3}$. Conversely, the deeper center (g) at 345 meV has been observed in Er-implanted GaAs only for $\Phi_{\text{Er}} \geq 10^{13} \text{ cm}^{-2}$. Also, center (g) has been observed in the Er-doped MBE-grown GaAs sample with $[\text{Er}] = 4.6 \times 10^{19} \text{ cm}^{-3}$, but it is absent for $[\text{Er}] = 5 \times 10^{16} \text{ cm}^{-3}$.

Finally, in the MBE material, a center with a very large concentration has been detected in the vicinity of 100–150 meV above the valence band. This center has been found to dissociate when annealed between 750 and 825 °C, and it has only been observed at high Er-doping densities ($[\text{Er}] = 4.6 \times 10^{19} \text{ cm}^{-3}$), which exceeds the solubility limit of Er ($[\text{Er}] \approx 7 \times 10^{17} \text{ cm}^{-3}$) reported by Poole (72). It is difficult to determine whether this center is primarily attributable to the effect on the crystal structure due to the formation of ErAs micro-precipitates or to an Er-related center. Further studies are necessary to resolve this question.

6.3.4.2 Non Er-Related Hole Trap in GaAs In addition to the Er-related centers, other centers have been found to act as hole traps in Er-doped GaAs. They are probably related to unintentionally-doped impurities or to the effect of Er on the crystal structure. That is, the available evidence suggests that they are not caused by transitions occurring directly at an Er-center. The centers (b), (c), (e), (i), (j), and (k) observed in the Er-implanted layers seem to fall into this category.

Center (c) has an activation energy for hole emission that is approximately 77 meV, which is attributable to the first acceptor level of the Ga antisite defect, Ga_{As} (14:R74). This level was first seen in material grown with a Ga-rich melt, where Yu and Reynolds (105) observed p-type conductivity and a photoluminescence peak at 1.44 eV. The behavior of this luminescence with temperature, excitation energy, and intensity indicates that it is due to an acceptor level located

77 meV above the valence band. It has also been investigated using the temperature-dependent Hall effect by Ta et al. (87) and by Yu et al. (104). Ta actually considered this center to be related to boron incorporation, suggesting that it was a complex of boron and an intrinsic defect. However, its concentration does not correlate well with that of boron, and infrared absorption measurements performed by Elliot et al. (26) confirm that this defect has T_d symmetry. Since it was found that B does not occupy such sites, it was concluded that this center was almost certainly due to the Ga_{As} . Furthermore, Yu et al. (104:532) have fit their temperature-dependent hole concentration with two centers, one at 71 meV and the second at 199 meV above the valence band, claiming that this second level is due to the second acceptor level of Ga_{As} . They have also performed DLTS measurements, and they found a hole trap with an apparent activation energy of 130 meV, but claim that this center has an activated capture cross section given by

$$\sigma = \sigma_{\infty} \exp(-E_{\infty}/kT) = 7.1 \times 10^{-15} \text{ cm}^{-2} \exp(-50 \text{ meV}/kT). \quad (75)$$

The activation energy of the capture cross section is subtracted from the apparent activation energy to obtain the true depth of the level, 80 meV. Yu concluded that the first acceptor level of Ga_{As} was responsible for the hole trap he observed by DLTS. Evidently there is a large discrepancy between the results from the present study and the only other reported measurement of the Ga_{As} centers by DLTS. In the present study, center (c) has been observed in almost all implanted samples with an apparent activation energy of 77 meV, which agrees well with the Hall effect measurements, without the need to deduct an activated capture cross section. This center, therefore, does not have an activated capture cross section. The cause of the discrepancy may be that Yu et al. performed the DLTS measurements on a sample which was not controllably doped with shallow acceptors. Although these researchers detected the presence of C, which acts as a shallow acceptor in GaAs, with spark source mass spectrometry, its concentration was reported to be less than the concentration of the 77 meV center obtained by their DLTS measurements. Therefore, Yu et al. simply formed Schottky diodes on the undoped sample which was p-type due to the presence of Ga_{As} centers. In effect, these researchers have used the Ga_{As} acceptors to measure the Ga_{As} , instead of the usual DLTS procedure in which a larger concentration of a much shallower center is used to provide the carriers necessary to charge the deep centers to be measured. This procedure is not recommended, because as the temperature is decreased, the center freezes out, and virtually no holes are available to charge the centers (the only holes available are coming from this center itself). In fact, the activated capture cross section reported

in equation (75) by Yu et al. is possibly due to the activation of the hole concentration. As there have been no other reports of measurements of this center by DLTS, the first direct measurement of the center by DLTS has been performed in this investigation.

Further evidence that this center is Ga_{As} evolves from the observation that it exhibits a field-enhanced emission as shown in Figure 46. According to the Poole-Frenkel theory, the emission is enhanced when the empty trap is charged, and thus, the trapped hole experiences a longer range coulomb potential. The hole emission from this center corresponds to the transition



The centers (d-e) have, however, shown some signs of possessing temperature-dependent cross sections. Figure 48 reveals that the measured transients increase in both amplitude and time-constant magnitude with increasing temperature. Such behavior is indicative of incomplete capture during the trap-charging phase of the bias sequence, due to either a temperature-dependent capture cross section or to a center with a very large concentration. This center can be confirmed to have a large concentration with the observation that $\Delta C/C \gtrsim 0.1$. This atypical Arrhenius behavior is observed only with the two higher Er implant fluences, $\Phi_{\text{Er}} = 10^{13}$ and $5 \times 10^{13} \text{ cm}^{-2}$. In order to determine if this center has a temperature-dependent capture cross section, it would be necessary to independently measure the capture cross section. This was not possible because of equipment limitations. The sample implanted with $\Phi_{\text{Er}} = 5 \times 10^{12} \text{ cm}^{-2}$ has shown normal Arrhenius behavior, and it yields an activation energy of $E_T = 150 \text{ meV}$, and a capture cross section of $\sigma = 3.5 \times 10^{-15} \text{ cm}^2$. A level with this energy has been reported by Lang and Logan (54:1058) (Table 12), who attributed it to a Cu-related center. However, in the current study, measurements accomplished on Cu-implanted GaAs in p-type material have resulted in a center with a much different behavior, as indicated in the rate-window plot in Figure 50. The shallow center detected in these samples had an activation energy of $E_T = 116 \text{ meV}$, and a very large capture cross section ($\sigma = 6 \times 10^{-12} \text{ cm}^2$). Thus, the center (e) is most likely not due to Cu contamination, but to a native defect which was enhanced by the implantation process.

In contrast, the DLTS measurements performed on the Cu-implanted GaAs shown in Figure 50 indicate that the shallower center associated with the Cu atom has an emission which is very similar to that of center (b). In fact, taking into account the uncertainties of the measured

activation energies for center Cu1 and (b), these could be the same center with an activation energy of approximately (100 ± 20) meV. Lang (54) reported the activation energy for this Cu-related center to be approximately 140 meV. However, the signal he obtained for this center seems relatively weak, and so there could be a large uncertainty in the value he reported. Also, he did not give a capture cross section, and this prevents a direct comparison of the Arrhenius behavior of his Cu-related center with that observed for Cu1 and (b) in this investigation.

The original interpretation given to the two Cu-related levels by Milnes (63:49), presumably Cu1 and Cu2, was that they were different charge states of the same defect Cu_{Ga} . With the 140 meV center corresponding to $\text{Cu}_{\text{Ga}}^{-1}$, and the 440 meV center HB4 being attributed to $\text{Cu}_{\text{Ga}}^{-2}$. However, if center (b) is in fact related to Cu, the results from this investigation conflict with the above interpretation since field dependence was not observed for center (b) (Figure 46). Data from this investigation indicates that this center was neutral before capturing the hole. Other measurements have been performed by Willman (101; 100), indicating that these two Cu levels have different site symmetries. Lang also confirmed this finding, noting that the concentrations of these two Cu-related centers are not equal, as would be expected if they were merely different charge states of the same center.

The concentration of center (b) increases in the extremities of the implant region relative to the Er-implanted region. This behavior could be related to diffusion of the Cu impurities from the substrate into the implanted region. Since the Cu primarily diffuses interstitially, the large amount of implant damage which exists nearer the surface is expected to interfere with the diffusion. However, center (b) does not manifest itself in any of the p- or n-type control substrates, indicating that if center (b) is indeed related to Cu, it must be a complex of Cu and a defect produced by the heavy ion implantation; i.e., a center which would otherwise not form in the control sample.

Another explanation concerning the origin of center (b), if it is indeed Cu-related, is that since this center has been consistently observed in the Er-implanted layers, but not observed in the control samples, which were treated alike in all respects except for the Er-implantation, then the Cu could have been introduced during the implantation of Er. The Er source used to generate Er ions consists of 99.999% pure Er_2O_3 which was pressed with small beads of Cu into an Al cylinder. This mixture was then sputtered with a 6 keV cesium beam (69:98). At high temperatures, Cu_2O will form preferentially relative to CuO (21), which has a mass that is

approximately 143 amu. This mass is much less than the mass of Er which is 168 amu, and so it would normally not be directed to the target by the ion implanter's electrostatic mass analyzer. However, if Cu_2O were produced in much large quantities, and if only a small fraction of this species were passed, it could account for a detectable concentration of Cu-related deep centers.

Several hole traps in the range of $E_T = 0.3$ to 0.55 eV were observed in this investigation (centers labeled (g), and (i) through (k)). Center (g) is probably due to Er, or more specifically to an Er_i . Centers (i) and (j) appear to be related to implantation damage, since both have been observed in the Er and Pr-implanted samples, but have not been observed in the control substrates.

A center with activation energy similar to that of (i) has been reported in as-grown VPE GaAs by Mitonneau et al. (64:667), designated as HL5, and by Lang and Logan (54:1058) in as-grown LPE material, designated as HB5. According to Lang (54:1059), this center is so regularly observed that it must be due to a native defect or unavoidable chemical impurity always present in the growth system. It seems unlikely that center (i) is HB5 or HL5, since, as shown in Table 12, these centers have a capture cross section which is nearly two orders of magnitude larger than the value observed for center (i). Thus, center (i) is possibly a defect caused by ion implantation.

A center with activation energy similar to that of (j) has been reported in GaAs:Cu by Mitonneau et al. (64:667) after diffusing Cu into VPE GaAs, and by Lang and Logan (54:1058), after adding Cu to the Ga melt in LPE-grown GaAs. The values obtained by these researchers are given in Table 12. The measurements obtained with the Cu-implanted GaAs in this investigation for the second Cu-related hole trap did not agree well with the Arrhenius behavior of center (j). In fact, the Arrhenius behavior of Cu_2 detected in the Cu-implanted sample agrees much better with HB4, the center attributed to Cu, as measured by Lang (Figure 51). The signature of center (i) is also very close to the signature for Cu_2 as well as HB5. Therefore, this center cannot be conclusively ruled out as being related to Cu impurities.

Center (j) and possibly (i) seem to be related to ion-implantation damage. Most studies on the effect of damage to the crystal structure have been accomplished using high-energy electron irradiation. Of these, most work has been performed on electron traps in n-type material. Five electron traps (E centers) resulting from irradiation, labeled as E1 — E5, and situated at $E_c - 45$ meV, $E_c - 140$ meV, $E_c - 300$ meV, $E_c - 760$ meV, and $E_c - 960$ meV, have been reported as a result of electron-irradiation. Their properties are discussed in the review

article by Pons and Bourgoin (71:3844). Studies of the independence of the introduction rates of these defects in substrates with varying impurity concentrations indicate that they are all due to intrinsic defects, or more specifically, interstitials and vacancies (71:3850). Further, their dependence on the orientation of the electron beam implies that they are contributed primarily from the As sublattice (71:3847). Finally, all of these defects anneal according to first order kinetics, with typically greater than 90 % of the defects annealing in the vicinity of 200 °C, which is consistent with the recombination of the vacancy interstitial pair (71:3847). Thus, the E centers are most likely due to a distribution of $V_{As}-As_i$ centers. Additionally, $V_{Ga}-Ga_i$ centers are also invariably produced during irradiation, but they are expected to recombine immediately, even at lower temperatures, due to a coulomb attraction between the V_{Ga} and Ga_i (71:3847).

Pons reviewed (71) many studies on defects caused by electron irradiation which act as electron traps. In p-type material, fewer studies have been performed. The irradiation-induced defects acting as hole traps are labeled H0 — H5, and they are situated at $E_v + 60$ meV, $E_v + 250$ meV, $E_v + 420$ meV, $E_v + 540$ meV, $E_v + 790$ meV, and $E_v + 850$ meV (84). Contrary to the case of electron traps in n-type material, these defects have a nature and a concentration which depend strongly on the type and dopant concentration in the material (58), indicating that they are complex defects formed by the association of intrinsic defects with impurities present in the material. Stievenard et al. (84:4049) conducted extensive studies on the annealing behavior of these centers in p-type material, and they found that H0 and H1 are related to vacancy-interstitial pairs, while H2–H5 are complex defects involving As_i and impurities contained in the material. Further, these defects anneal in the vicinity of 200 °C with an activation energy of 0.5 eV, and thus, the thermal annealing of these complex defects appears to occur through the mobility of the As_i .

A critical finding from the work of Stievenard et al. (84:4053) was that annealing treatments caused the H2 trap at $E_v + 420$ meV to manifest the behavior of two distinct centers, with a split DLTS peak. These two traps were designated as H2 and H2", with characteristics, $E_v + 360$ meV, $\sigma_p = 2.5 \times 10^{-15} \text{cm}^{-2}$, and $E_v + 440$ meV, $\sigma_p = 6.9 \times 10^{-15} \text{cm}^{-2}$, respectively. Based upon the previous work done with Cu-doped GaAs, Stievenard speculated that the impurity involved in these As_i -impurity complexes was indeed Cu.

The energies reported for H2 and H2" are very similar to the energies obtained for centers (i) and (j) in this investigation. In fact, any differences in the trap energies and capture cross

sections are probably related to the uncertainties involved in obtaining the emission rates for such closely spaced centers. Further, Stievenard did not specify the means by which the respective temperature-dependent emission rates were determined for these two centers. If the standard rate-window analysis was used, as opposed to analyzing isothermal capacitance transients for double exponential decays, then activation energies and capture cross sections in the Stievenard study could have had relatively large uncertainties.

Finally, center (k) has been observed in the p-type, Er-implanted sample with $\Phi_{Er} = 5 \times 10^{12} \text{ cm}^{-2}$, as well as in the unimplanted control sample (Figure 52). This center is also probably present in the n-type Er-doped samples as manifested in the rate-window plots in Figure 45, but it is less clear in this case. Nevertheless, center (k) is evident in the Pr-implanted samples as shown in Figure 49. The activation energy and capture cross section of this center agree well with a level HB3 reported by Lang (54) in Fe-diffused samples. Since it appears in the control samples, as well as in the Er-implanted samples, it may indeed be related to an Fe impurity introduced during growth or diffused from the substrate during growth or annealing. In Figure 52 and 49, the concentration of (k) increases with increasing Er and Pr fluence, further supporting the conclusion that this center is a complex between Fe and a native defect. This center has a similar activation energy value compared to H3 reported by Stievenard(84), and as stated above, H3 is an As_i -impurity complex, in agreement with the results in this investigation. Thus, center (k) may be attributed to an As_i -Fe complex.

6.3.4.3 Effect of Er Implantation on EL2 and M3 Electron Traps The effect of Er-doping on native defects already present in the substrate is of interest because in many instances their microscopic nature is known. An increase or decrease in their concentrations with Er-doping is indicative of the effect of Er incorporation on the crystal structure, as with the electron traps EL2 and M3, which are found in MOCVD-grown GaAs substrates used for Er-implantation.

The native defect EL2 was present in all measured n-type samples, control samples, and Er-implanted samples in the present study. EL2 is typically the defect of highest concentration in GaAs grown by LPE and MOCVD techniques. It is mainly attributed to the As antisite defect, As_{Ga} , and occasionally attributed to complexes of this center with other native defects, as explained by Bourgoin in a review of antisite defects in GaAs (14:R79). EL2 has certainly been

studied more than any other defect in GaAs, since it acts as a compensating center for residual acceptor impurities, such as carbon, thereby insuring that GaAs substrates are semi-insulating.

Figure 55 shows that for the lowest Er fluence of $\Phi_{Er} = 5 \times 10^{12} \text{ cm}^{-2}$, the EL2 center seems to shift slightly to lower temperatures on the rate-window plot, yet becomes somewhat deeper in energy. That is, there seems to be a conversion from center (n), with an activation energy of 785 meV, to center (m), which has an activation energy of 842 meV. In fact, a wide variation in activation energies and capture cross sections has been reported for the EL2 defect in the literature. According to Wang et al. (97:196), most researchers have EL2 situated between $E_c - 750 \text{ meV}$ and $E_c - 830 \text{ meV}$. The justification for this spread in observed activation energies is controversial. Some believe that the effect is due to the presence of other impurities such as chromium (Cr), which may act as an electron trap with a level between $E_T = 780$ and 840 meV (61), or it may even be due to the presence of oxygen, which has been found to introduce a midgap energy level that has been verified by photoluminescence studies (104). For instance, Lagowski et al. (50) performed DLTS measurements on Bridgman-grown GaAs crystals using controlled oxygen doping, and they observed an increase in the concentration of centers near 0.8 eV with a shift of the normal EL2 DLTS peak to lower temperatures. After fitting the capacitance transients and performing the Arrhenius analysis, these researchers concluded that oxygen contributed to a level with nearly the same activation energy as EL2, but with a cross section four times greater than that of EL2. This finding may be due to the effect of high trap concentrations, which has previously been hypothesized based on similar observations in this investigation (1). However, the two traps (m) and (n) have shown significantly different activation energies, and so they may be attributed to two distinct centers. Similarly, Wang et al. (97), after observing a broadening and shifting of the EL2 emission, attributed it to the presence of two distinct centers, EL2a and EL2b, with activation energies of 830 meV and 760 meV, respectively. Based upon an analysis of kinetic rate equations and electric-field-enhanced emission rate, EL2a was thought to consist of the isolated As antisite, As_{Ga} , while EL2b was attributed to the antisite vacancy complex, $As_{Ga}-V_{As}$.

The EL2 concentration decreases as the Er fluence increases from $\Phi_{Er} = 5 \times 10^{12}$ to $5 \times 10^{13} \text{ cm}^{-2}$ as shown in Figure 55. As the Er fluence increases, the GaAs substrate will experience an increase in the state of amorphization. With incomplete amorphization, which may be the case for lower Er fluences, the As_{Ga} concentration could increase due to the large

concentration of displaced As and Ga atoms. In fact, a 3-fold increase in the EL2 concentration was observed for the GaAs sample with $\Phi_{\text{Er}} = 5 \times 10^{12} \text{ cm}^{-2}$ over and above the concentration in the substrate. However, as the Er fluence increases, the implanted region will reach a state of complete amorphization. In this case, the annealing procedure would essentially result in a complete regrowth of the crystal from the substrate. Further, the concentration of the EL2 defect is highly dependent upon the means by which the crystal is grown. For example, with epilayers grown by MBE, the EL2 defect is simply not observed (11). Similarly, for crystals grown by liquid encapsulated Czochralski (LEC) technique, the concentration of the EL2 defect depends upon the thermal history of the sample, or, the rate of cooling (38). In the case of an amorphous layer, the annealing treatment will result in a complete regrowth of the layer. Thus, depending upon the annealing conditions, there may well be less EL2 than is normally present in the MOCVD-grown material, accounting for the finding that for $\Phi_{\text{Er}} = 5 \times 10^{13} \text{ cm}^{-2}$, the concentration of EL2 is less than in the substrate.

Another possible source for the concentration dependence of the EL2 defect with Er fluence is that the Er may prevent the occurrence of EL2 by stopping displaced As atoms from occupying Ga sites. The Er atoms either occupy Ga sites by virtue of the isoelectronic center (a), or that they may be somewhat displaced from this site towards the $\langle 110 \rangle$ direction, as indicated by center (g) and the correlation of RBS measurements. Furthermore, the large concentration of Ga_{As} defects explains what is happening to these displaced Ga atoms. For displaced As atoms, it seems that the most reasonable explanation seems to be that they remain mobile in interstitial positions or form As_i -impurity complexes, as suggested by Stievenard(84). Similarly, in this investigation, a large concentration of centers (i) and (j) were detected, and they were thought to be the same As_i -impurity complexes, H_2 and H_2'' . For instance, in Figure 45, the concentration of center (i), and more so (j), are correlated with the concentration of the Ga_{As} center (c).

Figure 55 shows the presence of an electron trap in both the control sample and the Er-implanted samples, with an activation energy of approximately 610 meV. Unlike the EL2 trap, its concentration increases drastically with Er fluence. This center has only been reported for MOCVD-grown GaAs, and Buchwald et al. (16) identified it as M3, a configuration of a metastable defect. These workers attributed this center to the pairing of a native-acceptor defect or defect complex with a shallow donor. This model is consistent with the work in the current study, since this center was not observed in the n^+p diodes under injection biasing conditions.

Further, the increase in the concentration of this center with increasing Er fluence correlated well with the increase in native acceptor defects (c) and (e) which increase for increasing Er fluence. Thus, the increase in the concentration of this center is probably related to ion-implantation damage, since this damage increases the concentration of native acceptor defects.

6.3.4.4 Er-Implantation Effect on Deep Centers in AlGaAs DLTS measurements have been made on Er-implanted $\text{Al}_x\text{Ga}_{1-x}\text{As}$ with $\Phi_{\text{Er}} = 10^{13} \text{ cm}^{-2}$ at 1 MeV. The results showed that for $x \lesssim 0.1$, the Er-related centers, as well as the damage-related centers, were still present. For $x = 0.1$, it appears that the Er-related hole trap (g) moves deeper into the band gap, but has a similar concentration to that observed for GaAs:Er. For $x \gtrsim 0.2$, both the Er-related center (g) and the damage-related centers (i) and (j) have virtually disappeared. One possible explanation is that the Er-related center (g) continues to move deeper into the band gap as the Al mole fraction x increases, while the damage-related centers do in fact tend to disappear.

Recently, there have been reports indicating that ion-implanted AlGaAs suffers substantially less lasting-implantation damage than does similarly treated GaAs. For instance, Cullis et al. (22) studied the effect of Ar^+ ion implantation on GaAs/AlAs/GaAs-layered structures by implanting the Ar ions with a fluence of $\Phi_{\text{Ar}} \sim 5 \times 10^{14} \text{ cm}^{-2}$ and an energy of 150 keV and characterizing with RBS and cross-sectional TEM measurements. These authors found that the as-implanted GaAs layers were in an amorphous state. However, even though Monte Carlo simulations predict that the AlAs layers will suffer the same numbers of nuclear displacements as the cladding GaAs layers, Cullis et al. found that this layer retained its crystallinity and exhibited only point-defect-cluster disorder. Mobile defects in AlAs were speculated to mediate *in situ* annealing processes during the implantation process. Further, after rapid thermal annealing at either 800 or 900 °C for 10 seconds, the point defect clusters in the AlAs layers were slightly larger, while the GaAs recrystallized and contributed large and widely-spaced dislocation loops. These authors believe that the Ar atom has little effect on the annealing process.

The observation of Cullis et al. was verified after more in-depth studies were accomplished by Jencic et al. (43). TEM measurements were performed on GaAs and $\text{Al}_x\text{Ga}_{1-x}\text{As}$ layers, with $x = 0.2$ and 0.85, which were implanted with 50 keV Ar^+ ions, or with 50 keV or 1.5 MeV Xe^+ ions as a function of ion fluence and substrate temperatures (30 and 300 K). Under all irradiation conditions, i.e., substrate temperature, ion species, and fluence, the AlGaAs was more

resistant to amorphization than GaAs. This resistance increased with increasing Al content, and decreased with decreasing irradiation temperature, which may be attributed to differences either in the mechanism by which a region is rendered amorphous (direct impact amorphization or the accumulation of point defects) or to differences in the stability of individual amorphous zones in these two materials. Regardless of the actual mechanism, Jencic et al. (43:1292) have partially quantified this effect by observing that the implantation of 1.5 MeV Xe⁺ ions with a dose of 10¹⁵ cm⁻² was necessary to produce a crystalline to amorphous transition in Al_{0.85}Ga_{0.15}As. In GaAs, a similar amorphous state was produced after a fluence of only 10¹³ cm⁻², illustrating the significance of the phenomenon.

In the present study, the sudden and complete disappearance of implantation-related centers observed in AlGaAs for $x \gtrsim 0.2$, as illustrated in Figure 59, is most likely due to this effect. In this situation, the hole trap observed in Al_{0.1}Ga_{0.9}As, as well as the electron traps observed in Al_{0.3}Ga_{0.7}As and Al_{0.4}Ga_{0.6}As, may very well be due to the Er-related center (g) which is moving away from the conduction band and towards the valence band with increasing Al mole fraction.

Finally, the concentration of the DX center in Al_xGa_{1-x}As:Er, for $x = 0.2, 0.3$, and 0.4 is unaffected by Er implantation and annealing. Since this center is due to an isolated donor (Si) tied to the X-conduction band, Er is not forming complexes with Si in Si-doped AlGaAs, since such a complex would drastically affect the DX concentration. Further, since the Er diffusion coefficient is even larger in AlGaAs than in GaAs, and since the Er atom is not expected to interact much differently with Si in GaAs as compared to AlGaAs, the observed reduction in electron concentration in GaAs is not due to donor gettering by Er atoms. Instead, based upon the very large concentrations of damage-related centers (c), (d), (i), (j) and the Er-related center (g), it is likely that the carrier reduction is related to compensation from these centers. This interpretation is also consistent with previous observations that, for $x \gtrsim 0.2$, little or no reduction in the electron concentration occurred in Si-doped, Er-implanted Al_xGa_{1-x}As as determined by the CV profiles (Figure 38).

6.4 Annealing Studies and Excitation Mechanisms of Er in GaAs and AlGaAs

The DLTS measurements reviewed in the last section show that there are both damage-related centers and Er-related centers which are observed in Er-implanted GaAs. The fact that very

similar centers are observed in GaAs doped with Er during MBE growth is a strong confirmation that Er centers form at least two deep centers in GaAs, a 35 meV and a 345 meV hole trap. However, an obvious limitation with the studies performed on the ion-implanted material is that they were all accomplished at a single and relatively high annealing temperature of 825 °C. Pomrenke et al. (70:608) found that the rapid thermal annealing technique gave more intense Er-4f luminescence compared to the conventional furnace annealing, and that the best annealing temperature for maximizing the Er-4f luminescence is between 750 and 800 °C. Furthermore, the Er-4f luminescence was observed to fall sharply after 800 °C. An initial limited annealing study performed to confirm this result indicated that the Er-4f emissions decreased by a factor of two when the annealing temperature was increased from 750 to 825 °C. However, the best rapid thermal annealing conditions for Mg and Si implants in GaAs were expected to be in excess of 850 °C. Therefore, in order to study both the deep levels by DLTS and to enhance the likelihood of obtaining Er-4f injection electroluminescence, the GaAs:(Er+Mg) or GaAs:(Er+Si) implanted samples were annealed at an intermediate temperature of 825 °C for 12 seconds.

The failure to obtain Er-4f injection electroluminescence suggested the need for a more in-depth annealing study. Annealing conditions, temperature, and time are essentially the only adjustable parameters available to enhance Er emissions in Er-implanted material. For annealing temperatures which are too low, or for times which are too short, very little crystal damage will be repaired, and this situation will cause the bandgap energy to be channelled into nonradiative damage centers. Additionally, if the semiconductor is still in an amorphous state, the incident laser excitation may pass through the implanted region and be absorbed by the substrate. On the other hand, if the annealing conditions are too extreme, the Er may diffuse to lattice sites where it becomes optically inactive, or it may form complexes with other defects giving rise to nonradiative recombination centers. For some intermediate annealing conditions, the Er will form a maximum concentration of optically active centers.

6.4.1 Effect of Annealing Conditions on Er-Implanted GaAs Semi-insulating substrates implanted with Er at a fluence of $\Phi_{\text{Er}} = 10^{13} \text{ cm}^{-2}$ at an energy of 1 MeV were annealed at various temperatures typically for 15 seconds. PL measurements were performed at 4 K on these samples with excitation by the 488 nm line of the Ar-ion laser. The intensity of the beam was 150 mW with spot size of 3 mm in diameter. Figure 63 shows the emissions from 10,000

to 18,000 Å, or 1 to 1.8 μm. The sharp emissions near 15,400 Å are due to the intra-4f shell transition, $^4I_{13/2} \rightarrow ^4I_{15/2}$ of the Er^{3+} ion. The intensity of these emissions increases with annealing temperature up to 750 °C, and thereafter it decreases. Other anneals were performed at 750 and 775 °C for various times ranging from 15 to 120 seconds. The spectra for the anneal at 750 °C for 60 seconds are also shown, since these conditions seem to manifest the most intense Er^{3+} emissions. For the lower annealing temperatures, there are broad bands which are more intense than the Er^{3+} emissions. These spectra are not corrected for the response of the spectrometer/grating and detector. However, by comparing these bands with the response curve in Figure 22, there are at least 3 broad bands which can be identified in this spectral range; they exist at 1.1, 0.83, and 0.76 eV. All three broad bands decrease with increasing annealing temperature, and also with annealing time, as indicated by the spectra for the samples annealed at 750 °C for 15 and 60 seconds. The broad bands indicate recombination at deep centers.

For low annealing temperatures, a large concentration of unannealed damage-related deep centers dominate the spectra. The Er^{3+} emissions are weak because nonradiative recombinations at these centers consume energy, which might otherwise be transferred to the Er-4f shell. As the annealing temperature increases, the concentration of the damage-related centers may be reduced, or the centers may recombine (for instance, interstitials with vacancies), and consequently the intensity of the broad bands decreases. Simultaneously, the Er atoms diffuse to sites where they are optically active (sites where the Er^{3+} -4f shell is easily excited) and from which the Er-4f shell is likely to radiatively emit its energy. As the annealing temperature increases, the Er atoms diffuse to sites where they are optically inactive. That is, they diffuse to sites where the energy from the crystal cannot be efficiently transferred to the 4f shell, or where the excited Er^{3+} ion tends to nonradiatively decay, and thus, transfer energy back to the crystal.

Another annealing study was performed on p-type substrates implanted with an Er fluence of $\Phi_{\text{Er}} = 10^{13} \text{cm}^{-2}$ at an energy of 1 MeV. The p-type substrates were chosen because it appears from the previous measurement that Er-related centers are forming hole traps. The samples were annealed at four different temperatures, 650, 750, 850, and 900 °C, each for 15 seconds. PL measurements were performed on these samples, and subsequently, Schottky diodes were fabricated on the samples to correlate the deep centers with the Er PL intensity.

In Figure 64, the CV profiles for each of the annealing conditions are presented. For the sample annealed at 650 °C, the profile starts at about 0.7 μm with no applied bias. This

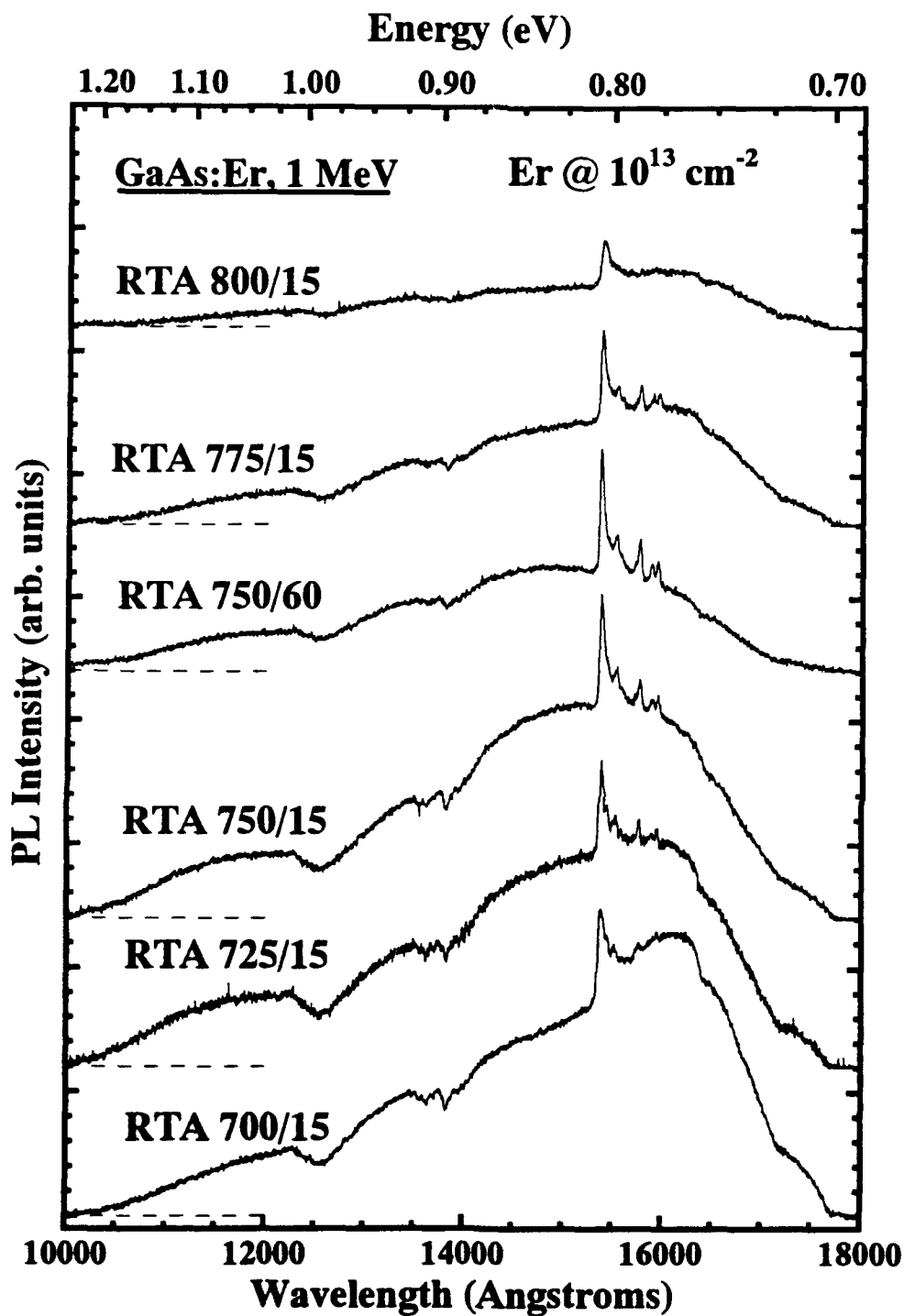


Figure 63. PL of the Er^{3+} -4f transition near $1.54 \mu\text{m}$, as well as broad bands in the semi-insulating GaAs sample implanted with Er at a fluence of $\Phi_{\text{Er}} = 10^{13} \text{ cm}^{-2}$ and at an energy of 1 MeV as a function of annealing temperature

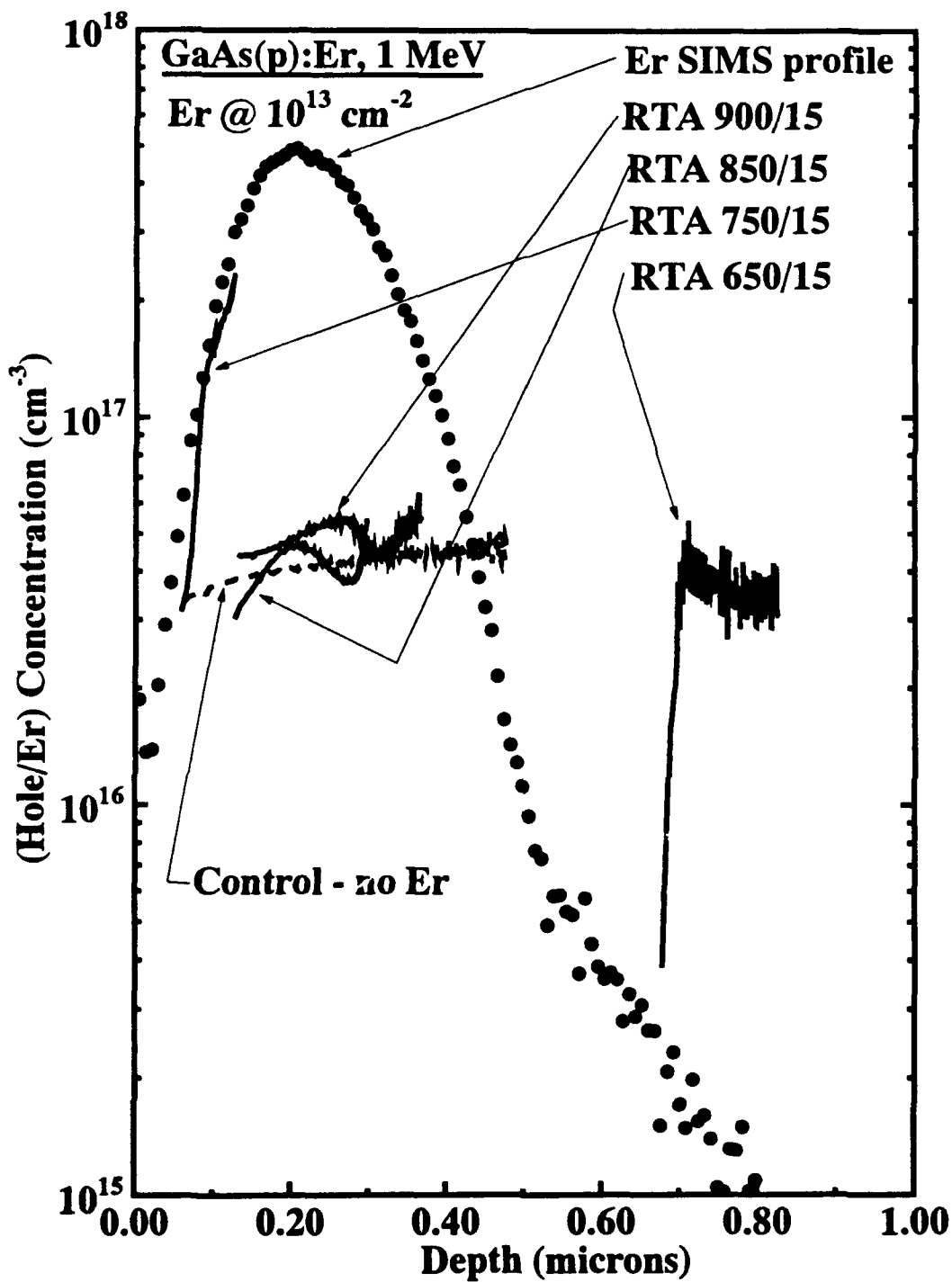


Figure 64. CV profiles obtained using Schottky diodes on the p-type GaAs substrate 3B-PR-840 implanted with Er at a fluence of $\Phi_{\text{Er}} = 10^{13} \text{ cm}^{-2}$ and at an energy of 1 MeV that was rapid thermally annealed at 650, 750, 850, and 900 °C for 15 seconds

feature indicates that this annealing temperature repairs very little of the damage in the implant region, and so this region acts only as a dielectric spacing layer. As the reverse bias voltage is increased, the carrier concentration becomes equal to the substrate value. For the higher annealing temperature of 750 °C, the p-type carrier concentration is much higher than the substrate value in the region of the implant. In fact, the additional acceptors seem to follow the Er profile measured by SIMS. As the annealing temperature is further increased to 850 and 900 °C, the p-type conductivity in the implant region returns to the substrate value, indicating that the acceptor center giving rise to the increased hole concentration is dissociating.

Figure 65 shows the rate-window plots for the DLTS measurements on this sequence of samples. A majority carrier biasing sequence was used, so that essentially only holes were introduced into the junction for capture. Thus, the negative signals in the plot represent hole traps. For the sample annealed at 750 °C, there is a hole trap with high concentration dominating the spectrum. The rate-window plots for the n-type samples with Er-implanted at fluences of $\Phi_{\text{Er}} = 10^{13}$ and $5 \times 10^{13} \text{ cm}^{-2}$ are also shown to demonstrate that the hole trap corresponds well with the previously measured center (g). Damage-related centers (c), (e), (i) and possibly (j) are also observed for this sample. However, center (g) now clearly manifests the dominant peak, and the concentrations of the damage-related centers do not interfere as much as previously observed in the Arrhenius analysis for the activation energy and capture cross section of this center. The concentration of center (g) is still fairly large compared to the free-hole concentration by virtue of the relatively large value of $\Delta C/C \approx 0.1$. For the samples annealed at 650 °C and 900 °C, a peak labeled (g_a) appears on the high temperature side of peak (g), and the peak (g_a) represents a much smaller concentration in both cases. The emitting centers in the samples annealed at 650 °C are probably located near the edge of the implant region at about 0.7 μm , since the majority carrier biasing sequence of (0,-1) does not introduce any holes into the unannealed region of the implant. This center has a very similar activation energy to center (g) measured in the sample annealed at 750 °C; however, they differ in capture cross section by nearly one order of magnitude. That is, for center (g)

$$E_T = 367 \pm 10 \text{ meV}, \sigma_p = 2.5 \times 10^{-13} \text{ cm}^2, \quad (77)$$

while for center (g_a)

$$E_T = 364 \pm 10 \text{ meV}, \sigma_p = 1.5 \times 10^{-14} \text{ cm}^2. \quad (78)$$

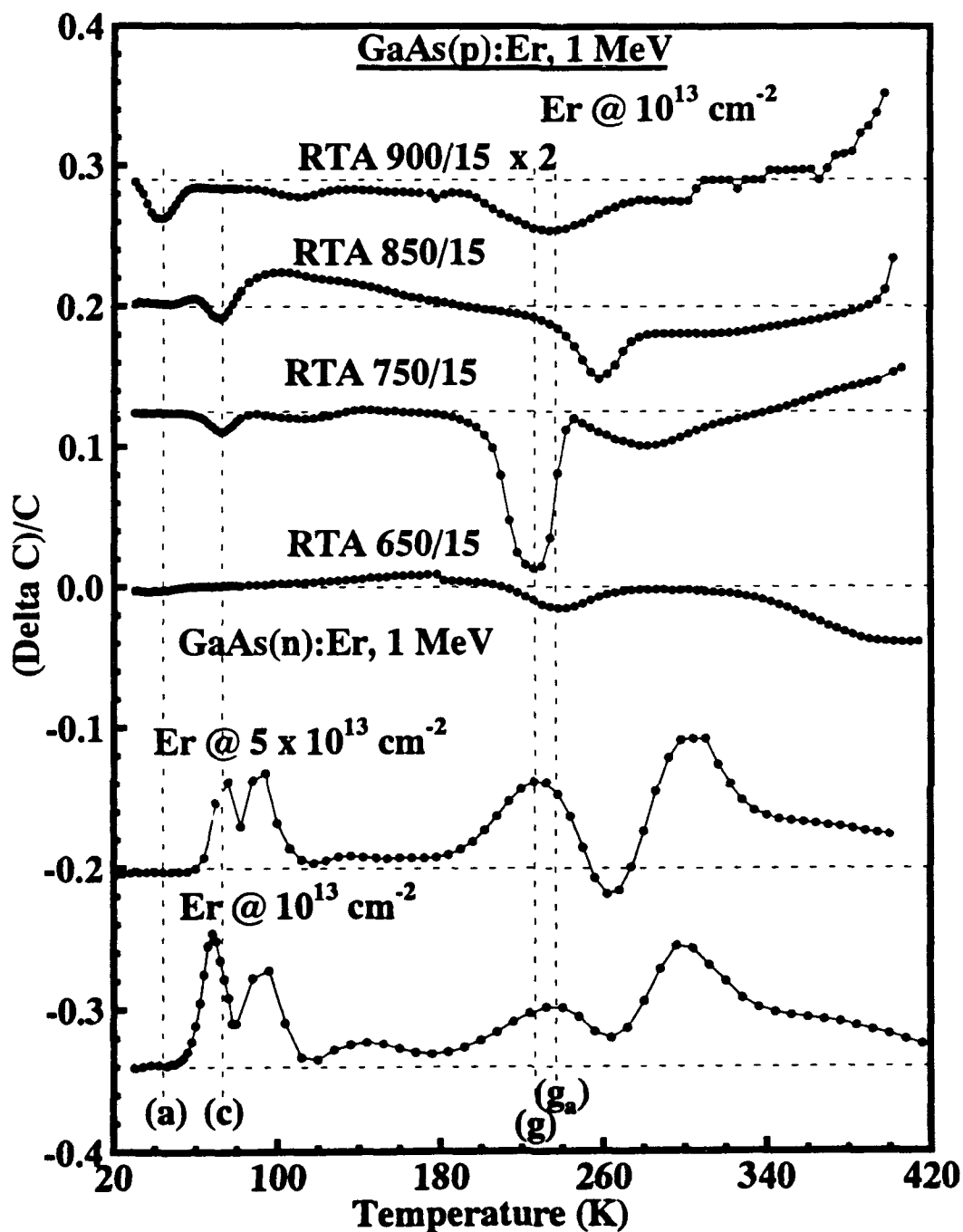


Figure 65. DLTS measurements of the p-type GaAs substrate 3B-PR-840 implanted with Er at fluence of $\Phi_{\text{Er}} = 10^{13}$ and at an energy of 1 MeV that was rapid thermally annealed at 650, 750, 850, and 900 °C for 15 seconds (Each sample was measured with a majority carrier biasing sequence of 0 V forward and 1 V reverse (0,-1). DLTS measurements on the Er-implanted p⁺n GaAs diodes using injection biasing are shown for comparison. The rate window is 29706 s^{-1} .)

The Arrhenius plot in Figure 66 shows the least-square fits for these two centers.

These two peaks seem to correspond to the same center, and the shift in the peak is probably related to the very high concentration of the center in the sample annealed at 750 °C. As demonstrated in section 3.2.5.1, the qualitative effect of a large concentration of deep levels compared to the shallow level is to broaden the DLTS peak, and to shift it to lower temperatures (that is, to enhance the apparent emission rate). In fact, the analysis of traps with concentrations larger than 10% of the shallow-doping density can result in an Arrhenius analysis which apparently yields two deep levels with parallel signatures on the Arrhenius plot. This behavior should not mistakenly be attributed to the presence of two distinct centers with an identical activation energy, but rather with different capture cross sections. In Figure 65, the rate-window plot for the n-type sample with the lowest Er fluence of $\Phi_{Er} = 5 \times 10^{12} \text{ cm}^{-2}$ shows a peak which is closer to (g_a) than to (g). Thus, center (g) and (g_a) are identical, and their corresponding DLTS peaks are shifted due to the large concentration of this center.

As the annealing temperature is increased to 850 °C, the concentrations of the damage-related centers (c), (i), and (j) increase relative to center (g). Also peak (a), attributed to the isoelectronic center Er_{Ga} , is barely discernible. After annealing at 900 °C, the concentration of center (a) drastically increases, while the concentration of all other damage-related centers decreases below the detection limit, except for a detectable concentration of center (g). The conclusions for the DLTS study are:

- Annealing below 650 °C is insufficient to repair the damage to the crystal, and therefore it probably remains in an amorphous state.
- After annealing at 750 °C, there is a large concentration of damage-related centers, with the Er-related center (g) being dominant. This center is possibly related to Er_i . From the CV measurements, it appears that, due to the large concentration of center (g) at this annealing temperature, the hole concentration is enhanced.
- After annealing at 850 °C, the Er-related center (g) largely dissociates, and a relatively large concentration of damage-related centers are formed.
- While the center (g) is still detectable after annealing at 900 °C, center (a), which is probably related to Er_{Ga} , is dominant. Most damage-related centers have been removed by annealing at this temperature. The CV profile shows that the hole concentration for the

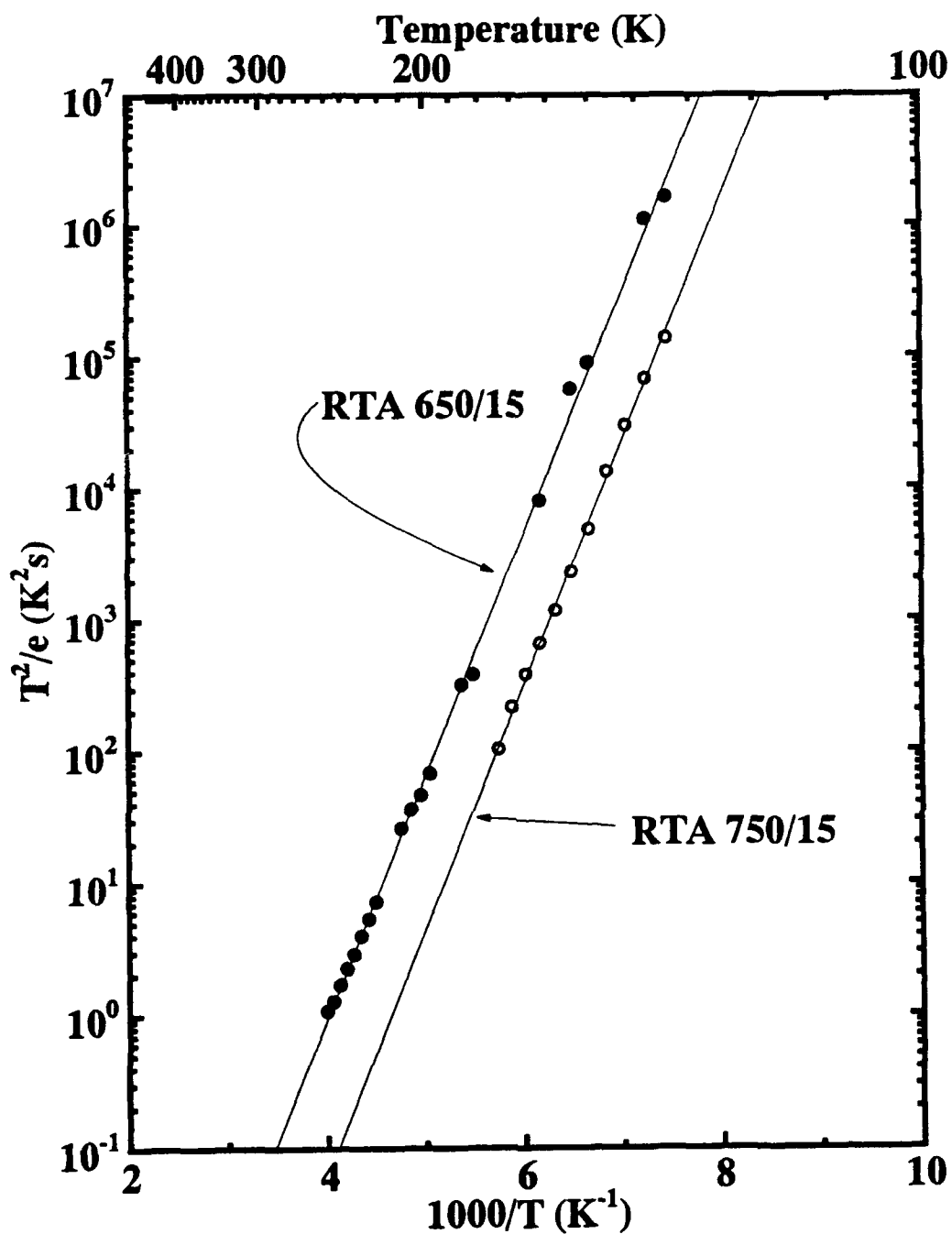


Figure 66. Arrhenius analysis of the (g) center in the p-type GaAs sample implanted with Er at a fluence of $\Phi_{\text{Er}} = 10^{13} \text{ cm}^{-2}$ and at an energy of 1 MeV that was annealed at either 650 or 750 °C for 15 seconds (The shift in the trap signature is due to the large concentration of the level in the sample annealed at 750 °C.)

sample implanted with Er and annealed at 900 °C is close to the profile obtained for the unimplanted and unannealed substrate.

A critical conclusion was uncovered by comparing the results of the DLTS measurements with the PL measurements of the Er-implanted GaAs. The PL for each annealed sample was measured from 10,000 to 18,000 Å of emission wavelength, and the results are shown in Figure 67. These emissions were acquired at 4 K with excitation from the 488 nm line of the Ar-ion laser. The concentration of center (g) was clearly correlated with the intensity of the Er-4f emissions, indicating that center (g), which had the maximum concentration for the anneal temperature of 750 °C, may be associated with an optically-active Er center. Additionally, the Er-related center (a), which is formed for higher annealing temperatures, is a nonoptically-active center, that is, the 4f shell of the Er^{3+} ion in this center is not as easily excited, or if excited, is likely to nonradiatively transfer its energy back to the crystal. Thus, the Er is forming two different centers upon annealing, as confirmed by Figure 68, which shows the spectra between 15,000 and 16,000 Å from Figure 67. For the two lower anneal temperatures, the peak in the 1.54 μm region is centered at 15,370 Å, while for the two higher anneal temperatures, the Er-4f emissions have clearly shifted to 15,400 Å. Thus, it is likely that center (g) is associated with emissions at 15,370 Å, while center (a) is associated with the emissions at 15,400 Å.

Figure 69 shows near-band-edge PL at 4K for the sequence of annealing temperatures as well as for the unannealed GaAs substrate 3B-PR-840. The emission at 1.49 eV agrees well with the energies given for the free-to-bound recombination at a neutral acceptor, (e, A^0) (99:328). Most shallow acceptors have an emission near 1.49 eV, since they are approximately 30 meV above the valence band maximum. However, since substrate 3B-PR-840 was zinc-doped with $[\text{Zn}] = 4 \times 10^{16} \text{ cm}^{-3}$, this emission is almost certainly due to recombination at a neutral Zn atom. The intensity of this emission increases with increasing annealing temperature because an increasing number of Zn atoms are occupying Ga sites, and because the damage-related centers decrease with increasing anneal temperature. This observation can be confirmed by comparing Figure 69 with the results obtained from the DLTS measurements in Figure 65 and the PL measurements in Figure 67, where it is observed that the nonradiative and damage-related radiative transitions at these deep centers dominate at the lower annealing temperatures.

No additional emissions are observed in the near-band edge, which could be correlated either with free-to-bound recombination or bound-exciton recombination at the isoelectronic hole

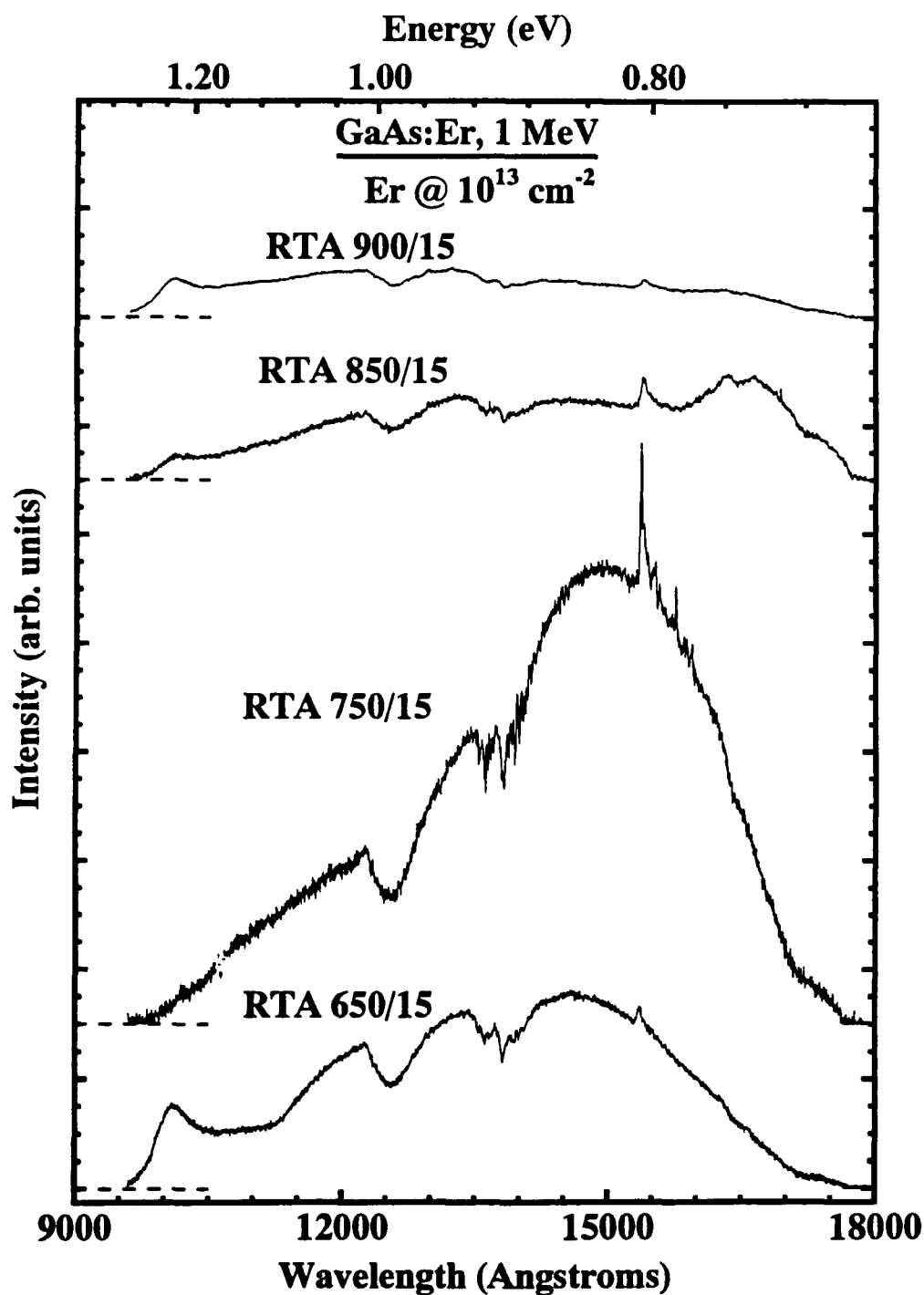


Figure 67. PL of the p-type GaAs substrate 3B-PR-840 implanted with Er at a fluence of $\Phi_{\text{Er}} = 10^{13} \text{ cm}^{-2}$ and at an energy of 1 MeV that was rapid thermally annealed at 650, 750, 850, and 900 °C for 15 seconds (This plot shows the broad bands as well as Er-4f emissions near $1.54 \mu\text{m}$.)

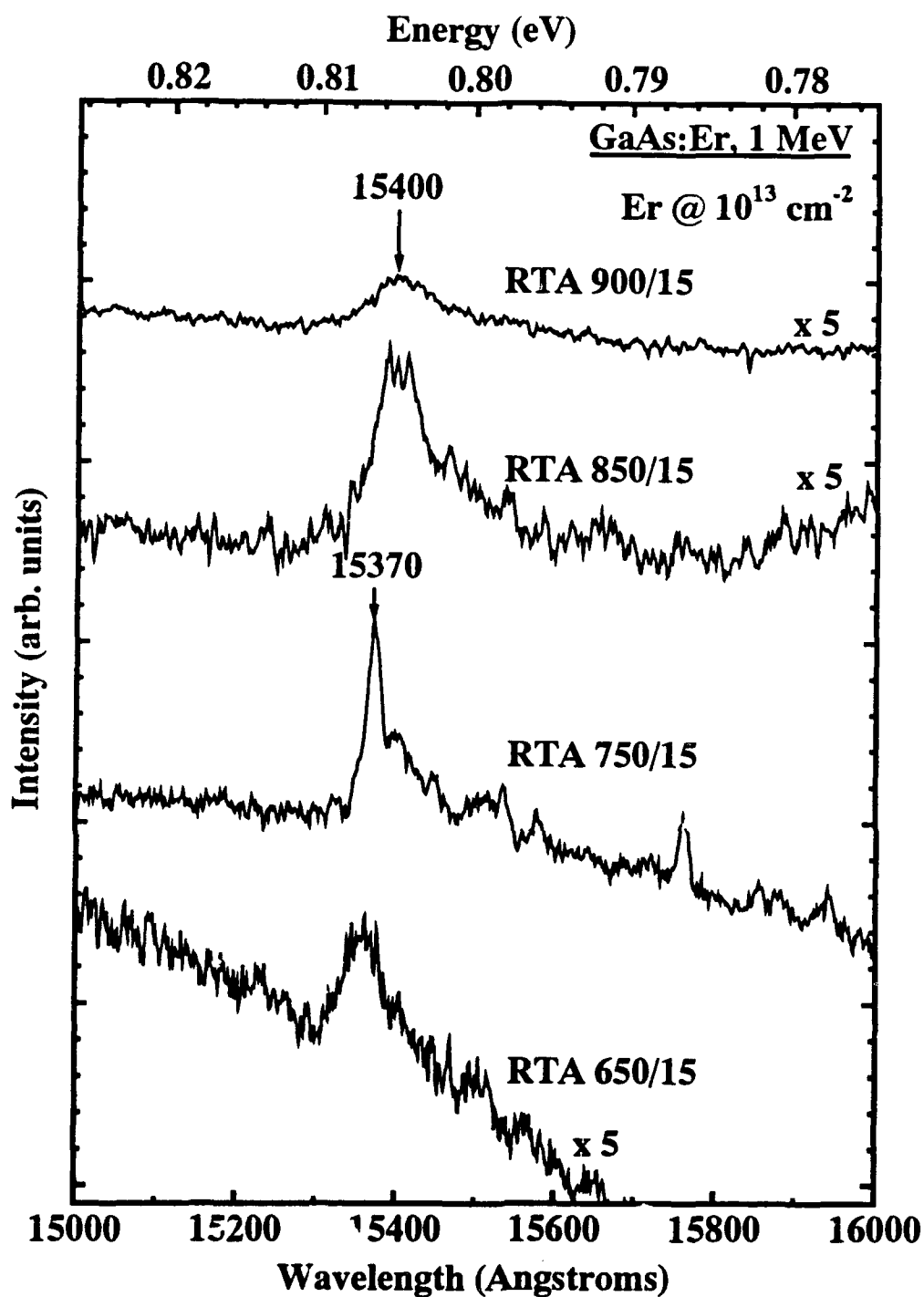


Figure 68. PL of the p-type GaAs substrate 3B-PR-840 implanted with Er at a fluence of $\Phi_{\text{Er}} = 10^{13} \text{ cm}^{-2}$ and at an energy of 1 MeV that was rapid thermally annealed at 650, 750, 850, and 900 °C for 15 seconds (The structure of the Er-4f emissions near 1.54 μm is shown to demonstrate the presence of at least two centers.)

trap. Conversely, as demonstrated in the review concerning the experimental observations of isoelectronic centers by Dean (23), bound-exciton emissions at isoelectronic centers were found to be intense. The same observation has been made by Takahei et al. (89) for the isoelectronic electron trap formed by Yb in InP, which was presented as partial evidence to support their conclusion that a bound exciton nonradiatively excites the Yb^{3+} -4f shell. This may also be an excitation mechanism for Er in GaAs.

At even lower energies, a broader emission near 1.45 eV occurs, which is in agreement with reports of the free-to-bound transition attributed to the Ga_{As} antisite defect (105). Center (c) is clearly visible in the DLTS measurements shown in Figure 65, further confirming that center (c) is indeed the first acceptor level of the Ga antisite defect.

A clear deficiency in this investigation is that the annealing temperature interval in this sequence is too widely spaced. It would be desirable to have gradual trend which correlates the concentration of center (g) with the intensity of the Er-4f emissions. Therefore, another annealing study was accomplished with the same p-type GaAs substrate implanted with Er at a fluence of $\Phi_{\text{Er}} = 5 \times 10^{12} \text{ cm}^{-2}$ and annealed at temperatures of 725, 750, 775, and 800 °C for 15 seconds. The Er-related PL is shown in Figure 70, and the corresponding rate-window plots from the DLTS measurements are shown in Figure 71. By comparing the rate-window plots for all of the annealing conditions, at least three hole traps appear to participate in the emission between 220 and 320 K. Two of these centers, (g) and (i), have been described previously. The center labeled (h) dominates the spectrum for higher annealing temperatures. Additionally, a more gradual trend occurs which indicates that the concentration of center (g) increases up to the annealing temperature of 750 °C, and thereafter it decreases for the annealing temperatures of 775 and 800 °C. This behavior correlates well with the intensity of the Er-4f emissions in Figure 70, which increase up to an annealing temperature of 750 °C, and then decrease for higher annealing temperatures.

For the two higher annealing temperatures of 775 and 800 °C, the center (h) increases in concentration, and at an annealing temperature of 800 °C, it dominates the others. The Arrhenius analysis of the sample for this highest annealing temperature yielded an approximate activation energy of 230 meV for this center. Figure 71 also shows that, as the annealing temperature increases, the concentration of center (c) also increases. This center has been identified in the previous section as the first acceptor level of the Ga_{As} defect. Furthermore, the 230 meV

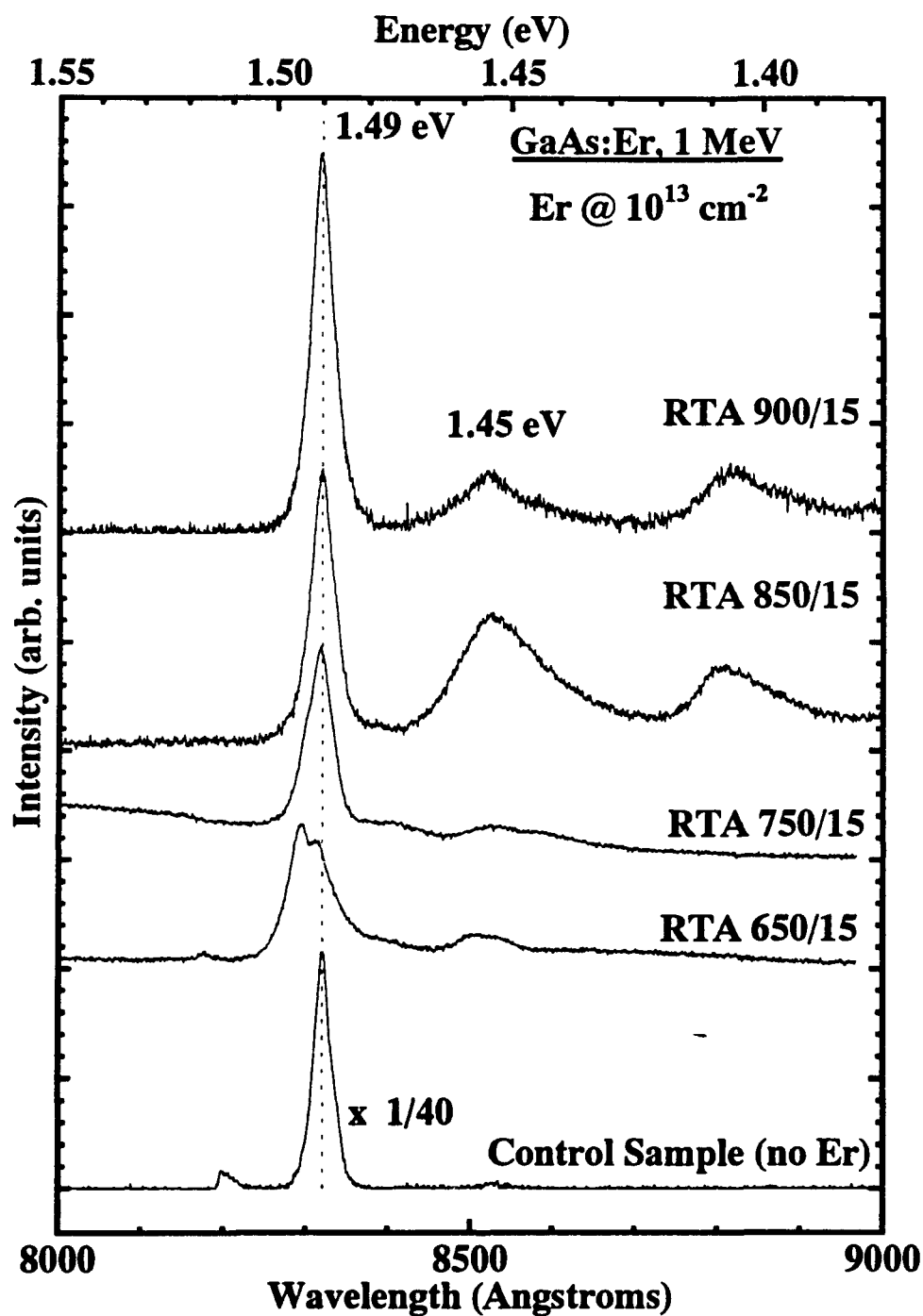


Figure 69. Near-band-edge PL of the p-type GaAs substrate 3B-PR-840 implanted with Er at a fluence of $\Phi_{\text{Er}} = 10^{13} \text{ cm}^{-2}$ and at an energy of 1 MeV that was rapid thermally annealed at 650, 750, 850, and 900 °C for 15 seconds

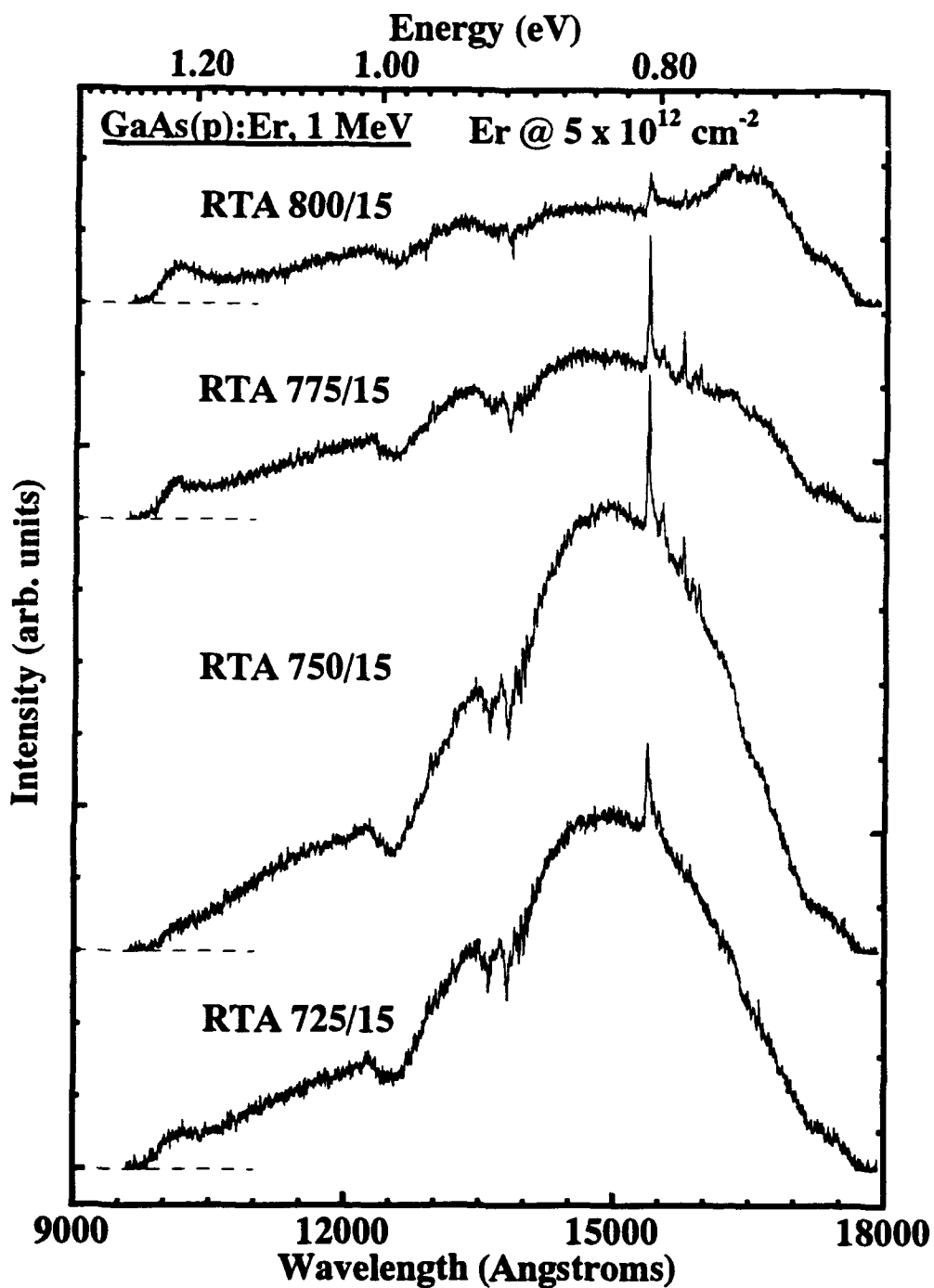


Figure 70. PL of the p-type GaAs substrate 3B-PR-840 implanted with Er at a fluence of $\Phi_{\text{Er}} = 5 \times 10^{12} \text{ cm}^{-2}$ and at an energy of 1 MeV that was rapid thermally annealed at 725, 750, 775, and 800 °C for 15 seconds (This plot shows broad bands as well as Er-4f emissions near $1.54 \mu\text{m}$)

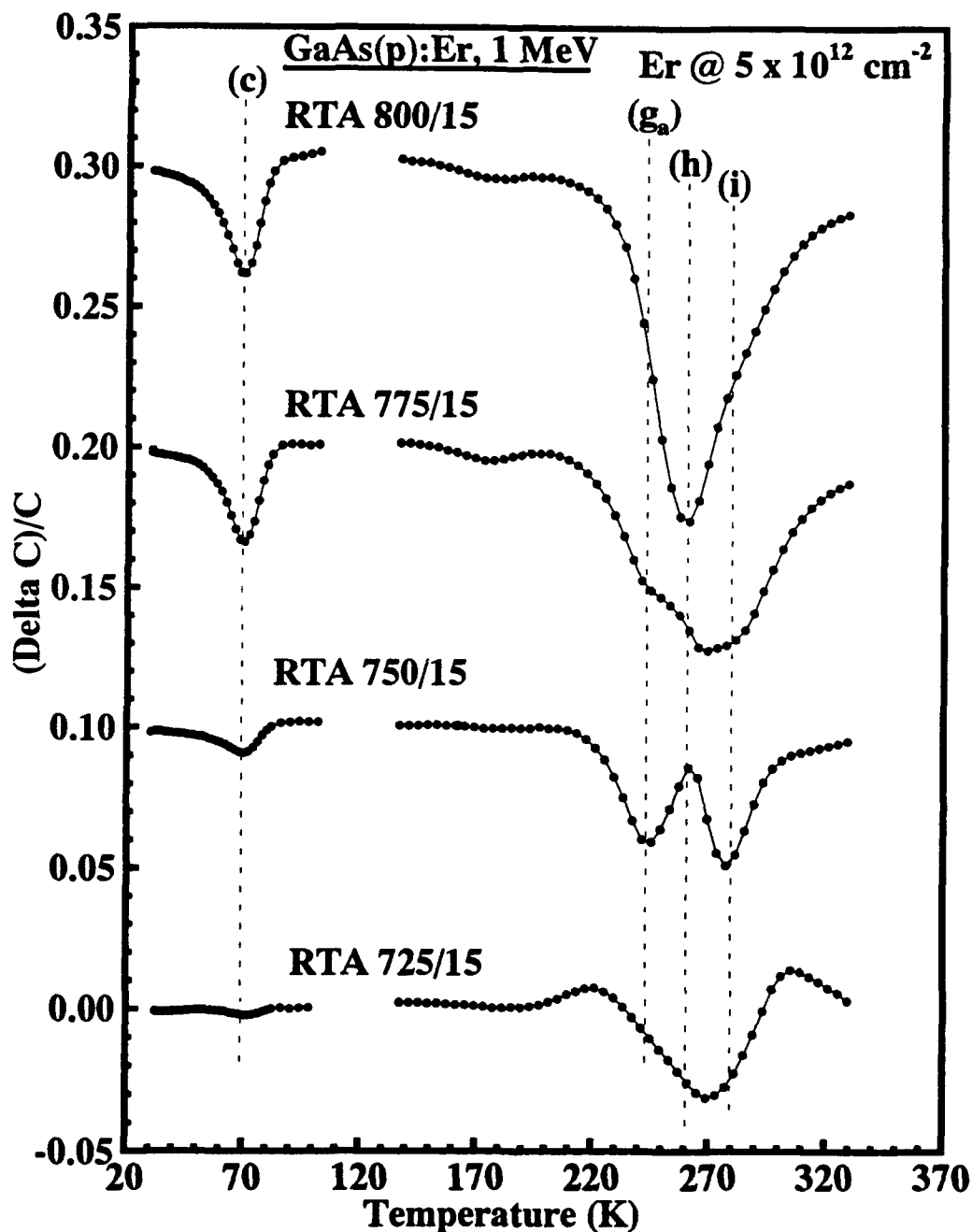


Figure 71. DLTS measurements of the p-type GaAs substrate 3B-PR-840 implanted with Er at a fluence $\Phi_{Er} = 5 \times 10^{12} \text{ cm}^{-2}$ and at an energy of 1 MeV that was rapid thermally annealed at 725, 750, 775, and 800 °C for 15 seconds (Each sample was measured with a majority carrier biasing sequence of 0 V forward and 1 V reverse (0,-1). The rate window is 29706 s^{-1} .)

activation energy reported here agrees well with that previously reported by Yu et al. (105) for the second acceptor level of GaAs. Yu et al. used temperature-dependent Hall effect measurements to establish the hole concentration vs. temperature, and they least-squares fitted this data to determine the concentrations and activation energies of the first and second acceptor levels of GaAs. This center was also observed in the previous annealing study with Er implanted at a fluence of $\Phi_{Er} = 10^{13} \text{ cm}^{-2}$, as shown in Figure 65, after annealing at 850 °C. The concentration of center (c) was again the highest. After annealing at 900 °C, both center (c) and center (h) are not present. Thus, center (h) is probably due to the second acceptor level of GaAs.

Peak (h), observed under injection biasing in the n-type GaAs samples, was previously attributed to an electron trap. This feature was shown originally in Figure 45, where a negative peak occurred between the positive Er-related peak (g) and the positive damage-related peak (i). The transients of negative amplitude which gave rise to this DLTS signal were observed only on the fastest time scale, and it was not possible to formulate a trustworthy Arrhenius analysis, although it appeared that this electron trap had an activation energy of roughly 300 meV. However, in later annealing studies, a negative peak was found in the p-type samples, corresponding to a majority-carrier hole trap, which was coincident with this peak as shown in Figure 45. This signal is apparently due to the second acceptor level of the GaAs defect. The contradiction is resolved by accounting for the fact that under injection biasing conditions, the shape of capacitance transient is determined, according to Sah (78:777), by the ratios of electron and hole capture and emission coefficients. In the present study, since the second acceptor level of GaAs in the n-type material manifested a negative DLTS signal under injection biasing, condition (1) is satisfied; that is,

$$e_n^t/e_p^t > c_p^t/c_n^t. \quad (79)$$

Furthermore, since the hole emission rate is expected to be larger than the electron emission rate, this situation implies that

$$c_n^t \gg c_p^t \text{ or } \sigma_n^t \gg \sigma_p^t. \quad (80)$$

Thus, Ga_{As}^{-1} is much more likely to capture a second electron from the conduction band and become Ga_{As}^{-2} than it is for the second electron on the Ga_{As}^{-2} to recombine with a hole in the valence band and become Ga_{As}^{-1} . It is now evident that at least four centers are present in the n- and p-type ion-implanted GaAs which act as hole traps and occur between 230 and 450 meV above the valence band: the Er-related center (g), the second acceptor level of GaAs (h), and the As_i-related centers (i) and (j).

6.4.1.1 Er-Doped, MBE-Grown AlGaAs One of the limiting factors for obtaining strong Er-related luminescence in GaAs is the incorporation of a large quantity of this element into the crystal structure of the semiconductor. In the ion implantation technique, the doping density is usually limited by the mass-selected beam current which is directed towards the substrate. If a low-beam current is generated, as is typically the case for the RE-ion implantation, the implantation may take a long time and be quite expensive. However, in the MBE technique, the Er-doping density is readily changed over many orders of magnitude by simply adjusting the temperature of the Er-effusion cell. Yet, Er luminescence in MBE-grown, Er-doped GaAs remains comparable to that of Er-implanted GaAs. This behavior is related to the low solubility limit of Er in GaAs. Poole (72) found that when doping Er greater than $7 \times 10^{17} \text{ cm}^{-3}$, the Er began to form micro-precipitates of ErAs which had a cubic NaCl structure. In fact, Smith et al. (83:50) found that the Er emissions reached a maximum intensity in Er-doped GaAs with $[\text{Er}] = 4 \times 10^{17} \text{ cm}^{-3}$, and then they began to decrease in intensity. This behavior is probably related to the increase in the radii of these precipitates as the Er-doping density increased (72). Nonradiative recombination of excitons at the surface of these precipitates, or at defects in the crystal caused by their incorporation, will prevent the transfer of the crystal's energy to the Er-4f shell.

As previously mentioned, the current MBE studies were confined mostly to AlGaAs, in which an Er-doping study on $\text{Al}_{0.5}\text{Ga}_{0.5}\text{As}$ was performed. The sample structures were described previously in Figure 9. Hall effect measurements were performed on the top layer, which was co-doped with Si. However, for the PL measurements, the top Si-doped layer was etched off, leaving approximately $1 \mu\text{m}$ of Er-doped GaAs. The PL measurements performed on sample x027 doped with $[\text{Er}] = 1.5 \times 10^{19} \text{ cm}^{-3}$ produced the most intense Er emissions observed in this study, as shown in Figure 39. Figure 72 shows the Er-related, 4f-luminescence intensity and Hall electron concentration as a function of Er-doping density. The intensity of the Er-4f emissions increases up to $[\text{Er}] = 1.5 \times 10^{19} \text{ cm}^{-3}$, and then it falls off quite sharply. Similarly, the electron concentration measured by the Hall effect, as shown in this figure and listed in Table 10, also decreases dramatically for Er-doping between 10^{19} and $5 \times 10^{19} \text{ cm}^{-3}$. This behavior indicates the formation of a large concentration of compensating centers, probably due to the formation of ErAs precipitates. Thus, the solubility limit of Er in $\text{Al}_{0.5}\text{Ga}_{0.5}\text{As}$ is between 10^{19} and $5 \times 10^{19} \text{ cm}^{-3}$, a value much higher than for GaAs.

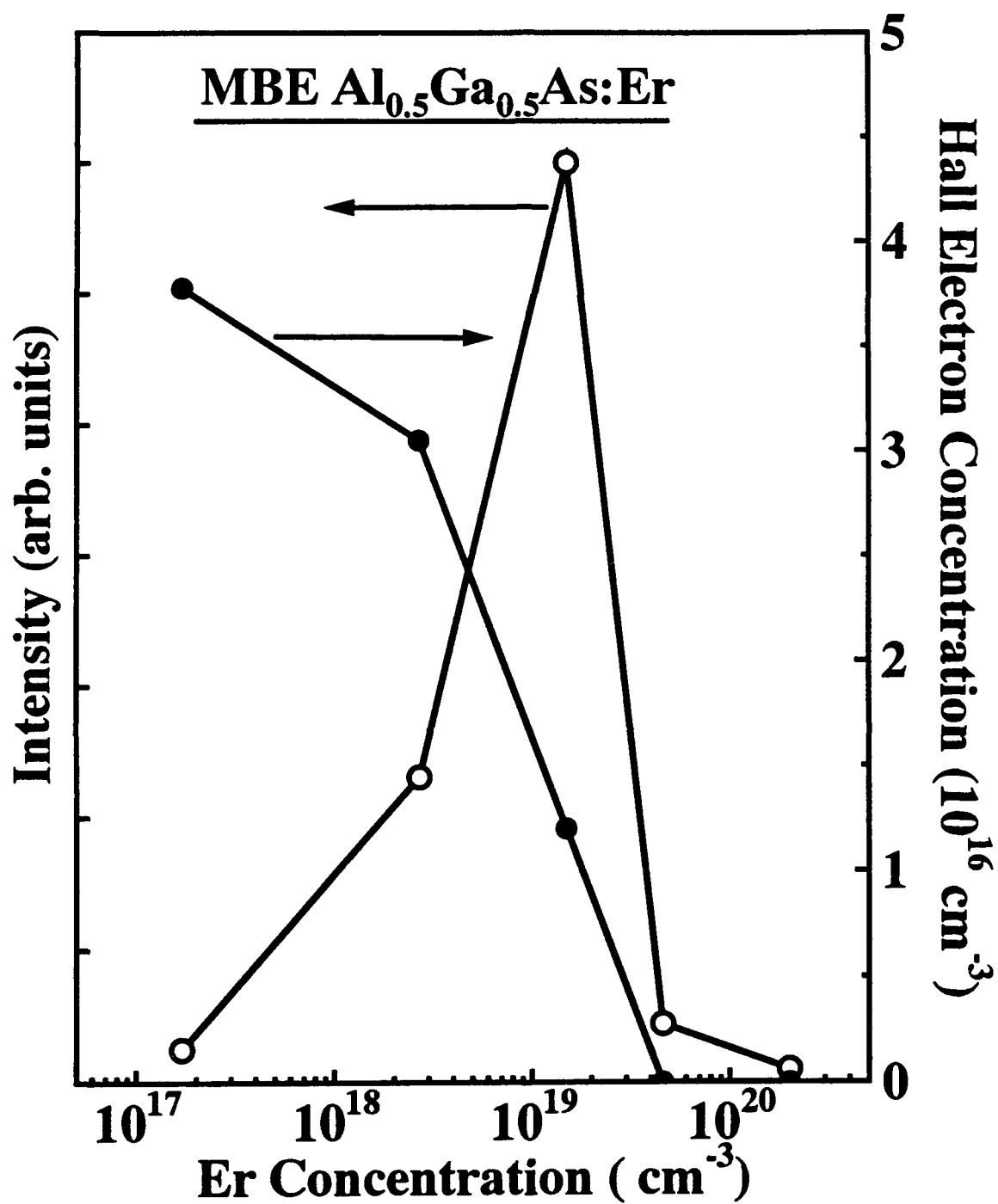


Figure 72. Er-4f PL intensity and Hall effect electron concentration as a function of the Er-doping density in MBE-grown Er-doped $\text{Al}_{0.5}\text{Ga}_{0.5}\text{As}$

6.4.2 Discussion Overall, the two Er-related deep centers observed in the previous section are correlated with the Er-4f emissions from two different Er centers. For center (g), the maximum concentration of this center as well as the maximum PL intensity of the Er-4f emissions occur at an annealing temperature of 750 °C. As the annealing temperature is increased further, the Er-4f luminescence intensity decreases, as does the concentration of center (g). For much higher annealing temperatures on the order of ~ 900 °C, center (a) appeared, and a noticeable shift in the 4f emissions to lower energies occurred. These emissions were much weaker than the emissions associated with center (g). Previously, center (a) had only been observed in n-type ion-implanted material. Now, it has been observed in both n-type and p-type MBE-grown, Er-doped and Er-implanted GaAs.

This finding agrees well with the measurements performed by Kozanecki (49), for Er-implantation at 150 keV with an Er fluence of $\Phi_{\text{Er}} = 10^{15} \text{ cm}^{-2}$ (section 6.3.4.1). The Er-implanted samples were annealed using the RTA technique at temperatures between 700 and 1000 °C, and RBS and PL measurements were performed. For lower annealing temperatures, the Er-4f PL was more intense, and there was a correspondingly large concentration of Er interstitials. However, after annealing at 1000 °C, the PL was essentially extinguished, and less than 3% of the Er atoms occupied interstitial positions. Kozanecki attributed this behavior to the tendency for the Er atom to migrate from the interstitial to the substitutional Ga site at higher annealing temperatures. In the present study, if center (g) is the Er_i , and center (a) is the Er_{Ga} , then the DLTS results confirm Kozanecki's findings. The current study also confirms Kozanecki's observation that energy transfer is apparently much more efficient to center (g) than it is to center (a).

The disparity in the intensity of the Er-4f emissions from these two centers may be attributable to the crystal field at their locations in the lattice. It is well known that the contributions to the oscillator strength for an atomic transition are dominated by the electric dipole (ED) moment. After this, the magnetic dipole (MD) transitions are most intense, but are several orders of magnitude weaker. Unfortunately, ED transitions between the levels of the 4fⁿ configurations of the RE ions are forbidden by the parity rule. That is, ED transitions are not allowed between states having the same parity (25:117). This rule is valid whenever the field in which the electrons move is centrosymmetric; i.e., has a center of symmetry. This is of course true for the free RE ions. However, when the RE ion is placed in a crystalline environment which is noncentrosymmetric, ED transitions may be allowed. Boyne identifies the mechanisms

by which these transitions are allowed (15:16):

- Even-parity, free-ion states (d and g states) are admixed to the odd-parity 4f states under the action of the odd components of the crystal field, H_{cf} .
- The admixture of ligand states to the 4f states (covalency effects) may result in a relaxation of the parity selection rule.
- Transitions of the ED character also occur due to the indirect interaction between the 4f states and the radiation field, which is mediated by the dipolar polarization induced in the ligand system (dynamic coupling mechanism).

That is, the crystal field for a center lacking inversion symmetry has odd components, which are capable of mixing 5d-states into the 4f-configuration. Since the ED interactions are typically five orders of magnitude larger than the MD interactions, even a small perturbation of this type can result in a large enhancement in the oscillator strength, or, the Er-4f excitation efficiency. In the current study, center (a) appears to be caused by the isolated Er_{Ga} center, which has T_d symmetry. On the other hand, center (g) is thought to be related to an Er_i , which has a lower symmetry. The movement of the Er atom from the T_d site (Er_{Ga}) into the interstitial position (Er_i) will likely enhance the oscillator strengths for ED transitions in the Er-4f shell due to the presence of additional odd components of the crystal field and due to an increased interaction of the Er 4f electrons with the ligand states. This behavior may explain the weak Er-4f luminescence from the Er_{Ga} site, center (a), and the relatively intense Er-4f luminescence from the Er_i , center (g), and also provides further evidence that these assignments are correct.

Center (g) has also been observed in the MBE samples under higher doping densities. It may also be responsible for the increase in the 4f luminescence in that material. For instance, Smith et. al. (83:50) observed a 600-fold increase in the Er PL intensity for Er doping between 10^{17} and $4 \times 10^{17} \text{ cm}^{-3}$. This behavior was probably caused by the appearance of the Er_i , which was found to occur only at higher Er concentrations in the present study. As doping densities were increased further, the Er PL intensity decreased, and it was weaker by a factor of 4 for $[Er] = 1.8 \times 10^{19} \text{ cm}^{-3}$. This decrease is probably related to the appearance of ErAs micro-precipitates, which Poole (72) reported for Er doping above $7 \times 10^{17} \text{ cm}^{-3}$.

As shown in Figure 72, the Er PL intensity increases more gradually with increasing Er concentration in $Al_{0.5}Ga_{0.5}As$ as compared to GaAs. The maximum Er PL intensity occurred at $[Er] = 1.5 \times 10^{19} \text{ cm}^{-3}$, followed by a much sharper decrease than that which was observed for

GaAs by Smith et al. (83:50). Based upon the findings for Er-doped GaAs in the current study, the increase in the Er-4f PL intensity observed in AlGaAs may also be due to the introduction of Er into an optically active interstitial site, while the sudden decrease may be due to the formation of ErAs micro-precipitates. This reasoning leads to the important conclusion that the Er solubility limit in $\text{Al}_{0.5}\text{Ga}_{0.5}\text{As}$ is $[\text{Er}] \approx 2 \times 10^{19} \text{ cm}^{-3}$, which is approximately 30 times larger than in GaAs. Thus, more intense emissions are expected in AlGaAs.

Klein et al. (46) measured the Er^{3+} PL, Er^{3+} PL decay, and the Er^{3+} EPR signal as a function of annealing temperature for Er-implanted GaAs. The primary differences between their samples, and the samples used in this investigation, is that Klein et al. performed three Er implants with energies of 1.5, 3, and 5 MeV into an MOCVD-grown substrate, with varying doses, so as to obtain uniform Er-doping of $[\text{Er}] = 5 \times 10^{17} \text{ cm}^{-3}$ in a 1.0 to 1.5 μm thick layer. Thus, Klein et al. had much stronger Er luminescence compared to this investigation, which utilized a single Er implant at an energy of 1 MeV that extended to a depth of 0.5 μm . Klein et al. capped their samples with Si_3N_4 and furnace annealed them at various temperatures, T_A , from 600 to 875 $^{\circ}\text{C}$. They found, as in this investigation, that for lower T_A , the spectrum was characterized by a large number of sharper emission lines, while for high anneal temperatures, a relatively simple and somewhat weaker and broader spectrum was observed. Klein et al. observed 20 distinct lines and plotted the intensity of each as a function of T_A , concluding that each of the lines followed one of three temperature dependences, indicating that there are at least three distinct Er centers present in this material. The three centers are labelled T1, T2, and T3. T1 emissions consist of at least 10 separate lines, while type T2 and T3 each consist of at least 5 emission lines. Since the $^4\text{I}_{15/2}$ ground state of Er^{3+} is 5-fold degenerate at cubic sites, and at most 8-fold degenerate under low symmetry conditions, the T1 site must be composed of at least two distinct sites (T1A and T1B). Further, Klein et al. was able to measure the temperature dependence of the PL intensity and the decay times for each type of center. An analysis of this data yields a thermal activation energy for the luminescence quenching process. Klein et al. also determined the temperature dependence of the Er^{3+} -4f emissions in Er-doped, MBE-grown GaAs. A brief description of the behavior of each type of center can be summarized as:

- T1. The intensity increases gradually to a peak at $T_A = 725^{\circ}\text{C}$, and then decreases sharply, becoming at least two orders of magnitude weaker for an annealing temperature of 850 $^{\circ}\text{C}$. These centers are thermally deactivated according to two energies, $E_1 = 457 \text{ meV}$ and $E_2 = 65 \text{ meV}$. There are actually two distinct centers, which are labelled T1A and T1B.

T2. The intensity gradually increases and peaks near $T_A = 700$ °C, and then it gradually decreases to a level 50 times weaker than the maximum intensity for an annealing temperature of 875 °C. Klein et al. did not give an activation energy for thermally quenching the luminescence from this center.

T3. The intensities of these emissions gradually increase until $T_A = 800$ °C, and thereafter decrease, possibly very slowly. The most intense peak in this set shifts to slightly higher energies as T_A increases, as compared to the most intense peaks observed for the T1 and T2 centers. The emissions of this center were thermally deactivated according to two processes, with energies of $E_1 = 198$ meV and $E_2 = 12$ meV.

MBE. The temperature dependence of the Er^{3+} -4f emissions in the Er-doped MBE-grown GaAs exhibited two thermally activated luminescence processes with $E_1 = 146$ meV and $E_2 = 36$ meV.

Klein et al. also claims to have measured the absolute concentration of the Er^{3+} centers using the EPR technique. For annealing temperatures below 700 °C, with an uncertainty factor of ~ 3 , the $[\text{Er}^{3+}]$ was found to be relatively constant and less than 0.1% of the Er-doping density; it then increases by a factor of ~ 5 when annealed over the temperature range of 700 to 875 °C. This behavior apparently contradicts the PL measurements, which indicate that nearly all of the Er was contributing to the observed Er^{3+} luminescence. This led Klein et al. to conclude that prior to excitation, these Er-centers were apparently in the 2+ charge state, and then upon excitation, they were promoted to the 3+ charge state. Klein et al. expected the Er atom to be in the 3+ charge state if it substitutes for the Ga atom. However, referring to the RBS measurements of Kozanecki, Klein et al. indicated that Er may be occupying interstitials, and speculated that the Er may form a complex with a neighboring defect or impurity via the charge transfer of its two weakly-bound 6s electrons, thus remaining in the Er^{2+} core state.

Much of Klein's data compares favorably with the DLTS results in the present study. For instance, the values reported for the thermal deactivation energies for the PL emissions of the T1A and T1B centers are very close to activation energies reported for centers (c) and (j) in this study. Center (c) was identified as the first acceptor level of the Ga antisite defect, $\text{Ga}_{\text{As}}^{-1}$, and center (j) was identified as being related to the As interstitials, As_i . Thus, it seems quite possible that the T1 sites are related to the $\text{Er}_{\text{Ga}} - \text{Ga}_{\text{As}}$ and $\text{Er}_{\text{Ga}} - \text{As}_i$ complexes. Each of these complexes lack inversion symmetry, and thus, they would have a higher probability for electric

dipole transitions. The values Klein et al. reported for the MBE material are also consistent with the results of this investigation. Klein et al. found that the Er^{3+} -4f PL in the MBE-grown GaAs:Er was thermally deactivated by processes with energies of 35 meV and 146 meV. These energies agree well with the two prominent levels reported in this study for MBE-grown GaAs:Er. The former was attributed to an isolated Er_{Ga} center which acts as an isoelectronic hole trap, and the latter to a defect related to the formation of ErAs microprecipitates. The second center was observed only in MBE-grown GaAs, and it found to dissociate for annealing temperatures between 750 and 800 °C. For the T3 centers, Klein reports two activation energies which do not agree well with any of the deep levels found in the present study. The annealing behavior of this center is, however, very similar to the behavior observed for the Er_{Ga} center acting as an isoelectronic trap. That is, the appearance of this center and the shift in the Er^{3+} -4f emissions to slightly longer wavelengths were only observed for higher annealing temperatures. Furthermore, according to Klein et al., this center has 5 lines, which is consistent with the 5-fold degeneracy expected for the T_d isolated Er_{Ga} center. Unexpectedly, the Er-4f PL for the T3 centers should show two thermal deactivation processes, even though the emissions were dominated by a single center. Klein's explanation is that the Er^{3+} is a nonequilibrium state, and a nonexponential decay is consistent with a second process involving a relaxation of the Er^{3+} excited state back to the Er^{2+} state. However, Klein et al. does not provide uncertainties with the temperature dependent fits. Since the emissions from the T3 centers are the weakest of all types of Er-centers, and since some of the T1 or T2 type emissions might also be contributing at these higher annealing conditions, an even more likely explanation than that given by these authors is that some of the emissions from the T1 or T2 centers were also detected along with the T3 emissions. If this data were fit for only one center, it might agree more closely with the 35 meV isoelectronic Er_{Ga} center.

Unfortunately, Klein does not provide the thermal deactivation energy for the T2 emissions. Possibly, this is because the behavior of these emissions are similar to the T1 emissions, and they are, therefore, difficult to resolve (Klein does not state the reason). Five lines are associated with the T2 emissions, suggesting that they may be attributed to a single center. Further, the intensity of these emissions attain a maximum at an annealing temperature similar to the T1 type centers, suggesting that this center may be related to center (g). In this investigation, as in that performed by Klein et al., the concentration of the (g) or T2 type center peaked at a slightly lower temperature compared to the T1 type centers, which are probably the (i) and (j) centers.

As discussed above, center (g) is thought to be due to an Er_i .

6.4.2.1 Er-4f Luminescence Excitation and Quenching Mechanisms As discussed in the background chapter, a successful excitation – de-excitation model has been proposed for Yb in InP by Takahei et al. (89). This model utilized a nearly-resonant transfer of the energy of an exciton bound to the isoelectronic electron trap formed by an isolated Yb_{In} in InP into the Yb^{3+} -4f shell. Takahei explains that the quenching of the Yb-4f luminescence is due to an Auger back transfer of the energy from the excited core to an electron bound at the trap, thus de-exciting the core and sending the electron deep into the conduction band. His assumption was that the excited Yb^{3+} would essentially have the same electron-attractive potential as the ground state Yb^{3+} , and thus, it could still bind an electron.

There are two main differences between the InP:Yb and GaAs:Er. First, in InP:Yb, whether prepared by MOCVD, ion implantation, or LPE, there has only been one center identified. On the other hand, there have been several different centers observed in Er-doped GaAs, depending upon whether the crystal was doped by ion implantation, or while growing MOCVD or MBE layers. Thus, while one excitation mechanism is dominant for Yb in InP, there may be a different excitation mechanism for each Er center in Er-doped GaAs. The second major difference is that in InP:Yb, the Yb-4f transition was nearly resonant with the band gap. However, in the current study, the energy of the Er-4f transition, 0.8 eV, is roughly half the magnitude of the band gap energy (1.5 eV). This feature implies that a third particle must be present near the RE site, which acts to absorb the excess energy in the form of an Auger transition.

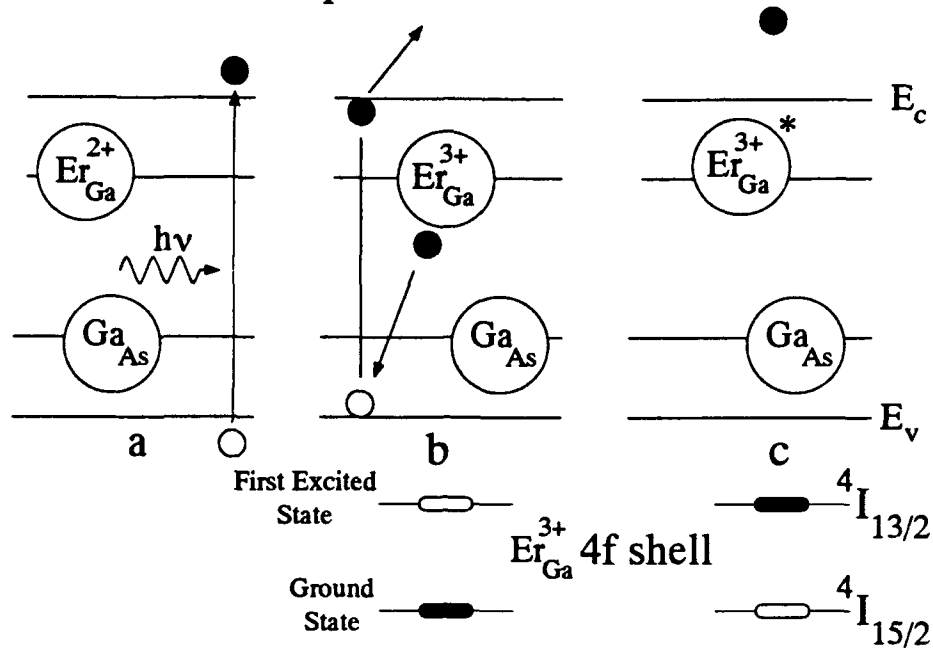
The proposed models should account for the observed excitation and quenching of the Er^{3+} -4f emissions. These models should also be consistent with the DLTS observations in this investigation, as well as the EPR experiments of Klein, which indicate that the Er is largely in the 2+ charge state, at least at low temperatures. Upon annealing, the Er may occupy the Ga site, and the displaced Ga atom occupies a nearest-neighbor As site, thereby forming an $\text{Er}_{\text{Ga}} - \text{Ga}_{\text{As}}$ complex. Further, following the suggestion of Klein et al., since the Er_{Ga} is near another defect (Ga_{As}), the Er may remain in the 2+ charge state, with a $4f^{12}$ shell. The overall charge at the Er_{Ga} site is thus, -1. Also suppose that the Ga_{As} still behaves essentially as the same double acceptor, despite the presence of the Er on the nearby Ga site. Then, at low temperatures, the Ga_{As} will be neutral, with the first acceptor level at approximately 77 meV, unoccupied by an

electron. The situation is shown in Figure 73 a. Above-band-gap laser excitation will generate electron hole pairs. Since the Er_{Ga} is in the $2+$ charge state, it is negatively charged, and it will attract a hole. In turn, this hole will then attract an electron, thereby forming a bound exciton at the Er^{2+} center; i.e., the Er_{Ga}^- center. The exciton may then decay, simultaneously ejecting a $4f$ electron into the conduction band and transferring the remaining energy into the $\text{Er}^{3+} 4f^{11}$ shell, thus, lifting it to the first excited state, $^4\text{I}_{13/2}$. Alternatively, this transition may be viewed as the direct recombination of the extra $4f$ -electron in the Er - $4f$ shell with a valence band hole, exciting the Er - $4f$ shell and simultaneously transferring the excess energy to the electron in the conduction band (Figure 73 b). In order for this scheme to be energetically feasible, the extra $4f$ electron must be bound to the Er core with less energy than the difference between the bound exciton recombination energy and the excitation energy of the $4f$ -shell; that is, a value approximately equal to 0.7 eV . The excited Er^{3+} - $4f$ shell will then radiatively emit energy, and return to the ground state, where it can recapture the first available electron, and thus, return to the Er^{2+} state.

At higher temperatures, the first acceptor level of Ga_{As} will be filled. Since no previously unreported electron trap was found in this investigation, the electron occupying this Ga_{As} center may have been transferred from the Er^{2+} - $4f$ shell, forming Er^{3+} , as shown in Figure 73 d. Therefore, the Er_{Ga} center becomes neutral, and the Ga_{As} will become negatively charged, and thus able to efficiently bind the excitons. Now when the exciton decays, the released energy may elevate the electron at this center into the conduction band with no energy being transferred into the Er^{3+} . Thus, no luminescence from the Er^{3+} is expected. This luminescence-quenching mechanism is demonstrated in Figure 73 d-f, effectively explaining the 65 meV Er PL deactivation process for the T1A center observed by Klein.

Similar Er - $4f$ luminescence excitation and quenching processes may be envisioned for the T1B center, which presumably consists of a complex involving $\text{Er}_{\text{Ga}} - \text{As}_i$. These models are consistent with the EPR measurements by Klein et al., showing that a small percentage of the Er is in the $3+$ charge state at low temperatures. It is also consistent with the large concentration of Ga_{As} centers and As_i -related centers observed in the current study by DLTS. Finally, the appearance of the intense, broad band under the Er emissions may be due to the recapture of an electron into the Er^{3+} - $4f$ shell, or it may arise from the pseudo-donor-acceptor-pair transition in Figure 73 b. This broad band is not associated with the EL2 defect, and it is not related to

Low Temperature: Er PL Excitation



High Temperature: Er PL Quenching

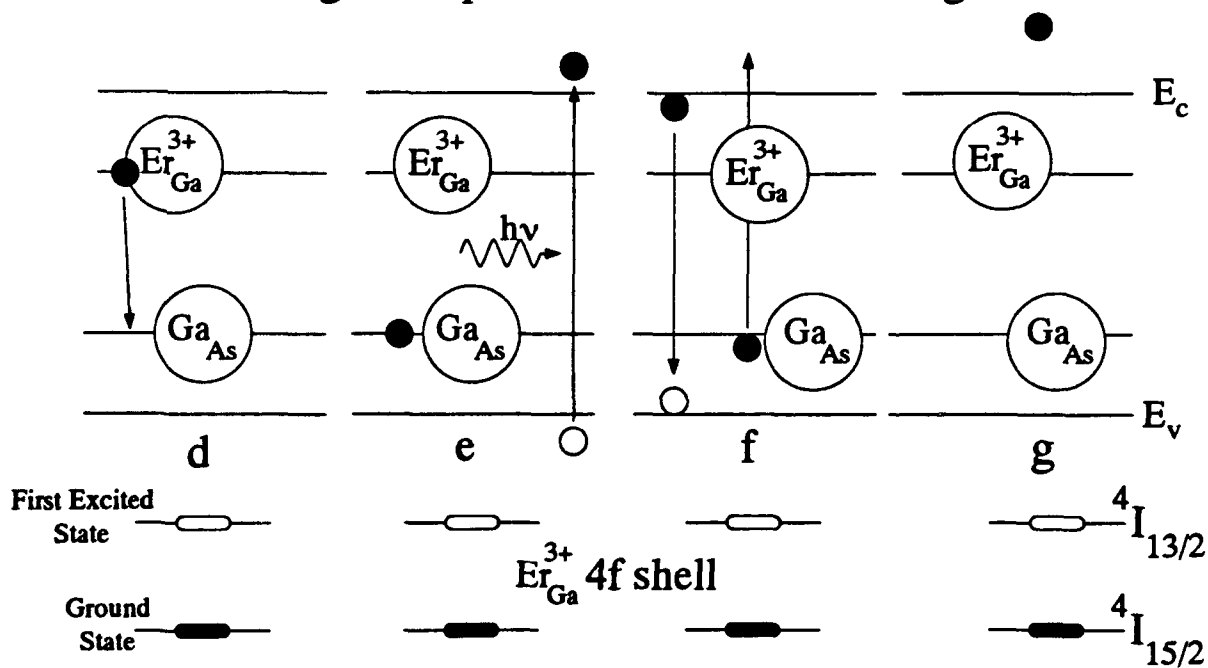


Figure 73. Exciton-mediated Er^{3+} -4f PL excitation and thermal quenching model for the type T1 center in GaAs:Er

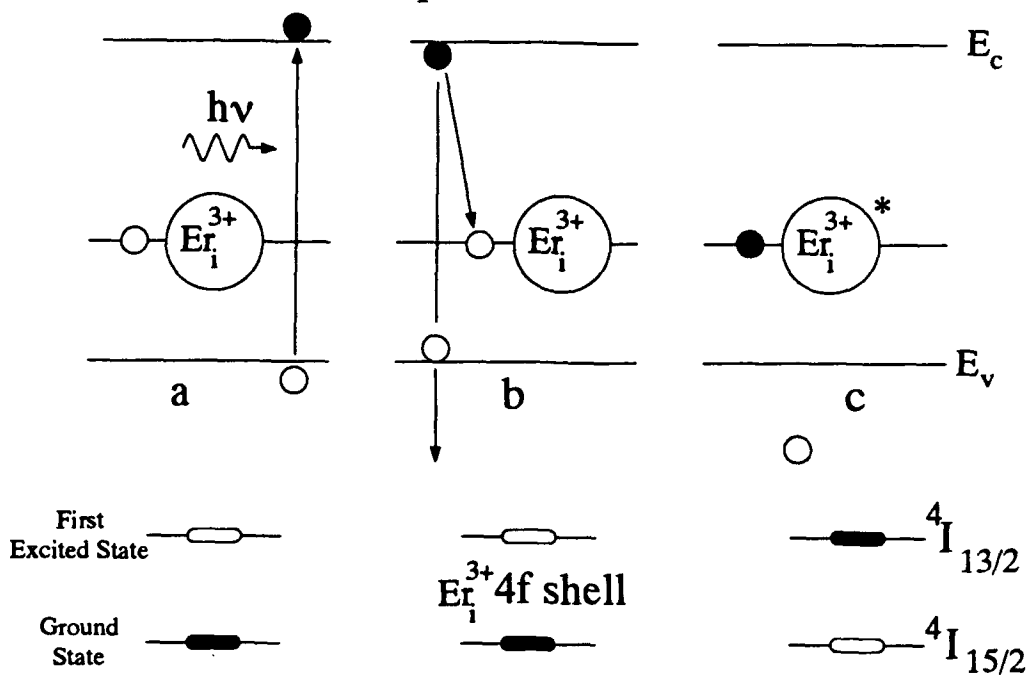
ion-implantation damage, since annealing studies on Nd and Pr-implanted GaAs manifested no such band (section 7.3). Therefore, the broad band is definitely related to Er.

Overall, Klein's T2 type center corresponds to the center (g) found by the DLTS measurements. This center is thought to be associated with an Er_i , with the Er atom located in the $\langle 110 \rangle$ channel. While the isolated Er_{Ga} is expected to give Er in the 3+ charge state, when the Er atom enters the interstitial, it may retain the 12th 4f electron, and produce an Er in the 2+ charge state. Thus, there are two distinct physical interpretations possible for the hole emission from center (g). First, the hole emission from center (g) could be related to an $\text{Er}^{3+}(4f^{11})/\text{Er}^{2+}(4f^{12})$ transition, with transfer of a hole bound in the 4f-shell to the valence band. Alternatively, it could be related to the emission of a hole which is localized outside of the core, with the 4f-shell remaining in the $4f^{11}$ configuration.

This latter case, in which the 4f-core of the Er_i is always in the 3+ charge state, independent of temperature, acting as a hole trap with the hole capture and emission occurring at a state external to the core, is considered first. At low temperatures, the center (g) will be unoccupied, i.e., this center will be occupied by a hole, as shown in Figure 74 a. Above-band-gap-laser excitation generates excitons which migrate to this center. The electron recombines with the hole bound at this center, exciting the Er-4f shell, and the excess energy is absorbed by the free hole in the valence band. The transition probability for this process is enhanced by the location of the Er in an interstitial site, and so the crystal field will tend to mix 5d states into the 4f configuration. At higher temperatures, an electron occupies center (g), and hence this process can no longer take place. This would account for quenching of the 4f luminescence at higher temperatures. This model, designated as T2a, is demonstrated in Figure 74.

There is another possibility for exciting the Er-4f shell of the T2 center if it is indeed attributed to the Er^{3+} configuration. This model is designated as T2b, and it is illustrated in Figure 75. Again, at low temperatures, center (g) is occupied with a hole. Upon laser excitation, a photon of energy greater than (0.36 eV + 0.8 eV) can simultaneously transfer an electron from the valence band to this unoccupied state, as well as excite the Er atom to the $^4I_{13/2}$ first excited state (Figures 75 a-c). The quenching of the Er^{3+} luminescence may be governed by two processes. First, suppose the laser excitation is above the band gap energy and the Er^{3+} is already in the excited state ($^4I_{13/2}$). Then, an exciton-mediated de-excitation process can occur, as shown in Figure 75 d and e. An exciton may be efficiently bound to this negatively-charged

Low Temperature: Er PL Excitation



High Temperature : Er PL Quenching

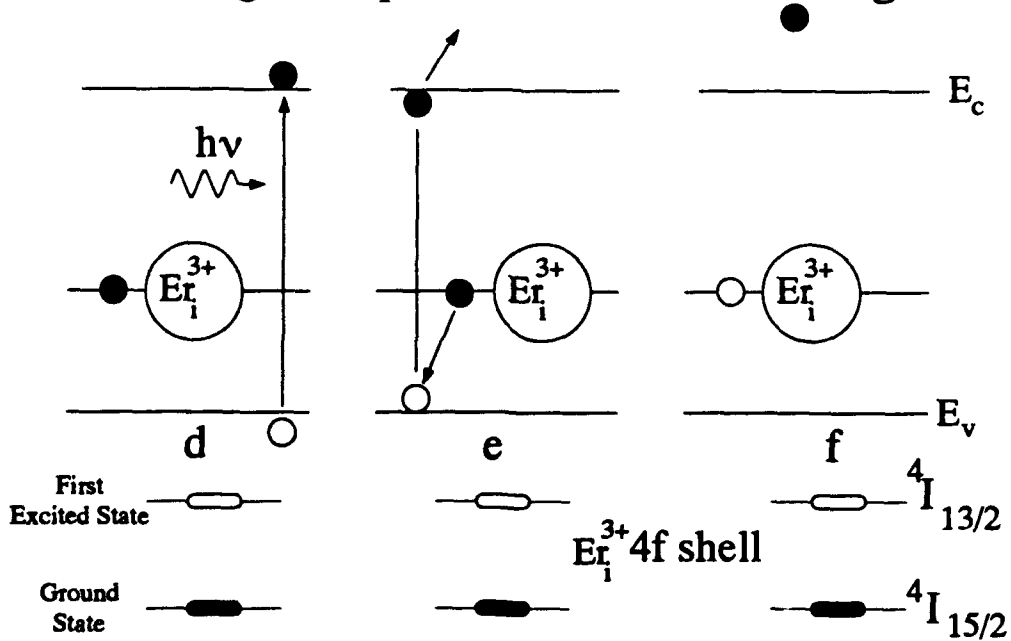


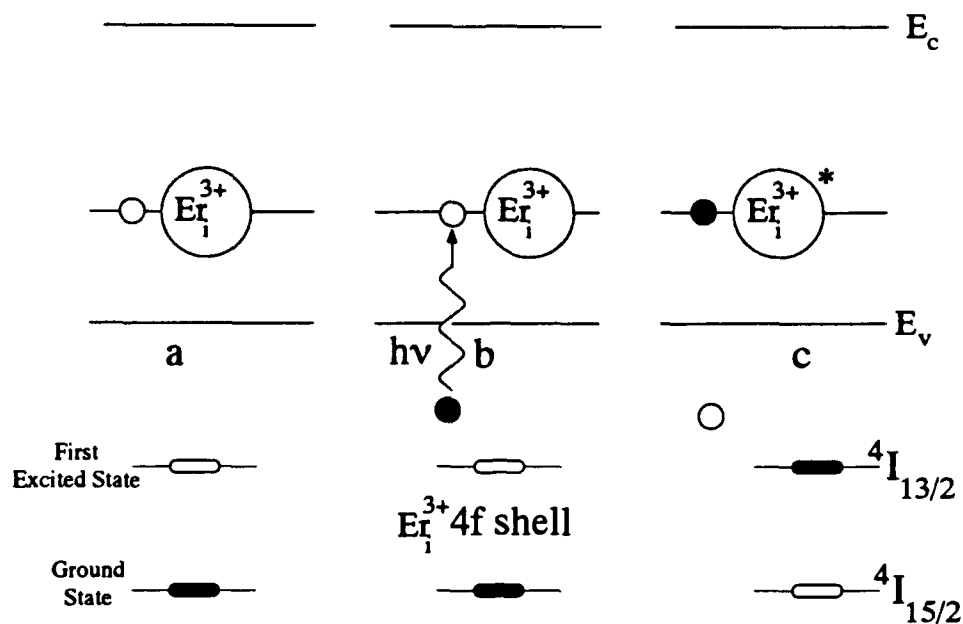
Figure 74. Excitation model T2a for exciton-mediated excitation of the Er^{3+} -4f shell and thermal quenching for the type T2 center in GaAs:Er

excited center. The electron trapped at this center may recombine with the hole, simultaneously releasing the energy in the excited 4f-shell into an Auger process, which sends the conduction band electron much deeper into the conduction band. In addition, the luminescence from this center can be thermally quenched, since as temperature increases, an electron will be more likely to occupy this center, and hence, the transition shown in Figure 75b will not be possible.

In fact, below-band-gap excitation of the Er^{3+} emissions has been observed both by Colon et al. (19:673) and by Klein et al. (46:669), for both Er-implanted and MBE-grown Er-doped GaAs. They have found below-gap-excitation extending to wavelengths as low as $1.1 \mu\text{m}$ or 1.12 eV, which is near the 1.06 eV cut-off wavelength expected for this transition (Figure 75 b). Klein has also observed that the below-gap excitation is as much as one order of magnitude weaker for the samples in which T3 emissions dominate, compared to the samples in which T1 and T2 type centers dominate. This behavior is consistent with the current model, since Klein's T2 type center is thought to be the Er_i center (center (g) in this investigation). While Klein's below-gap excitation resulted in weaker Er-4f emissions than for above-band-gap excitation, Colon observed the opposite effect, i.e., stronger Er-4f emissions for below band gap excitation. This unexpected result can easily be explained using model T2b. With above-band-gap excitation, both the exciton mediated de-excitation and thermal quenching mechanisms shown in Figure 74 can occur. However, with excitation below $E_g - E_{ex}$, where E_{ex} is the exciton binding energy, there will be no excitons available for the de-excitation mechanism shown in Figure 75 d and e, and therefore, the Er-4f PL may be more intense. Colon's observation of more intense Er-4f emissions with below-band-gap excitation may be attributed to his sample annealing conditions (RTA of 750 °C for 15 seconds), which were the conditions under which the DLTS measurements have indicated a maximum in the concentration of (g) centers (T2 centers). On the other hand, the weaker below-band-gap excitation observed by Klein may be attributed to a higher concentration of T1 compared to T2 centers.

Further experiments can be conducted to firmly establish the below-bandgap-excitation proposed in model T2b. An excitation source capable of traversing the energy region at which the excitation cut-off should occur would conclusively prove this mechanism. Colon (19) used a Ti-sapphire laser for the selective excitation measurements. The lowest energy attainable by the Ti-sapphire laser is approximately 1.1 eV, which is very close to the expected cut-off energy of 1.06 eV, and consequently, this source is not acceptable. If a suitable excitation source is

Low Temperature: Er PL Excitation



Er PL Quenching

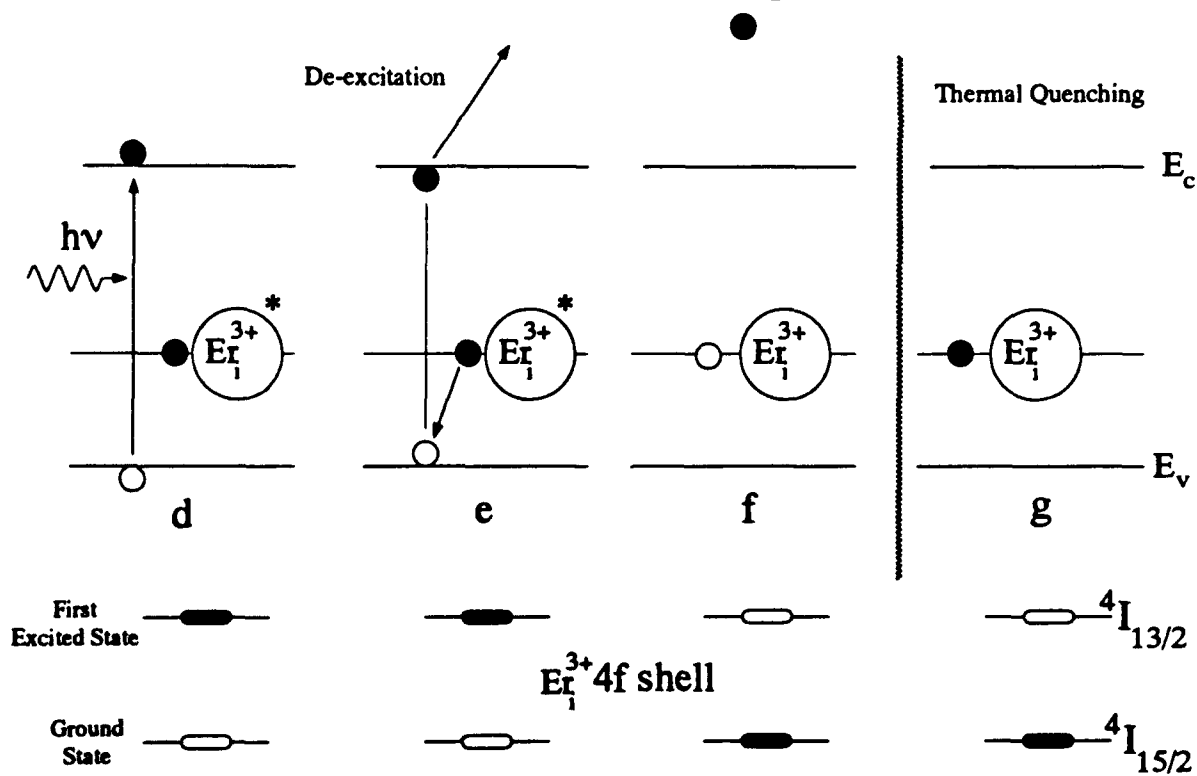


Figure 75. Excitation model T2b for excitation and quenching of the Er^{3+} -4f PL of the T2 center in GaAs:Er

not available, then the T2b model can also be tested by measuring the temperature-dependence of the Er-4f emissions with below-band-gap excitation. Only the thermal quenching of the Er-4f emissions can occur. Thus, the temperature-dependence of their intensities should yield an activation energy of 360 meV. These measurements should be performed upon an otherwise undoped sample annealed so that the (g) center dominates; i.e., 750 °C for 15 seconds.

The hole trap corresponding to center (g) may be caused by the Er-4f core transitioning between the 2+ ($4f^{12}$) and 3+ ($4f^{11}$) charge states. The Er^{3+} -4f shell can only be excited if an electron occupies this center (Er is in the 2+ charge state), and a photon of energy greater than $(1.16 + 0.8)$ eV then transfers this electron to the conduction band, and simultaneously excites the Er^{3+} 4f-shell (Figure 76 a-c). As the temperature increases, the center (g) is more likely to be occupied by an electron (and thus be in the 2+ charge state), so an increase in the intensity of the emission from this center with increasing temperature is expected. This might imply that the Er-4f luminescence intensity continually increases with temperature. However, as the temperature increases further, the hole emission rate will tend to increase, and it will eventually surpass the spontaneous decay of the excited Er^{3+} ($^4I_{13/2}$) state. Further, the energy required to support this process is readily available from the 4f core. Thus, the quenching of the Er-4f emissions in this model will proceed similar to that proposed for the de-excitation of Yb^{3+} in InP by Takahei (89). That is, the energy stored in the 4f core may transfer as an Auger process, sending the trapped hole deep into the valence band and thereby nonradiatively de-exciting the Er^{3+} . This model is referred to as T2c, and these excitation and de-excitation processes are demonstrated in Figure 76.

This model predicts that the Er-4f PL intensity may first increase at lower temperatures, reach a maximum, and thereafter decrease when the de-excitation process dominates. Another way to verify this model is to compare the Er-4f PL intensity using laser excitation both above and below the energy threshold for excitation, $(1.16 + 0.8)$ eV. For instance, the 488 nm line of the Ar-ion laser could provide above-threshold excitation, and the Ti-sapphire laser could be used to accomplish below-threshold excitation.

Klein did not report a deactivation energy for the Er^{3+} emissions from the T2 type center. However, his data would favor the latter model, since this center was found to have a luminescent intensity similar to the type T1 center. Taken together, along with his assertion that he was able to excite nearly all the Er centers, but that only a very small Er^{3+} signal was detectable by EPR

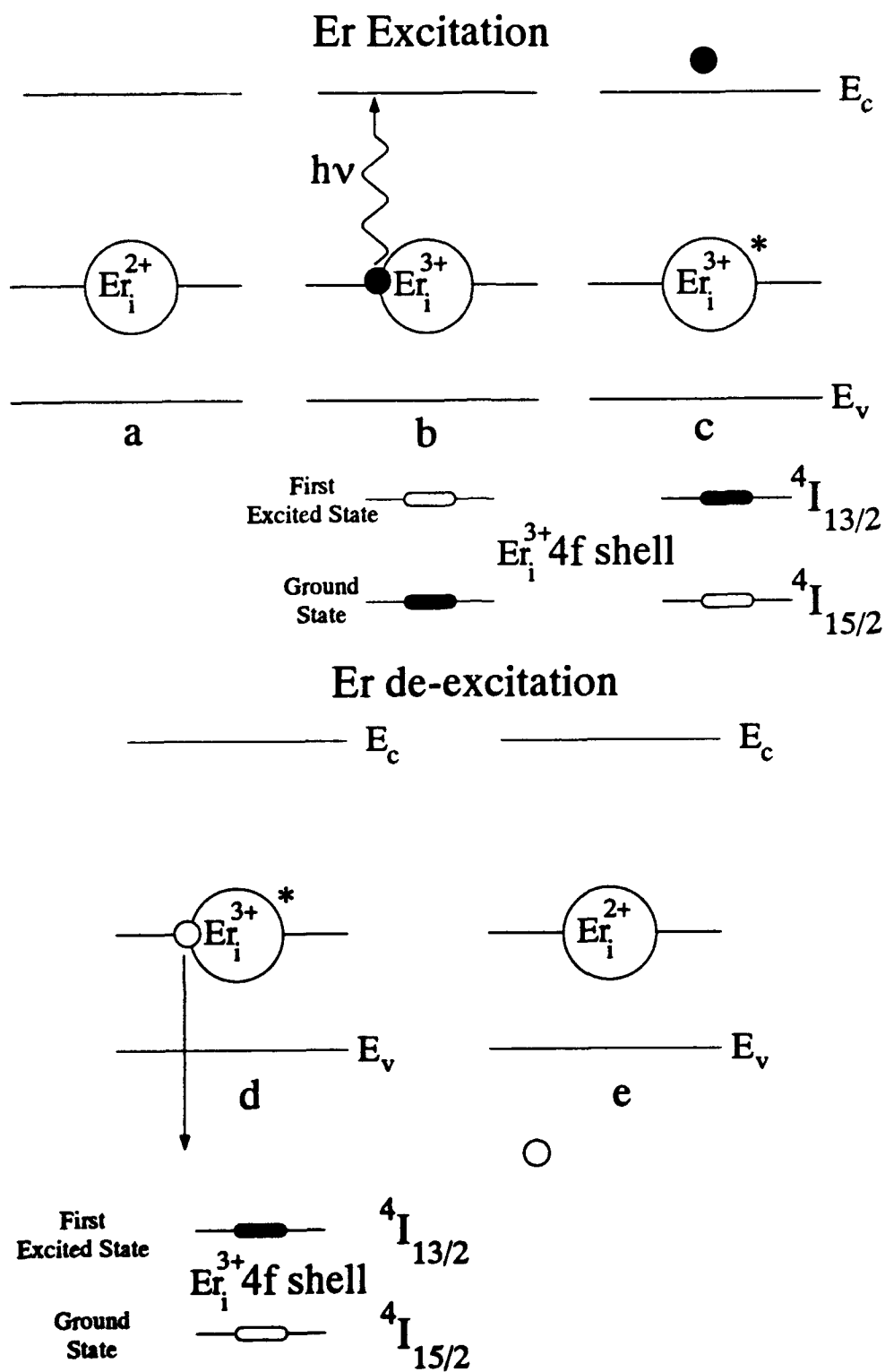


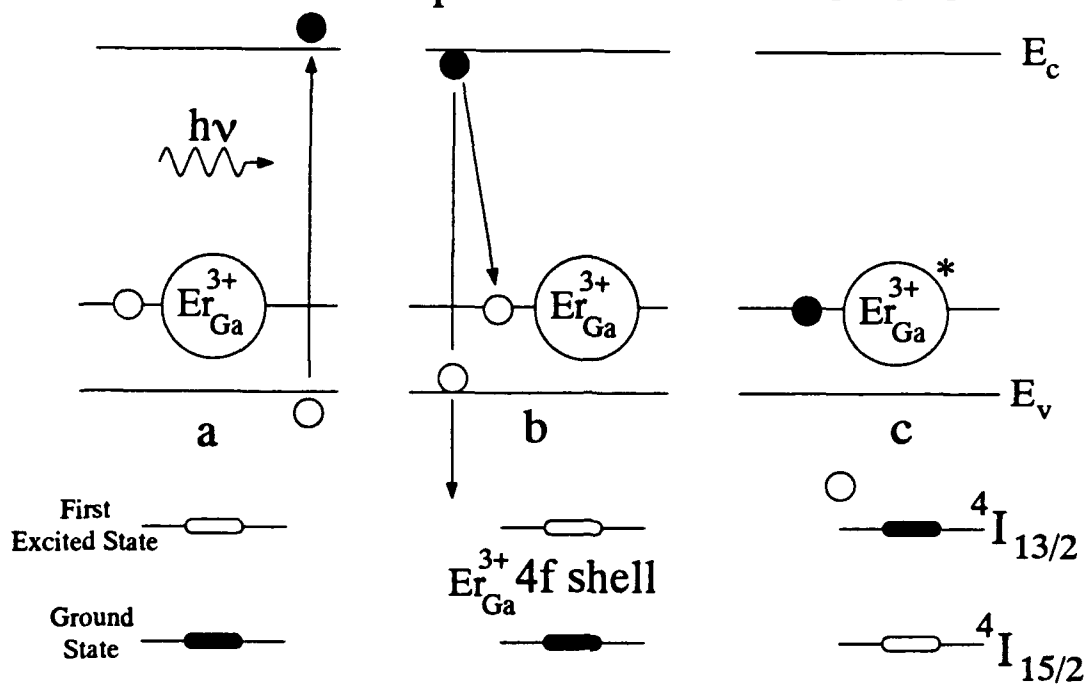
Figure 76. Excitation model T2c for direct excitation of the Er^{3+} -4f shell and Auger de-excitation for the T2 center in GaAs:Er

measurements, implies that the T2 and T1 centers are in the 2+ charge state at low temperatures. Nevertheless, the EPR results are not necessarily in conflict with models T2a and T2b either, since the Er in the interstitial site may have the 5d states mixed with the 4f levels to such an extent that the Er^{3+} EPR signal is not observable. Further work needs to be done to determine the excitation and quenching mechanisms for this center.

For the T3 centers, which are assumed to be isolated Er_{Ga} , the Er core is always in the 3+ charge state. This center acts as an isoelectronic trap which has a potential attractive to holes. However, these holes are localized strictly outside of the 4f-shell. This center gives rise to a localized level only 35 meV above the valence band maximum. At low temperatures, this level will not be occupied with an electron. That is, a hole will be trapped at the center, as shown in Figure 77 a. Upon above-band-gap laser excitation, electron and hole pairs will be formed, and they may recombine in the presence of the neutral Er^{3+} center, exciting the 4f electrons and satisfying the energy balance requirement by propelling the weakly bound hole deep into the valence band. Alternately, this process can be envisioned as a conduction band electron recombining with the hole trapped at the Er^{3+} and, simultaneously, exciting the Er-4f shell, sending the valence band hole roughly 0.7 eV deeper into this band. These excitation mechanisms are illustrated in Figure 77 a-c. The electron transferred to the isoelectronic center cannot contribute to de-excitation of the excited Er^{3+} , since Auger transfer of the bound electron to the conduction band, similar to the mechanism proposed by Takahei (89), is not possible, because there is not sufficient energy in the 4f-core. The neutrality, T_d site location, and short-range isoelectronic impurity potential of the isolated $\text{Er}_{\text{Ga}}^{3+}$, may all contribute to the weak excitation of this center.

At higher temperatures, the Er^{3+} isoelectronic level will be occupied with an electron (Figure 77 d). That is, the weakly bound holes will have been ionized. Therefore, this center will be negatively charged, and so the excitation process shown in Figure 77 b cannot occur. However, an exciton may still be efficiently bound to this center. When this exciton decays, its energy may lift the electron at this site into the conduction band, with no energy remaining to excite the Er^{3+} 4f-core. This quenching mechanism, shown in Figures 77 d-f, explains the 35 meV process Klein observed for the thermal deactivation of the Er^{3+} emissions in Er-doped MBE-grown GaAs, and it was further confirmed by the presence of the Er_{Ga} isoelectronic center, found in this investigation.

Low Temperature: Er PL Excitation



High Temperature: Er PL Quenching

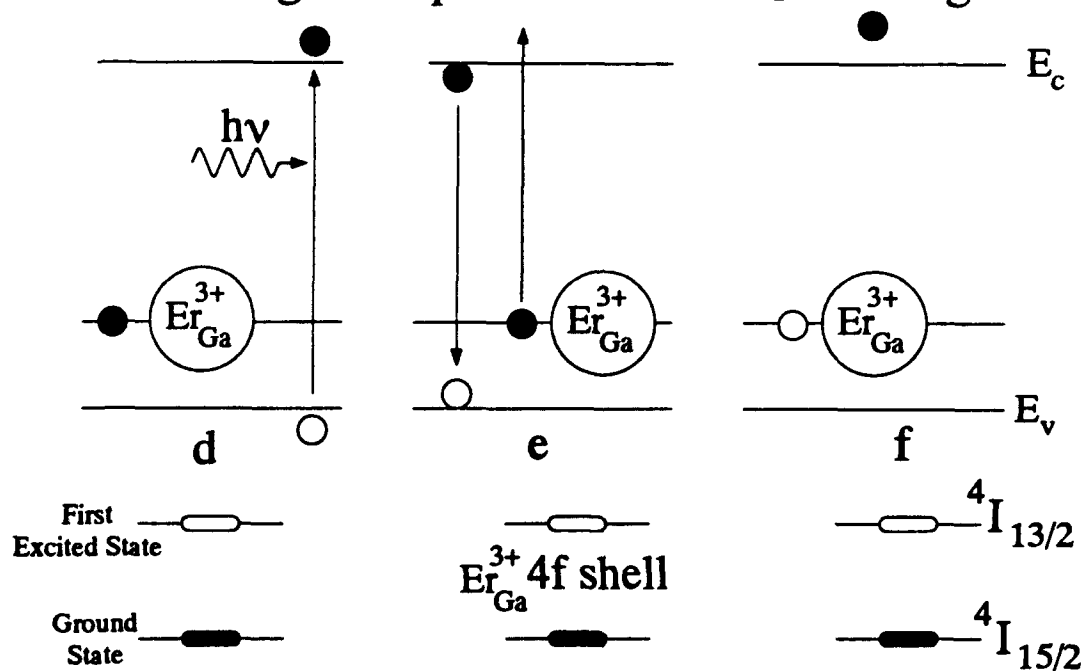


Figure 77. Er^{3+} PL excitation and quenching model for the T3 center in GaAs:Er

These models are also consistent with the PL measurements of Colon on n-type and p-type Er-implanted GaAs. For identical Er-doping and annealing conditions, the Er-4f luminescence was more intense in p-type compared to n-type GaAs samples. This is consistent with the excitation and quenching models given above, since in p-type material the Fermi level will be near the valence band. Therefore, these Er-centers are more likely to be in the low-temperature configuration.

The Er-4f luminescence excitation processes described here are consistent with experimental observations and satisfy energy balance requirements. The theoretical justification for the Auger transfer of primary crystal excitations, that is, excitons, into the core states of transition metal and post transition metal (RE) ions has been addressed by Robbins and Dean (76). As a primary hypothesis, they assumed that the energy transfer process occurs as a result of the electrostatic perturbations between the core electrons of the 'structured' impurity and the electron-hole pair in the vicinity of that impurity. The electron-hole pair may be truly localized to form a bound state, or it may be that the transfer occurs through an inelastic scattering process, in which the energy of an essentially free exciton is lost to the localized core excited states. They calculated the transition probability for energy transfer directly into the excited states of the core based upon this interaction and found two conditions for efficient transfer (76:522):

- The impurity should have electric-dipole transitions quasi-resonant with the lattice absorption edge, and
- These quasi-resonant impurity transitions should be strongly coupled to the lattice phonons.

The latter condition is stated to accommodate small energy mismatches. However, with GaAs:Er, the energy mismatch is too large to be accounted for by emission or absorption of phonons, and the extra energy is probably carried away by ionization of a bound electron for the T1 centers or a bound hole for the T2 and T3 centers. Although they did not rigorously consider this complicated situation, they speculated that when the energy mismatch is so large that phonon-coupling is impossible, the energy mismatch may also be accommodated by ionizing a tightly bound hole (76:522). The transition probability for this three-body process is expected to be significantly smaller compared to the nearly-resonant excitation. This situation may account for the relatively strong Yb-4f nearly-resonant emissions in InP compared to the nonresonant 4f emissions of Er in GaAs.

6.5 Electroluminescence of Er-Doped GaAs

One of the original goals was to compare the effect of Er-related deep states with the luminescence efficiency of Er in GaAs, thereby identifying the most likely excitation paths of the Er in GaAs. As previously discussed, the Er-PL efficiency was correlated with the Er-related deep centers or Er-defect complexes identified through DLTS measurements. An even more direct comparison of the Er-related deep states with the luminescent efficiency of the Er centers can be achieved by comparing the 4f emissions obtained by forward biasing the same p^+n or n^+p diodes used for the DLTS measurements. Thus, a comparison can be made between the injection electroluminescence of the Er-4f emissions and the concentration of Er-related deep centers.

In fact, 1.54 μm Er-related injection electroluminescence has been reported for Er-implanted GaAs by Klein et al. (47) and Er-doped MBE-grown GaAs and AlGaAs by Galtier et al. (33). Klein's samples were different from the samples used in the present study in two respects. First, Klein used thick layers composed of three Er-implants, with energies ranging from 1.5 to 5 MeV and Er fluences adjusted to obtain a uniform Er-doping density of $[\text{Er}] = 5 \times 10^{17} \text{ cm}^{-3}$. Second, they annealed their samples using conventional furnace annealing. CV measurements revealed that the near-surface region of their n-type substrate was converted to p-type conductivity after the anneal, so that there was no need to produce the p^+ region by other means. They later claimed that this conversion was due to the formation of Si_{As} acceptors (65). Er-related electroluminescence was observed at 4 and 77 K, but it was found to be approximately 2 orders of magnitude weaker than the Er emissions measured by PL. Apparently, much stronger Er-related electroluminescence was observed by Galtier et al. (33) for the MBE-grown layers. They formed double heterostructure LEDs with $\text{Al}_{0.7}\text{Ga}_{0.3}\text{As}$ cladding layers, and GaAs and $\text{Al}_{.11}\text{Ga}_{0.89}\text{As}$ active layers with a nominal Er-doping density of $[\text{Er}] = 3 \times 10^{16} \text{ cm}^{-3}$. They obtained room-temperature electroluminescence in both cases, but showed that their devices had an external quantum efficiency of only 10^{-6} . They concluded that much optimization would have to be undertaken before practical devices could be realized.

In an attempt to form efficient p^+n or n^+p diodes, the implanted $\text{GaAs}:(\text{Er}+\text{Mg})$ or $\text{GaAs}:(\text{Er}+\text{Si})$ samples were annealed at 825 °C. This was considered to be a compromise between the ideal annealing temperatures of at least 850 °C for a high activation efficiency of the Mg acceptors and Si donors, and the optimum annealing conditions for Er emissions, which appeared

under laser excitation to be near 750 °C. Unfortunately, the critical dependence of the Er-4f emissions on annealing temperature was not realized until late in the research. That is, the Er-4f PL was quenched for samples annealed at 825 °C. Consequently, no Er-4f emissions were obtained upon injection electroluminescence. This behavior is demonstrated for several p⁺n and n⁺p Er-doped samples in Figure 78. This figure shows the luminescence resulting from the injection of holes into the n-type GaAs substrate 02-PR-1748, or the injection of electrons into the p-type GaAs substrate 3B-PR-840, which were implanted with Er at a fluence of $\Phi_{Er} = 10^{13} \text{ cm}^{-2}$. Also shown is the injection electroluminescence from the MBE-grown, Er-doped layer x009b, which was subjected to the same low energy, high fluence Mg implantation in order to form a p⁺n junction. All samples were annealed at 825 °C for 12 seconds prior to fabricating the diodes. These results were obtained by applying a forward bias of typically 3V to 8 parallel diodes, which yielded a total surface area of 0.018 cm². The measurements were implemented at a temperature ranging from 4 and 8 K.

The spectra shown in Figure 78 were obtained with no filters in place, and the wavelength counter on the spectrometer was scanned from 7500 to 9000. Since the grating in the spectrometer had 600 lines/mm, the first order wavelength in the range of 15,000 to 18,000 Å were actually dispersed for this scanning range. Thus, the Er emissions at 1.54 μm appear in the first order of the grating, while the band edge emissions are observed in second order, with their wavelengths coincident with the dial reading. The Er emissions were not detectable in any of these samples, although the band edge emissions are clearly seen in all cases. In fact, they were used to align the diodes to the spectrometer. Also shown, for comparison, is the PL spectrum obtained with 150 mW of excitation at 488 nm for semi-insulating GaAs substrates with the same Er implant but annealed at 750 and 800 °C for 15 seconds. While the higher annealing temperatures may have indeed resulted in better diodes, they also resulted in a decrease in the concentration of optically active Er-centers. In fact, from the findings of the preceding section, it is likely that annealing at 825 °C produced only type T3 centers which correspond to an isolated Er_{Ga}. Because the Er is occupying this rather placid site with T_d symmetry, it is very difficult to excite, and thus, electroluminescence of the Er-4f emissions is not expected.

Future attempts to obtain injection electroluminescence from Er-implanted GaAs should, therefore, be restricted to the optimum annealing conditions for the Er emissions, specifically 750 °C for 60 seconds. These conditions were found to be superior to annealing at 750 °C for 15

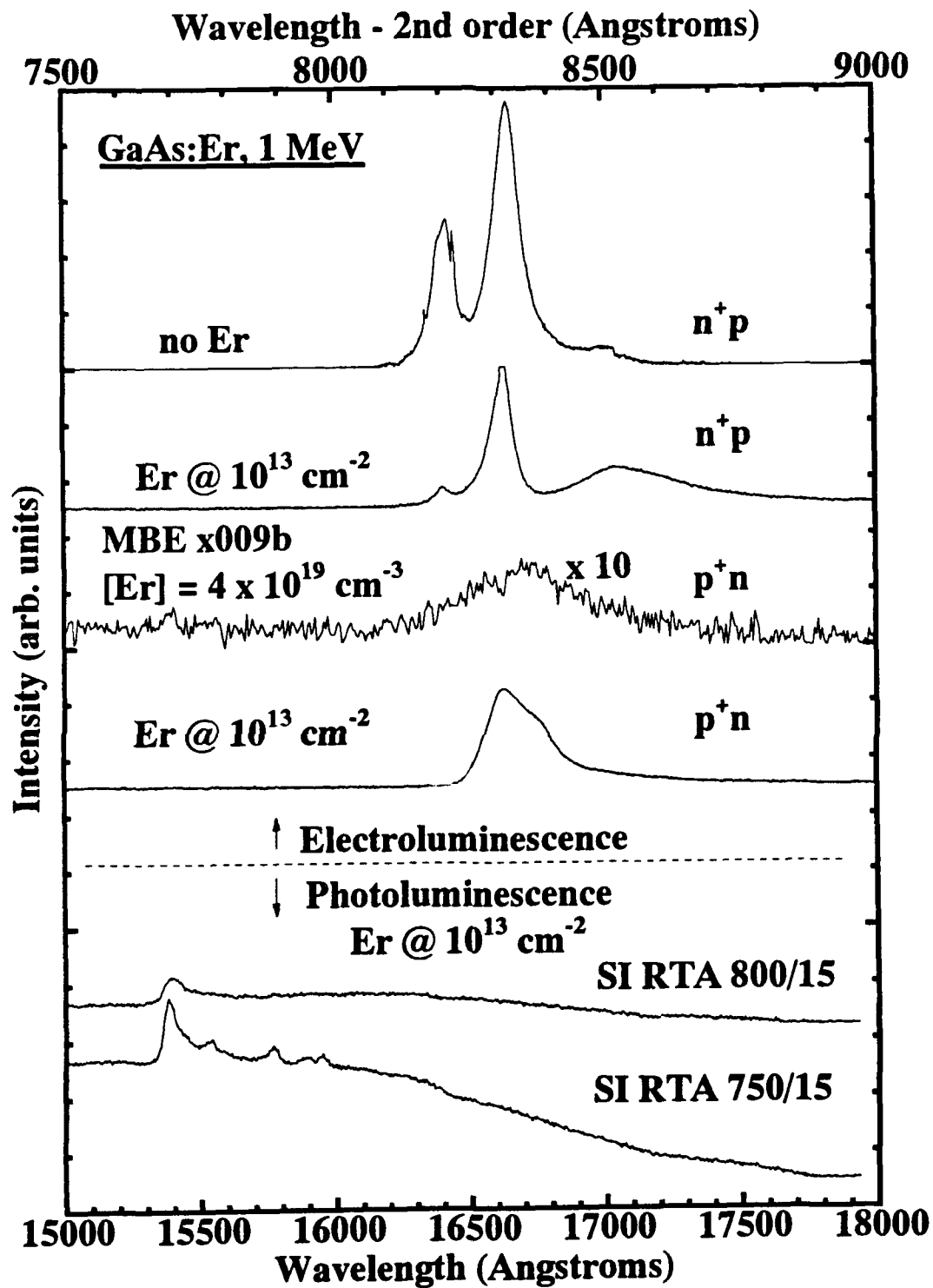


Figure 78. Injection electroluminescence measurements of p^+n and n^+p Er-doped GaAs diodes

seconds, since the Er emissions were slightly more intense, and the broad bands were significantly diminished for the longer annealing (Figure 63). Alternatively, in the case of Er-implanted into n-type GaAs, the p^+ contacts could be formed with a low temperature Zn diffusion after the high temperature anneal of the Er-implant. Further, it may also be possible to eliminate the p^+ doping altogether, since the center (g) was found to enhance the hole concentration. This in fact may be the mechanism by which the surface layer was converted to p-type conductivity, as observed by Klein et al. (46).

VII. Conclusion and Recommendations

The following objectives were established at the beginning of this investigation:

- a. The primary objective was to resolve the electrical behavior of selected rare earths in GaAs and $\text{Al}_x\text{Ga}_{1-x}\text{As}$, by determining whether these atoms behave as donors or acceptors, whether they introduce deep levels, or whether they act to purify these materials by gettering shallow donors.
- b. A subsequent objective was to characterize the nature of deep levels introduced into the band gap in RE-doped material by determining whether they were due to an isolated RE center, a RE-donor or acceptor complex, or RE-induced crystal defects such as interstitials or vacancies.
- c. An additional goal was to compare the measured electrical properties with the RE luminescent efficiency, thereby determining the role of impurity states in the excitation and de-excitation mechanism of the RE.
- d. A continual goal throughout the study was to examine the effect of different growth or doping techniques on the electrical behavior of GaAs:RE.

Previously, little attention has been given to the electrical characterization of Er-doped GaAs and AlGaAs. Instead, most studies have focused only upon their optical characterization, such as, by photoluminescence measurements. However, previous work on InP:Yb, the III-V:RE system studied most, revealed that an understanding of both the electrical and optical properties was necessary to formulate the excitation and de-excitation mechanisms for the 4f shell of Yb. Thus, in the current study, electrical characterization by Hall effect and DLTS measurements, and optical characterization by photoluminescence measurements, were utilized to discern the excitation and de-excitation mechanisms of the Er-4f shell in GaAs and AlGaAs.

The broad objective was to study a selection of REs in GaAs and AlGaAs with a focus on the rare earth erbium. This atom is of particular technological importance because the Er^{3+} 4f-4f transition $^4\text{I}_{13/2} \rightarrow ^4\text{I}_{15/2}$, is characterized by a wavelength at $1.54 \mu\text{m}$, which is near the minimum attenuation for silica-based optical fibers. Thus, an understanding of both the electrical and optical behavior of this ion will significantly enhance the material and physical knowledge required to fabricate optoelectronic devices, such as LEDs and semiconductor lasers, which utilize this transition. While some measurements on GaAs:Pr and GaAs:Nd were also performed in the

course of this research, no systematic study was undertaken, and therefore, the results were only presented when they provided clarification of the results obtained for GaAs:Er.

7.1 Contributions

Significant contributions were made in areas (a) through (c) listed above for various Er-doped GaAs and AlGaAs samples. Further, measurements were performed on GaAs and AlGaAs samples doped with Er by ion implantation as well as during MBE-growth, in accordance with objective (d) that was stated above. The results obtained will be summarized for both of these materials according to the categories (a) through (c), above.

(a) Basic Electrical Trends

Hall effect and CV measurements showed that there was a significant reduction in the free-electron concentration upon Er-implantation and post annealing treatments in n-type GaAs and $\text{Al}_x\text{Ga}_{1-x}\text{As}$ for $x \lesssim 0.1$, but not for $x \gtrsim 0.2$. Major findings include the following:

- In ion-implanted material, it was conclusively shown that the carrier reduction was not related to the effect of donor gettering by doped Er atoms, since there was little effect on the DX center (attributed to an isolated Si donor) in Er-implanted AlGaAs.
- Free electron reduction was due in part to compensation by a large concentration of unannealed native defects resulting from Er implantation. Center (c), which is related to Ga_{As} , and centers (i) and (j), which were related to As_i s or possibly As_i -impurity complexes, as well as center (k), which is definitely related to an As_i -impurity complexes, all contributed to compensation.
- Compensation by a large concentration of the Er-related center (g) also contributes to the free-electron reduction.
- In the Er-implanted and annealed n-type $\text{Al}_x\text{Ga}_{1-x}\text{As}$ for $x \gtrsim 0.2$, a reduction in electron concentration was not observed. This behavior was found to be related to the disappearance of damage-related centers, as well as to a reduction in the concentration of Er_i centers. Further, the Er_i moved deeper into the band gap, away from the valence band and towards the conduction band, apparently changing from a hole trap to an electron trap.

In Er-implanted p-type GaAs annealed at 750 °C, the hole carrier concentration was greatly enhanced relative to the substrate value. Furthermore, the profile of the density of holes by CV measurements followed the Er distribution measured by SIMS. Since a large concentration of the Er_i center was found by DLTS measurements for this sample, it was probably the Er_i center which was responsible for the increased p-type conductivity. Annealing at higher temperatures returned the hole profile of the Er-implanted sample to the uniform hole-carrier concentration of the substrate and reduced the concentration of the Er_i center, as verified by DLTS measurements.

In Er and Si co-doped MBE-grown GaAs, a significant reduction in the electron concentration was also observed. The DLTS measurements showed that this reduction was related to the appearance of the Er_i center, as well as to a hole trap located 150 meV above the valence band, which was not observed in the implanted samples. This center dissociated between the annealing temperatures of 750 and 825 °C. Since these samples were doped with Er at concentrations much in excess of the Er solubility limit in GaAs, it was thought that this center was related to the formation of ErAs micro-precipitates. However, for MBE-grown GaAs doped only with Er, p-type conductivity was observed. Temperature-dependent Hall effect measurements found a thermal activation energy of 340 meV, and thus, this conductivity was probably due to the Er_i center; i.e., center (g).

The mechanism for free-electron reduction in Si and Er co-doped, MBE-grown GaAs has not been conclusively established. Furthermore, for low Er concentrations, the electron concentration was not significantly reduced, indicating that neutral Er-Si complexes were not forming. Instead, the reduction in the free-electron concentration observed for $[Er] \gtrsim 2 \times 10^{19} \text{cm}^{-3}$ occurred suddenly (Figure 72). Therefore, this behavior appeared to be associated with the introduction of compensating defects induced when the solubility limit of Er in $Al_{0.5}Ga_{0.5}As$ was exceeded. Thus, the solubility limit of Er in $Al_{0.5}Ga_{0.5}As$ was apparently 30 times higher than in GaAs, explaining the fact that Er emissions in MBE-grown AlGaAs were typically much more intense than in GaAs.

(b) Deep centers:

In the course of this research, as many as 14 different deep centers were identified. Their locations in the band gap, as well as descriptions of their possible microscopic natures, are given in Table 16. The assignment of a microscopic nature to each defect was based upon a review of the literature, as well as observations of the occurrence of the centers in the Er-doped samples.

Table 16. Summary of the various deep levels found in GaAs:Er and their likely microscopic natures

Center	Energy	Occurrence	Nature
Hole Traps			
(a)	$E_v + 35 \text{ meV}$	n-type and p-type Er-implanted GaAs, n-type and p-type Er-doped MBE-grown GaAs	Isolated Er_{Ga} center giving rise to an isoelectronic hole trap
(b)	$E_v + 96 \text{ meV}$	n-type and p-type Er-implanted GaAs, Cu-implanted GaAs	Cu-related center
(c)	$E_v + 77 \text{ meV}$	n-type and p-type Er-implanted GaAs, n-type Pr-implanted GaAs	Native defect; First acceptor level of Ga_{As}
(d)	Same as center (e)		
(e)	$E_v + 150 \text{ meV}$	n-type and p-type Er-implanted GaAs, n-type Pr-implanted GaAs	Native defect Related to damage
(f)	roughly $E_v + 200 \text{ meV}$	n-type Er-implanted GaAs	Native defect
(g)	$E_v + 360 \text{ meV}$	n-type and p-type Er-implanted GaAs, n-type Er-doped MBE-grown GaAs	Er_i
(h)	$E_v + 230 \text{ meV}$	n-type and p-type Er-implanted GaAs	Native defect; Second acceptor level of Ga_{As}
(i)	$E_v + 395 \text{ meV}$	n-type and p-type Er-implanted GaAs, n-type Pr-implanted GaAs	As_i -related or $\text{As}_i - \text{Cu}$ complex

Table 16. (Continued) Summary of the various deep levels found in GaAs:Er and their likely microscopic natures

Center	Energy	Occurrence	Nature
(i)	$E_v + 445 \text{ meV}$	n-type and p-type Er-implanted GaAs, n-type Pr-implanted GaAs	Native defect; As _i -related
(k)	$E_v + 540 \text{ meV}$	n-type and p-type Er-implanted GaAs, n-type Pr-implanted GaAs, n-type and p-type MOCVD GaAs	Fe-related or Fe-Native defect complex
Electron Traps			
(l)	$E_c - 610 \text{ meV}$	n-type Er-implanted GaAs, n-type MOCVD GaAs	M3 center; native acceptor - shallow donor complex
(m)	$E_c - 840 \text{ meV}$	n-type Er-implanted GaAs, Only observed for Er fluence of $5 \times 10^{12} \text{ cm}^{-2}$	Native defect; EL2a of isolated As _{Ga}
(n)	$E_c - 785 \text{ meV}$	n-type Er-implanted GaAs, n-type MOCVD GaAs	Native defect; EL2b of As _{Ga} - V _{As} complex

Centers (a) and (g) have been observed in both Er-implanted and MBE-grown Er-doped GaAs, and both are thought to be Er-related centers. Center (a) was assigned to an isolated Er_{Ga} acting as an isoelectronic center since:

- It has a very weak potential, typical of isoelectronic centers.
- Isoelectronic centers have been reported for Er and Yb in InP.
- REs preferentially occupy the cation site.
- It occurs preferentially for higher annealing conditions, consistent with the RBS measurements of Kozanecki(49), which showed that Er atoms were substitutional after high tem-

perature anneals.

Similarly, center (g) was assigned to the Er_i since:

- RBS measurements indicated that GaAs:Er, highly doped either by ion implantation or during MBE growth, has a large concentration of Er in the interstitial positions.
- With the Er-implanted samples, RBS measurements showed that the concentration of interstitial Er decreased with increasing annealing temperature, similar to the DLTS results for center (g) obtained in the present study.
- Er has been shown to diffuse interstitially by Zhao (109).

(c) Excitation and Quenching Mechanisms

The assignment of the (a) and (g) centers to the Er_{Ga} and Er_i , respectively, were made on the basis of the DLTS measurements and annealing studies performed in this research, as well as the RBS measurements performed by Kozanecki (49). These measurements showed that the Er_i has a much higher probability for excitation than does the Er_{Ga} , based on an enhancement of the electric dipole transition moment for the Er_i by the noncentrosymmetric crystal field.

The excitation models proposed for the Er-4f shell are similar to the model for the excitation of the Yb-4f shell in InP proposed by Takahei, since both utilize a localized and mobile electric dipole, or an exciton. However, unlike the case of Yb in InP, the energy of the first excited state of the Er-4f shell is far from resonance with the exciton energy, requiring the presence of a third particle in all the excitation models in order to conserve energy. Due to the location of the Er-related electron levels in the band gap, the particle carrying away the excess energy must be a hole.

Models T2b and T2c have also been proposed to explain the excitation and quenching of the 4f luminescence of the (g) center. These processes involve the direct absorption of a laser photon, exciting the 4f shell and exchanging an electron between the (g) center and the bands. Model T2b agrees with the observations of below-band-gap excitation of the Er-4f shell by Colon et al. (19) and Klein et al., (46).

In addition to the (a) and (g) centers, Klein et al. (46) have identified two other optically-active centers. The thermal quenching of the 4f emissions of these centers provided activation energies which were similar to the activation energies measured by DLTS for the Ga_{As} center (c) and the As_i -related center (j). The intensities of the 4f emissions associated with these centers

were similar to those of the Er_i center, suggesting that they were also related to Er on noncubic sites. Klein also found from absolute EPR measurements that only a minute fraction of the Er was in the $3+$ charge state, while the PL measurements indicated that a much larger fraction participated in the 4f emissions of the Er^{3+} . This behavior implied that the Er centers were in the $2+$ charge state prior to excitation, and in the $3+$ charge state after excitation. A model was proposed to account for all of these observations. Since the DLTS measurements have found a large concentration of Ga_{As} defects and As_i -related centers, it is reasonable to assume that the T1a and T1b centers which Klein measured are due to the $\text{Er}_{\text{Ga}} - \text{Ga}_{\text{As}}$ and $\text{Er}_{\text{Ga}} - \text{As}_i$ centers, respectively. It was further assumed that, because of the presence of the neighboring defect, the Er is more likely to be in the $2+$ charge state. Upon laser excitation, an exciton is generated, which recombines at this center, simultaneously ionizing it and exciting the 4f shell.

While the excitation and quenching mechanisms postulated here agree with the available experimental evidence, they do not constitute a conclusive proof. Further experimental and theoretical work is necessary. For instance, experiments have already been suggested to verify or refute excitation and quenching models T2b and T2c. Furthermore, a definitive model would require a complete agreement between the experimental observations and quantum-mechanical predictions of the transition probabilities. As already mentioned, the quantum-theoretical predictions for the transfer of an exciton-recombination energy into the 4f core has only been considered for the case of a near resonance transition (76). The quantum-mechanical calculations become much more complicated with the presence of a third particle which is necessary for the conservation of energy during the excitation of the Er-4f shell in GaAs. In fact, calculations which have been limited to the simplest case of determining the energy position of the one-electron 4f-states with respect to the band edges. These calculations have only been performed for the configuration in which the RE is on the cation site. In contrast, calculations performed while the RE in an interstitial position would certainly be much more challenging. Even in the former relatively simple situation, there is a lack of consensus. For instance, using the self consistent Green's function technique, Delerue and Lannoo (24) have concluded that the 4f levels for Er_{In} are typically resonant with the valence band in InP. However, the more recent calculations by Sato and Kimura (79) using local-density-functional DV- $X\alpha$ cluster calculations have found that the 4f states for Er^{3+} and Yb^{3+} ions in InP, GaP, and GaAs appear in the energy gap of these semiconductors, usually just above the valence band. Thus, regardless of the model

proposed, it may be difficult to prove theoretically. Nevertheless, the models proposed here may be used as a guide for future theoretical investigations.

7.2 Overall Behavior of Er-Doped GaAs

When the heavy Er atom is accelerated to an energy of 1 MeV and driven into the GaAs crystal, there is little doubt that the region of the implant will be in an amorphous or nearly amorphous state (of course except for very low Er fluences). As the implanted sample is annealed, this damaged epilayer will tend to regrow, with the substrate acting as a seed crystal. The Er atoms, metallic ions with a similar valence to the Ga atom, will have a tendency to occupy the Ga site in the GaAs crystal. For annealing temperatures below 700 °C, very little crystal damage will be repaired. Thus, for optical excitation, most of the laser energy may pass through this layer without generating electron-hole pairs to excite the Er. As the annealing temperature is increased, the crystal structure will be increasingly restored. However, a large concentration of the Er atoms will continue to occupy interstitial sites or will form complexes with other native defects. Consequently, the laser excitation can generate electron hole-pairs which will migrate to these Er_i -centers or Er-defect complexes. The 4f shells of these Er centers have a much higher probability for excitation than an isolated Er^{3+} center, because they are on sites which lack inversion symmetry. Therefore, the crystal field will tend to mix in 5d states, greatly enhancing the probability for an electric dipole transition. As annealing temperatures are increased, Er tends to occupy a Ga site with As nearest neighbors. Thus, an isolated Er_{Ga} center is formed. The Er is in the 3+ charge state and gives rise to an isoelectronic impurity potential which tends to bind holes. Unfortunately, the crystal field at this T_d site apparently does not act to enhance the oscillator strengths for electric dipole transitions in the 4f-shell. Consequently, the Er-4f luminescence for the GaAs:Er samples annealed at higher temperatures, where isolated Er_{Ga} centers are dominant, is weak.

In the case of the MBE-grown, Er-doped GaAs, the formation of various Er-centers seems to be controlled primarily by the doping density. For low Er-doping, only the shallow isoelectronic center Er_{Ga} is formed, and so no Er^{3+} emissions are observed. However, as the Er doping density increases, there is an increased likelihood of the Er occupying an interstitial position, as evidenced by the 360 meV hole trap found in the heavily Er-doped MBE samples. Finally, for higher doping densities, the Er begins to form micro-precipitates of ErAs, which quenches

the Er-4f luminescence.

7.3 Recommendations

This work should be used as a guide for future studies into the electrical and optical properties of RE elements in III-V semiconductors. Research should continue along two general lines:

- A broader study of other REs in III-V semiconductors.
- An attempt to maximize the Er-4f luminescence excitation, leading to possible LED applications.

Broader Study:

The primary motivation for studying the RE Er was that the transition from its first excited state $^4I_{13/2}$ to its ground state $^4I_{15/2}$ gives an emission with a wavelength close to the wavelength of minimum attenuation for optical fibers. In an initial study, Pr emissions were found to be much more intense than Er emissions. Further, as shown in Figure 1, the Pr emissions at $1.3\ \mu\text{m}$ are also near the minimum in attenuation, as well as the minimum in dispersion. Thus, the Pr atom may provide a good alternative to Er for LED applications.

It may also be possible to form a more complete understanding of the electrical and optical behavior of the REs in III-V compounds by studying the similarities and differences in a sequence of these elements. For example, preliminary Hall effect measurements have shown that like Er, the RE elements praseodymium (Pr) and neodymium (Nd) do not show a clear trend of introducing shallow donors or acceptors in GaAs. This feature may indicate that they form the same type of centers as Er forms in GaAs. Thus, a DLTS study of the deep centers formed by these REs would be useful. Additionally, since these atoms have somewhat larger ionic radii, it would be interesting to determine if they also give rise to isoelectronic hole traps in GaAs. In addition, the study of a sequence of REs in GaAs may facilitate a more general understanding of the nature of the isoelectronic impurity potential and the contribution of the 4f core electrons to this potential.

Nd and Pr in GaAs have more intense 4f luminescence than does Er, as demonstrated in the annealing studies given in Figures 79 and 80. There are two interesting points of contrast between these annealing studies and those of Er shown previously. First, for both Pr and Nd, there are no broad bands, as was observed for the Er-doped sample in the annealing study shown

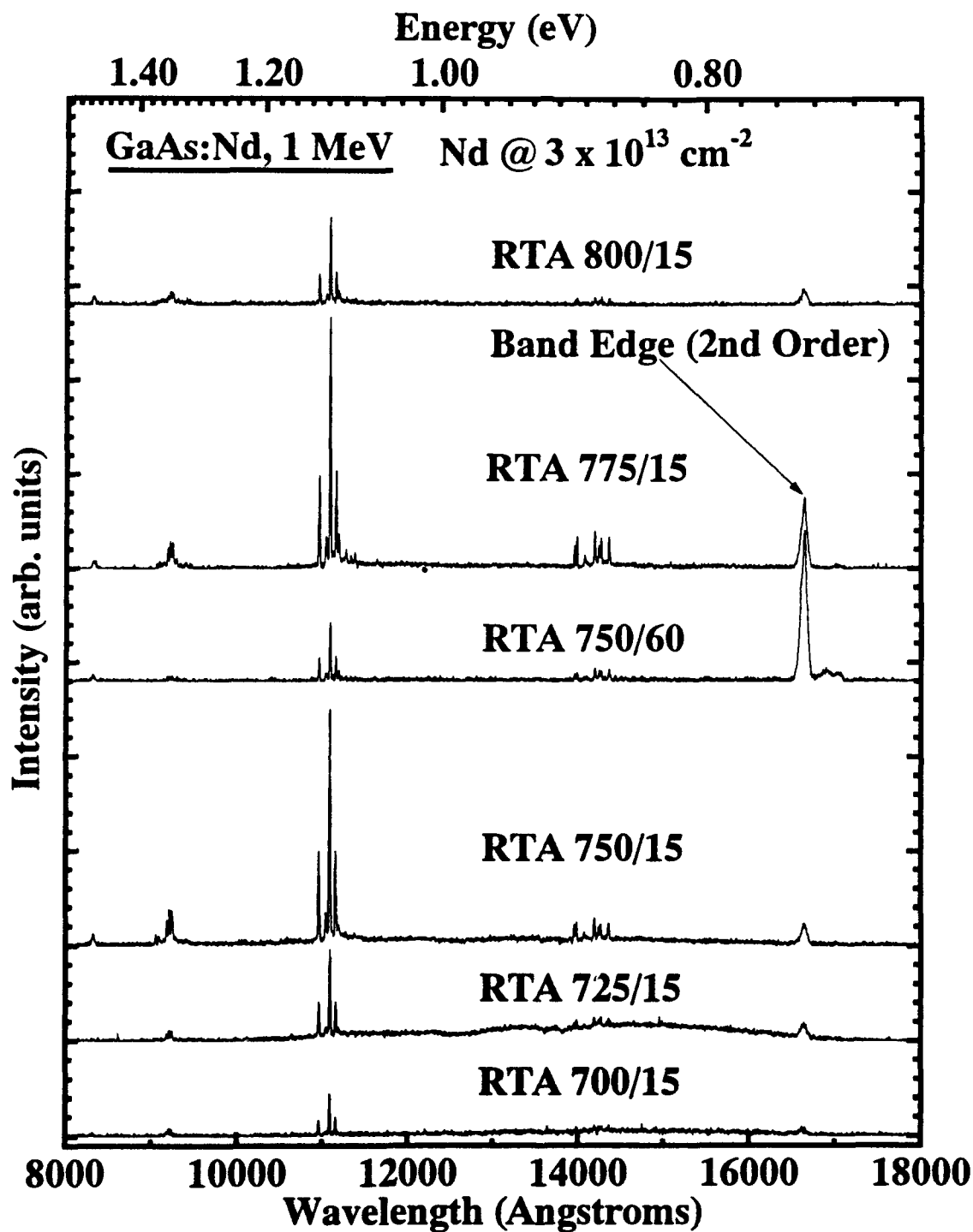


Figure 79. PL measurements of GaAs:Nd, with Nd implanted at a fluence of $\Phi_{\text{Nd}} = 3 \times 10^{13} \text{ cm}^{-2}$ and at an energy of 1 MeV that was rapid thermally annealed under the conditions listed in the figure

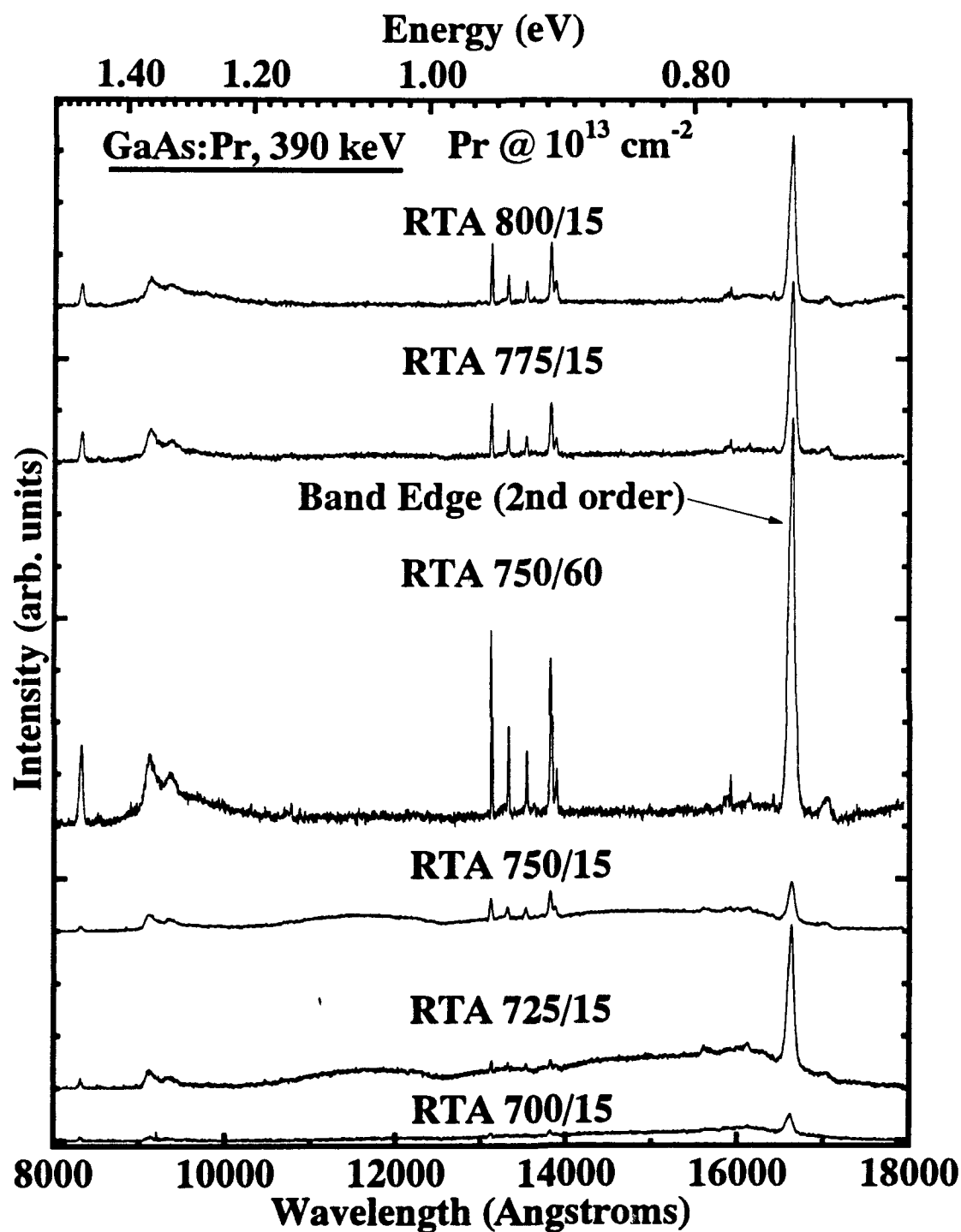


Figure 80. PL measurements of GaAs:Pr, with Pr implanted at a fluence of $\Phi_{\text{Pr}} = 10^{13} \text{ cm}^{-2}$ and an energy of 390 keV that was rapid thermally annealed under the conditions listed in the figure

in Figure 63. Thus, the intense broad band observed in the Er-doped sample is possibly related to a transition at the Er-atom, and is not due to implantation damage. It is possibly a radiative emission related to the pseudo-donor-acceptor transition shown in Figure 73 b. Secondly, in the Pr-doped samples, the 4f emissions correlate well with the band-edge emissions (strong or weak emissions in both observed at the same annealing temperature), while there seems to be a more complex behavior exhibited by the Nd-doped samples. Yet, in the Er-doped sample, the intensity of the band-edge emissions increases with annealing temperature, while the Er-emissions peak at 750 °C and then fall off sharply. Thus, future electrical and optical studies of the other REs in GaAs and AlGaAs are motivated.

Enhanced Er-luminescence:

The attempts at attaining Er-related electroluminescence in this study were unsuccessful, since they were accomplished before a careful study of the material properties of the Er-doped GaAs was completed. Such an investigation should be accomplished prior to the fabrication of devices. The findings in this dissertation may be used to obtain enhancement of the Er-4f emissions in GaAs and AlGaAs, and hopefully will contribute to the development of efficient electroluminescent devices.

Injection electroluminescence can be obtained for Er-implants into GaAs. Future Er-implantation should use various fluences and the highest energies possible (up to 5 MeV), so that thick, uniformly-doped layers may be produced. These layers will be useful both for electroluminescence as well as for characterization. P⁺ contacts for injection of minority carriers should be formed by Zn diffusion after an optimum anneal using the RTA of 750 °C for 60 seconds. However, the optimum annealing conditions may change for deeper Er implants, and another annealing study should be conducted.

The optimum annealing condition for GaAs:Er found in this study produced a maximum concentration of the optically-active Er_i center. Unfortunately, it is not possible to independently control the concentration of this center. Instead, an optically-active center whose concentration can be altered by selective doping is desirable. For instance, based upon the DLTS results, the optically-active T1 centers are thought to be related to Er_{Ga} - Ga_{As} or Er_{Ga} - As_i complexes. The concentration of these centers can be enhanced, either by implanting Ga or As, or growth under Ga-rich or As-rich conditions in the case of MBE or MOCVD material.

Alternately, other impurities which form optically-active complexes with Er may be introduced into the Er-doped layer, as was done in a study recently conducted at AFIT involving the co-implantation of O and Er into GaAs and AlGaAs substrates (20). In GaAs substrates, the O co-doping did not enhance the Er emissions. However, in $\text{Al}_x\text{Ga}_{1-x}\text{As}$ for $x \gtrsim 0.1$, a significant enhancement in the Er emissions was observed. Figure 81 shows the PL measurements at 4 K on an $\text{Al}_{0.29}\text{Ga}_{0.71}\text{As}:(\text{Er}+\text{O})$ with Er-implanted at a fluence of $\Phi_{\text{Er}} = 5 \times 10^{13} \text{ cm}^{-2}$ and at an energy of 1 MeV with O implanted at 110 keV at the various fluences as shown. All samples were annealed at 750 °C for 15 seconds using the RTA method. Further, the annealing study in Figure 82 shows that these emissions are definitely attributable to a different center than previously found, since they continue to increase even up to an annealing temperature of 850 °C. Finally, these emissions have been observed up to room temperature, so that the quenching or de-excitation involved with this O-related Er center is not as pronounced as with the other Er centers. Further studies, including an electroluminescence study, should definitely be conducted on AlGaAs:Er co-doped with O.

As found in this work, the solubility limit of Er in AlGaAs appears to be much higher than in GaAs. Therefore, if a source for MBE or MOCVD growth is available, further concentration-dependent studies should be performed. The most intense Er emissions observed were from an MBE-grown $\text{Al}_{0.5}\text{Ga}_{0.5}\text{As}:\text{Er}$ layer with $[\text{Er}] = 1.5 \times 10^{19} \text{ cm}^{-3}$. Unfortunately, p-type dopants were not available in the MBE system during this investigation, and so it was not possible to form p⁺n junctions for electroluminescence.

Finally, the impact excitation mechanism should also be investigated. Again, the findings of this work may be useful. For instance, the optically-active center (g) was found to be related to an Er_i , probably in the <110> crystal channel. This center would presumably have a much larger cross section for impact ionization than the center (a), attributed to an isolated Er_{Ga} . Implantation or growth carried out on a <110> oriented substrate might provide a significant enhancement for the likelihood of impact excitation.

In conclusion, through this work much knowledge of the electrical and optical behavior of Er in GaAs and AlGaAs has been gained. This information may be used as a guide for future research, which may eventually lead to the enhancement of the Er-4f emissions to such an extent that Er-doped LEDs or even semiconductor lasers may be feasible.

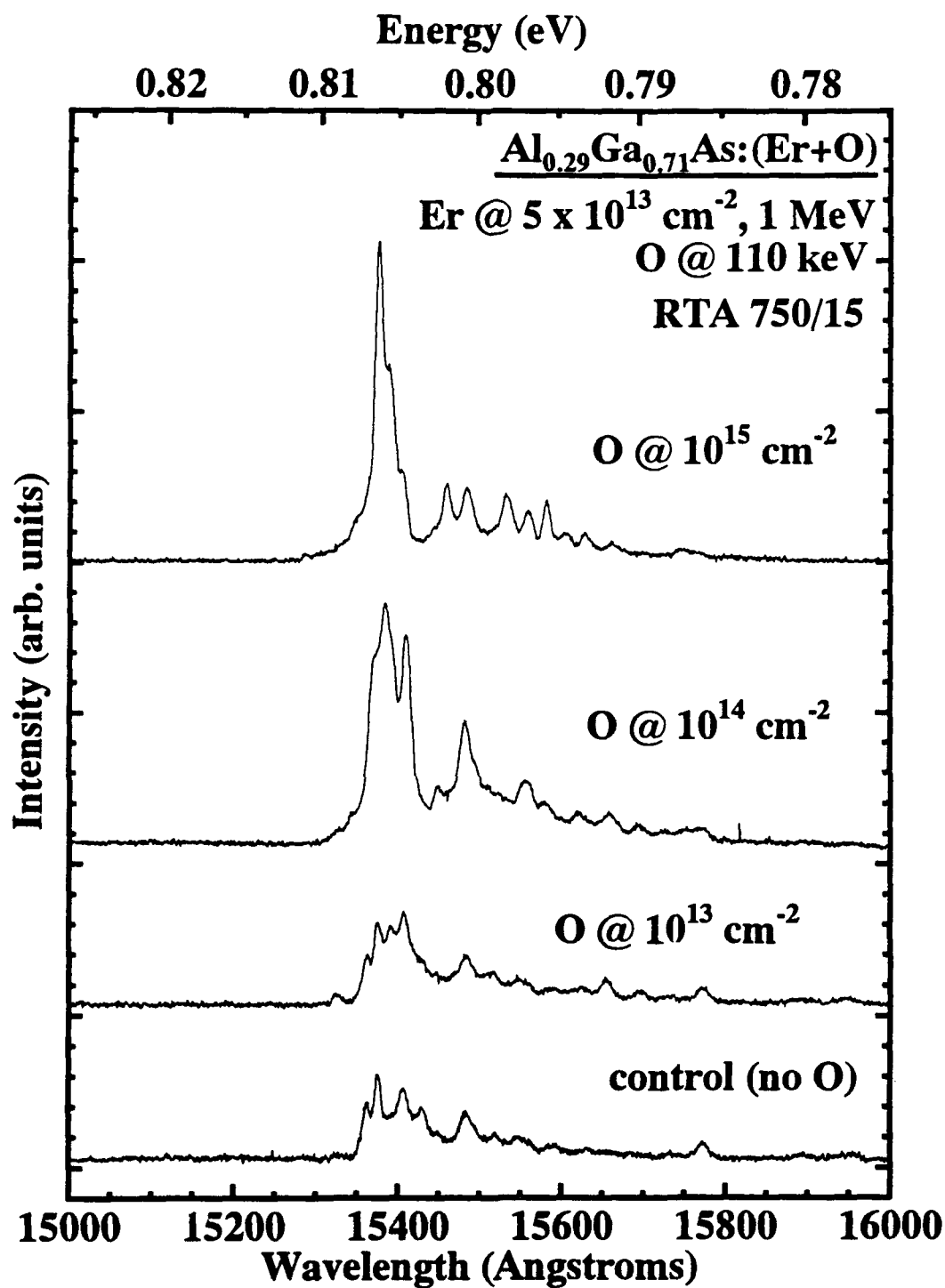


Figure 81. PL measurements of $\text{Al}_{0.29}\text{Ga}_{0.71}\text{As}:(\text{Er}+\text{O})$ with: (i) Er implanted at a fluence of $\Phi_{\text{Er}} = 5 \times 10^{13} \text{ cm}^{-2}$ and at an energy of 1 MeV, and (ii) O implanted with various fluences at an energy 110 keV, and rapid thermally annealed at 750 °C for 15 seconds

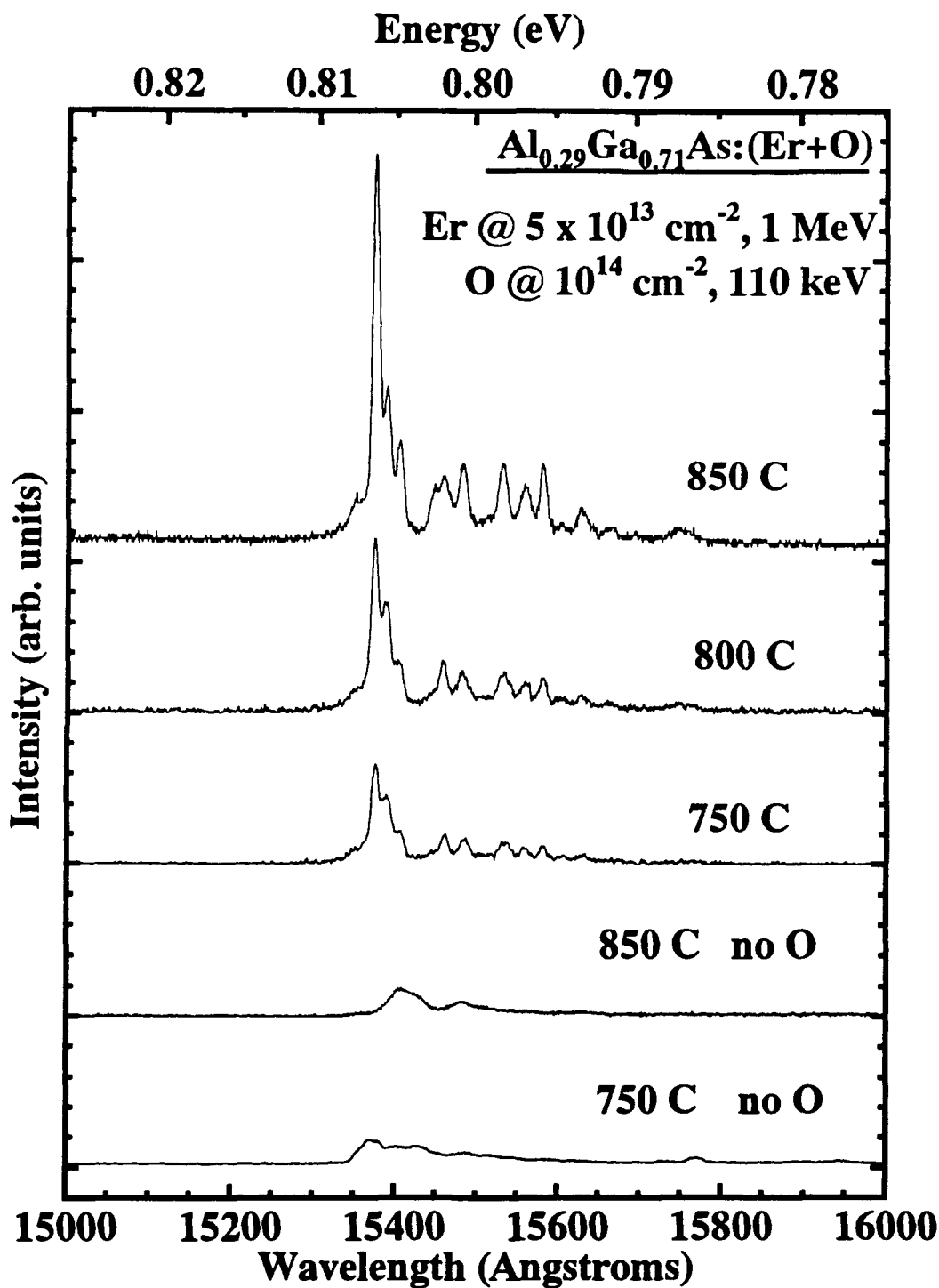


Figure 82. PL measurements of $\text{Al}_{0.29}\text{Ga}_{0.71}\text{As}:(\text{Er}+\text{O})$ with: (i) Er implanted at a fluence of $\Phi_{\text{Er}} = 5 \times 10^{13} \text{ cm}^{-2}$ at an energy of 1 MeV, and (ii) O implanted at a fluence of $\Phi_{\text{O}} = 10^{14} \text{ cm}^{-2}$ at an energy of 110 keV, and rapid thermally annealed under the conditions listed in the figure

Bibliography

1. Allen, J. W. "Isoelectronic impurities in semiconductors: a survey of binding mechanisms," *J. Phys. C: Solid State Phys.*, 4:1936–1944 (1971).
2. Ashcroft, Neil W. and N. David Mermin. *Solid State Physics*. Philadelphia: Saunders College, 1976.
3. Bagraev, N. T., et al. "Influence of rare-earth elements on the carrier mobility in epitaxial InP and InGaAs films," *Sov. Phys. Semicond.*, 18(1):49–50 (January 1984).
4. Baldereschi, A. "Theory of isoelectronic traps," *J. Luminescence*, 7:79–91 (1973).
5. Balramov, B. K., et al. "Influence of rare-earth elements on the properties of bulk InP single crystals," *Sov. Phys. Semicond.*, 23(8):927–929 (August 1989).
6. Bantien, F., et al. "Incorporation of erbium in GaAs by liquid-phase epitaxy," *J. Appl. Phys.*, 61(8):2803–2806 (April 1987).
7. Baranskii, P. I., et al. "Influence of ytterbium on electrophysical properties of epitaxial n-type GaP films," *Sov. Phys. Semicond.*, 22(1):98–100 (January 1988).
8. Bauerlein, R. "Displacement Thresholds in Semiconductors." *Radiation Damage in Solids*. 358–374. New York: Academic Press, 1962.
9. Bebb, H. Barry and E. W. Williams. "Photoluminescence I: Theory." *Semiconductors and Semimetals 8*, edited by R. K. Willardson and Albert C. Beer, chapter 4, New York: Academic Press, 1972.
10. Bleicher, M. and E. Lange. "Schottky-barrier capacitance measurements for deep level impurity determination," *Solid-State Electronics*, 16:375–380 (1972).
11. Blood, P. and J. J. Harris. "Deep states in GaAs grown by molecular beam epitaxy," *J. Appl. Phys.*, 56(4):993–1007 (August 1984).
12. Böer, Karl W. *Survey of Semiconductor Physics*, 2. New York: Van Nostrand Reinhold, 1992.
13. Bourgoin, J. and M. Lannoo. *Point Defects in Semiconductors II*. Berlin: Springer-Verlag, 1983.
14. Bourgoin, J. C., et al. "Native defects in gallium arsenide," *J. Appl. Phys.*, 64(9):R65–R91 (November 1988).

15. Boyn, R. "4f-4f luminescence of rare-earth centers in II-VI compounds," *Phys. Stat. Sol. (b)*, 148(11):11-46 (1988).
16. Buchwald, W. R., et al. "New metastable defects in GaAs," *Appl. Phys. Lett.*, 50(15):1007-1009 (April 1987).
17. Chand, Naresh, et al. "Comprehensive analysis of Si-doped $\text{Al}_x\text{Ga}_{1-x}\text{As}$ ($x=0$ to 1): theory and experiments," *Phys. Rev. B*, 30(8):4481-4492 (October 1984).
18. Chandra, Amitabh, et al. "Surface and interface depletion corrections to free carrier-density determinations by Hall measurements," *Solid-State Electronics*, 22:645-650 (1979).
19. Colon, J. E., et al. "Excitation mechanism of the erbium 4f emissions in GaAs." *Proceedings of the 16th International Conference on Defects in Semiconductors* 83-87. Materials Science Forum, edited by Gordon Davies, et al. 671-676. Trans. Tech. Publications, 1992.
20. C6lon, Jos6 E. *Luminescence Study of Ion-Implanted and MBE-Grown Er-doped GaAs and $\text{Al}_x\text{Ga}_{1-x}\text{As}$* . PhD dissertation, School of Engineering of the Air Force Institute of Technology, 1992. AFIT/DS/ENP/92-4.
21. Cotton, F. A. and G. W. Wilkinson. *Advanced Inorganic Chemistry* (2nd Edition). New York: Wiley & Sons, Interscience Publishers, 1966.
22. Cullis, A. G., et al. "Material-dependent amorphization and epitaxial crystallization in ion implanted AlAs/GaAs layer structures," *Appl. Phys. Lett.*, 55(12):1211-1213 (November 1989).
23. Dean, P. J. "Isoelectronic traps in semiconductors (experimental)," *J. Luminescence*, 7:51-78 (1973).
24. Delerue, C. and M. Lannoo. "Theory of Substitutional Rare Earth Impurities in Semiconductors." *Proceedings of the 16th International Conference on Defects in Semiconductors* 83-87. Materials Science Forum, edited by Gordon Davies, et al. 659-664. Trans. Tech. Publications, 1992.
25. Dieke, G. H. *Spectra and Energy levels of Rare Earth Ions in Crystals*. New York: Wiley & Sons, Interscience Publishers, 1968.
26. Elliot, K. R., et al. "Infrared absorption the 78-meV acceptor in GaAs," *Appl. Phys. Lett.*, 40(10):898-901 (May 1982).

27. Ennen, H. and J. Schneider. "Luminescence of rare earth ions in III-V semiconductors." *Proceedings of the Thirteenth International Conference on Defects in Semiconductors*, edited by L. C. Kimerling and Jr. J. M. Parsey. 115-127. 1984.
28. Ennen, H., et al. "Photoluminescence excitation measurements on GaAs:Er grown by molecular-beam epitaxy," *J. Appl. Phys.*, 61(10):4877-4879 (May 1987).
29. Evans, K. R., et al. "Molecular-beam epitaxial growth and characterization of erbium-doped GaAs and AlGaAs," *J. Vac. Sci. Tech. B.*, 10(2):870-872 (March 1992).
30. Faulkner, Roger A. "Toward a theory of isoelectronic impurities in semiconductors," *Phys. Rev.*, 175(3):991-1009 (November 1968).
31. Frenkel, J. "On pre-breakdown phenomena in insulators and electronic semiconductors," *Phys. Rev.*, 54:647 (1938).
32. Galtier, P., et al. "Erbium doping of GaAs, GaAlAs and GaAs/GaAlAs quantum wells by molecular beam epitaxy." *Inst. Phys. Conf. Ser. 96*. IOP Publishing, Ltd., 1988.
33. Galtier, P., et al. "1.54 μm room-temperature electroluminescence of erbium-doped GaAs and GaAlAs grown by molecular beam epitaxy," *Appl. Phys. Lett.*, 55(20):2105-2107 (November 1989).
34. Ghandi, Sorab K. *VLSI Fabrication Principles Silicon and Gallium Arsenide*. John Wiley and Sons, 1982.
35. Gorelenok, A. T., et al. "Density and mobility of electrons in InP and $\text{In}_{0.53}\text{Ga}_{0.47}\text{As}$ doped with rare-earth elements," *Sov. Phys. Semicond.*, 22(1):21-26 (January 1988).
36. Hemstreet, L. A. "The electronic states of a substitutional ytterbium atom in indium phosphide." *Defects in Semiconductors 10-12*. Materials Science Forum, edited by H. J. von Bardeleben. 85-90. Trans. Tech. Publications, 1986.
37. Henderson, B. and G. F. Imbush. *Optical Properties of Inorganic Solids*. Oxford: Clarendon Press, 1989.
38. Holmes, D. E., et al. "Effect of thermal history on properties of LEC GaAs." *Semi-Insulating III-V Materials*, edited by D. C. Look and J. S. Blakemore. 205-213. Cheshire, Eng: Shiva Publishing, 1984.
39. Hopfield, J. J., et al. "Isoelectronic donors and acceptors," *Phys. Rev. Lett.*, 17(6):312-315 (August 1966).

40. Ikossi-Anastasiou, Kiki. *Transient Capacitance Spectroscopy of Deep Levels in Epitaxial Silicon*. PhD dissertation, University of Cincinnati, 1986.
41. Ilegems, M., et al. "Optical and electrical properties of Mn-doped GaAs grown by molecular-beam epitaxy," *J. Appl. Phys.*, 46(7):3059–3065 (July 1975).
42. Jaros, M. *Deep Levels in Semiconductors*. Bristol: Adam Hilger, Ltd., 1982.
43. Jencic, I., et al. "A comparison of the amorphization induced in $\text{Al}_x\text{Ga}_{1-x}\text{As:Er}$ and GaAs by heavy-ion irradiation," *J. Appl. Phys.*, 69(3):1287–1292 (February 1991).
44. Kasatkin, V. A. and V. P. Savel'ev. "Excitation of ytterbium luminescence in gallium and indium phosphides," *Sov. Phys. Semicond.*, 18(9):1022–1023 (September 1984).
45. Keithley Instruments, Inc. *System 110: Hall Effect Measurement System User's Manual*. Cleveland, Oh, 1990.
46. Klein, P. B., et al. "Spectroscopic investigation of the Er site in GaAs:Er." *Proceedings of the 16th International Conference on Defects in Semiconductors* 83–87. Materials Science Forum, edited by Gordon Davies, et al. 665–670. Trans. Tech. Publications, 1991.
47. Klein, P. B., et al. "1.54 μm electroluminescence in MeV ion-implanted Er-doped GaAs." *Proceedings of the 16th International Conference on Defects in Semiconductors* 83–87. Materials Science Forum, edited by Gordon Davies, et al. 665–670. Trans. Tech. Publications, 1992.
48. Körber, W. and A. Hangleiter. "Excitation and decay mechanism of the intra-4f luminescence of Yb^{3+} in epitaxial InP:Yb layers," *Appl. Phys. Lett.*, 52(2):114–116 (1988).
49. Kozanecki, A., et al. "Lattice location of Er implanted into GaAs," *Solid-State Communications*, 78(8):763–766 (May 1991).
50. Lagowski, J., et al. "Identification of oxygen-related midgap level in GaAs," *Appl. Phys. Lett.*, 44(3):336–338 (February 1984).
51. Lambert, B., et al. "Electrical and optical properties of rare earth dopants (Yb, Er) in n-type III-V (InP) semiconductors," *Journal of Physics: Condensed Matter*, 2:479–483 (1990).
52. Lambert, B., et al. "Electrical activity of Yb in InP," *Electron. Lett.*, 24:1446–1447 (1988).
53. Lang, D. V. "Deep-level transient spectroscopy: a new method to characterize traps in semiconductors," *J. Appl. Phys.*, 45(7):3023–3032 (July 1974).

54. Lang, D. V. and R. A. Logan. "A study of Deep Levels in GaAs by Capacitance Spectroscopy," *J. Elec. Mater.*, 4(5):1053-1066 (1975).
55. Lannoo, M. and J. Bourgoin. *Point Defects in Semiconductors I: Theoretical Aspects*. Berlin: Springer-Verlag, 1983.
56. Look, D. C. "Statistics of multicharge centers in semiconductors: applications," *Phys. Rev. B*, 24:5852-5862 (November 1981).
57. Look, David C. *Electrical Characterization of GaAs Materials and Devices*. New York: John Wiley & Sons, 1989.
58. Loualiche, S., et al. "Electron irradiation in p-type GaAs," *J. Appl. Phys.*, 53:8691-8696 (December 1983).
59. Lozykowski, H. J. "New step impact electroluminescent devices," *Solid-State Communications*, 66(7):755-759 (1988).
60. Maiman, T. H. "Stimulated optical radiation in ruby masers," *Nature*, 187:493 (1960).
61. Martin, G. M., et al. "Electron traps in bulk and epitaxial GaAs crystals," *Electron. Lett.*, 13(7):191-192 (March 1977).
62. Maserov, V. F. and L. F. Zakharenkov. "Rare-earth elements in III-V semiconductors," *Sov. Phys. Semicond.*, 24(4):383-396 (April 1990).
63. Milnes, A. G. *Deep Impurities in Semiconductors*. New York: John Wiley & Sons, 1973.
64. Mitonneau, A., et al. "Hole traps in bulk and epitaxial GaAs crystals," *Electron. Lett.*, 13(22):755-759 (October 1977).
65. Moore, F. G., et al. "Type conversion of epitaxial GaAs layers after heavy ion MeV implantation and annealing," *Nuclear Instruments and Methods in Physics Research B*, 59-60:1103-1105 (1991).
66. Pantelides, Sokrates T. "The electronic structure of impurities and other point defects in semiconductor," *Rev. Mod. Phys.*, 50(4):795-858 (October 1978). Review Article.
67. Pearsall, T. P. and M. A. Pollack. "Compound Semiconductor Photodiodes." *Lightwave Communications Technology 22. Semiconductors and Semimetals*, edited by W. T. Sang, 173-245, New York: Academic Press, 1985.
68. Phillips. "Correlation Theorem for isoelectronic impurity binding energies," *Phys. Rev. Lett.*, 22:285 (1968).

69. Pomrenke, Gernot S. *Luminescence of Lanthanides and Actinides Implanted into Binary III-V Semiconductors and AlGaAs*. PhD dissertation, School of Engineering of the Air Force Institute of Technology, 1989. AFIT/DS/ENP/89-4.
70. Pomrenke, Gernot S., et al. "Photoluminescence optimization and characteristics of the rare-earth element erbium implanted in GaAs, InP, and GaP," *J. Appl. Phys.*, 59(2):601-610 (January 1986).
71. Pons, D. and J. C. Bourgoin. "Irradiation-induced defects in GaAs," *J. Phys. C: Solid State Phys.*, 18:3839-3871 (1985).
72. Poole, I., et al. "Growth and structural characterization of molecular beam epitaxial erbium-doped GaAs," *J. Crystal Growth*, 121:121-131 (1992).
73. Press, William H., et al. *Numerical Recipes*. New York: Cambridge University Press, 1986.
74. Raczynska, J., et al. "Donor gettering in GaAs by rare-earth elements," *Appl. Phys. Lett.*, 53(9):761-763 (August 1988).
75. Ransom, C. M., et al. "Modulating functions waveform analysis of multi-exponential transients for Deep-Level Transient Spectroscopy," *Mat. Res. Soc. Symp. Proc.*, 69:337 (1986).
76. Robbins, D. J. and P. J. Dean. "The effects of core structure on radiative and non-radiative metal ion substituents in semiconductors and phosphors," *Advances in Physics*, 27(4):499-532 (1978).
77. Sah, C. T. "Bulk and interface imperfections in semiconductors," *Solid-State Electronics*, 19:975-990 (1976).
78. Sah, C. T., et al. "Thermal and optical emission and capture rates and cross sections of electrons and holes at imperfection centers in semiconductors from photo and dark junction current and capacitance experiments," *Solid-State Electronics*, 13:759-788 (1970).
79. Saito, Riichiro and Tadamasa Kimura. "Cluster calculations of rare-earth ions in semiconductors," *Phys. Rev. B*, 46(3):1423-1428 (July 1992).
80. Schroder, Dieter K. *Semiconductor Material and Device Characterization*. New York: John Wiley and Sons, 1990.
81. Seghier, D., et al. "Electrical behavior of Yb ion in p- and n-type InP," *Appl. Phys. Lett.*, 60(8):983-985 (February 1992).

82. Shockley, W. *Electrons and Holes in Semiconductors*. New York: Van Nostrand, 1950.
83. Smith, R. S., et al. "Erbium doping of molecular beam epitaxial GaAs," *Appl. Phys. Lett.*, 50(1):49-51 (January 1987).
84. Stievenard, D., et al. "Irradiation-induced defects in p-type GaAs," *Phys. Rev. B*, 34(6):4048-4057 (September 1986).
85. Stradling, R. A. and P. C. Klipstein. *Growth and Characterization of Semiconductors*. Bristol: Adam Hilger, 1990.
86. Sze, S. M. *Physics of Semiconductor Devices*. New York: John Wiley & Sons, 1981.
87. Ta, L. B., et al. "Evidence of the role of boron in undoped GaAs grown by liquid encapsulated Czochralski," *Appl. Phys. Lett.*, 41(11):1091-1093 (December 1982).
88. Taguchi, Akihito, et al. "Optical and electrical properties of ytterbium-doped GaAs grown by metalorganic chemical vapor deposition," *J. Appl. Phys.*, 68(7):3390-3393 (October 1990).
89. Takahei, K., et al. "Intra-4f-shell luminescence excitation and quenching mechanism of Yb in InP," *J. Appl. Phys.*, 66(10):4941-4945 (November 1989).
90. Takahei, Kenichiro and Akihito Taguchi. "Energy transfer in rare-earth-doped III-V semiconductors." *Proceedings of the 16th International Conference on Defects in Semiconductors* 83-87. Materials Science Forum, edited by Gordon Davies, et al. 641-652. Trans. Tech. Publications, 1992.
91. Tsang, W. T. and R. A. Logan. "A new high-power, narrow-beam transverse-mode stabilized semiconductor laser at 1.5- μ m: the heteroepitaxial ridge-overgrown laser," *Appl. Phys. Lett.*, 45(10):1025-1027 (November 1984).
92. Tsang, W. T. and R. A. Logan. "Observation of enhanced single mode operation in 1.5- μ m GaInAsP erbium-doped semiconductor injection lasers," *Appl. Phys. Lett.*, 49(25):1686-1688 (December 1986).
93. Uwai, Kunihiko, et al. "Yb-doped InP grown by metalorganic chemical vapor deposition," *Appl. Phys. Lett.*, 50(15):977-979 (April 1987).
94. van der Pauw, J. P. "A method for measuring specific resistivity and Hall effect of discs of arbitrary shape," *Phillips Res. Reports*, 13(1):1-9 (February 1958).
95. van der Ziel, J. P., et al. "Single longitudinal mode operation of Er-doped 1.5- μ m GaInAsP lasers," *Appl. Phys. Lett.*, 50(19):1313-1315 (May 1987).

96. Voronina, T. I., et al. "Properties of epitaxial gallium arsenide films doped with rear-earth elements," *Sov. Phys. Semicond.*, 22(1):91-92 (January 1988).
97. Wang, W. L., et al. "On the physical origins of the EL2 center in GaAs," *J. of the Electrochemical Society*, 133(1):196-199 (1986).
98. Whitney, Peter S., et al. "Electrical properties of ytterbium-doped InP grown by metalorganic chemical vapor deposition," *Appl. Phys. Lett.*, 53(21):2074-2076 (November 1988).
99. Williams, E. W. and H. Barry Bebb. "Photoluminescence II: Gallium Arsenide." *Semiconductors and Semimetals 8*, edited by R. K. Willardson and Albert C. Beer, chapter 5, New York: Academic Press, 1972.
100. Willmann, F., et al. "Optical properties of excitons bound to copper-complex centers in gallium arsenide," *Phys. Rev. B*, 7:2473-2480 (March 1973).
101. Willmann, F., et al. "Complex nature of the copper acceptor in gallium arsenide," *Solid-State Communications*, 9:2281-2284 (1971).
102. Wu, Meng-Chyi, et al. "Erium doping in InGaAsP grown by liquid-phase epitaxy," *J. Appl. Phys.*, 71(1):456-461 (January 1992).
103. Yariv, Amnon. *Quantum Electronics* (2nd edition Edition). New York: John Wiley & Sons, 1975.
104. Yu, Phil Won, et al. "Evidence of intrinsic double acceptor in GaAs," *Appl. Phys. Lett.*, 41(6):532-534 (September 1982).
105. Yu, Phil Won and D. C. Reynolds. "Photoluminescence identification ~ 77-meV deep acceptor in GaAs," *J. Appl. Phys.*, 53(2):1263-1265 (February 1982).
106. Zakharenkov, L. F., et al. "Photoluminescence of epitaxial InP:Yb films," *Sov. Phys. Semicond.*, 15(8):946 (1981).
107. Zakharenkov, L. F., et al. "Influence of the electron density on the efficiency of excitation of Yb³⁺ in InP:Yb," *Sov. Phys. Semicond.*, 23(8):941-942 (August 1989).
108. Zakharenkov, L. F., et al. "Influence of Lanthanoids on electrical properties of bulk InP crystals," *Sov. Phys. Semicond.*, 21(2):211 (February 1987).
109. Zhao, Xinwei, et al. "Diffusion and photoluminescence of erbium in GaAs and InP." *Gallium Arsenide and Related Compounds 1988* Number 96 in Inst. Phys. Conf. Ser., 277-282, IOP publishing, 1988.

Vita

Captain David W. Elsaesser was born on 7 March 1962 in Cincinnati, Ohio. He graduated from Elder High School of Cincinnati in 1980. He remained in this fine city to attend Xavier University, from which he earned a Bachelor of Science degree in Physics in 1984. Upon graduation he received a reserve commission in the USAF and was directly extended into the Graduate Engineering Physics program at the Air Force Institute of Technology, Wright-Patterson AFB, in pursuit of a Master's degree. He received that degree in December of 1985, having performed a thesis entitled, "Surface Depletion Width Correction to Carrier Profiles by Hall Effect Measurements". With this background in the electrical characterization of semiconductors he served as a Semiconductor Research Physicist at the Air Force Avionics Laboratory (now Solid State Electronic Directorate of Wright Labs). His duties mainly involved the electrical characterization of semiconductors using the Deep Level Transient Spectroscopy experimental technique. While at the Lab he received a regular commission in the USAF. After serving at Wright Labs for three and a half years he was accepted into the doctoral program of the School of Engineering of the Air Force Institute of Technology. His present position is that of a Semiconductor Research Physicist at Rome Laboratory, Hanscom AFB. His duties involve growth and characterization of indium phosphide.

PermanentAddress:

215 Anderson Ferry Rd.
Cincinnati, Ohio
45238

REPORT DOCUMENTATION PAGE			Form Approved OMB No 0704-0188	
<small>Public reporting burden for this collection of information is estimated to average 1 hour per response, including the time for reviewing instructions, searching existing data sources, gathering and maintaining the data needed, and completing and reviewing the collection of information. Send comments regarding this burden estimate or any other aspect of this collection of information, including suggestions for reducing this burden, to Washington Headquarters Services, Directorate for Information Operations and Reports, 1215 Jefferson Davis Highway, Suite 1204, Arlington, VA 22202-4302, and to the Office of Management and Budget, Paperwork Reduction Project (0704-0188), Washington, DC 20503.</small>				
1. AGENCY USE ONLY (Leave blank)		2. REPORT DATE December 1992		3. REPORT TYPE AND DATES COVERED Doctoral Dissertation
4. TITLE AND SUBTITLE Excitation and De-excitation Mechanisms of Er-doped GaAs and AlGaAs			5. FUNDING NUMBERS	
6. AUTHOR(S) David W. Elsaesser, Captain, USAF				
7. PERFORMING ORGANIZATION NAME(S) AND ADDRESS(ES) Air Force Institute of Technology, WPAFB OH 45433-6583			8. PERFORMING ORGANIZATION REPORT NUMBER AFIT/DS/ENP/92-05	
9. SPONSORING MONITORING AGENCY NAME(S) AND ADDRESS(ES) Lt Col Gernot S. Pomrenke AFOSR/NE (Bldg 410) Bolling AFB DC 20332-6448			10. SPONSORING MONITORING AGENCY REPORT NUMBER	
11. SUPPLEMENTARY NOTES				
12a. DISTRIBUTION AVAILABILITY STATEMENT Approved for public release; distribution unlimited			12b. DISTRIBUTION CODE	
13. ABSTRACT (Maximum 200 words) <p>Electrical and optical characterization have been performed on GaAs and Al_{0.3}Ga_{0.7}As samples doped with Er either by ion implantation or during Molecular Beam Epitaxial (MBE) growth. Deep Level Transient Spectroscopy (DLTS) and Temperature-Dependent Hall Effect (TDH) measurements indicated the presence of two hole traps in Er-doped GaAs, at 35 and 360 meV above the valence band maximum. The former (shallower) center was thought to be due to Er substituting for a Ga atom (Er_{Ga}) and giving rise to an isoelectronic impurity potential. The second center was attributed to an Er atom occupying an interstitial position (Er_i). Annealing studies performed on Er-implanted GaAs indicated that the Er_{Ga} center preferentially formed at higher annealing temperatures (> 850 °C), with the Er_i reaching a maximum concentration at an annealing temperature of around 750 °C. Optical characterization performed by Photoluminescence (PL) measurements showed that the Er_i center gave a much stronger Er-related intra-4f shell emission. Mechanisms for the excitation of the 4f shells of these two centers are discussed. Similar optically active Er_i centers may be forming in AlGaAs.</p>				
14. SUBJECT TERMS rare earth, Er, DLTS, isoelectronic, GaAs, AlGaAs, ion implantation, MBE, luminescence, Hall Effect			15. NUMBER OF PAGES 212	
			16. PRICE CODE	
17. SECURITY CLASSIFICATION OF REPORT Unclassified	18. SECURITY CLASSIFICATION OF THIS PAGE Unclassified	19. SECURITY CLASSIFICATION OF ABSTRACT Unclassified	20. LIMITATION OF ABSTRACT UL	